Numerical simulation of a forced- and freely-vibrating cylinder at supercritical Reynolds numbers

Master of Science Thesis

A.H.P. Derksen

Delft University of Technology

TU Delft

SIEMENS Gamesa
RENEWABLE ENERGY

Numerical simulation of a forced- and freely-vibrating cylinder at supercritical Reynolds numbers

Master of Science Thesis

by

A.H.P. Derksen

For obtaining the degree of Master of Science in Aerospace Engineering
at Delft University of Technology

May 30, 2019

Student number:	4231368	
Project duration:	January 15, 2018 – June 12, 2019	
Thesis committee:	Prof. Dr. S.J. Watson	TU Delft - Chairman
	Dr. Ir. A.H. van Zuijlen	TU Delft
	Dr. Ir. M. Pini	TU Delft
	Dr. Ir. A.C. Viré	TU Delft - Supervisor
	M.A.M. Folkersma, MSc	TU Delft
	Dr. Ir. S.N. Voormeeren	Siemens Gamesa Renewable Energy
	Ir. K. Sarwar	Siemens Gamesa Renewable Energy

Wind Energy Research Group, Faculty of Aerospace Engineering, Delft University of Technology

Siemens Gamesa Renewable Energy

TU Delft Delft University of Technology

SIEMENS Gamesa RENEWABLE ENERGY

Summary

Introduction One of the main consequences of recent innovations in wind turbines, for improvement of the cost effectiveness, is the scaling up of the rotor size and hence the turbine tower. The larger tower geometries make wind turbines more susceptible to vortex-induced vibrations. Besides the higher probability of vortex-induced vibrations with modern wind turbine structures, another factor that impacts the behaviour of the phenomenon is the large Reynolds numbers. Typically, because of the large structure and considerable wind speeds, the wind turbines may reach Reynolds numbers as high as $Re > 3.5 \cdot 10^6$ (known as the supercritical Reynolds regime). It has appeared that the vortices behind the turbine tower may show different features at these high Reynolds numbers. The following research objective was defined for this MSc thesis: *To help Siemens Gamesa define a more physically representative VIV model accounting for the large-scale effects by analyzing the critical parameters influencing VIV.* From the literature study, it was concluded that the combination of investigating an oscillating cylinder at supercritical Reynolds number is a novel research area. Furthermore, the Reynolds number and the cylinder oscillations (fluid-structure interaction) are both considered to be a critical influencing parameter causing VIV. Therefore, the following research question was defined: *What is the fluid-structure interaction effect of a transversely oscillating cylinder exposed to VIV at supercritical Reynolds numbers?*

The present MSc research has investigated VIV by conducting a computational fluid dynamics (CFD) simulation with the open-source code *OpenFOAM* [1]. The following three canonical VIV cases have been investigated in the present research: stationary, forced-vibrating and free-vibrating cylinder. All these three cases have been analyzed for both the laminar regime (which was defined as $80 < Re < 200$) and supercritical Reynolds regime ($Re > 3.5 \cdot 10^6$).

Laminar regime In the laminar regime, $80 < Re < 200$, all three modelling set-ups (stationary, forced- and freely-vibrating) have been verified by comparing the results with other numerical studies. All three modelling configurations showed good agreement with literature. Grid and temporal convergence has been achieved for the stationary and forced-vibrating cylinder cases. It was concluded confidence was obtained on the three models to use them for the turbulent cases.

Supercritical regime: stationary cylinder The stationary cylinder case in the supercritical regime showed the turbulence model was deemed as reliable, although no spatial convergence was observed. The verification study demonstrated the presently used turbulence model performed well as the results fell within the range of numerical data found in literature. The URANS performed well compared to two different DES studies found in the supercritical regime. The validation study showed the predicted lift coefficient and separation angle by URANS agreed fairly well with the experimental values, while the mean drag coefficient and Strouhal number deviated considerably. It was reasoned that URANS was not able to capture the separation phenomenon well, leading to an inaccurate drag coefficient and Strouhal number.

Supercritical regime: forced-vibrating cylinder Firstly, a clear lock-in band has been observed for the forced-vibration model by analyzing the predicted aerodynamic forces, phase angle behaviour and effective added mass coefficient. It was shown by the forced-vibrating results that under certain operating conditions, a unusual large lift magnification factor was predicted. This prediction has been explained by the added mass effect. Just before the critical frequency, an unstable trajectory was observed where the aerodynamic damping increased for higher oscillation amplitudes. Around the critical frequency, the wake showed a change of the vortex pattern which coincided with a phase angle switch. This in turn yielded a negative aerodynamic damping. This 'switching mechanism' observed in the wake corresponded with earlier observations in literature. Then, after the switch the phase angle increased again and approached a value around zero degrees.

The comparison of the forced-vibration results with the wind-tunnel experiment of [2] showed the lift magnification and aerodynamic damping predicted by the present CFD model agreed fairly well with the experiment before the critical frequency for $y^*_{max} = 0.015-0.025$. The results for the lowest amplitude, $y^*_{max} = 0.0035$, showed bigger deviations between the experiment and the CFD model. Moreover, the experiment

showed a sharper rise of the aerodynamic damping around the critical frequency which the CFD model did not predict. Nevertheless, the predicted switching mechanism and timing of this mechanism was predicted well by the CFD model compared to the wind-tunnel experiment.

Supercritical regime: free-vibrating cylinder The following operating conditions were investigated: $1.9 < U^* < 10.7$; $2.8 \cdot 10^6 < Re < 1.6 \cdot 10^7$; $m^* = 29.6$ and $\zeta = 0.003$. A lift magnification factor of $M_{C_L} \approx 10$ and drag magnification factor of $M_{C_D} \approx 1.5$ were both found to be the largest magnifications. The maximum non-dimensional oscillation amplitude was found to be $y^*_{max} = 0.52$. The typical characteristics of VIV found for lower Reynolds number in the literature (see compilation in [3]) were found to be present for supercritical Reynolds numbers.

During lock-in, the aerodynamic force signals did not show a constant amplitude over time. In fact, it was demonstrated by the phase angle behaviour and changes in the wake pattern that a continuous alteration between self-excitation and self-limitation of the FSI was present. The wake restructuring was found to be in line with the 'switching mechanism' found earlier for the forced-vibration results. Because of the alteration, no steady-state equilibrium was found where the energy transfer between the structure and fluid remained constant over time. Closely before the critical frequency, divergence was observed. It was believed the divergence was mathematically plausible and not a consequence of a numerical problem. This was supported by the convergence of the relative transverse (cylinder) velocity error. The divergence was believed as realistically possible. The results from the forced-vibration cases from the present work and the wind-tunnel data from [2] showed that unstable trajectories can occur under the operating conditions where divergence was observed. The damping coefficient, it was concluded, was too small to suppress this unstable trajectory.

Besides these observations, the effect of the mass coefficient and damping coefficient on the fluid-structure interaction was addressed as well in the present research. It was suggested that a sufficiently large mass coefficient would lead to a nearly stationary response (say $m^* > 59$). For a very low mass ratio ($m^* < 3$), the cylinder supposedly showed a stronger lock-in response. When the mass ratio was in-between the critical mass ratio and the very small mass ratio ($10 < m^* < 40$), it appeared the system yielded a more dynamic FSI response where the energy transfer between the structure and the fluid varied over time. These cases yielded high aerodynamic peak forces and were the most susceptible to changes in response when the reduced velocity was varied. The effect of the damping coefficient was considered to be less severe compared to the effect of the mass coefficient as the time series remained more similar when the damping was varied. For some of the operating conditions an increased damping coefficient lead to a significantly different response, in magnitude and qualitatively in the time series signal.

Conclusion In conclusion, this research has aimed to open up the relative new research area for supercritical Reynolds numbers by demonstrating the current CFD infrastructure (*OpenFOAM*, URANS and FSI coupling) is suitable for engineering work. Since no other numerical study has been found in the literature which has performed a similar combination of supercritical Reynolds numbers with FSI, the present research has delivered new insights and numerical data for this novel research area. Various typical VIV characteristics, known from the literature, have been observed in the supercritical regime. In addition, the FSI at supercritical Reynolds numbers has been investigated thoroughly by analyzing the aerodynamic damping, phase angle and wake patterns. All these results have addressed the research question. These insights have served to reach the research objective. From a practical perspective, relevant data was obtained by the CFD model for potential optimisation of a phenomenological model predicting VIV. At the same time, more importantly, the insights obtained regarding the fluid-structure interaction at supercritical Reynolds numbers have contributed to a better understanding of the VIV phenomenon for Siemens Gamesa. The addressed research question has provided a fundamental analysis of how the phenomenon originates and how it is influenced by two of the main influencing parameters. Although no effort has been undertaken in the present research to investigate the phenomenological models in more detail, this theory-oriented thesis indeed showed that the Reynolds number and the fluid-structure interaction effects should be modelled carefully in a phenomenological model. Further practical improvements of the phenomenological model are within the capabilities of the CFD infrastructure as has been demonstrated in the present research. This research has deliberately shared its modelling experiences and possible recommendations for future work to further exploit the potential of CFD to improve phenomenological models.

Acknowledgements

The project started with exploring all the possible research directions on vortex-induced vibrations. I realized that the topic vortex-induced vibrations offers plenty of research opportunities. After the research objective was defined, the project started to hit full throttle. Now, when I am reading my almost-finished report, I realize it has been quite a journey. I am proud we stuck to the initial research plan, although it was very ambitious. As the cliché goes: I have learned a lot on so many different levels, which I did not expect on beforehand. I am very happy with the final result and I truly hope more will come out of this research in the near future.

From Siemens Gamesa, I would first like to thank Kumayl Sarwar for all his help on this very exciting research project. As the topic was very broad, you have helped me in shaping the research very well and in defining a solid focus. Also, I appreciate your support on a personal level a lot. I would also like to thank Sven Voormeeren, for your refreshing views and for helping me to keep the overall picture. Furthermore, I would like to thank a few people in special from Siemens. Pim Versteijlen, for your tips and tricks and setting up the 'plan of attack'. Tom Broekhuijsen, for your fine jokes and the inspiring 1-on-1's. Ronald Verlinde, for running additional simulations with your structural model and for your input for the 3D beam. I also would like to thank my fellow students at Siemens for their advices, good conversations and football table games. Moreover, I would like to thank Siemens for offering me the great opportunity of writing my thesis there and for the inspiring environment. I have enjoyed it a lot to experience the very dynamic and exciting off-shore wind sector at first-hand.

From the TU Delft, I would first like to thank Axelle Viré for giving me the possibility to work on this novel and collaborative research project. Thank you for your continuous support during this project, patience and critical view on my work. Also, I am very grateful for your interest in sharing the work at the WESC conference. I would like to thank Mikko Folkersma for all his essential contributions to the CFD model and to the research in general. In addition, thank you for exploring the boundaries of *OpenFOAM*. Without that, most of the research ambitions would not have been realized. A special thank you to Alexander van Zuijlen for your interest in my research and all your help regarding the fluid-structure interaction. This has helped me greatly with solving most of the FSI-related modelling problems.

Last but not least, I would like to thank my father and sister in special for their relentless support and continuous encouragement during this project. This accomplishment would not have been possible without you. Furthermore, I would like to thank all my friends and family members who have supported me during the project. Thank you.

A.H.P. Derksen
Rotterdam, May 2019

Contents

List of Figures

List of Tables

Nomenclature

Symbol	Description	Unit
c	Structural damping	$N \cdot s/m$
c_a	Aerodynamic damping	$N \cdot s/m$
C_A	Truly added mass coefficient	$[-]$
C_L	Lift coefficient	$[-]$
C'_L	Fluctuating lift coefficient	$[-]$
$\overline{C'_L}$	Time-averaged fluctuating lift coefficient	$[-]$
$C_{L,max}$	Lift coefficient amplitude	$[-]$
$C_{L,rms}$	RMS of lift coefficient	$[-]$
$C_{L,rms,FSI}$	RMS of lift coefficient for oscillating cylinder	$[-]$
$C_{L,y}$	Lift coefficient in phase with transverse velocity	$[-]$
$C_{L,\dot{y}}$	Lift coefficient in phase with transverse velocity	$[-]$
$C_{L,\ddot{y}}$	Lift coefficient in phase with transverse acceleration	$[-]$
C_D	Drag coefficient	$[-]$
C'_D	Fluctuating drag coefficient	$[-]$
$C_{D,mean}$	Mean drag coefficient	$[-]$
Co	Courant number	$[-]$
C_p	Pressure coefficient	$[-]$
$C_{p,b}$	Base-pressure coefficient at $\theta = 180°$	$[-]$
C_f	Skin friction coefficient	$[-]$
C_{EA}	Effective added mass coefficient	$[-]$
D	Cylinder diameter	m
f_{shed}	Vortex shedding frequency	Hz
$f_{shed,stat}$	Vortex shedding frequency for stat. cylinder	Hz
$f_{shed,FSI}$	Vortex shedding frequency for oscillating cylinder	Hz
f_{cyl}	Forced cylinder vibration frequency	Hz
f_{nat}	Natural frequency	Hz
f^*	Frequency ratio	$[-]$
F_y	Transverse force (lift force)	N
F_x	In-line force (drag force)	N
F_c	Lift force component in phase with cylinder motion	N
F_s	Lift force component in phase with vortex shedding	N
k	Turbulence kinetic energy	m^2/s^2
k_{FS}	Freestream turbulence kinetic energy	m^2/s^2
k_a	Aerodynamic stiffness	N/m
k_s	Structural stiffness	N/m
k^*	Non-dimensional structural stiffness	$[-]$
k^*_{eff}	Effective elasticity	$[-]$
L	Cylinder height (z-direction)	m
L_1	Inflow length of computational domain	m
L_2	Outflow length of computational domain	m
L_3	Height of computational domain	m
L/D	Aspect ratio	$[-]$
Ma	Mach number	$[-]$
M_A	Effectively added mass	kg
M_X	Magnification factor of quantity X	$[-]$
m^*	Mass ratio	$[-]$
m_a	Added mass of air	kg

m	Structural mass of cylinder body	kg
n_{cells}	Number of cells	[−]
p	Fluid pressure	$kg/(m \cdot s^2)$
p	Order of convergence	[−]
Re	Reynolds number	[−]
R_{12}	Spanwise correlation coefficient	[−]
S_G	Skop-Griffin parameter	[−]
St	Strouhal number	[−]
Ti	Inlet turbulence intensity	%
Ti_a	Ambient turbulence intensity	%
t	Time	s
t^*	Non-dimensional time	[−]
ΔT	Time-step	s
T_s	Vortex shedding period	s
T_{nat}	Natural oscillation period	s
U	Freestream velocity	m/s
U^*	Reduced velocity	[−]
$\mathbf{u}$	Velocity vector	m/s
u	Velocity component in x-direction	m/s
$\overline{\mathbf{u}}$	Mean velocity	m/s
$\mathbf{u}'$	Fluctuating velocity	m/s
u_τ	Dimensionless wall velocity	[−]
v	Velocity component in y-direction	m/s
v_{wall}	Velocity component in y-direction at cylinder wall	m/s
$\mathbf{w}$	Mesh velocity field	m/s
y	Transverse displacement	m
y'	Fluctuating transverse displacement	m
$\overline{y'}$	Time-averaged fluctuating transverse displacement	m
y^*	Dimensionless transverse displacement	[−]
$\dot{y}$	Transverse velocity	m/s
$\ddot{y}$	Transverse acceleration	m/s^2
y_{max}	Transverse displacement amplitude	m
y_{wall}	Distance of cell adjacent to wall	m
y^+	Dimensionless wall distance	[−]
$\mathbf{z}$	Mesh displacement field	m
β_n	Newmark solver constant	[−]
γ_n	Newmark solver constant	[−]
γ_m	Diffusion coefficient for mesh	[−]
ϵ	Turbulence dissipation	m^2/s^3
ζ	Damping ratio	[−]
θ	Circumferential angle cylinder, starting at stagnation point	°
θ_{sep}	Flow separation angle	°
μ	Dynamic viscosity of the fluid	$N \cdot s/m^2$
μ_τ/μ	Inlet eddy viscosity ratio	[−]
μ_τ/μ_a	Ambient eddy viscosity ratio	[−]
ν	Kinematic viscosity of the fluid	m^2/s
ν_t	Turbulence eddy viscosity	m^2/s
ξ	Vorticity magnitude	$1/s$
ρ	Fluid density	kg/m^3
τ_w	Wall shear stress	N/m^2
ϕ	Phase angle between lift force and transverse displacement	°
χ	Numerical damping term	[−]
ψ	Relaxation factor	[−]
ω	Specific turbulence dissipation	$1/s$
ω_n	Angular (natural) frequency	rad/s

1 Introduction

1.1. Motivation

The interest in alternative energy sources to the conventional, polluting and depleting fossil fuels has increased tremendously over the past decades. Off-shore wind has shown an impressive growth over the last 16 years, in which around every 3rd year the total capacity doubled [6]. While off-shore wind energy has proven its high potential, improving the cost effectiveness is (still) highly important to ensure that the sector matures into an attractive alternative energy provider [7]. One of the main consequences of recent innovations in wind turbines, for improvement of the cost effectiveness, is the scaling up of the rotor size. The scaling up increases the power capacity of the turbine. This design motivation has led to increasingly larger turbine towers.

As a consequence of these recent developments, the off-shore wind turbine towers of today can be as tall as 150 meters. One of the major engineering challenges that has come along with these new turbines is dealing with an aerodynamic phenomenon called *vortex-induced vibrations* (VIV). The larger tower geometries make wind turbines more susceptible to vortex-induced vibrations. The larger structures lead to a higher Strouhal number and decreased natural frequency of the system. These two effects reduce the critical wind speed, i.e. the wind speed where VIV are most likely to occur. As this reduced critical wind speed is closer to or falls within the typical wind speed envelope for off-shore wind, the large-scale structures will yield a higher probability of VIV occurring. VIV may excite the towers in their eigenfrequencies. Such resonant circumstances are disastrous for the tower structure. Even when the eigenfrequency is not reached, the vibrations could result in fatigue stresses which impact the designed lifetime.

Besides the higher probability of vortex-induced vibrations with modern wind turbine structures, another factor that impacts the behaviour of the phenomenon is the large Reynolds numbers. Typically, because of the large structure and considerable wind speeds, the wind turbines may reach Reynolds numbers as high as $Re > 3.5 \cdot 10^6$ (known as the supercritical Reynolds regime). It has appeared that the vortices behind the turbine tower may show different features at these high Reynolds numbers.

Between the manufacturing and the final installation, the turbines undergo various stages of transport and storage. During these stages, the turbine towers are in different configurations leading to different natural frequencies for each of these systems. The structure is usually uncoupled from the rotor-nacelle assembly during these stages, while it is being clamped at the bottom. Vortex-induced vibrations have appeared to be the most critical in these stages prior to installation, when the eigenfrequencies can differ for which the damping is not always optimal to phase out the aerodynamic excitation. Fig. 1.1 illustrates two examples stages before final installation. On the left side of fig. 1.1, the tower is being installed. On the right side of the same fig. 1.1, three turbine towers are grouped and being transported by a vessel.

Siemens Gamesa - Renewable Energy, one of the off-shore wind technology leaders, has shown a dedicated interest to improve their understanding of vortex-induced vibrations and to develop a more robust solution which would mitigate the adverse effects of this phenomenon. At the same time, it seems this topic has attracted plenty of research from various engineering backgrounds [8]. This master thesis report will demonstrate that the phenomenon vortex-induced vibrations imposes great research challenges because of its complexity and dependency on different engineering disciplines. At this moment there is still a clear need from the body of science for more studies on this topic to fully understand the physics behind vortex-induced

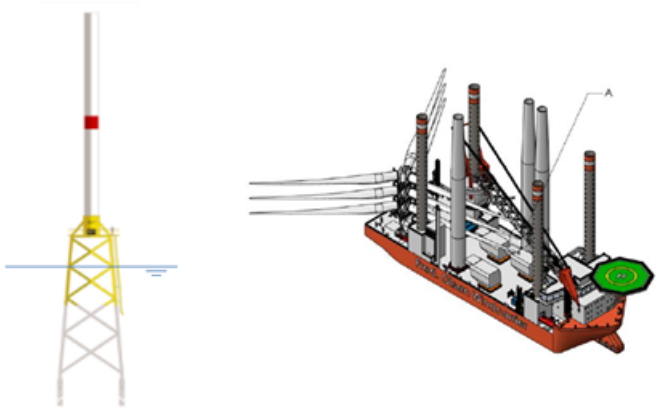

Figure 1.1. Example load cases of the wind turbine tower with no rotor and nacelle mounted.

vibration at supercritical Reynolds numbers. With these research objectives in mind, from the engineering and academical perspectives, the author of the present report has commenced a master thesis on the topic of vortex-induced vibrations. The master thesis has taken place in close agreement between Delft University of Technology and Siemens Gamesa.

1.2. Research approach

Three different approaches to investigate vortex-induced vibrations have been identified from the literature: experimental research, numerical study and analytical (or phenomenological) modelling [9]. According to [10], numerous efforts have been made in the last decades to improve the accuracy of analytical models of predicting VIV. The phenomenon tends to be so complex that these phenomenological models are not able to predict VIV very well. The analytical models were able to predict and clarify some of the physical parameters involved in VIV, but they still require further calibration and improvements to fully capture the phenomenon accurately. Experimental research, when executed properly, provides the most accurate results as they capture the phenomenon closest to reality. Yet, these types of research require a lot of resources, expertise and they can be tedious. On top of that, since a high Reynolds number is expected with the full-scale of a wind turbine, experiments would become very complex and costly. The present MSc research has therefore chosen to conduct its research in the computational domain, providing a good compromise between accuracy and feasibility [11].

Vortex-induced vibrations have been addressed and modelled in many, different ways [8], [3], [10]. Presumably, most of the approaches in the literature have simplified and tailored the problem to their research ambitions. All these modelling assumptions for the present MSc research have been pointed out clearly in the present report. The first distinction, to simplify the problem, is to focus on a stand-alone tower instead of grouped towers. It is believed the investigation of the stand-alone tower already provides a challenging research case, especially in the supercritical Reynolds regime where the physics is not fully understood.

1.3. Research objective and question

To design an ideal engineering solution which eliminates all the risks from VIV, it is firstly required to accurately capture and predict the phenomenon for the conditions relevant to the ever-growing modern wind turbine towers. The phenomenological models that are available today still require input from experimental or numerical work to allow useful predictions, since the underlying physics is usually missing in these models [4]. For these reasons, this MSc research has been a theory-oriented project where the main influence parameters causing VIV were investigated. Understanding the influence of these parameters will help the industry in developing a better understanding of the phenomenon, how it originates and how the fluid-structure interaction (FSI) evolves. It will give the opportunity to critically test the theoretical assumptions behind the existing phenomenological models. Therefore, the following research objective was defined for this MSc thesis: *To help Siemens Gamesa define a more physically representative VIV model accounting for the large-scale effects by analyzing the critical parameters influencing VIV.*

Regarding phenomenological models, two modelling shortcomings were observed. The first modelling

drawback is that fluid-structure interaction is considered in a very limited way. Furthermore, the models usually fall short in taking higher Reynolds numbers into account. Relating these two modelling assumptions back to the available studies in the literature, it seems no numerical study has simulated the effect of the transverse cylinder displacement on the cylinder at supercritical Reynolds numbers so far. In fact, in the thesis of [4], it was specifically mentioned that most of the numerical data has been generated only for low Reynolds numbers which is of limited use for phenomenological models. The study [2] demonstrates that in 1969 only their experimental work was the first study ever to investigate the effect of a moving cylinder on the lift force in the supercritical regime. In the more recent study of [12] in 2006, it has been shown that most of the state-of-the art experimental and numerical work so far has focused on moving cylinder research cases up to a Reynolds number of $Re = 33000$ and all at very low mass-damping. From an academic perspective, it may be concluded the combination of investigating an oscillating cylinder at supercritical Reynolds number is a novel research area. Furthermore, as will be shown in the literature review in chapter 2, the Reynolds number and the cylinder oscillations (FSI) are both considered to be a main influencing parameter causing VIV. Therefore, investigating these two influence parameters would be in the direct interest of the earlier defined research objective.

As was rightly pointed out in the review of Bearman [13], the higher Reynolds numbers regime is important to many practical applications. Furthermore, it was stated in the critical review of [14] that there is dedicated interest from the (offshore) industry to investigate VIV at supercritical Reynolds numbers (to investigate large-scale effects). The present MSc research aims to open up this research space in the supercritical regime by conducting a computational fluid dynamics (CFD) simulation with the open-source code *OpenFOAM* [1].

All these findings have led to the following research question: *What is the fluid-structure interaction effect of a transversely oscillating cylinder exposed to VIV at supercritical Reynolds numbers?*

1.4. Thesis Outline

The thesis report is organized as follows:

- In chapter 2 the literature on vortex-induced vibrations will be reviewed. Chapter 2 addresses the *what* and the *how* of the research:
  - *What are the influencing parameters that play an important role in VIV?*
  - *What has been done before on VIV experimentally and numerically?*
  - *What knowledge does the MSc research wants to obtain?*
  - *How is the research question addressed in the most efficient, complete and reliable way?*
- In chapter 3 the modelling settings will be explained in more detail. Chapter 3 focuses on the *how* as well, but more technical:
  - *How will the fluid be modelled?*
  - *How will the fluid-structure interaction be modelled?*
  - *How will the results be post-processed?*
- In chapter 4 the results will be presented for the numerical simulations. The following two questions will be emphasized:
  - *What do the results show?*
  - *How do the results compare against other work in the literature?*
- In the last chapter, chapter 5, the research question will be addressed and the progress towards the research objective will be evaluated. The focus of this chapter is on the discussion, recommendations and conclusions of the thesis research:
  - *How does the model perform?*
  - *What can be done better for future work?*
  - *What are the main outcomes of the results?*

2

Literature review

In this chapter a literature review will be presented focused on the previously done studies on vortex-induced vibrations (VIV). First, a brief introduction and explanation is given to the phenomenon vortex-induced vibrations. Then, in the interest of the research objective defined in the previous chapter, the main influence parameters of VIV will be identified and elaborated. After that, previous relevant modelling experiences will be reported. Since a numerical study will be performed in this MSc research, the focus of these modelling experiences was mostly on previous computational fluid dynamics (CFD) studies. In addition, the fluid-structure interaction modelling of VIV is briefly examined as well. Lastly, conclusions of the literature will be shared. Based on these conclusions the research plan and methodology will be defined.

This chapter addresses the *what* and the *how* of the research:

- *What are the influencing parameters that play an important role in VIV?*
- *What has been done before on VIV experimentally and numerically?*
- *What knowledge does the MSc research wants to obtain?*
- *How is the research question addressed in the most efficient, complete and reliable way?*

2.1. Vortex-induced vibrations

At certain flow speeds (and hence Reynolds numbers) the flow around a cylinder separates. When the boundary layer has separated from each side of the cylinder, two free shear layers will form which trail aft and border the near-wake. Within the two shear layers (in the wake) the inner flow part has a lower flow speed (resulting from the cylinder) compared to the outer part (which moves adjacent to the free stream). This momentum difference causes the free shear layers to 'roll' over into the wake where they coalesce into swirling vortices [15]. Under certain conditions, these vortices may shed regularly from an alternating side of the cylinder, which creates a vortex pattern. This pattern is called the Kármán vortex street, which is named after Theodor von Kármán [16]. The photograph in fig. 2.1 captured by Taneda from Van Dyke [17, p. 56, fig. 94] shows the Vortex Street behind a cylinder at $Re = 140$.

The aerodynamic excitation force that is responsible for vortex-induced vibrations is caused by pressure fluctuations around the cylinder. The flow field around a 2D cylinder is illustrated in fig. 2.2 [8].

Four flow regions are shown in fig. 2.2 (where V is the local time-averaged velocity and V_0 is the free stream velocity both in $[m/s]$):

i Retarded flow (in a narrow region at the front of the cylinder).

ii The boundary layer, which is attached to the cylinder wall.

iii Sidewise accelerated flow regions.

iv Region of separated flow, downstream of the cylinder (also known as wake).

After the flow has reached the cylinder, some of the fluid particles will continue to follow the cylindrical shape and some fluid particles will retard. The fluid particles will attach at the stagnation point of the cylinder,

Figure 2.1. A Kármán vortex street behind a cylinder at $Re = 140$. Photograph by S. Taneda from Van Dyke [17].

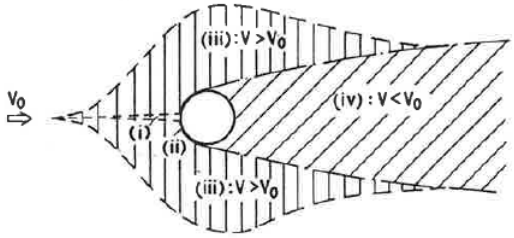

Figure 2.2. Flow field around a 2D cylinder [8].

this is where the boundary layer starts to develop [3], region (ii). The pressure of the fluid will increase from the free stream pressure to the stagnation pressure at the attachment point (meaning, $Cp = 1$). At the widest point of the cylinder ($\theta = 90°$), the pressure minimum is reached and, from there on, the flow is subjected to an adverse pressure gradient. In this part, the flow is highly prone to separate as the boundary layer is not able to cope with the strong adverse pressure gradient (as a consequence of the high curvature of the cylinder). While the theoretical curve (inviscid) remains attached in fig. 2.3, the subcritical and supercritical experimental curves separate. This separation can be identified in fig. 2.3 by the constant pressure plateau. In last region, (iv), the velocity is smaller than the free stream velocity, while the pressure is not able to recover to the total pressure at the front of the cylinder (see experiments in fig. 2.3). This pressure imbalance results in the in-line force: the drag force (x-direction).

It has appeared that the interaction between the shedded vortices from each cylinder side leads to a varying flow field around the upper and lower side of the cylinder. This variation generates a pressure distribution around the cylinder which changes over time. Then, the fluctuating lift force results from the pressure imbalance between the upper and lower part of the cylinder. The frequency of the lift force can be considered to be equal to the vortex shedding frequency [3]. The drag force can also fluctuate over time when vortex shedding is present.

Relating these forces back to the problem that was explained in section 1.1, an illustration of the turbine tower is given in fig. 2.4 [18]. The circular cylinder in fig. 2.4 may be interpreted as a wind turbine tower, where the cross-section serves as the cylinder body that is exposed to VIV in the transverse direction (y-direction). The spring (with spring constant k_s in $[N/m]$) and the damper (with damping constant c in $[Ns/m]$) can be applied in the transverse direction to measure the structural response .

Naturally, it is possible that VIV are initiated at a shedding frequency that is not necessarily equal to the natural frequency [19]. When the shedding frequency is close to the natural frequency, the cylinder can experience short bursts of displacement motion in the transverse direction. If this motion is large enough such that a correlated vortex wake is triggered along the span, the cylinder can suddenly jump to a larger displace-

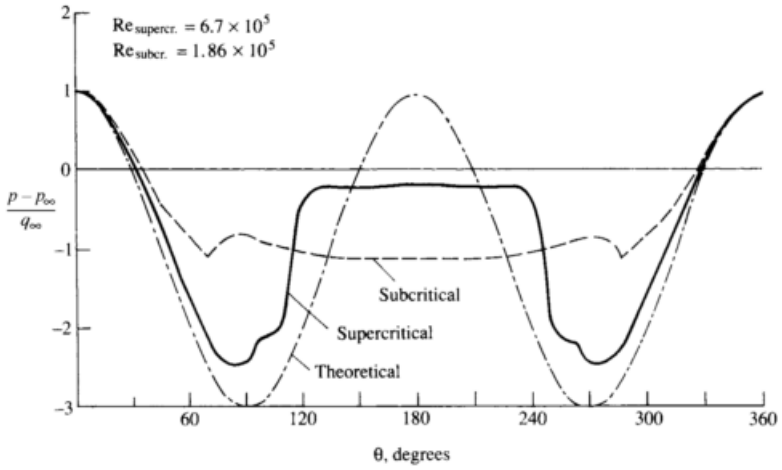

Figure 2.3. Pressure distributions around a 2D cylinder for the theoretical and experimental case [16].

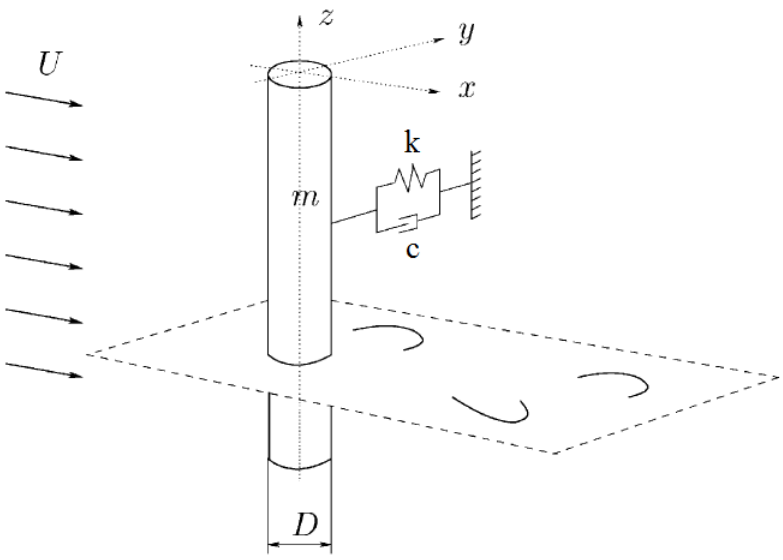

Figure 2.4. The flow problem illustrated for a circular cylinder [18].

ment amplitude. If the latter situation applies, the cylinder's moving frequency will shift towards the natural frequency and an harmonic oscillation is reached. After that, the wake is dictated by the cylinder frequency. This phenomenon, because of the interaction between the cylinder motion and the wake is called *lock-in*, as will be explained later in more detail.

This type of VIV initiation is typically referred to as *free-vibrations* or *self-excitement* in the literature. Another way of investigating VIV is by actively controlling the cylinder displacement, i.e. by prescribing a sinusoidal motion to the cylinder. This type of VIV is usually labelled as *forced-vibrations* in the literature. In these types of experiments, the cylinder is not at rest initially but is always moving at the prescribed motion.

2.2. Main influencing parameters of VIV

2.2.1. The Reynolds number

The well-known Reynolds number, as will be shown in this section, is one of the main governing parameters in the present MSc research. It is defined as:

$$Re = \frac{\rho U D}{\mu} \tag{2.1}$$

with ρ as the density of air $[kg/m^3]$, U as the freestream velocity $[m/s]$, D is the diameter of the cylinder (characteristic length of cylinder) $[m]$ and μ the dynamic viscosity $[kg/m \cdot s]$. The Reynolds number represents the ratio of inertial forces to viscous forces [16] and is an indicator of when transition from laminar to turbulent flow can occur. J.H. Lienhard (see fig. 2.5 for an illustration) [20], [16] and [3] have all summarized the qualitative aspects of the flow around a cylinder at different Reynolds regimes.

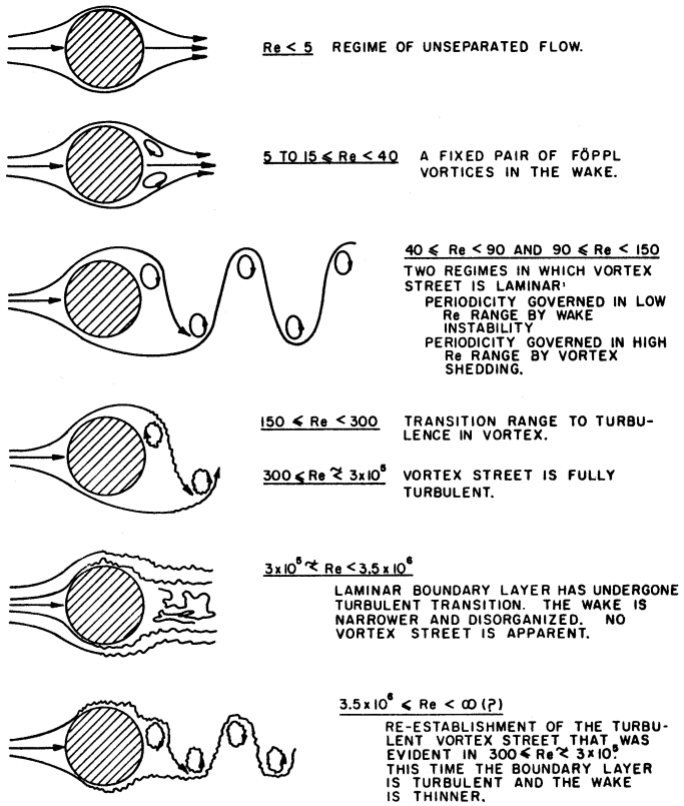

Figure 2.5. Various flow regimes over a 2D cylinder. Illustration from J.H. Lienhard [20].

It has to be noted that this transition point between laminar and turbulent flow depends on other influencing parameters such as the cylinder roughness, free-stream turbulence level, measurement errors, wind-tunnel circumstances (blockage ratio). Hence, these Reynolds number ranges are indicative.

As was already observed in the closure of Farell on his own work [21], there has been some confusion in the literature about the terminology concerning the different flow regimes. The terminology of the more recent summary of the flow regimes provided in the book of Blevins [3] is adopted in the present work. Three flow regimes have been listed in that work: the subcritical, the transitional and the supercritical Reynolds number range.

The subcritical regime For very low Reynolds numbers ($Re < 5$), the flow remains attached to the cylinder. In this regime (where the viscous forces dominate the inertial forces) the flow is called *Stokes flow* [16]. For $5 < Re < 40$, the flow separates from both sides of the cylinder. The two vortices at both sides can be considered symmetric and stable. In the next flow regime, $40 < Re < 150$, the wake becomes unstable and the vortices are shed alternately from the cylindrical body. This alternating pattern of vortices is also shown in the photograph by S. Taneda from Van Dyke in fig. 2.1 [17, p. 56, fig. 94]. In this regime, the vortex street is still laminar. Between $150 < Re < 300$, the flow transitions to turbulent in the vortex wake. Then, when the Reynolds number is within $300 < Re < 3 \cdot 10^5$, the vortex street has become fully turbulent. The boundary layer is still laminar. The Reynolds number range of $300 < Re < 1.5 \cdot 10^5$ is also known as the subcritical range, where the boundary layer remains fully laminar and the drag coefficient is nearly constant (as can be seen in fig. 2.6).

The transitional regime From around $Re > 1.5 \cdot 10^5 - 3 \cdot 10^5$, it is possible that the turbulent flow in the wake reattaches to the aft part of the cylinder. After reattachment, the flow will separate again. This phenomenon, also known as the laminar separation bubble, will make the wake thinner and hence result in a lower pressure drag on the cylinder. In this Reynolds number range, the flow still shows symmetric pressure distributions, although the uniformity across the cylinder height decreases [22]. The reason for the thinner wake is that the turbulent boundary layer has more energy to cope with the strong adverse pressure gradient experienced by the flow compared to a laminar boundary layer [23]. This range, where multiple laminar separation bubbles can occur is called the transitional range, which is $1.5 \cdot 10^5 < Re < 3.5 \cdot 10^6$. This range can be spotted clearly in fig. 2.6, where the drag coefficient starts to drop significantly (also known as the *drag crisis*). Multiple studies have clearly shown that the laminar separation bubbles are causing the drag coefficient to drop rapidly [2]. Once these separation bubbles cease to exist, the drag coefficient starts to increase again (that is, the supercritical region). This flow regime (where laminar separation bubbles are formed) is highly sensitive to inflow turbulence and surface roughness, therefore measurements of C_d are more scattered in this region [24]. This scatter can be seen in fig. 2.6, in the transitional range.

The supercritical regime The Reynolds number range from $Re > 3.5 \cdot 10^6$ is called the supercritical range. The transition point moves forward on the cylinder while increasing the Reynolds number [23]. At these Reynolds numbers, the transition to turbulence will occur directly (meaning, no laminar separation bubbles are observed at the cylinder). In the study of [25], it was found that the drag coefficient increases from 0.3 to 0.7 between a Reynolds number of $10^6 < Re < 3.5 \cdot 10^6$. After $Re > 3.5 \cdot 10^6$, the drag coefficient becomes constant. This is line with the curve observed in fig. 2.6. The same study was the first one to suggest no laminar separation bubbles would occur any more in the supercritical range and that the transition would be immediate. The increase of drag after the *drag crisis* was explained by [2] and it was reasoned that the turbulent boundary layer thickens the wake compared to the laminar boundary layer. Hence, this upfront moving transition point increased the low-pressure region behind the cylinder. On the other hand, increasing the Reynolds number also makes the wake thinner (more momentum is added to the flow). This latter effect will at one point trump the turbulent thickening effect at a certain Reynolds number. Therefore, as seen in fig. 2.6, the drag coefficients firstly increases after the *drag crisis* and then remains at a constant plateau again. In the present work, the emphasis of the vortex-induced vibrations research is on Reynolds numbers in the range of $Re > 3.5 \cdot 10^6$. This range falls within the operating envelope of the wind turbine towers of Siemens Gamesa and is therefore in the interest of the offshore industry.

2.2.2. The Strouhal number

The Strouhal number is the dimensionless ratio between the vortex shedding frequency times the characteristic length and the flow velocity:

$$St = \frac{f_{shed} D}{U} \tag{2.2}$$

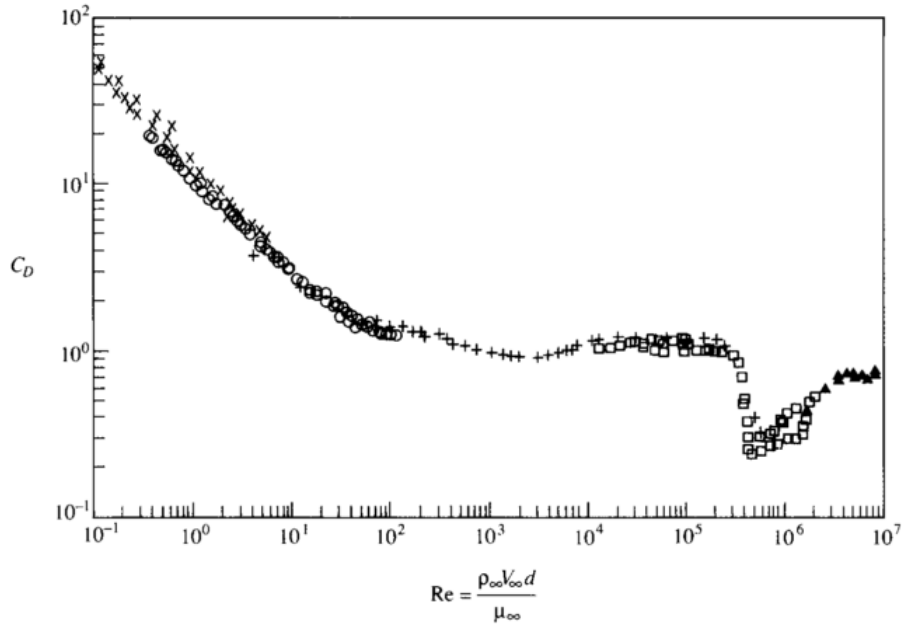

Figure 2.6. The drag coefficient of a cylinder with varying Reynolds number. Experimental data compiled in [26].

where f_{shed} is the (predominant) vortex shedding frequency $[Hz]$, U is the freestream velocity $[m/s]$ and D is the cylinder diameter $[m]$ (which is the characteristic length in the case of a cylinder). Usually, in the literature, the frequency in eq. 2.2 is defined as f rather than f_{shed}. In the present research, f_{shed} is used for clarification purposes. It is found in the literature that the shedding frequency of the vortices are in phase with the frequency of the corresponding time-varying lift force. Yet, the recurrence of the oscillating drag force takes place at two times the shedding frequency [3].

Fig. 2.7 shows the Strouhal-Reynolds number relationship for smooth and rough circular cylinders, this data has been compiled by Lienhard [20, p. 12, fig. 5]. The rough cylinder curve is the lower dashed line in the transitional range, while the smooth cylinder shows the substantial jump in Strouhal number in the transitional range.

The subcritical regime At very low Reynolds numbers, also called *creeping flow* [8], the flow remains attached to the cylinder and hence no vortex shedding occurs ($Re < 5$). At higher Reynolds number, $5 < Re < 40$, the flow starts to separate. The near wake is closed (see fig. 2.5) in this range. Still, no vortex shedding is present. Then, when the Reynolds number is increased to the range of $40 < Re < 150$, vortex shedding starts to occur. It starts with a sinusoidal wake oscillation of the shear layers [8] and then as Re is increased further the flow develops into the well-known von Kármán street. So far, these ranges have been for fully laminar flow. From $Re > 150$, the transition starts to occur in the wake and at $Re > 350-400$ the transition takes place in the free shear layer. These different transition states can influence the eddy shedding mode and this could lead to a small variation of the St number [8], as seen in the small jumps in fig. 2.7. Yet, it can be expected that in the subcritical range, except for the very low Reynolds number, regular vortex shedding will occur.

The transitional regime Experiments from [23] showed no regular vortex shedding in the transitional range with an aspect ratio of $L/D = 3.38$. Yet, with a higher aspect ratio of $L/D = 6.75$, the wake showed more periodic fluctuations. These periodic fluctuations were found at a broader fluctuation spectrum than the one observed at lower Reynolds numbers in their study (meaning, did not show the consistent periodicity as was observed at lower Reynolds numbers). They concluded, after careful testing, that vortex shedding at the lower aspect ratio circular cylinder was suppressed because of 3D wake effects. For all roughness parameters that have been tested in their study, the Strouhal number showed an increment in the transitional range, where the drag coefficient showed a significant decrement as was explained before. Also, in the high Reynolds number study of [25], no spectral peak frequency for vortex shedding was found in the transitional range (and hence

no regular vortex shedding was observed). P.W. Bearman investigated why regular vortex shedding stopped occurring in the transitional range in [24]. Out of his measurements it turned out that until $Re = 5.5 \cdot 10^5$, regular vortex shedding was observed. After this Reynolds number, the power spectral density of the measured vortex-shedding became broader, which would indicate that the shedding is less regular. Also, the observed power of this broader spectrum was of smaller magnitude. That means that the fluctuating pressure around the cylinder is not only less regular at this Reynolds number but also has a weaker effect on the cylinder compared to the subcritical regime. These measurements are in line with the earlier indicated regions of irregular vortex shedding. Oil flow patterns in the same study of [24] indicated that after placing any disturbances on the cylinder (dust particle for example) would suppress the formulation of laminar separation bubbles. These protuberances on the surface would not only lead to disrupted flow locally, but along a certain span length of the circular cylinder. This effect was identified as the measured base-pressure coefficient along the span became non-uniform. Once this non-uniform spanwise flow was triggered, the strong spectral density peaks became weaker and of a broader-band type. Therefore, [24] suggested that regular shedding ceased because laminar separation bubbles are disrupted at different locations along the span, caused by the three-dimensionality of the potentially turbulent flow.

The supercritical regime For the supercritical flow regime, [25] found that regular vortex shedding is again present. In the same study, a Strouhal number of 0.27 was found in this flow regime, which is higher than the typical subcritical Strouhal number of 0.21. Other studies have found a smaller St number in the supercritical range, which yielded $St = 0.25$ (lower bound of fig. 2.7). Referring back to the research of [2], for $3.5 \cdot 10^6 < Re < 6.0 \cdot 10^6$, the frequency response of the lift-time signal became more narrow-banded compared to the transitional range. Lastly, for $Re > 6.0 \cdot 10^6$, the response was very dense and quasi-periodic. The Strouhal number found for the range of $8 \cdot 10^6 < Re < 17 \cdot 10^6$, was approximately constant at $St = 0.30$, which was at that time the first measured Strouhal number at this Reynolds number range.

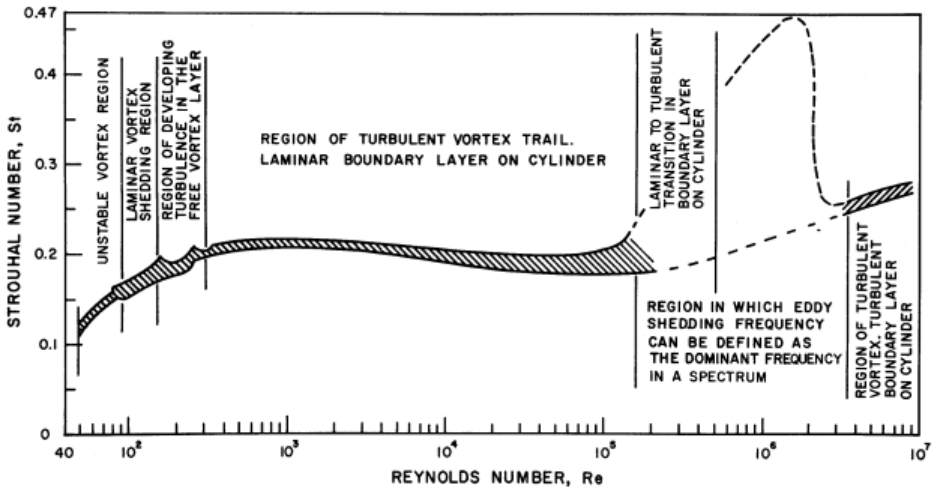

Figure 2.7. The Strouhal number of a cylinder with varying Reynolds number. Experimental data compiled in [20].

2.2.3. Other influencing parameters

Besides the Reynolds number and the Strouhal number, which are both governing parameters for VIV, there are other influencing parameters that impact VIV as well. In fig. 2.8 all the influence parameters are illustrated, as they were brought together by [8]. The other influence parameters illustrated in fig. 2.8 tend to have a smaller effect on VIV than the Reynolds number or Strouhal number, except for the cylinder oscillations (see fig. 2.8(g) and (h)) [8], [3]. The reason why cylinder oscillations do have a more severe effect on VIV has been explained in the next section. Besides the smaller effect of most of the influencing parameters, their effects have been investigated already at high Reynolds numbers. The interested reader is referred for example to studies of [27], [23], which addressed the surface roughness and free stream turbulence at supercritical Reynolds numbers, respectively. Concerning the present research, all the known influencing parameters de-

picted in fig. 2.8 have been monitored closely to make sure their effect is minimized or controlled.

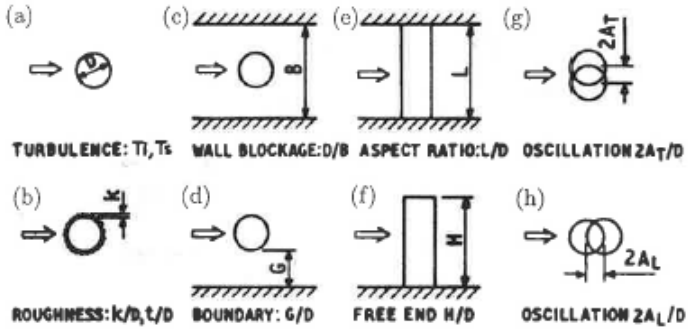

Figure 2.8. Typical disturbances that have an impact on VIV [8].

2.2.4. Effect of cylinder motion on wake

In addition to the Reynolds number, the present research has focused on the effect of the cylinder oscillations on vortex-induced vibrations. An oscillating cylinder (fig. 2.8g and h) can become a governing parameter, while overriding all other disturbances from fig. 2.8 [8]. A distinction between in-line oscillations and transverse oscillations has been made (in reality, both occur at the same time). The study of [28] found similar response branches for a 2-DOF experiment as in transverse 1 degree-of-freedom (DOF) studies. It was concluded that 2DOF XY motion studies do not lead to significant variations in maximum resonant amplitudes compared to Y-only studies. Under the conditions when natural frequency is equal in both directions, it was shown in the study of [28] that the response amplitude is 20% larger and the critical velocity range is also 20% larger. It was reasoned that the transverse oscillations were the main driver of the response amplitude and the critical wind speed range. Therefore, the effect of the in-line DOF on VIV was left outside the scope of the present MSc thesis.

According to [3], there are five effects of the *transverse* cylinder motion on the wake. When the vortex shedding frequency is in the vicinity of the cylinder vibration frequency, the following five effects can occur (simultaneously):

1 The shedding frequency (f_{shed}) can be shifted towards the transverse cylinder displacement frequency (this is called lock-in/synchronization).
2 The strength of the shedded vortices increases.
3 The spanwise correlation of the wake increases.
4 The in-line force increases (drag component).
5 The phase, sequence and pattern of vortices in the wake is affected (qualitative analysis of vortex shedding).

Lock-in In the literature, lock-in has been expressed in multiple, different ways in the literature [8]. In the present research, the most classical definition of lock-in has been used, which was suggested by [29]. This definition of lock-in or synchronization is defined as the flow regime where the shedding frequency (f_{shed}) and the cylinder vibration frequency (f_{cyl}) are nearly equal to the natural frequency of the system (f_{nat}). In that way, $f_{shed}/f_{nat} = f_{cyl}/f_{nat} \approx 1$. In [30] the frequency, amplitude and phase angle between the exciting force and displacement of cylinder have been measured for varying wind velocities in a free-vibration experiment. A more detailed explanation on the phase angle definition can be found in the next chapter, in section 3.3.6. These measurements have been plotted in fig. 2.9 with a dimensionless mass parameter $n = 0.00267$ and dimensionless damping coefficient $\beta = 0.00103$. On the upper left y-axis, the frequency ratio is plotted. From the frequency ratio, f_n stands for the natural frequency (f_{nat}) and f for either the shedding frequency (f_{shed}) or cylinder motion frequency (f_{cyl}). On the lower right y-axis, the dimensionless transverse displacement amplitude is plotted: $\overline{Y} = A_y/D$. Then, on the upper right y-axis the phase angle between the fluctuating surface pressure (exciting force) and cylinder displacement is plotted (ϕ°). U on the x-axis is the reduced velocity: $U = \frac{V}{2\pi f_{nat} D}$. It must be noted, that the definition of the dimensionless velocity may differ in the literature. For example, in the present research the dimensionless velocity has been defined as: $U^* = \frac{V}{f_{nat} D}$ without the 2π reduction (see tab. 4.4).

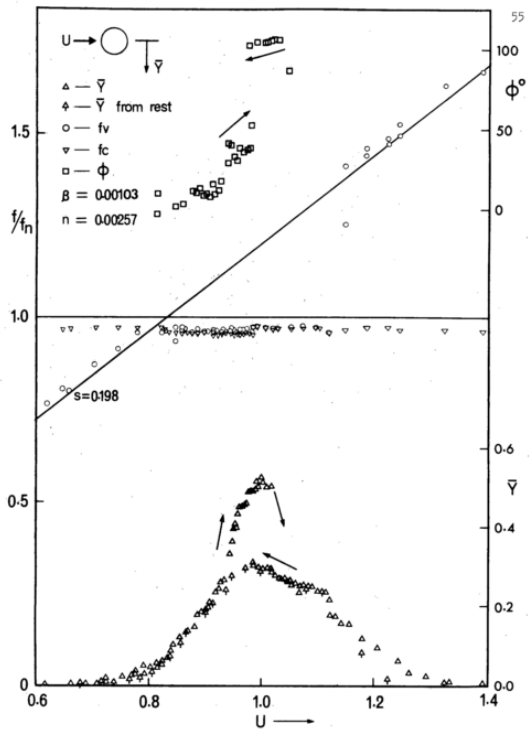

Figure 2.9. Oscillation phenomena for a free-vibration case with varying wind velocity ($10^4 < Re < 5 \cdot 10^4$), from [30].

By rearranging the Strouhal relation found in eq. 2.2, the vortex shedding frequency may be calculated by the following equation:

$$f_{shed} = \frac{U \cdot St}{D} \tag{2.3}$$

Combining the dimensionless velocity from [30] with eq. 2.3 results in the following linear relation:

$$\frac{f_{shed}}{f_{nat}} = St \cdot 2\pi \cdot U \tag{2.4}$$

At a dimensionless wind velocity of $U^* = 1$, the ratio between $f_{shed}/f_{nat} = St \cdot 2\pi$. It was stated in [30], that $St = 0.198$ at $10^4 < Re < 5 \cdot 10^4$. That means that at $U^* = 1$, the frequency ratio with shedding frequency should be: $f_{shed}/f_{nat} = 0.198 \cdot 2\pi = 1.244$. This number is according to the linear Strouhal relation and this number is one data point of the straight line observed in fig. 2.9. Hence, the straight line is a consequence of the linear Strouhal relation.

As can be seen in fig. 2.9, the Strouhal relation does not hold for all wind velocities. At $0.8 < U^* < 1.2$, the measured shedding frequencies deviate from the linear Strouhal relation (the straight line with $St = 0.198$). In this region lock-in occurs (and this region is also called the lock-in band [3]). Indeed, both f_{shed} and f_{cyl} are clearly equal to the natural frequency in this region ($f^* \approx 1$), which satisfies the classical definition of lock-in expressed earlier. The reason that lock-in does happen at different wind velocities (while resonance does not), is because of fluid-structure interactions. The cylinder motion dictates the eddy-shedding frequency, which means that vortex shedding 'locks on' or 'synchronizes' to the cylinder motion [8]. Hence, the wake is directly affected by the cylinder motion. Yet, as the shedding frequency moves further away from the cylinder natural frequency (by a change of wind speed for example), the cylinder body loses its control over the shedding process. At one point, the vortex shedding has detuned from the cylinder frequency and it follows the linear Strouhal relation again. The cylinder displacement amplitude versus the reduced velocity is known as a lock-in map or lock-in curve, where the operating range of lock-in is easily spotted by the occurring displacements.

Increased strength of shedded vortices According to [3], at lower displacement amplitudes the motion of the cylinder organizes the wake, increases the spanwise correlation and then enhances the vortex strength to grow. This will lead to a higher lift coefficient, which is supported by the experimental results from the study of [2]. In this study, forced-vibration experiments for a circular cylinder were done at supercritical Reynolds numbers ($Re > 5.5 \cdot 10^6$). This motion-dependent lift force increases with higher motion amplitudes. The range of frequencies where the motion-dependent force was measured increased as well at higher amplitudes. The highest amplification factor was measured at a cylinder motion frequency nearly equal to the linear Strouhal frequency ($\frac{f_h D}{V} / St = 0.99$).

As the cylinder displacement amplitude increases, at one point the cylinder will outrun the shedded vortices. This will suppress the vortex pattern and then the lift coefficient starts to drop considerably. Typically, the maximum lift coefficient is reached at $A^* = 0.5$. This means that vortex-induced vibrations have a self-limiting property which eventually diminishes the lift force. This property is independent of the structural damping, while it is dependent on the fluid-structure interaction [3].

An important relation within the VIV studies that has received a lot of attention is between the maximum response amplitude of the cylinder and the system mass and damping [29]. Griffin et al. [31] were the first to use the product of the mass ratio, the damping ratio and the Strouhal number:

$$S_G = 2\pi^3 St^2 (m^* \zeta) \tag{2.5}$$

This parameter is known as the Skop-Griffin parameter. The classical Griffin plot [29] is based on this S_G parameter. In this plot, the maximum amplitude is plotted on the y-axis and the S_G parameter is plotted on the x-axis. Ever since this plot was originally used in [32] by O. Griffin, the plot has been used extensively in the literature for amplitude response data and was later labelled as the Griffin plot [29]. In the study of [33], various experiments for air and water have been compiled and put in the classical Griffin plot, see fig. 2.10. Yet, despite the various efforts and studies in the last 25 years there is still not a uniquely, well defined Griffin plot that is able to collapse peak-amplitude data from different VIV cases (free vibration, forced vibrations, etc.) [29], [12]. For example, when fig. 2.10 is plotted on a linear Y-axis scale significant scatter becomes apparent [12].

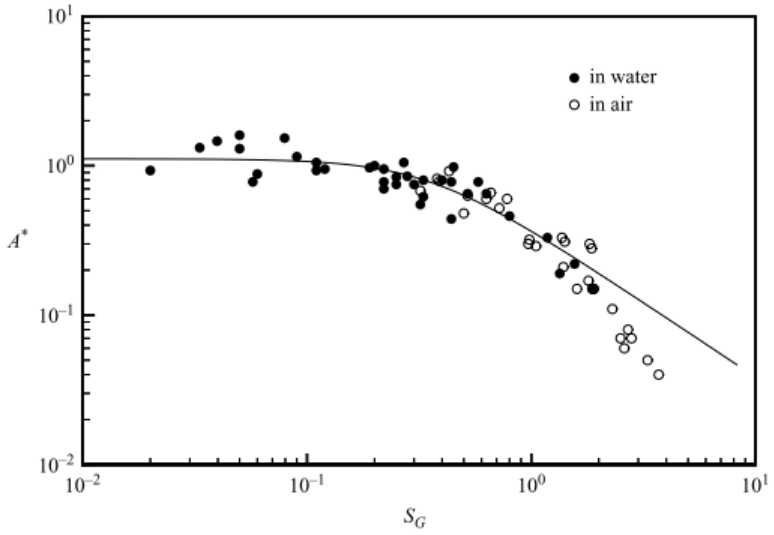

Figure 2.10. The classical log-log Griffin plot, compiled with various experimental studies by [33].

The self-limiting response of VIV becomes apparent in fig. 2.10. If there would be no limitation, the amplitude A^* would go to infinity when the Skop-Griffin parameter was lowered to nearly zero. Yet, the amplitudes stay within a bounded region, which implies that there is an effect of the cylinder vibrations on the wake which suppresses the aerodynamic forces. In the numerical study of [34], the same reasoning was found.

Span-wise correlation One way to quantify the effect of the aspect ratio on the 2-dimensionality of the flow is by calculating the spanwise correlation. To evaluate the coherence of vortex shedding along the span of the circular cylinder, the pressure or velocity fluctuations can been measured at different locations along the span [8]. When these measured signals show good correlation along the span, it can be concluded that the flow behaves coherent along the span. The correlation coefficient between two spanwise velocity fluctuations is for example expressed as follows:

$$R_{12} = \frac{(v_1' + v_2')^2 - (v_1' - v_2')^2}{4(v_1' \cdot v_2')^{1/2}} \tag{2.6}$$

When the flow is fully 2D, the measured velocity fluctuations inherently will be in phase and show the same magnitude, this will result in 100% correlation of the two signals: $R_{12} = 1$. Fig. 2.11 [10, p. 118, fig. 7.9] shows the correlation coefficient along the circular cylinder height for a stationary and an oscillating cylinder at three different vibration amplitudes (amplitude defined as a in fig. 2.11).

It was observed that for oscillating cylinders the correlation length is higher, which is seen back in fig. 2.11. The reason for this increment is explained in [3] by the effect of the cylinder motion on wake. The cylinder motion organizes the wake (since the vortex shedding is synchronized with the cylinder vibration), this in turn enhances the spanwise correlation.

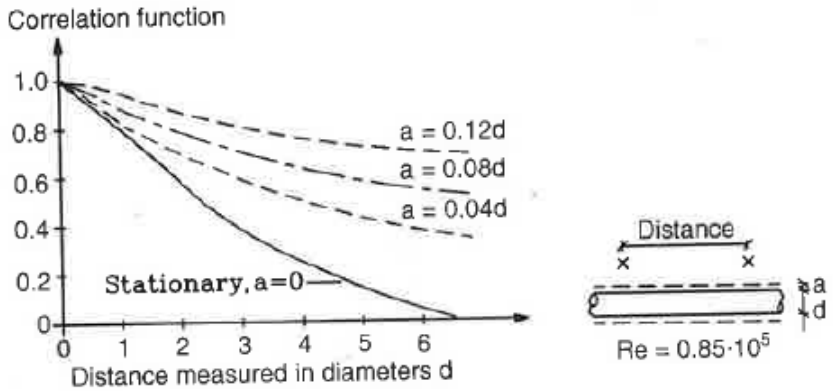

Figure 2.11. Effect of transverse vibrations on spanwise correlation coefficient at $Re = 0.85 \cdot 10^5$, measured by [35] and the figure is reproduced by [10].

Increment of in-line force Besides the increment of the lift force, the in-line force component will also be influenced by transverse displacement motions of the cylinder [3]. In fig. 2.12 the drag multiplication factor is plotted against the transverse vibration amplitude. These results were obtained at relatively low Reynolds numbers. Multiple attempts have been made to describe the relation between the in-line force and the transverse vibration amplitude in an equation, after careful experimental research. For instance, for low Reynolds number the following three equations may be used:

$$\frac{C_{D,A_y>0}}{C_{D,A_y=0}} = \begin{cases} 1 + 2.1A^* & \text{Curve fit of fig. 2.12, by [3]} \\ 1 + 1.043(2Y_{rms}/D)^{0.65} & \text{[36]} \\ 1 + 1.16([1 + 2A^*) f_{nat}/f_{shed}] - 1)^{0.65} & \text{[37]} \end{cases}$$

These three equations compute the drag force within 15% when $f_{nat} = f_{shed}$ [3].

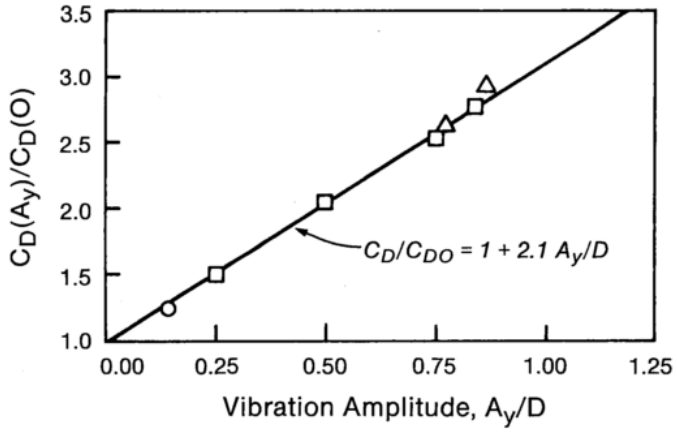

Figure 2.12. Drag increment with increasing transverse displacement amplitude of rigid cylinders during lock-in. Experimental data compiled by [3]: ○ $Re = 4000$, □ $Re = 8000$, △ $Re = 15.000$.

Phase angle, sequence and pattern As was shown in fig. 2.9 by [30], the phase angle between the exciting force and the cylinder displacement jumps around the location where a maximum displacement amplitude was measured. It was shown by [38] by visualizations of previous researches that this phase jump is caused by a switch in the timing of vortex shedding.

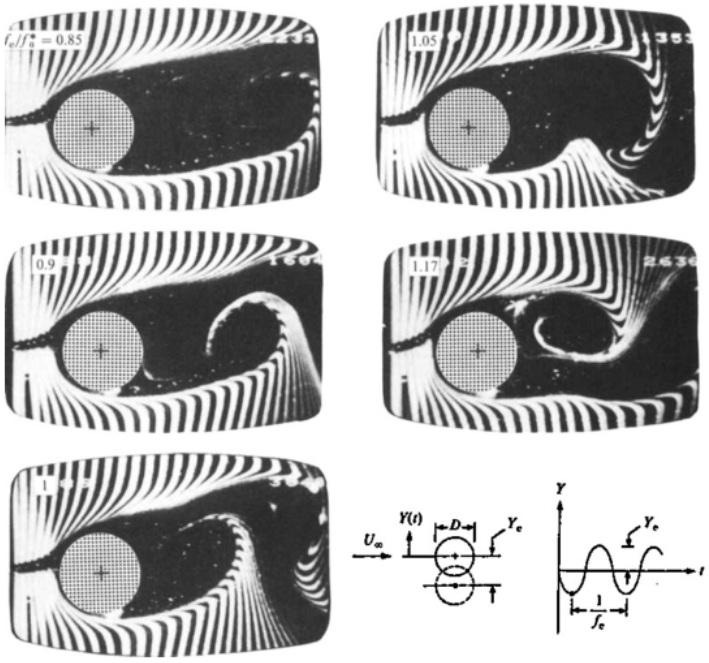

Figure 2.13. Photographs of vortex shedding at different excitation frequencies (f_{cyl}) relative to the stationary shedding frequency (f_{shed}), from [39]. All photos are taken at the maximum negative displacement of the cylinder at $584 < Re < 1300$.

In the studies of [39] and [40], extensive forced VIV experiments have been done to investigate the phase jump. In fig. 2.13, five photographs are shown at different excitation frequencies (f_{cyl}). These experiments were done at relatively low Reynolds numbers. In fig. 2.13, the excitation frequency is detonated as f_e and the stationary shedding frequency as f_0^*. Before the cylinder motion frequency is equal to the shedding frequency, the vortices are being shed initially at the upper side of the cylinder. From $f_{cyl}/f_{shed} = 0.85$ until $f_{cyl}/f_{shed} = 1$, the vortices tend to shed initially from the lower side of the cylinder, as seen in fig. 2.13. As the excitation frequency was increased to (to $f_{cyl}/f_{shed} = 1.05$), the vortices start to shed from the upper side of

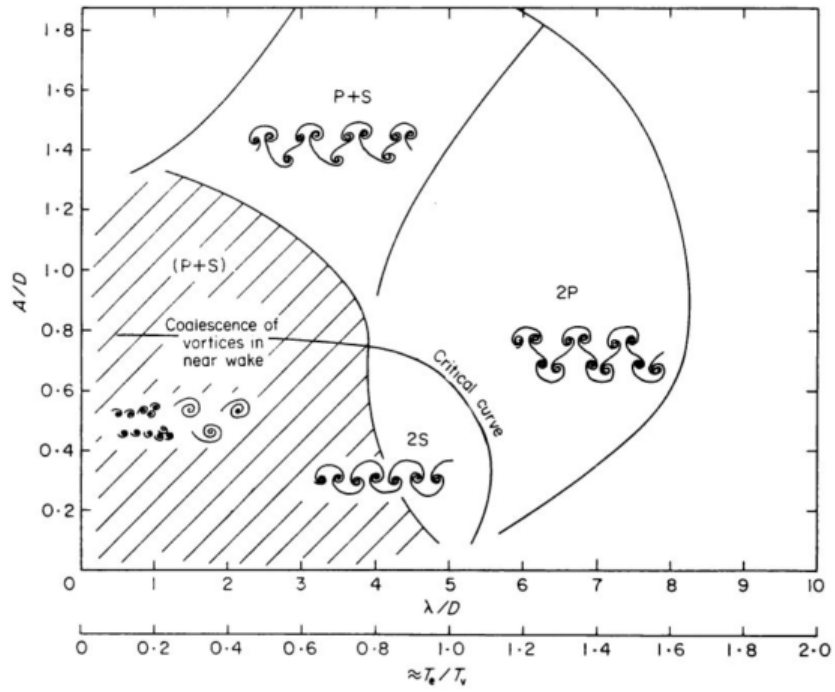

Figure 2.14. Map of identified vortex wake modes in the synchronization regime at $300 < Re < 1000$, for varying amplitude (y-axis) and wavelength (x-axis), found by [15].

the cylinder rather than the lower side, which explains the phase jump from [30] in fig. 2.9. Hence, the phase jump is caused by the fact that the vortices tend to be shed at the alternative side of the cylinder body at a certain cylinder vibration frequency. More recent studies, also by means of simulation or by PIV, have found this switching phenomenon to be the reason of the phase jump [29].

The jump in phase angle is related to the sequence and pattern of the vortex wake. In the research of [15], a forced-vibration experiment was carried out to study the vortex wake patterns behind a cylinder at $300 < Re < 1000$ by flow visualizations. In this research, different type of so-called *vortex wake modes* have been identified.

A periodic vortex was either observed as a single vortex (S) or a vortex pair (P). Different kind of patterns can occur at different vibration conditions, for example P+S or 2S as plotted in fig. 2.14. These vortex regimes can be linked to certain branches of free vibration. The jump in phase angle, observed by [30] in fig. 2.9, can be explained by a changing from the 2S vortex mode to the 2P mode. This is also in line with the earlier presented explanation, by [39] and other studies [29].

2.2.5. Oscillating cylinder at supercritical Reynolds numbers

As can be expected, which was also the case for the stationary cylinder, the available literature on high Reynolds number studies on moving cylinders is limited. In fig. 2.16 the researches for stationary and moving cylinders was summarized in a graph for varying Reynolds number. At the y-axis, the forced cylinder vibration frequency is non-dimensionlized by the diameter and the velocity ($\frac{f_h D}{V}$, f_h is defined as f_{cyl} in the present research). Hence, the studies that were plotted at the bottom of the graph are for stationary cylinders (since theW cylinder vibration frequency is zero). The parameter on the y-axis is highly similar to the Strouhal number (see eq. 2.2). The typical Strouhal number for a large Reynolds number range is $St = 0.21$, which was stated earlier in section 2.2.2. The 'critical Strouhal number range' in fig. 2.16 is based on the situation when the forced cylinder frequency (f_{cyl}) is nearly equal to the shedding frequency (f_{shed}), which is where most of the fluid-structure interaction can be expected. After 1969, not too many experiments have been done at high Reynolds numbers for moving cylinders. C. Williamson and R. Govardhan compiled in [12] some of the state-of-the-art VIV researches at different Reynolds numbers. In fig. 2.15, the amplitude responses of cylinders against various Reynolds numbers were plotted. A logarithmic relation between the Reynolds num-

ber and the peak amplitude was found. Also, as is clearly demonstrated in fig. 2.15, the response amplitude is strongly dependent on the Reynolds number. Not enough experimental data was available to extend the logarithm relation beyond $Re = 40.000$.

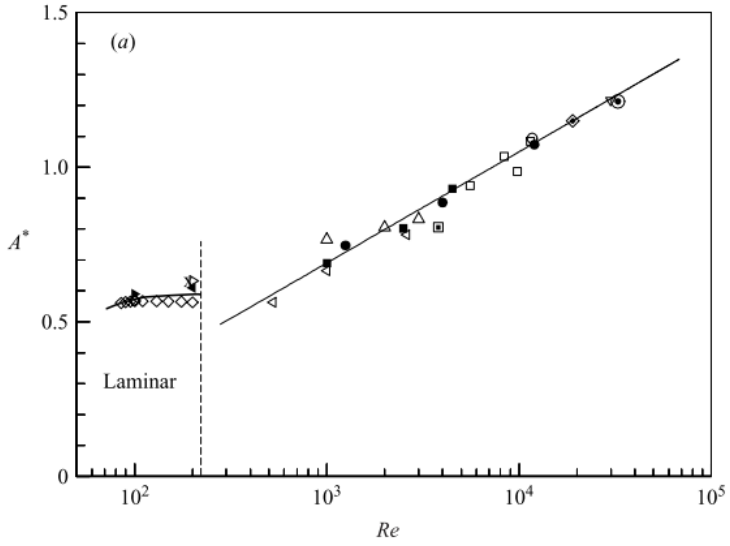

Figure 2.15. Compiled state-of-the-art experiments and CFD simulations for moving cylinders at different Reynolds numbers in 2011. Figure from [12].

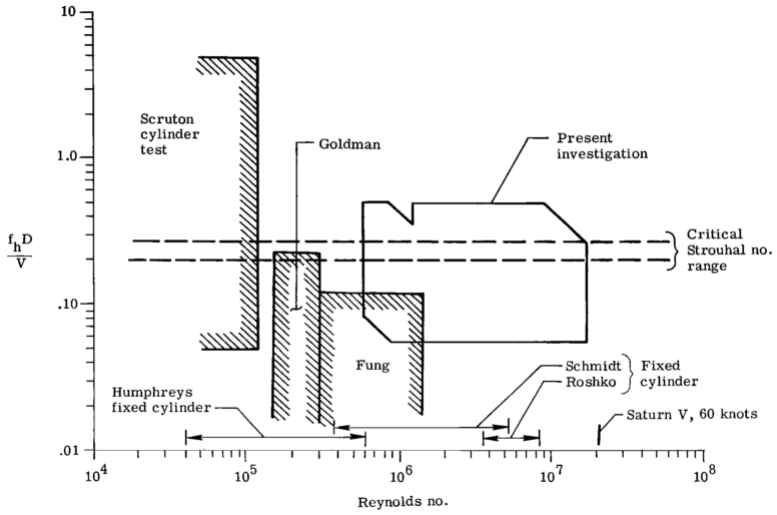

Figure 2.16. Available experiments for stationary and moving cylinders at different forced cylinder frequencies and Reynolds numbers in 1969. Illustration and *present investigation* from [2].

2.3. Modelling of VIV

The complicated fluid-structure interaction effects seen for vortex-induced vibrations has attracted plenty of numerical research. There is still an ongoing effort to further understand the complex interaction between the flow field around the cylinder body and the structural motion. In addition, it has been observed in the literature that this phenomenon serves as a test case for newly developed numerical codes. As has been stated before in Chapter 1, a numerical approach was favoured above an experimental approach to investigate VIV in the present MSc thesis. In the following sections, a brief summary has been presented on the experiences in

the literature with the fluid solver and the fluid-structure interaction coupling. The fluid solver in the present research is better known as Computational Fluid Dynamics (CFD).

2.3.1. Computational Fluid Dynamics

Before the modelling experiences will be reported, a small recapitulation on the governing equations of fluid dynamics is presented. These fundamental equations have provided a clear and essential starting point before the models are treated in to more detail. Computational fluid dynamics rests on numerically solving the full governing equations describing a viscous fluid [41]. The governing equations in present research are reduced to the (incompressible) Navier-Stokes equations for a Newtonian fluid:

$$\frac{\partial \mathbf{u}}{\partial t} + \nabla \cdot (\mathbf{u}\mathbf{u}) + \frac{1}{\rho}\nabla p - \nabla \cdot (\nu \nabla \mathbf{u}) = 0 \tag{2.7}$$

$$\nabla \cdot \mathbf{u} = 0 \tag{2.8}$$

With $\mathbf{u} = (uv)^T$ where u is the x-velocity component and v is y-velocity component, respectively. The flow around the cylinder is incompressible since typical wind speeds of $2[m/s] < U < 50[m/s]$ have been expected. These velocities lead to a Mach number of $Ma < 0.3$, which indeed supported the incompressible assumption. The governing equations of fluid dynamics also consist of the energy equation, which ensures conservation of energy. Yet, since the flow is incompressible and assumed to be isothermal (flow quantities remain constant with temperature), only the kinetic energy will be of importance in the energy equation [42]. Hence, the energy equation is decoupled from the system of equations described in eq. 2.7 and eq. 2.8.

It is possible to numerically solve eq. 2.7 and eq. 2.8 directly at low Reynolds numbers (laminar flow). Yet, at higher Reynolds numbers, when the flow transitions to turbulence, it is much harder to numerically solve these equations as they are [42] with a direct numerical simulation (DNS). Turbulence introduces larger flow fluctuations for a wider range of length and time scales compared to laminar flows. For all scales to be resolved, the size of the grid scales with $Re^{9/4}$, which would require massively high computational power at $Re > 3.5 \cdot 10^6$. Therefore, within CFD engineering, it is common practice to further simplify the governing equations depicted in eq. 2.7 and eq. 2.8 to predict turbulent flows. One of the most widely used approaches for turbulent flows is an unsteady Reynolds Averaged Navier-Stokes Simulation (URANS). In this approach, the two governing equations are time-averaged while all the turbulence motion is modelled. Within URANS, a lot of different turbulence models have been developed over the last decades.

Besides DNS and URANS, there is the third CFD option which is known as Large-Eddy Simulation (LES). In this approach, parts of the flow are resolved while other parts of the flow are modelled by applying a filter to the governing equations. The distinction between modelling and resolving is based on the turbulence length scales. Since URANS only computes the average while the complete turbulence spectrum is modelled, the computational time is greatly reduced compared to DNS or compared to the LES. At the same time, it may be expected that URANS would lead to less accurate results compared to DNS and LES. Especially the large turbulent scales are very hard to model properly since they tend to vary a lot in different types of flow problems [43]. This is the main reason why in LES the large scales are simulated and the small scales are modelled, since the latter ones are seen as more universal.

Then, as a combination of LES and URANS, detached-eddy simulation (DES) is a hybrid turbulent model. In this model the attached boundary layer is being solved by URANS and the wake region is captured by the LES approach. It has appeared that turbulent boundary layer flows tend to be captured better with some of the reliable RANS turbulence models compared to sub-grid scale modelling of LES [43], [44]. This has stimulated the use of a DES.

In the present research the objective is capture vortex-induced vibrations at supercritical Reynolds numbers ($Re > 3.5 \cdot 10^6$). Because of the large Reynolds number, a very dense grid is required which would imply high computational cost. Next to that, the inclusion of fluid-structure interaction would require a structural solver and a moving mesh. This would also indicate a larger demand of computational power. Based on these reasons it was concluded that modelling the governing equations with URANS would be the best suitable approach.

Turbulence models of URANS For the Reynolds Averaged Navier-Stokes equations, there is a need to model the Reynolds stress tensor to fully close the set of equations. The derivation of the Reynolds stress tensor will be done in chapter 3, section 3.1.1. Numerous models have been developed to estimate the Reynolds stress tensor, which are known as the turbulence models. These closure approximations can be divided roughly into

two models: the Eddy Viscosity Models (EVM) and the Reynolds Stress Models (RSM). The EVM introduces the eddy viscosity, nu_t a scalar field quantity. It has been assumed that the eddy viscosity is isotropic, which is a significant simplification. The different EVM are distinguished by the amount of transport equations that must be solved. The Spalart-Allmaras (SA) model requires only one transport equation. This model has proven to be good for boundary layer flows under a reasonable pressure gradient, while free shear layer flows and flows with a sharp separation are less well predicted. The S-A model was included in the original detached-eddy simulation method. Regarding the two-equation models, the most well-known models are: k-ϵ, k-ω and SST k-ω. It is known that the $k-\epsilon$ model is suitable for external flows without a strong pressure gradient or flow separation. At the same time, the $k-\omega$ model is better in capturing boundary layer flows where pressure gradients are observed and possible flow separation. The k-ω SST model is based on two last models: the $k-\omega$ [45] and $k-\epsilon$ [46] model. The idea of Menter's $k-\omega$ SST turbulence model is to blend the best properties of the $k-\epsilon$ and $k-\omega$ models in one turbulence model. Hence, the model applies the $k-\omega$ model inside the boundary layer and switches to the $k-\epsilon$ model outside the boundary layer in the free shear flow. The $k-\omega$ shear stress transport (SST) turbulence model [47] has been chosen for solving the turbulence viscosity field quantity in the present research, because of it good capabilities in predicting flow separation.

In contrast to EVM, the Reynolds Stress Models directly solves the transport equations to obtain the Reynolds stress tensor. This means that the isotropic simplification of the EVM is avoided. On the other hand, RSM typically require more CPU time because of the extra transport equations to be solved. Furthermore, convergence can become an issue because of the closing of the coupled terms.

CFD studies at supercritical Reynolds numbers In the literature different experiences with URANS have been shared by CFD studies. For example, scatter has been observed between the URANS from Catalano et al. [48], Ong et al. [49] and Singh and Mittal [50]. These differences have been attributed to different wall function implementations between the URANS models or due to the choice of a 2D simulation of turbulent flow. In most of the numerical studies at supercritical Reynolds numbers, the results deviated significantly from the experiments, especially with URANS. Yet, [49] still suggested that for engineering purposes URANS would lead to *satisfactory* results in the supercritical flow regime. Their simulation was done in 2D with the $k-\epsilon$ turbulence model. In contrast with that, [51] argued that URANS is not able to capture the flow field of a cylinder accurately because the eddy-viscosity turbulence models are based on an isotropic eddy viscosity and homogeneous Reynolds stresses. In the numerical study of [43] different turbulence models, three-dimensional effects and different CFD approaches have been evaluated at two different Reynolds numbers, $Re = 9.4 \cdot 10^4$ and $Re = 5 \cdot 10^5$. Both these Reynolds numbers correspond to the drag-crisis region. It was concluded in the study, when looking to quality of the results versus computational cost, that the 2D URANS $k-\omega$ SST model is the best choice. In fact, it was shown in their study that a 3D URANS $k-\omega$ SST simulation compared to 2D URANS $k-\omega$ SST simulation increased the CPU time by a multiplier of 2.4. The study of [51] argued that URANS in 3D would not contribute much to the accuracy as the predicted spanwise gradients of the Reynolds stress tensors are likely not significant enough to yield production and transport of turbulent kinetic energy in the z-direction. This is again caused by the fact that URANS embodies a homogeneous Reynolds stress tensor in the modelling. Their statement was backed up by earlier studies. These experiences from the literature have motivated to use a 2D URANS model instead of 3D in the present research. It was expected that adding the 3rd dimension would not lead to more accurate results and hence would not outweigh the increased computational time.

Another observed modelling hurdle at supercritical Reynolds numbers is that the flow is usually laminar and turbulent before separation, meaning transition is still present. With the standard URANS turbulence models, the flow is assumed to be fully turbulent. Based on [8], it is not expected that a Reynolds number will be reached in reality where the flow is fully turbulent at the attachment point. Indications show that a fully turbulent attached flow is reached at $20 \cdot 10^6 < Re < 50 \cdot 10^6$, which is far away from the aimed number in the present research. It has been observed in the experimental work of [52] that even at $Re = 3.6 \cdot 10^6$ the boundary layer was still laminar for a big portion of the cylinder. In the study of [53], the flow around a 2D cylinder at $Re = 8.5 \cdot 10^5$ was simulated with the SST $k-\omega$ turbulence model coupled to the $\gamma - Re_\theta$ transition model. The augmented model lead to more accurate results than the standard $k-\omega$ SST model because transition was simulated.

In the URANS and DES study of [54], a distinction was made between laminar and turbulent separation in their simulations. The first type of separation implies presence of the drag crisis, while the second type is found back in the supercritical regime. It appeared that URANS agreed very well with the DES for the turbulent separation cases, while for the laminar separation there was a big difference. It was suggested in

their study that for the turbulent separation, the wake was expected to be narrower and the shedding to be weaker. Both developments would have reduced the size of large eddies which in turn enhanced the URANS prediction. In line with these statements, in the numerical study of [49] it was found that the URANS k-ϵ model captured more accurate results at higher Re after the *drag crisis*. The study concluded that a higher Re moved the transition more upstream and hence this resulted in more overall turbulent flow along the cylinder body, which comes closer to the turbulent modelling assumption of URANS.

Besides the Reynolds number, the turbulence intensity of the freestream flow could contribute to the turbulence of the boundary layer around the cylinder, as was shown by multiple studies [27], [3]. However, the effect of the turbulence intensity on the vortex shedding will not be addressed in the present research.

The experiences of LES applied to the flow around a cylinder are diverse at high Reynolds numbers. For instance, [55] concluded that after more than 30 years of research, LES will eventually fall short because of fundamental limitations in the sub filter eddy-viscosity model. However, other studies, like [56] showed good agreement between a LES simulation and experimental work at $Re = 1.4 \cdot 10^5$. Yet, the same study also noted that at even higher Reynolds numbers it is expected that the computational cost will get closer to a DNS run because the viscous sub layer height decreases. This was also noted by the study of [51].

Besides the computational argument for using URANS that was stated before, there is an additional argument to use this approach to see how well this computationally appealing approach performs in the supercritical regime. It was observed in the literature that not many numerical simulations have been done before to simulate and model the fluid flow around a cylinder at supercritical Reynolds number (this was also noted by [49]). The present research aims to demonstrate the capabilities of the widely-used URANS approach and to see if this approach is able to predict the flow field at these large Reynolds numbers with satisfactory accuracy.

It has been stated before that the relevant operating range for Siemens Gamesa is considered to be $Re > 3.5 \cdot 10^6$. There are a few additional reasons to limit the MSc research on investigating the supercritical region ($Re > 3.5 \cdot 10^6$) rather than the transitional regime ($1.5 \cdot 10^5 < Re < 3.5 \cdot 10^6$) or the subcritical regime $300 < Re < 1.5 \cdot 10^5$. Firstly, during the *drag crisis* in the transitional regime, too many complex flow phenomena are present as was explained in section 2.2.1. Complex flow features that might be present in this regime are for example laminar separation bubbles or strong spanwise (3D) boundary layer interaction. As was rightly pointed out and supported by results in the numerical study of [43], the modelling errors can become very apparent in the drag crisis region when using the URANS approach. In the subcritical regime, while the boundary layer might be fully laminar the wake is starting to become more and more turbulent in this regime. This leads to either very large demands on computational power when using a DNS or to an intrinsically wrong modelled flow when performing URANS. In other words, to get the most out of the URANS approach in this fundamental cylinder problem, the flow field in the supercritical regime was expected to give the smallest modelling errors as a big portion of the flow is becoming turbulent (in boundary layer and in wake). In fact, it was stated before that the accuracy of URANS only improves when increasing the Reynolds number in the supercritical regime.

It is clear now that the supercritical Reynolds number regime has been chosen as the regime of interest for the present research. Hence, all the turbulent simulations have been performed in the regime where $Re > 3.5 \cdot 10^6$. Besides this regime of interest for the present research, the model has also been used to simulate rather low Reynolds numbers. In fact, most of the model assessments have been performed at low Reynolds numbers: $80 < Re < 200$. This range has been defined as the laminar flow regime in the present research. More information on the model assessments will be provided in the next two sections.

2.3.2. Fluid-structure interaction modelling

As was slightly introduced before, there is a clear distinction between two types of experiments when the cylinder is no longer stationary: forced-vibration and free-vibration experiments. The pros and cons of these two set-ups are discussed briefly in the following section. Then, the set-up chosen for the present research is reported. After that, the different coupling strategies for the oscillating cylinder simulation is briefly discussed.

Forced and free-vibration experiments The forced-vibration experiment is achieved by prescribing a motion to the cylinder body while the Reynolds number (and hence the inflow velocity) is kept constant. Regarding free-vibration experiments, the cylinder motion is not actively controlled and usually the wind velocity is varied [14]. The forced-vibration experiments can be considered as a 1-way coupled fluid-structure interaction problem. In these experiments, only the effect of the cylinder motion on the fluid is investigated and not

the other way around. The free-vibration experiments can be interpreted as a 2-way coupled FSI problem. In these experiments, the effect of the cylinder motion on the fluid is considered and vice versa as well.

In the review of [13], the pros and cons of forced and free-vibration experiments were presented. The main advantage of forced-vibrations is that frequency and amplitude can be controlled very precisely. On the contrary, when free-vibration is studied, a small wind speed increment can lead to significant changes in oscillation amplitude and phase jumps can occur. Such phenomena can be challenging to measure accurately and can be become more complex than desired. However, in forced-vibration experiments, a lot of data needs to be acquired to measure the effect of the fluid on the cylinder. This would imply that forced-vibration tests will take up more running time. Also, self-exciting vibrations are closer to reality. For example, in reality, the displacement amplitude is not constant and the motion is not pure sinusoidal. Furthermore, as was pointed out by [14], the flow is history dependent. This means that separation points, pressure distributions and correlation lengths are dependent on the flow history. Hence, comparing the instantaneous quantities between forced and free-vibration experiments can lead to differences in the observed results. Based on these findings, it might be concluded here that the forced-vibration experiment is expected to be less complex. However, the forced-vibrating experiment simplifies the reality as well, by neglecting the effect of the wake on the cylinder motion.

Another potential benefit of the forced-vibration experiments is the utilization of the output data to further develop existing phenomenological models. One method of using forced-vibration experimental results in a phenomenological model was carefully explained in the doctoral thesis of [4]. The concept behind this method starts with the assumption that once the complete system is in steady-state, the structural damping should be equal to the aerodynamic damping as the oscillation amplitude remains constant over time. If this assumption holds, it is possible to solve the structural oscillation amplitude by only knowing the aerodynamic damping from the forced experiments. The wake can be described by one single parameter which is why this method is very pragmatic. Typically, the aerodynamic damping can be presented in a contour map where the (prescribed) reduced frequency f^* is on the x-axis and the (prescribed) non-dimensional amplitude A^* is on the y-axis. This method will be illustrated and presented later in this report. Other studies in the literature in which forced-vibration experimental data was used as input in a structural model and compared against free-vibration experiments are: [57] and [28]. The study of [57] compared his forced-vibration data with the experiment of C. Feng [30]. His study found various regions where the agreement was good but also some regions where the comparison was not successful. From an engineering perspective, it would be highly practical if the CFD results can be used to calibrate existing phenomenological models.

Furthermore, in contrast to the free-vibration experiments, the forced-vibration experiment is able to provide insights into non-equilibrium operating points. It is possible to prescribe a structural motion which is for example far away from the lock-in region. In the free-vibration experiments, the system would most likely return to the equilibrium points found at the typical lock-in curve (see for example fig. 2.9). This equilibrium in a 2-way coupled system is then guaranteed by the energy conservation between fluid and structure, while in the 1-way coupled experiments the motion is forced. These non-equilibrium points can address more fundamental answers on how the wake would react under artificial conditions. These insights can help in obtaining a general relation between structure and fluid and to understand the sensitivity of the wake to different operating conditions.

As summarized by [29] and [13], it is still an ongoing debate if forced-vibration experiments are useful to predict the free-vibration situation. This is also in line with the review of [14], which addresses the importance of determining whether forced and free-vibration cases are 'sufficiently alike to extract reliable information from each'. It was argued in the same review that many more experiments should be done for both cases to address this. In the study of [58], forced and free-vibration experiments were performed at $Re \approx 3800$ to compare these two approaches. They found that the lift phase angle and lift amplitude agreed well for forced and free experiments, while the cross-correlation coefficient showed differences. The study of [59] performed a DNS on flow over a flexible cable at $Re = 100,200$ and $Re = 300$, where the cable was forced and free to vibrate. The authors concluded that the results of the two cases did not show good agreement. They observed that the flow transition in the wake was delayed when the vibrations were forced compared to free-vibration simulations. One of the plausible explanations found in the literature is that for the free-vibrating cases, the cylinder motion is not necessarily purely harmonic. The study of [60] showed that frequency modulation (i.e. a changing excitation frequency over time) can have a substantial impact on the wake patterns. In addition, in a previous study from the same authors, it was found that the wake can also change significantly when the amplitude of the cylinder motion is modulated over time [61]. A summary of more studies on the effect of the cylinder motion modulation on the wake is given in the study of [61]. These studies suggest that a different

harmonical excitation signal can already have a substantial effect on the wake. Typically, the prescribed motion for forced-vibration experiments or simulations is purely harmonic while the motion trajectory found in the free-vibrations cases may not be purely harmonical.

In the present research both a forced-vibration and free-vibration set-up will be analysed. The following reasons, based on the literature review of before, have supported the choice of using both an 1-way and a 2-way coupled set-up in the present research:

1 The data generated from the 1-way coupled model can be used as input data for phenomenological models. It appeared the forced-vibration results were also useful to explain some of the phenomena occurring in the free-vibration simulations. In addition, this type of coupling has allowed the fluid solver to simulate the wake under non-equilibrium structural operating conditions which fall outside the capabilities of the 2-way coupled model.
2 In order to get the full picture on the FSI effects described earlier in section 2.2.4, the main goal of the thesis was to model the free-vibration experiment and to predict a realistic response of the system. The free-vibration experiment has allowed to vary the structural parameters. The sensitivity of the wake to different structural parameters could therefore be investigated.
3 The forced-vibration experiment provided a good intermediate research step between the stationary and the freely-moving (2-way coupled) cylinder. The degree of modelling complexity was expected to be smaller for the forced-vibration simulations compared to the free-vibration experiments. Furthermore, the only FSI study found in the literature in the supercritical regime was a forced-vibration experiment. The 1-way coupled model gave the possibility of using this wind-tunnel data for validation in the supercritical regime.
4 It was aimed to include a comparison of the 1-way and 2-way coupled models to contribute on the on-going debate how well these two canonical cases match (at supercritical Reynolds number).

Numerical modelling of FSI Considering the *forced-vibration* simulations, the FSI modelling is mostly done by enforcing a prescribed motion to the cylinder body. This set-up is quite similar to the stationary set-up, but for the forced-vibrations the cylinder evidently moves. The cylinder should be considered as a moving geometry within the computational domain. The moving cylinder has no mass and is not attached to a damper/spring. Hence, there was no 'structural domain' and no structural solver, only the flow field has been solved. Instabilities are therefore less likely to occur within the forced-vibration simulations compared to the free-vibration set-up, since only one solver is active. This solver, the fluid solver, is configured as much as possible in accordance with the stationary set-up.

There are two ways of setting up the coupling of the FSI scheme for *free-vibration* simulations: explicit and implicit. In the former type of coupling (loosely-coupled), the structure and fluid are only solved once per timestep. The other coupling strategy (strongly-coupled), implicit, multiple iterations between the structure and fluid are employed per timestep. These iterations ensure that convergence criteria are satisfied for each timestep and therefore provide an unconditionally stable system [62]. Because the explicit scheme does not resolve the fluid and structure for multiple times at each timestep, this method is more economical. On the other hand, this coupling strategy can become unstable under certain operating conditions. A more detailed explanation on the differences between these two algorithms will be reported in the next chapter, in section 3.2.2.

According to [63], the stability of the explicit coupled system with an incompressible fluid solver is proportional to the timestep, stiffness of the structure, thickness of the structure and the mass ratio m^*. The same system's stability is inversely proportional to the characteristic size of the structure, order of the numerical scheme and the viscosity of the fluid [62]. These relations stem from the presence of an additional artificial term, called 'added mass' in [62]. This term is not equal to the added mass typically known from fluid dynamics. It is a different term arising from an instability at the fluid-structure interface. In the present research low values for the viscosity were expected for air, implying enhanced stability. On the other hand, especially for finer meshes and higher Reynolds numbers, a smaller timestep was required to satisfy the Courant condition in eq. 3.22 (which is reported in the next chapter) and second order numerical schemes were used. In the research, moderate values for the mass ratio and stiffness of the structure are used to evaluate the sensitivity of the wake and overall's system response to these parameters. It is hard to draw a conclusion based on these implied operating conditions and settings regarding the preferred type of FSI solver.

Other VIV-FSI studies in the literature showed mixed experiences regarding the solvers' stability and accuracy. For example, the explicit FSI solver used in [64] showed good performance of predicting a transverse

freely-moving cylinder at Re = 100 and for low mass ratios. It was stated in their study that the numerical damping was reduced by an accurate prediction of the displacement. In the DNS study of [65], it was argued that since the timestep was adequately low as a consequence of the Courant restriction for the fluid solver, the explicit scheme was sufficient to yield stable simulations. Furthermore, the study of [66] also showed that their loosely-coupled scheme was able to predict the lock-in phenomenon of vortex-induced vibrations. At the same time, the study [67] argued that a strongly-coupled FSI solver is a necessity for low mass ratio cases.

Based on these experiences, it has been decided to start the present research with a weakly-coupled scheme to save computational power. Stability and convergence criteria are monitored to check if the weakly-coupled scheme is indeed sufficient.

2.4. Conclusions

Based on the findings in the literature, the research plan and methodology will be defined in this section. The previously identified studies on VIV and the modelling experiences found in the literature have both helped in determining the research plan and methodology. The literature review mostly addressed the questions: *What are the influencing parameters that play an important role in VIV?* and *What has been done before on VIV experimentally and numerically?*

The research plan emanated from the conclusions drawn from the literature review of this chapter. The research plan, bearing in mind the research objective defined in 1, aims to address the *what*: *What knowledge does the MSc research wants to obtain?* Then, the research methodology will address the *how*: *how is the research question addressed in the most efficient, complete and reliable way?* It was observed in the literature review that the reliability in numerical experiments on VIV is very crucial. For this reason, the verification and validation plan will be highlighted in the research methodology.

2.4.1. Research Plan

It was explained in chapter 1 that the wind turbine towers are subjected to a flow with a Reynolds number of $Re > 3.5 \cdot 10^6$. As was pointed out earlier in section 2.3.1, not many numerical simulations have been performed at supercritical Reynolds numbers. In fact, it was even pointed out by the recent review of Bearman [13] and in the recent review of Sarpkaya [14] that it is important for the industry to conduct more studies at high Reynolds number on VIV. Therefore, the first scope refinement is to focus the MSc research on supercritical Reynolds numbers, i.e. $Re > 3.5 \cdot 10^6$ and to provide the body of science with new, state-of-art insights/data in this regime. This Reynolds regime is also in the interest of Siemens Gamesa for full-scale applications on wind turbine towers. Since the availability is limited and the results of current available research is scattered in this regime, the present research has paid extra attention to the validation and verification process in this regime.

Next to the Reynolds number, the transverse oscillating cylinder parameter has proven to be the next relevant parameter for Siemens Gamesa to research. This parameter can become a governing parameter, while overriding all other influence parameters (see section 2.2.4). Although the other influencing parameters are also of interest, these tend to have a smaller effect on VIV as was explained in chapter 2. In addition, most of these parameters have been investigated already at high Reynolds numbers, for example the surface roughness and free stream turbulence (see section 2.2.3). Based on the compilations of [2] in 1969 and [12] in 2006, it was concluded that there is still a lack of moving cylinder experiments/numerical studies at high Reynolds number. The effects of the cylinder motion on the wake have been briefly discussed in section 2.2.4, yet most of the researches mentioned there were conducted at relatively low Reynolds numbers. Hence, for these reasons it has been concluded that the MSc research will zoom into the fluid-structure interaction at supercritical Reynolds numbers.

It was stated in section 2.2.4 that the effect of the in-line displacement on the wake is expected to be considerably smaller compared to the transverse displacement effect. Therefore, the in-line DOF is left outside the scope of the MSc research and only the transverse cylinder motion effect is researched. Part of the MSc research will focus on the qualitative aspects of these transverse cylinder motion effects and this will provide new insights in to how the fluid-structure interaction behaves at higher Reynolds number. The other part of the research will quantify the fluid-structure interaction and determine how big the effect is of the cylinder motion on the lift force for example. All the other influencing parameters mentioned in section 2.2.3, besides the Reynolds number and the cylinder oscillations, should be taken into consideration during the MSc research. Their effects should be minimized to make sure that the two aimed relational studies are researched independently.

Considering the five effects of the cylinder motion on the wake, especially the lock-in effect and the effect on the strength of the vortices are of primary interest to Siemens Gamesa. The lock-in region indicates what a feasible operating envelope for the wind turbines and where VIV can be expected at high Reynolds numbers. Once VIV is initiated, it is highly relevant to quantify the lift magnification factor caused by the transverse cylinder motion. The lift force can have a detrimental impact on the design lifetime, as was stated in chapter 1. It is therefore of the absolute importance to estimate the additional effects of the cylinder motion on the lift force.

2.4.2. Research Methodology

Research Stages URANS has been chosen for the supercritical Reynolds number simulations. This choice is motivated firstly by the fact that for turbulence modelling, URANS has proven to offer a good compromise between computational time and accuracy. Furthermore, the literature review showed that not many numerical studies have been conducted in the super critical regime. For a moving cylinder, no other numerical simulation was found in the literature. The present research has aimed to present new results in this regime and to demonstrate the capabilities of the widely used URANS approach.

The FSI effects have been researched in three stages. In all these stages some influence parameters have been kept constant and some varied (independent variable). Every stage resembles a different CFD case that has been investigated, see fig. 2.17. In the first stage, the cylinder has been kept stationary (no FSI has been modelled). This stage might be considered as the basic case, where most of the verification & validation (denoted as Ver. & Val. in fig. 2.17), spatial convergence (denoted as 'conv.' in fig. 2.17) and temporal convergence studies were performed. These assessments evaluated the reliability and accuracy of the CFD model. In addition to that, the first stage provided insights in to wake which is caused purely by the vortex-shedding mechanism. Hence, the purpose of this stage was to address the 'stationary' wake and to provide a reference perspective for later comparison when the cylinder was assigned to move in some way. The output of this stage can be considered as a typical CFD output: all the flow field data (pressure, momentum and if applicable k-ω) and the aerodynamic forces experienced by the cylinder body.

After the first stage, same way of coupling was added to the stationary model. As has been argued before in the literature review, both a *forced-vibration* (1-way coupled) and *free-vibration* (2-way coupled) simulation have been chosen to analyse VIV. The former simulation set-up has been done in the second stage. The 1-way coupling has introduced two additional input parameters: the prescribed cylinder displacement amplitude (y_{max}) and frequency (f_{cyl}). Eventually, the CFD simulations of this set-up would lead to the aerodynamic damping and force magnification besides the flow fields. The aerodynamic damping, which summarizes the fluid-structure interaction into one parameter, has appeared to be very useful to serve as calibration data for phenomenological models predicting VIV. The force magnification is a consequence of the introduced 1-way coupled cylinder motion. It has been observed that for some operating points, the motion usually magnifies the aerodynamic forces compared to the stationary case (1st stage). Hence, this output has been called the force magnification in fig. 2.17.

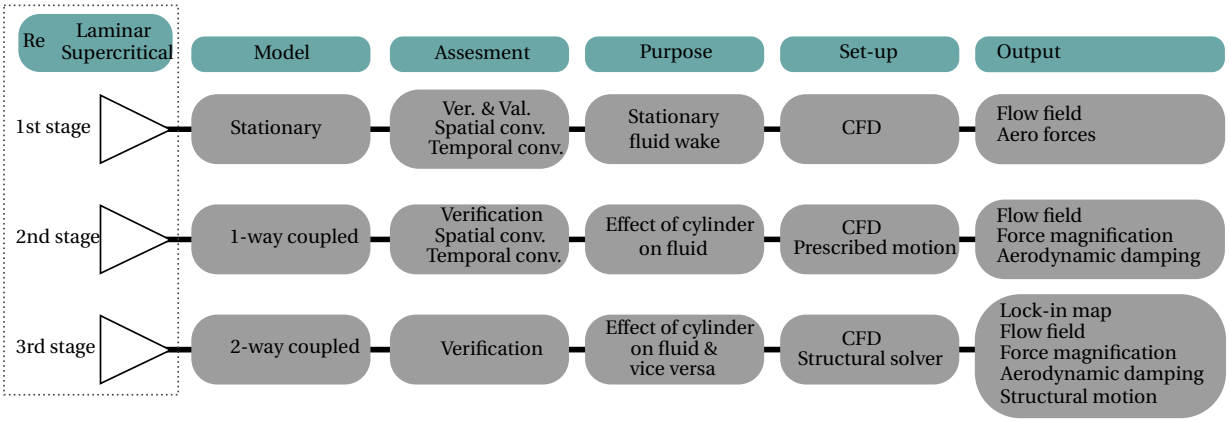

Figure 2.17. Research Stages

In the 3rd stage, the system was set-up to be two-way coupled. A structural solver has been implemented to predict the effect of the wake on the cylinder motion. In this stage, the additional input parameters are

the structural mass, spring stiffness and damping coefficient. While in the 2nd stage the cylinder motion was known a priori, in the 3rd stage this was variable which has been computed by the structural solver and was therefore only known a posteriori. Similar to the 1-way coupled case, the 2-way coupling leads to an aerodynamic damping coefficient, force magnification factor and flow fields around the cylinder. The lock-in map, as was explained in 2.2.4, is a very important outcome of the 2-way coupled simulation as it provides the operating range where lock-in occurs. In addition, if the aerodynamic forces are plotted on the y-axis (in contrast to the plotted displacement in fig. 2.9), it also shows the force magnification factor for different reduced velocities (and hence different wind speeds).

All three stages are executed at multiple Reynolds numbers, as indicated in fig. 2.17 by the 'laminar' and 'supercritical' detonation. The reason behind this distinction of flow regimes will be explained in the next section and in chapter 3.

Based on the framework of fig. 2.17, the following two hypotheses have been tested in the MSc thesis:

H0: *"FSI effects at supercritical Reynolds number caused by VIV of a 2D moving cylinder do not lead to an increased lift force and critical wind speed range compared to VIV of a 2D stationary cylinder."*

H1: *"FSI effects at supercritical Reynolds number caused by VIV of a 2D moving cylinder lead to an increased lift force and critical wind speed range compared to VIV of a 2D stationary cylinder."*

Verification and Validation All the type of assessments of the present research are listed in tab. 2.1, for each stage of fig. 2.17 and for the laminar/supercritical flow regime. The laminar flow regime has been defined before where the Reynolds number range is $80 < Re < 200$. The verification studies were aimed to obtain an indication of the numerical error (difference between the exact solution of the governing equations and the iterative solution of the discretized equations) and validation studies to get an indication of the modelling error (difference between the real flow and the exact solution of the governing equations) [41], [42]. The spatial convergence and temporal convergence study were both an assessment to guarantee that the discretization process was done unambiguously right and that the level of refinement lead to an adequately small discretization error. The discretization error is part of the numerical error which only describes the error because of the spatial/temporal discretization (i.e., the truncation error). It appeared the VIV fluid problem considered in the present research does not have an exact or perfect benchmark solution to compare to. The fluid problem requires at least a CFD approach as it is too complex to be captured accurately by a lower fidelity approach (analytical models for example). The numerical benchmark solutions found in the literature for VIV were all obtained by CFD. The verification study was performed against multiple CFD studies to ensure the presently obtained results fall within the 'bracket' of numerical results in the literature. However, it must be noted that uncertainty is present in this comparison as the exact solution is not known. The same holds for the grid and temporal refinement studies, where the solutions have been compared to the finest mesh (rather than a CFD solution from the literature).

Case	Flow Regime	Verification	Validation	Spatial Convergence	Temporal Convergence
Stationary	Laminar	X		X	X
	Supercritical	X	X	X	X
1-way coupled	Laminar	X		X	X
	Supercritical		X		
2-way coupled	Laminar	X			
	Supercritical				

Table 2.1: Assessment scheme

As was pointed out before and shown in fig. 2.17, the CFD model has mostly been assessed for the stationary case (1st stage). The first reason for this choice was supported by the observation that in the literature most of the experimental and numerical work has been done for a stationary cylinder rather than a moving cylinder. Besides that, the stationary case was deemed as the least complex case in the present research. The fundamental stationary case allowed the present research to conduct a more thorough assessment. Still, for the 1-way and 2-way coupled models verifications have been performed to ensure their reliability and accuracy as well. In fact, the 2-way coupled model has been compared against two independent CFD studies.

Like the stationary case, more assessments have been performed in the laminar regime as well. Numerical studies on the stationary cylinder have been found for all the three Reynolds regimes, although the modelling errors were sometimes significantly higher at higher Reynolds numbers. For laminar flows, the governing equations have been solved directly which tended to reduce the modelling errors. Yet, for turbulent flows, it was expected that the modelling error was larger because more modelling simplifications have been applied to the governing equations. Furthermore, it has turned out that in the laminar regime, the flow can be described adequately by 2D modelling [68]. This lower Reynolds number was also chosen based on the lower implied computational cost for laminar flows compared to turbulent flows which would be computationally more expensive as was explained before in section 2.3.1. The lower computational time allowed to run more simulations, tweak the CFD model and look for the most optimal CFD settings for different flow problems (stationary, forced and freely moving). In contrast to the numerical work, it has appeared that validation in the laminar regime is troubled by the fact that not a lot of experiments have been carried out at these low Reynolds numbers.

After the verification study in the laminar regime, the meshes and model have been adjusted to aim for the supercritical range. Where there was a lack of experimental work in the laminar regime, the supercritical regime attracted plenty of experimental research. Hence, no intermediate step between the laminar and supercritical regime has been taken to validate the CFD model. In fact, the validation study was only done for the supercritical numerical studies. It must be noted that a significant modelling error is expected at these large Reynolds numbers. 2D simulation, all flow falsely assumed by URANS to be turbulent and more turbulent approximations are expected to contribute to the modelling error. Yet, the validation was performed in this regime based on a couple of reasons. The first argument is that the modelling error caused by not modelling the transition can also be expected in the other Reynolds regimes. For example, even in the sub critical regime where the boundary layer is fully laminar the wake is in fact turbulent. Hence, a laminar CFD validation in the sub critical regime after the laminar regime would inherently also lead to modelling errors in the wake. Moreover, validation at supercritical Reynolds numbers gives the opportunity to draw conclusions on the shortcomings of the present CFD turbulence model. It has been inventorized in the literature that there are also some numerical studies available in the supercritical regime, all with their own modelling shortcomings. These numerical studies provided the opportunity to review the performance of the present turbulence model.

It has been reasoned that for every added coupling-complexity or when going from the laminar regime to the more challenging turbulent flow, fewer assessments would suffice as the model has been assessed adequately at the fundamental cases (laminar and stationary). Hence, the laminar flow regime and the stationary cylinder were assessed more than the cases with turbulent flow or a moving cylinder to gain confidence on the modelling. At the same time, while adding coupling or turbulence to the model, the available research peers to verify or validate the model became scarcer. Hence, as the complexity of the model enhances, the research progresses more towards novel research areas. Besides obtaining fundamental insights from the results and providing new data to address the research question, the research also aimed to add value by sharing the modelling experiences.

3
Modelling

All aspects of the CFD model and the FSI model will be covered in this chapter. First, the fluid solver (computational fluid dynamics) will be explained carefully. Then, the inclusion of the 1-way and 2-way coupled FSI models to the fluid solver will be treated. As was stated in chapter 1, both the fluid solver and FSI solver available within *OpenFOAM* [1] will be used in the present research. Finally, all the important post-processing metrics will be discussed.

This chapter focuses on the following three questions:

- *How will the fluid be modelled?*
- *How will the fluid-structure interaction be modelled?*
- *How will the results be post-processed?*

3.1. Fluid Solver

The concept of computational fluid dynamics can be explained by the following aspects:

1 Physical modelling.
2 Mathematical modelling.
3 Numerical modelling.

In the physical modelling, the governing equations of fluid dynamics are considered as the basis of the CFD model. Then, the resulting equations are discretized mathematically into a system of algebraic equations to be solved by the computer (mathematical modelling). These equations are solved by an iterative method to compute the flow quantities of interest, which is known as the numerical modelling. All three modelling aspects are a necessity for the fluid solver to work. These three aspects will be explained in the next three sections step by step.

3.1.1. Physical modelling

The physical modelling already started by cancelling out some of the terms of the three governing equations for fluid dynamics: momentum equation (conservation of momentum), the continuity equation (conservation of mass) and the energy equation (conservation of energy). Some of these modelling choices have been discussed briefly before in section 2.3.1 from the previous chapter. The fluid is assumed to be viscous, incompressible, Newtonian, isothermal and unsteady. This resulted in the decoupling of the energy equation. The assumed fluid properties are considered as the first physical modelling assumptions.

As has been argued before in section 2.3.1, for higher Reynolds number flows the flow will be predicted by URANS (because of computational cost). For lower Reynolds numbers, the laminar flow field will be obtained by solving eq. 2.7 and eq. 2.8 directly. Hence, no further modelling simplifications regarding the fluid physics will be done for the laminar simulations except for the simplifications to the governing equations.

The Reynolds-Averaged Navier-Stokes equations are based on the idea of O. Reynolds where eq. 2.7 and 2.8 are time-averaged. It has been stated before in section 2.3.1 that the flow field will be solved in only in two

dimensions, which is another simplification. For 2 dimensions, the Reynolds-Averaged approach assumes that the flow variables can be decomposed into a mean and fluctuating component:

$$\mathbf{u}(\mathbf{x},t) = \overline{\mathbf{u}}(\mathbf{x},t) + \mathbf{u}'(\mathbf{x},t) \quad \text{with} \quad \overline{\mathbf{u}'} = 0 \tag{3.1}$$

where $\mathbf{x} = (xy)^T$ is the position vector. In unsteady flows, typical with vortex shedding, the flow solution is obtained by ensemble averaging. The number of samples must be large enough to ensure that the fluctuations can be disregarded [42]:

$$\overline{\mathbf{u}}(\mathbf{x},t) = \lim_{N\to\infty} \frac{1}{N} \sum_{n=1}^{N} \mathbf{u}(\mathbf{x},t) \tag{3.2}$$

After substitution of the decomposed quantities into equations eq. 2.7 and eq. 2.8 and applying an averaging operator, the Reynolds-Averaged Navier-Stokes are obtained:

$$\frac{\partial \overline{\mathbf{u}}}{\partial t} + \nabla \cdot (\overline{\mathbf{u}}\overline{\mathbf{u}}) + \frac{1}{\rho}\nabla \overline{p} - \nabla \cdot (\nu \nabla \overline{\mathbf{u}}) = -\nabla \cdot \overline{\mathbf{u}'\mathbf{u}'} \tag{3.3}$$

$$\nabla \cdot \overline{\mathbf{u}} = 0 \tag{3.4}$$

While the linear terms of eq. 2.7 and eq. 2.8 give an identical term, the quadratic terms yield a non-linear term. These non-linear terms are known as the correlations and can be found on the right-hand side of eq. 3.3. This term is also known as the Reynolds stress tensor. Inspecting eq. 3.3 and eq. 3.4, it can be seen that there are more unknowns than equations, which implicates a closure problem. Although it is possible to further derive solvable equations, there will always remain more unknowns than equations. Hence, the Reynolds stress tensor must be approximated partly by additional models to arrive at a closed set of equations. The fluctuation terms that are still present because of the non-linearity in the Navier-Stokes is then attributed to turbulence and should be modelled by a turbulence model. Because only the mean is solved with URANS, a bigger timestep and mesh spacing is possible in contrast to when all the turbulence scales are resolved. In hindsight, URANS resolves the mean flow field and the Reynolds stress tensors models the effect of the turbulence on the mean flow. This saves a lot of computational time but implies that the complete turbulence spectrum is modelled.

There are multiple turbulence models available to approximate the RHS of eq. 3.3. It was explained before in section 2.3.1 that the k-ω SST model was chosen as turbulence model for the present research. This model is categorized as a linear Eddy Viscosity Model (EVM). EVM is based on the observation that turbulence leads to momentum exchange between fluid particles and eventually to chaotic movement of eddies. EVM models these fluid element movements as increased viscosity [41]. The stress tensor is modelled to be proportional to the shear in the mean flow by the eddy viscosity:

$$-\overline{u_i' u_j'} = 2\nu_T S_{ij} - \frac{2}{3}\delta_{ij} k \tag{3.5}$$

with the shear rate equal to:

$$S_{ij} = \frac{1}{2}\left(\frac{\partial \overline{u}_i}{\partial x_j} + \frac{\partial \overline{u}_j}{\partial x_i}\right) - \frac{1}{3}\delta_{ij}\frac{\partial \overline{u}_k}{\partial x_k} \tag{3.6}$$

with k the turbulent kinetic energy:

$$k = \frac{1}{2}\overline{u_i' u_i'} \tag{3.7}$$

The last term in eq. 3.5 ensures that the equation is still correct when both indices are assumed equal ($i = j$) [42]. Model variations have been suggested by Menter and more researchers over time to the 'standard' k$-\omega$ SST model of Menter in 1994 [47]. *OpenFOAM* uses the version that is based on the $k-\omega$ SST model found in [69] with a revised turbulence specific dissipation rate production term from [70]. For more information on these turbulence model changes, the reader is referred to the NASA website [71].

The turbulence specific dissipation rate ω is described by the following partial differential equation:

$$\frac{\partial \omega}{\partial t} + \frac{\partial u_j \omega}{\partial x_j} = \gamma \frac{\tilde{P_k}}{\nu_T} - \beta\omega^2 + \frac{\partial}{\partial x_j}\left[(\nu + \sigma_\omega \nu_T)\frac{\omega}{x_j}\right] + 2(1-F_1)\sigma_{\omega 2}\frac{1}{\omega}\frac{\partial k}{\partial x_j}\frac{\partial \omega}{\partial x_j} \tag{3.8}$$

The blending function F_1 is given by:

$$F_1 = \tanh\Big[\Big[\min\Big[\max\Big(\frac{\sqrt{k}}{\beta^*\omega\gamma}, \frac{500\nu}{\gamma^2\omega}\Big), \frac{4\sigma_{\omega 2}k}{CD_{k\omega}\gamma^2}\Big]\Big]^4\Big] \tag{3.9}$$

and:

$$CD_{k\omega} = \max\Big(2\sigma_{\omega 2}\frac{1}{\omega}\frac{\partial k}{\partial x_j}\frac{\partial w}{\partial x_j}, 10^{-10}\Big) \tag{3.10}$$

The second transport equation describes the turbulent kinetic energy k:

$$\frac{\partial k}{\partial t} + \frac{\partial u_j k}{\partial x_j} = \tilde{P_k} - \beta^* k\omega + \frac{\partial}{\partial x_j}\Big[(\nu + \sigma_k \nu_T)\frac{\partial k}{\partial x_j}\Big] \tag{3.11}$$

Where the limited production term $\tilde{P_k}$ is described by:

$$\tilde{P_k} = \min(P_k, 10\beta^* k\omega) \tag{3.12}$$

with:

$$P_k = \nu_T \frac{\partial u_i}{\partial x_j}\Big(\frac{\partial u_i}{\partial x_j} + \frac{\partial u_j}{\partial x_i}\Big) \tag{3.13}$$

The turbulence coefficients are:

Model coefficient	**Value** [−]
σ_{k1}	0.85
σ_{k2}	1.00
$\sigma_{\omega 1}$	0.50
$\sigma_{\omega 2}$	0.856
β_1	3/40
β_2	0.0828
γ_1	5/9
γ_2	0.44
β^*	0.09
a_1	0.31

Table 3.1: Turbulence model coefficients for the $k-\omega$ SST model

If needed, the constants are blended (typically close to the boundary layer) by the following interpolation:

$$\phi = F_1\phi_1 + (1 - F_1)\phi_2 \tag{3.14}$$

Where ϕ can represent any coefficient from tab. 3.1.
Once the two additional turbulence transport equations are solved, the eddy viscosity field is obtained by:

$$\nu_t = \frac{a_1 k}{\max(a_1\omega, \Omega F_2)} \tag{3.15}$$

Where Ω is the magnitude of the strain rate tensor. F_2 is the following blending function:

$$F_2 = \tanh\Big[\Big[\max\Big(\frac{2\sqrt{k}}{\beta^*\omega\gamma}, \frac{500\nu}{\gamma^2\omega}\Big)\Big]^2\Big] \tag{3.16}$$

3.1.2. Mathematical modelling

After the physical model is clear, either being URANS for turbulent flow or DNS for the laminar flow, the next step was to define the mathematical model. In order for the computer to solve the equations defined before (laminar: eq. 2.7 or eq. 2.8 or for turbulent flow: eq. 3.3 and eq. 3.4), these equations are discretized in a system of algebraic equations. *OpenFOAM* uses the finite volume method, meaning that the conservation laws are applied to a finite number of control volumes (also known as cells) within the defined computational domain. Within the CFD model, the governing equations are solved within an Eulerian framework (fixed computational domain around flow field). Then, the conservation laws are solved numerically in the integral form [42] for every cell for every discretized timestep. This means that the conservation laws are directly applied to each control volume inside the computational domain. The mass conservation should thus be conserved locally in each cell and globally for the complete domain. The mathematical operations required to numerically solve some of the (non-linear) terms in the governing equations are handled by a set of specified discretization schemes. To close the system of algebraic equations, a set of boundary conditions at the boundaries of the computational domain and initial conditions must be defined. In this section, all these steps involved within the mathematical modelling will be explained. This section starts with the definition of the computational domain, after which the boundary conditions and initial conditions will be listed. Then, the spatial discretization and temporal discretization are reported. Finally, the set discretization schemes used in the CFD model will be covered.

Computational Domain The domain size can vary considerable between the different numerical studies found in the literature on VIV. It is found in the study of [72] that the size of the computational domain can affect the results of 2D flow simulations over a circular cylinder. Especially the aerodynamic forces and the base-pressure coefficient (in contrast to the Strouhal number) are sensitive to different grids and blockage effects. Hence, it was suggested that for verification purposes, the drag and base-pressure coefficient should also be compared (rather than only comparing the Strouhal number). The same study focused on investigating the effect of the inflow length and height of the domain on the CFD results (independent of grid size). With a compromise between an adequately small error and reasonable computational time, an inflow length of $L_1 = 50D$ and domain height of $L_3 = 100D$ was recommended by the study. It is worth mentioning that for a moving cylinder it is possible that the blockage effects are more pronounced if the domain height is not sufficiently large. In line with that, a domain upper and lower boundary height of $50D$ should minimize these effects.

Concerning the outflow length, a length of $L_2 = 50D$ was chosen, based on the outflow length that was also used in [72]. This outflow length was suggested after tests in the unsteady regime and yielded accurate results when compared to experiments. On top of that, compared to the outflow lengths of other domain studies (see [72, p. 484, tab. 1]), an outflow length of $L_2 = 50D$ can be considered as wide. This length may be assumed as a safe distance where effects from the outflow boundary on the solution can be neglected. It must be noted that the domain size study of [72] was only done in the laminar flow regime, for $Re = 200$. A brief domain size study has been performed for the turbulent flow in the present research, as will be reported in chapter 4.

The computational domain is illustrated in fig. 3.1. Five boundary patches are defined in the computational domain: inlet, outlet, sides, far field and the cylinder. Four of them are displayed in fig. 3.1. The only boundary patch that is missing in the illustration is the 'sides' boundary patch. This patch represents the front and back of the domain (in z-direction, normal to the x-y surface). Although the equations were solved in 2 dimensions, *OpenFOAM* always works with 3D meshes. Hence, the computational domain has one cell in the z-direction.

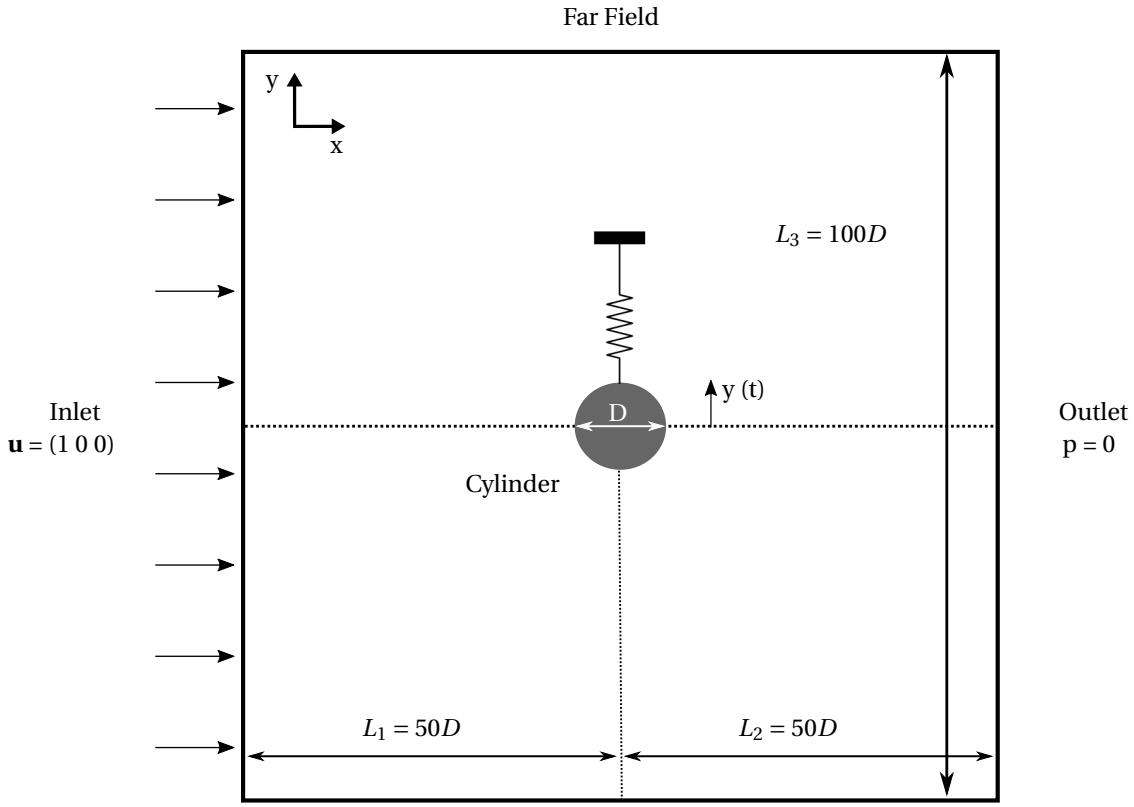

Figure 3.1. Illustration of the computational domain used in the present research

Boundary and initial conditions To ensure closure of the discretized system of equations boundary conditions for the flow parameters in eq. 3.3 and eq. 3.4 are required. The boundary conditions for the laminar and turbulent cases are no different except that for the turbulent case additional boundary conditions were applied to account for the turbulent properties. The boundary conditions did change when fluid-structure interaction effects were included.

The following boundary conditions have been used for the CFD model:

Case	Variable	Unit	Inlet	Outlet	Sides	Far Field	Cylinder	Initial Field
Stationary Cylinder	p	m^2/s^2	$\frac{\partial p}{\partial \mathbf{n}} = 0$	$p = 0$	Empty	Symmetry	$\frac{\partial p}{\partial \mathbf{n}} = 0$	$p = 0$
	$\mathbf{u}$	m/s	$\mathbf{u}$ = (1 0 0)	$\frac{\partial \mathbf{u}}{\partial \mathbf{n}} = 0$	Empty	Symmetry	$\mathbf{u}$ = (0 0 0)	$\mathbf{u}$ = (1 0 0)
Moving Cylinder	y	m	$y = 0$	$y = 0$	Empty	Symmetry	$y(t)$	$y = 0$
Turbulent Cases	k	m^2/s^2	$k = 0.00135$	$\frac{\partial k}{\partial \mathbf{n}} = 0$	Empty	Symmetry	$k = 1E-10$	$k = 0.00135$
	ω	$1/s$	$\omega = 487.4$	$\frac{\partial \omega}{\partial \mathbf{n}} = 0$	Empty	Symmetry	Wall Function	$\omega = 487.4$
	ν_t	m^2/s	Calculated	Calculated	Empty	Symmetry	$\nu_t = 0$	$\nu_t = 0$

Table 3.2: Boundary Conditions

It must be noted that, since in all the CFD cases the flow is assumed to be incompressible, the pressure unit is defined as m^2/s^2 which is equal to Pa/ρ. The fluid density was equal to $\rho = 1[kg/m^3]$ in the CFD cases, but it is possible to scale the resulting fluid properties to a different density when necessary. The internal field entails all the cells inside the computational domain, which are only used for the initialization (at $t = 0[s]$). Most of the boundary conditions that have been used are constant in time, except for the moving meshes.

A Neumann boundary condition was applied for the pressure at the inlet and cylinder wall and for velocity at the outlet. The velocity at the cylinder wall and at the inlet and the pressure at the outlet were specified with a Dirichlet boundary condition. The velocity at the cylinder wall was set to zero in all directions to ensure the *no-slip* condition. The boundary condition *empty* has been used to define that the governing equations normal to the sides boundary patch are not solved (z-direction). The *symmetry* boundary condition in *OpenFOAM* should be interpreted as a wall patch with *slip* condition. This means the flow at the far field walls is in parallel with the uniform inlet flow. This is a safe modelling assumption since the upper and lower height of the computational domain is sufficiently large, $50D$.

For the moving cylinder cases, forced and free-vibration, the no-slip condition at the cylinder wall was still active like the stationary cylinder. To ensure no flow rate m^3/s went through the cylinder body, it was necessary that v_{wall} was exactly equal to the cylinder velocity at every time instant. *OpenFOAM* has a standard boundary condition that has been built for moving meshes, which keeps the relative velocity zero during the simulation. As can be seen in tab. 3.2, the variable y has been included as a boundary condition and initial condition. Most of the boundary values and the initial values are set to zero, i.e. $y = 0$ as the cylinder is the only patch that is supposed to move. For the cylinder the boundary condition $y(t)$ has been defined, which will be worked out in the next section about the motion solver.

For the turbulent cases, the boundary conditions for **u** and p varied slightly. For the pressure, the outlet boundary condition was defined as an *ouletInlet* boundary condition. This boundary condition is equal to the boundary condition found in tab. 3.2 for the stationary case when there is no reversed flow. If there is backward flow, the boundary condition is specified by the same condition as the inlet (zero gradient, Neumann type). The same was done for the velocity boundary conditions in the turbulent case. This time the boundary condition was the opposite of the pressure boundary condition. When there was no reversed flow at the outlet, then the same Neumann condition as in tab. 3.2 was used (zero gradient). With reversed flow, the velocity at the outlet was set equal to the inlet velocity.

Additional boundary and initial conditions have been included for the turbulent properties. The initial turbulent kinetic energy (at $t = 0[s]$) is estimated by assuming isotropic turbulence with the following formula:

$$k = \frac{3}{2}(Ti\ u_{mean})^2 \tag{3.17}$$

In eq. 3.17, Ti is the turbulence intensity and u_{mean} is the mean flow velocity. In the present research u_{mean} is equal to the uniform, freestream inflow velocity $U = 1[m/s]$. The turbulence intensity defines the amount of freestream turbulence present at the inlet. Ti has been assumed to be 3%, which resembles a medium-turbulence case.

Besides the kinetic energy, the initial turbulence specific dissipation rate was estimated by:

$$\omega = \frac{\rho k}{\mu}\left(\frac{\mu_t}{\mu}\right)^{-1} \tag{3.18}$$

where $\frac{\mu_t}{\mu}$ is known as the eddy viscosity ratio, which was set equal to 10. The other flow quantities in eq. 3.18 have been reported before. The initial value of the eddy viscosity ν_t, from eq. 4.9, was set to zero (see tab. 3.2). The effect of the turbulence intensity (at the inlet) on the aerodynamic forces will be reported in chapter 4, section 4.2.1.

Regarding the boundary conditions for the turbulent properties in tab. 3.2, most of them were similar to the boundary conditions used for the pressure and velocity fields. The boundary conditions for the eddy viscosity for the inlet and outlet were calculated based on the boundary conditions specified for ω and k. At the cylinder wall different boundary conditions have been used for the turbulent properties. These boundary conditions depend on how the boundary layer is modelled. The following two dimensionless numbers are typically used for boundary layer analysis, the dimensionless wall distance y^+ and dimensionless velocity at the wall u_τ [41]:

$$y^+ = \frac{y_{wall}\, u_\tau}{\mu} \quad \text{with} \quad u_\tau = \sqrt{\frac{\tau_w}{\rho}} \tag{3.19}$$

The region for $y^+ < 1$ is called the viscous sublayer, which is mostly laminar. In the outer layer at higher values of y^+, the flow is expected to be fully turbulent. In between the viscous sublayer and the outer layer, there is a buffer layer. There are roughly two ways to impose wall conditions for the turbulent quantities. In the first option the turbulence in the boundary layer is modelled by wall functions, utilizing the predictable dimensionless boundary layer profiles. The other option is to resolve with URANS up to viscous sublayer which is adjacent to the wall. Both options influence the required cell size height applied to the grid at the cylinder wall. Option 1 is commonly pursued for higher Reynolds number flows, since the viscous sublayer becomes very thin with increasing Re [42]. This thin sublayer would require a smaller cell height at the wall leading to more grid nodes and hence higher computational cost. Yet, in the present research no wall functions have been used and the grid was constrained to a dimensionless wall distance of $y^+ = 1$ with a prism

layer type of mesh around the cylinder wall, increasing with a growth ratio of 1.2. In the present fluid dynamics problem, the near-wall region treatment was essential, since a lot of different flow features (such as flow separation) arise from the boundary layer [73]. This observation has motivated the choice for resolving up to the viscous sublayer rather than using wall functions. Bearing in mind that the viscous sublayer is dominated by viscous forces and is mostly laminar, the boundary conditions have to be chosen such that the turbulence at the wall is suppressed adequately [41]. For the turbulence kinetic energy at the cylinder wall, $k = 0[m^2/s^2]$ is recommended by [47]. Yet, to prevent the solver from dealing with zeros, k was set to $1E-10[m^2/s^2]$. For estimating ω at the cylinder wall, eq. 23 of [74] has been used which is: f

$$\omega = \frac{6\mu}{\beta_1 y_{wall}^2} \tag{3.20}$$

where $\beta_1 = 0.075$. This wall function is recommended for estimating ω for in the viscous sublayer and in line with the implemented turbulent wall function implemented in the *OpenFOAM* source-code. According to [74], the models should give accurate results if ω is large enough near the walls. The eddy viscosity was equal to zero at the wall, because the no-slip condition was active at the cylinder wall.

Spatial discretization For spatial discretization, a different mesh has been used for the laminar flow case and the turbulent flow case. In both flow cases, the same computational domain was used. The grid generation was done within the commercial software *ANSYS ICEM CFD* 16.2. The computational domain has been divided into blocks in which a structured hexahedral grid was created. The block around the cylinder was based on an O-grid mesh. The grid topology is shown in fig. 3.2. All the edges surrounding the grid blocks are shown in this figure. For the relevant edges, the number of cells are defined as $N1-4$, N_T and N_R as shown in fig. 3.2. The mesh characteristics are listed in tab. 3.3.

	Laminar cases					**Turbulent cases**			
Mesh	Coarse	Regular	Fine	Finer	Finest	Coarse	Regular	Fine	Finer
Mesh Number	m1.1	m1.2	m1.3	m1.4	m1.5	m2.1	m2.2	m2.3	m2.4
Number of cells	5.472	13.050	30.096	58.410	90.576	69.069	98.730	176.635	314.186
N_R	20	30	45	60	90	125	150	200	266
N_T	20	30	45	60	90	63	75	100	133
Cylinder wall cell height $[m]$	0.05	0.05	0.05	0.05	0.05	$7\cdot10^{-6}$	$7\cdot10^{-6}$	$7\cdot10^{-6}$	$7\cdot10^{-6}$
Minimum cell width $[m]$	0.0393	0.0295	0.0195	0.0145	0.0116	0.00166	0.00118	$5.5\cdot10^{-6}$	$4.1\cdot10^{-5}$
Mesh Quality $85-90\%$	24.6	0.4	0.2	0.1	0.141	0.1	0.2	0.149	0.122
Mesh Quality $90-95\%$	1.8	25.5	15.8	11.5	10.608	10.9	10.1	10.979	11.587
Mesh Quality $95-100\%$	73.6	74.1	84.0	88.4	89.251	89.0	89.7	88.872	88.290

Table 3.3: Mesh characteristics for different flow cases

The grid generation started at the cylinder wall by defining the cell height at the cylinder wall to ensure $y^+ = 1$. The cell height at the cylinder was estimated by using eq. 3.19 and solving for y with a desired $y^+ = 1$. The wall shear stress, required to calculate the dimensionless velocity, was approximated by using the Schlichting skin-friction formula [75]:

$$C_f = [2log_{10}(Re_x) - 0.65]^{-2.3} \quad \text{for} \quad Re_x < 10^9 \tag{3.21}$$

This equation is designed for flat plates and turbulent boundary layers. Yet, as will be shown later, the formula served as a good approximation of the skin friction coefficient for the laminar CFD cases. For the turbulent cases, this approach yielded a cell wall height at the cylinder of $y = 7\cdot10^{-6}$ which was considerably lower compared for the laminar cases where $y = 0.05$. After the cell wall height at the cylinder was defined, an exponential cell size growth was applied to the four radial edges in the O-grid block around the cylinder (N_R). The corresponding length of these four radial edges attached to the cylinder wall was $L_4 \approx 3.4D$, taken from the origin in the middle of the cylinder. N_T in fig. 3.2 and in tab. 3.3 shows the amount of cells distributed over the four tangential edges which enclosed the O-grid block. The O-grid block has been created to capture

the expected large flow fluctuations around the cylinder caused by the curvature. In addition, uniform grid block covering the wake was created until $L_5 = 10D$. This block gave the possibility to locally increase the mesh density in the wake, which would contribute to a better solution.

The grid has been generated by taking the following principles into account to reduce the numerical diffusion [42]:

1 Grid is as nearly as orthogonal as possible.

2 The grid is dense in the regions where large truncation errors are expected.

3 The grid transition over different blocks is smooth.

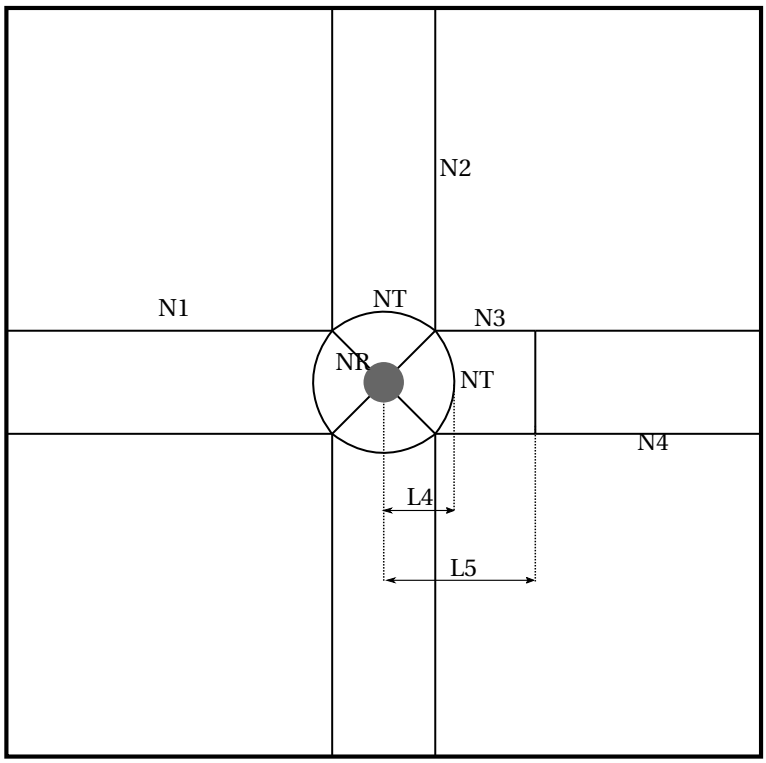

Figure 3.2. Illustration of the grid topology

According to [42], 'it is important that the grid refinement is *substantial* and *systematic*' in order to estimate the discretization error. To ensure this, all the block edges have been increased with the same refinement ratio of $r = 1.5$ for the laminar meshes and $r = 1.33$ for the turbulent meshes. In tab. 3.3 only the effect of grid refinement on the radial and tangential O-grid block edges is displayed, however, all the other block edges have been refined with the same ratio. The tutorial found on the website of NASA [76] suggested that a refinement ratio of $r > 1.1$ is the minimum to allow discretization error estimation. Because all the block edges have been refined with the same ratio systematically, the grid topology and relative spatial density has been conserved as much as possible. The refinement ratio has been lowered for the turbulent meshes, since their computational time was affected more severe with denser meshes compared to the laminar meshes.

The y^+ value was constant in all the refined meshes, hence the wall cell height was equal in the laminar and turbulent refined meshes. The effect of the y^+ value on the solution is treated later in section 4.1.1.

The mesh quality was evaluated by the pre-mesh quality tool available within *ANSYS ICEM*. This quality measure is based on a weighted diagnostic between the determinant, orthogonality and warpage of all the hexahedrals. The determinant and orthogonality weight factor can have a number between -1 and 1, while the warpage factor is normalized between 0 and 1. The orthogonality indicates the orthogonality of two hexahedrals next to each other. If two cells deviate with more than 90° from orthogonality, the weighted factor will be smaller than 0. The determinant checks the deformation of the cells, where the factor of 1 corresponds to perfect regular mesh element and negative values indicate inverted mesh elements. Lastly the warpage indicates the skewness of the mesh elements, where a warpage of 0° is equal to a weighted factor

of 1 and 180° is equal to a factor of 0 (indicated cell distortion). Finally, these normalized quality diagnostics have been evaluated for each hexahedral and transformed into a histogram by *ANSYS ICEM*. For example, in the turbulent fine mesh 112 cells show (which is equal to 0.1% of the total amount of cells) a quality between 85 – 90%, 7.512 cells (equal to 10.9% of the total amount of cells) in the range of 90 – 95% and 61.444 cells (which is 89.0% of the total amount of cells) in the last, best category of 95 – 100%. In other words, in this example and in all the meshes that have been generated none of the cells fall within the quality range of 0 – 85%. This indicates that all the meshes are of good quality.

Temporal discretization In the present research, the timestep was not fixed. The option adjustable timestep within *OpenFOAM* has been adopted in the CFD cases. Two constraints are imposed on the varying timestep: a maximum allowable Courant number and a maximum allowable timestep size during the simulation. The Courant number is defined as follows:

$$Co = U\frac{\Delta t}{\Delta x} \leq 1 \tag{3.22}$$

where U is the velocity magnitude in $[m/s]$, Δt the timestep size in $[s]$ and Δx the cell width size in $[m]$. According to the *Courant-Friedrichs-Lewy* condition, Co should be equal to or less than 1 to ensure a stable run [41]. Within *OpenFOAM*, it is only required to specify the maximum Courant number. When this maximum is specified, the solver ensures the timestep is adjusted accordingly to satisfy the desired Courant number. Manual computations of the Courant number or the timestep size with eq. 3.22 were done by using the minimum cell width listed in tab. 3.3 for Δx.

Timestep scheme	Co_{max}	ΔT_{mean}
m1.1	0.7	0.02793
m1.2	0.7	0.01830
m1.3	0.7	0.01226
m1.4	0.7	0.00927
m1.5	0.7	0.00745

Table 3.4: Timestep size variations for meshes m1.1 – 1.5 from tab. 3.3

The time-averaged timestep size for the refined meshes have been listed in tab. 4.1. In all the five cases, the maximum Courant number was kept equal. This ensured that the *Courant-Friedrichs-Lewy* condition was satisfied to same degree for all the refined meshes. It has been reasoned that when the mesh was refined, smaller cell widths were generally expected. The adjustable times-step scheme was therefore forced to lower ΔT to achieve the same maximum Courant number as for the coarser meshes. This reasoning is supported by the mean timestep sizes shown in tab. 4.1.

Discretization Schemes

Term	**Scheme**
Temporal derivative	Backward. 2nd order , implicit
Gradient	Gauss linear. 2nd order
Divergence	Gauss linearUpwind. 2nd order
	Turbulent quantity k: Gauss upwind. 1st order
	Turbulent quantity ω: Gauss upwind. 1st order
Laplacian	Laminar: Gauss linear limited. 2nd order
	Turbulent: Gauss linear corrected. 2nd order
Interpolation (cell to face values)	Linear. 2nd order
Surface normal gradients	Laminar: Limited
	Turbulent: Corrected

Table 3.5: Discretization schemes used in the simulations

The discretization schemes used in the present CFD model are tabulated in tab. 3.5. The laminar and turbulent discretization settings are nearly the same except for the Laplacian scheme, surface normal gradient scheme and additional schemes used for the turbulent quantities. For the turbulent transport equations, the upwind convective discretization scheme has been used. The study of [77] showed that this scheme yielded better agreement of the turbulent kinetic energy compared to the turbulent benchmark cases of NASA.

3.1.3. Numerical modelling

After the spatial and time discretization and after the equations have been discretized according to schemes in tab. 3.5, a system of linear algebraic equations has been formed. This system of equations is then usually solved by an iterative method [42]. The (linear) solvers used in the present simulations are tabulated in tab. 3.6.

Term	**Solver**	Pre-conditioner
p	PCG	DIC
u	PBiCG	DILU
ω	PBiCG	DILU
k	PBiCG	DILU

Table 3.6: Solver settings

The pressure has been solved by the preconditioned conjugate gradient (PCG) with the Diagonal-based incomplete Cholesky (DIC) preconditioner. According to [77], the diagonal incomplete-Cholesky (DIC) appeared to be the fastest solver while having the same accuracy as the other available pressure solvers. The velocity and turbulence field are solved by the preconditioned bi-conjugate gradient (PBiCG) with simplified Diagonal-based Incomplete LU preconditioner (DILU).

Considering the pressure-velocity coupling of eq. 2.7 and 2.8, the PIMPLE algorithm was used. This algorithm is a hybrid between the two segregated pressure-based solvers called SIMPLE (Semi-Implicit Method for Pressure-Linked Equations) and PISO (Pressure Implicit with Splitting Operators). Whereas SIMPLE is considered as a steady-state solver and PISO as a transient solver, PIMPLE is more often referred to as a pseudo transient solver. This indicates that the PIMPLE solver can cope better with larger timesteps or with unstable end solutions. Whereas the PISO transient solver strictly requires the Courant condition to be fulfilled (eq. 3.22), the PIMPLE solver can solve a transient flow problem with a timestep which implies Courant numbers larger than one. Additionally, this solver has the ability of running with a variable timestep size over time. It was observed this latter option significantly reduced the CPU time. Within *OpenFOAM*, there are two criteria for the PIMPLE solver to complete one timestep:

1 The specified tolerance criteria for the fluid solver have been satisfied.

2 Or the specified maximum number of PIMPLE iterations has been reached.

Besides the linear tolerances that were specified for all these four quantities, it was also possible to specify additional tolerances for these quantities to control the fluid solver convergence over multiple iterations within one timestep (criteria 1). Within *OpenFOAM* these additional iterations are called outer corrections. The tolerances for the outer corrector have been called outer tolerances and criteria 1-2 the outer criteria in the present report. For every outer correction (or iteration) it means that the complete fluid solver must run again. If the relative error of the pressure and velocity field over multiple, successive outer corrections reaches the specified tolerances, it may be concluded that the obtained solutions for the pressure and velocity were consistent with each other. In other words, they would satisfy the equations eq. 2.7 and eq. 2.8 or for turbulent flows eq. 3.3 and eq. 3.4. By employing these tolerances, the timestep continuity error should decrease (i.e. the continuity equation should be satisfied for each timestep). Next to the pressure and momentum outer tolerances, it was possible to specify these tolerances for the turbulent quantities k and ω to cope with highly turbulent flows (i.e., where the turbulence may vary substantially for every timestep). If the specified tolerances are not reached, the fluid solver runs again until the specified maximum number of iterations was reached (criteria 2).

Besides the specified number of outer correctors, the number *inner correctors*, number of *non-orthogonal correctors* and *momentum prediction* had to be specified for the PIMPLE algorithm. The number of inner

corrections specified how many times the pressure had to be corrected for each outer correction. Then, the number of non-orthogonal correctors specified how many times the pressure is additionally corrected within each inner correction. The momentum prediction settings provided an additional momentum prediction within each inner correction, providing additional stability for solving the velocity field. Lastly, the option *correctPhi* was available within the PIMPLE solver. This option made sure that the interpolation error as a consequence from mapping the pressure fields from the previous mesh to new mesh was minimized [78]. This latter option was therefore only used for the simulations with a moving mesh. Some additional PIMPLE settings have been discussed in more detail in the next section on the FSI coupling, as these options were more related to the motion coupling. A summary of all the settings for the PIMPLE solver is listed in tab. 3.7.

	Setting	**Laminar**	**Turbulent stationary**	**Turbulent moving**
Solver settings	momentumPredictor	yes	yes	yes
	nOuterCorrectors	2	1	100
	nCorrectors	2	2	3
	nNonOrthogonalCorrectors	1	1	1
	correctPhi	no	no	yes
Linear tolerances	$\mathbf{u}$	$1e-08$	$1e-08$	$1e-08$
	p	$1e-08$	$1e-08$	$1e-10$
	ω, k	–	$1e-08$	$1e-10$
Outer tolerances	$\mathbf{u}$	–	–	$1e-06$
	p	–	–	$1e-06$
	ω, k	–	–	$1e-06$

Table 3.7: PIMPLE settings

All the simulations have been performed at a maximum Courant number of $Co_{max} \leq 0.7$ (with the adjustable timestep option, as was explained in section 3.1.2). Therefore, considering the robustness of the PIMPLE algorithm pointed out above, it was expected only $1-2$ outer corrector loops were sufficient to capture the flow field accurately. More outer corrector loops are only desirable when the Courant number is higher than 1. Nevertheless, it appeared that for the turbulent moving cases, the fluid solver was more sensitive to these solver settings. In those cases, it was required to use tighter PIMPLE settings to ensure energy conservation at the fluid-structure interface was guaranteed (hereafter referred to 'tight' fluid solver settings). Therefore, in tab. 3.6, the solver settings for the turbulent moving cases are different compared to the laminar cases and the turbulent stationary case. The latter two case settings have been referred to as 'loose' fluid solver settings hereafter. The number of outer correctors was specified to such a large number for the turbulent moving cases to ensure that the outer tolerances were reached. Typically, the required number of outer correctors was therefore significantly lower than 100. More details on this observed sensitivity in the turbulent moving cases can be found in chapter 4, section 4.2.3.

3.2. Moving cylinder

When the 1-way coupling or the 2-way coupling are introduced, the following steps take place every timestep to incorporate this coupling in the fluid solver:

1 Determining the cylinder displacement: motion solver (2-way coupled) or prescribed motion (1-way coupled).
2 Move the cylinder body.
3 Mesh diffusion: SLERP (2-way coupled) or Laplace (1-way coupled).
4 Convective term correction (ALE).

The second step and fourth step are identical for the 1-way and 2-way coupled model. The first step and the third step differed for the 1-way and 2-way coupled model. For the 1-way coupled model, Laplace's equation has been used and solved to compute the displaced mesh cells. The SLERP interpolation method

was used to compute the mesh diffusion for the 2-way coupled model. All these steps have been explained in to more detail in the subsequent sections.

3.2.1. Forced-vibrations: 1-way coupling

Prescribed motion Concerning the forced-vibration cases (1-way coupling), the motion was prescribed by a harmonical sinus wave:

$$y' = y(t) = y_{max} \cdot sin(2\pi f_{cyl} t) \tag{3.23}$$

The motion prescribed by eq. 3.23 is only in the *transverse* direction (see fig. 3.1). This motion has been implemented as a boundary condition, as was described in section 3.1.2.

Mesh diffusion Regarding the moving cylinder simulations, the mesh needed to change over time to capture the changing flow field caused by the cylinder motion. In the present research, the mesh velocity field of the forced-vibration cases (1-way coupled) has been computed by Laplace's equation:

$$\nabla \cdot (\gamma_m \nabla \mathbf{z}) = 0 \tag{3.24}$$

Where γ_m is the diffusion coefficient and $\mathbf{z}$ is the mesh displacement field. *OpenFOAM* has calculated the mesh displacement field $\mathbf{z}$ and the mesh velocity field $\mathbf{w}$ for every timestep. Since the outer boundaries of the computational domain remain fixed during the simulation, the mesh motion had to be distributed through the grid by mesh diffusion. The diffusivity model was chosen to be inverse. Hence, the mesh diffusion was based on an inverse distance from the cylinder body. This diffusion model was considered as the most robust model where the mesh quality conservation was better compared to the other available diffusion models in *OpenFOAM* [79]. More information on mesh motion based on solving Laplace's equation and also on other dynamic mesh handlers in *OpenFOAM* can be found in the study of [80].

3.2.2. Free-vibrations: 2-way coupling

Regarding the free-vibration cases, the cylinder motion must be calculated at every timestep. While the governing fluid equations are solved in 2D, the structural system was implemented with only 1 degree-of-freedom (DOF) in the transverse direction. The structural system was constrained to allow movement only in the y-direction, while the other 5-DOF (rotational and x-z direction) were left out of the problem analysis.

The equation of motion for a 1-DOF single cylinder, fixed in the transverse direction and attached to spring and damper has been expressed as follows:

$$m\ddot{y} + c\dot{y} + k_s y = F_y \tag{3.25}$$

and as shown in appendix B this equation can be rewritten in to:

$$m\frac{d^2y}{dt^2} + 2m\zeta\omega_n\frac{dy}{dt} + k_s y = F_y \tag{3.26}$$

The natural frequency can be computed with the following relation:

$$f_{nat} = \frac{\sqrt{k_s/m}}{2\pi} \tag{3.27}$$

In the present free-vibration problem, eq. 3.25 can only be resolved if the external fluid force is known. The fluid force in turn is dependent on the structural motion. Hence, the free-vibration can be interpreted as a classical two-way coupled FSI problem.

FSI scheme In the present research, the FSI was modelled by a partitioned approached, where the flow field and structural system are solved alternately at every timestep. This approach was favoured above the monolithic approach, because it gave the opportunity to use the model for a wide variety of FSI cases. In addition, the monolithic approach would have implied higher computational cost because of the expensive additional derivatives required to solve the fluid and structure simultaneously. There are multiple algorithms available today that support a partitioned approached, which are usually divided into three coupling categories: explicit, semi-explicit and implicit. In the present FSI code, both an explicit and implicit FSI scheme have been employed. Both schemes fall within the capabilities of the standard *pimpleFoam* solver of *OpenFOAM*. Yet,

it has to be noted that the implicit solver was only found in the latest *OpenFOAM* version (OFv1806+). The schemes have been illustrated in fig. 3.3, which was adopted from [81].

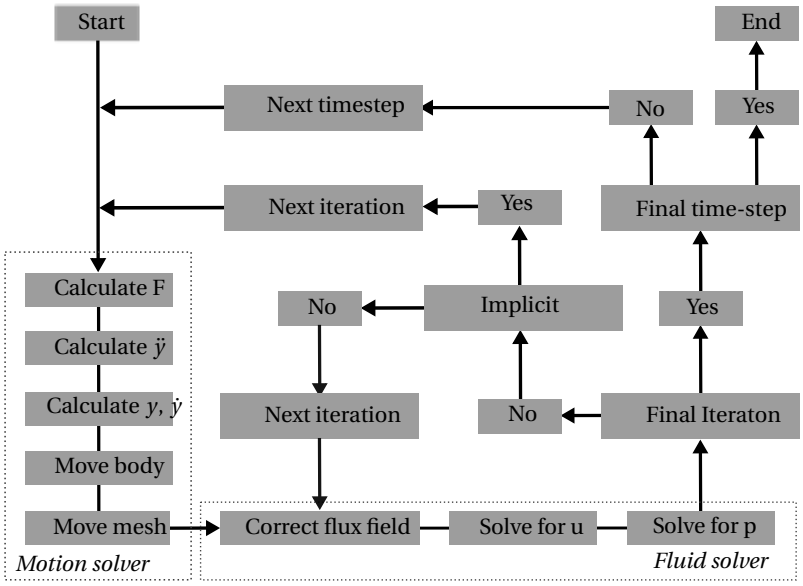

Figure 3.3. Block diagram of *PimpleFOAM* solver

When the solver has started for a timestep, the motion of the structure is solved before the fluid dynamics. After the motion is computed (that is, y, $\dot{y}$, $\ddot{y}$ are resolved), the geometry was moved with the obtained displacement from the motion solver, y. Then, the new (dynamic) mesh was evaluated by enforcing the new position of the body as a boundary condition. As was stated before, *OpenFOAM* ensured no mass flow through the cylinder and hence the relative fluid velocity was zero at the cylinder wall. From the new boundary condition, the mesh diffusion was calculated. The mesh diffusion was based on the SLERP interpolation. From here on, the fluid solver is taking over from the motion solver, still within the same timestep. The computed mesh velocity field is plugged in the Navier-Stokes equations to cope with the mesh motion (arbitrary Lagrangian-Eulerian formulation). After the alteration of the Navier-Stokes, the velocity, pressure and depending if turbulence is modelled, k and ω were being solved. Based on these quantities, the solver evaluates if the final iteration is reached or not (as was explained in section 3.1.3).

When the final iteration has not been reached yet, it would depend on the solver what happens in the next iteration. When the weakly-coupled scheme within *OpenFOAM* was used, the solver returns right back to the fluid solver where the alteration of the Navier-Stokes equations is still exactly the same as was for the previous iteration. In this scheme, the motion is always only solved once per timestep and the mesh also only moves once in each timestep. After the flow field has been recomputed by the fluid solver, the same final iteration criteria are evaluated by the solver to see if a next iteration would take place or not.

Within the strongly-coupled solver, the next iteration starts again with the motion solver. After the motion is solved in the next iteration, the mesh is being moved again and the fluid fields are re-computed for this new mesh again as well. After the fluid solver, the solver evaluates again if either the maximum number of iterations have been reached or if the outer tolerances were satisfied. The implicit scheme is characterized by the fact that the motion has been solved and the mesh has been moved multiple iterations within each timestep. These iterations are then referred to in the literature as subiterations, which define the additional runs of the structural and fluid solver within one timestep.

After the final PIMPLE iteration has been reached (for both the weakly- and strongly-coupled solver), the complete solver re-runs again for every timestep until the end of the simulation has been reached.

The explicit scheme and implicit scheme have been illustrated for one timestep in fig. 3.4 as well to clearly demonstrate which information is exchanged between the two solvers.

In fig. 3.4, the S stands for the structural solver and the F for the fluid solver. Only the quantities that have been exchanged between the two solvers are presented in fig. 3.4. The weakly-coupled scheme (left subfigure of fig. 3.4) is also known as a serial, partitioned coupling scheme. The first step is that the computed

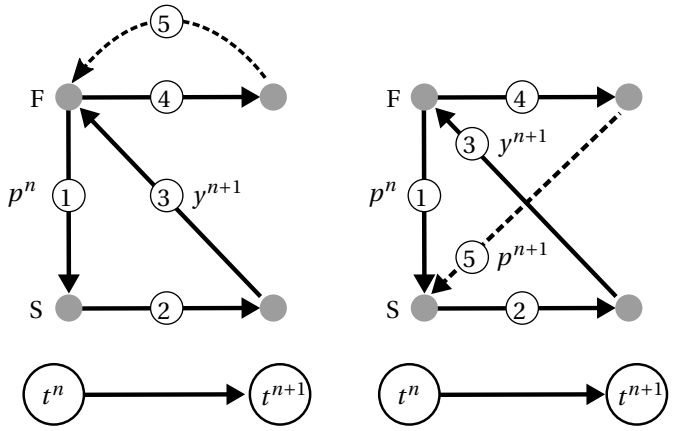

Figure 3.4. Explicit (left) and implicit (right subfigure) FSI coupling scheme

pressure field and shear stress from the previous timestep of the fluid solver is sent to the structural solver *S*. The structural solver uses these fields to compute the force exerted on the structural body and eventually to compute the structural displacement for the next timestep (step 2). Then, the obtained displacement is sent back to the fluid solver (step 3). The displacement is used to move the cylinder and the mesh subsequently. The fluid solver computes the flow fields for this new mesh after which the pressure for the next timestep is obtained (step 4). After that, the outer tolerances described earlier are evaluated. If the outer criteria are not met, the flow fields will be solved for another time until the criteria are met (step 5-4).

Concerning the implicit scheme (right subfigure of fig. 3.4), the first four steps are identical to the explicit scheme. Also, the outer criteria for the PIMPLE solver are identical for the strongly-coupled scheme compared to the weakly-coupled scheme. In this case, when the criteria are not met, the pressure and shear stress is sent back to the structural solver (step 5) for the next iteration. Based on these received quantities, the structural solver computes the new force which is exciting the structure. From there on, the scheme repeats itself and steps 2-3-4 are identical to the previous iteration. Steps 5-2-3-4 are repeated until the fluid solver has satisfied either one of the outer criteria.

Motion solver The structural motion (eq. 3.25) has been solved by the implicit Newmark scheme. However, this scheme was only found to be truly implicit when multiple iterations were employed during one timestep. For a comprehensive explanation and review on the Newmark scheme the reader is referred to the dictate of [82]. The subsequent steps for the motion solver are explained assuming that the strongly-coupled solver is used. The first step is that all the forces exerted on the structural body are calculated according to:

$$f_{global}{}_{i=1}^{n+1} = \sum_{j}^{body} p_j{}_{i=1}^{n} A_j + \sum_{j}^{body} \tau_j{}_{i=1}^{n} A_j \tag{3.28}$$

This equation shows the first iteration ($i = 1$) of the current timestep ($n+1$) where the $global$ force f_{global} is evaluated. This force represents all the forces exciting the structural body. For the first iteration, the pressure p and shear stress τ for each boundary face j have been obtained from the fluid solution of the previous timestep n. Each boundary face is defined by its area A_j. The force of gravitation has been disregarded in the present simulation, otherwise this force would have been included in eq. 3.29. The evaluation of the global force for the first iteration has been illustrated before by step 1 in the right figure of fig. 3.4. For all the next iterations, the global force is based on the solution of the fluid solver of the previous iteration i of the current timestep $n+1$:

$$f_{global}{}_{i+1}^{n+1} = \sum_{j}^{body} p_j{}_{i}^{n+1} A_j + \sum_{j}^{body} \tau_j{}_{i}^{n+1} A_j \tag{3.29}$$

This latter equation resembles step 5 of the right figure in fig. 3.4, where the obtained flow field from the last iteration is sent to the structural solver. After the force has been determined, the acceleration is readily computed by:

$$\ddot{y}_{i+1}^{n+1} = \frac{{f_{global}}_{i+1}^{n+1}}{m} \tag{3.30}$$

To which a relaxation factor (ψ) is applied such that the change from the state of the previous iteration to the state of the next iteration (or from the last iteration of the previous timestep to the first iteration of the current timestep) is not too big for the FSI solver:

$$\ddot{y}_{i+1}^{n+1} = \psi \cdot \ddot{y}_{i+1}^{n+1} + (1-\psi) \cdot \ddot{y}_{i}^{n+1} \tag{3.31}$$

Then the predictor-corrector equations of the Newmark scheme [82] are used to compute the velocity and displacement, respectively:

$$\dot{y}_{i+1}^{n+1} = \dot{y}^{n} + \chi(1-\gamma_n)\Delta T \ddot{y}^{n} + \chi\gamma_n \Delta T \ddot{y}_{i+1}^{n+1} \tag{3.32}$$

$$y_{i+1}^{n+1} = y^{n} + \Delta T \dot{y}^{n} + \chi\Delta T^2(\frac{1}{2} - \beta_n)\ddot{y}^{n} + \chi\Delta T^2 \beta_n \ddot{y}_{i+1}^{n+1} \tag{3.33}$$

Where χ is a numerical damping term which can be specified as an input in the FSI solver, ΔT was the timestep value of the motion solver dictated by the timestep size used for the fluid solver, β_n and γ_n are constants related to the explicit/implicit character of the Newmark solver. In the present motion solver, $\gamma_n = 0.5$ and $\beta_n = 0.25$ which is known as the average constant acceleration method. The average constant acceleration algorithm was deemed as 'the best unconditionally stable scheme' [82]. To make sure that the higher order frequencies were captured by the motion solver as well, a recommended timestep value for the motion solver was $\Delta T \leq T/4$ [82]. It has been observed that for the laminar and turbulent simulations, the timestep size of the fluid solver was adequately low to ensure that all the frequency content was captured by the motion solver. The artificial damping term χ was not actively used and set to $\chi = 1$. The artificial damping was not used because this term 'cuts off' a piece of the acceleration and hence the end solution. In contrast to the artificial damping term χ, the relaxation term ψ shown in eq. 3.31 does not affect the end solution of the FSI problem, as long as there are enough subiterations. All the terms denoted with i or $i+1$ are changing with every PIMPLE iteration within each timestep. The terms which are not dependent on the number of PIMPLE iterations but only on the previous timestep, always uses the obtained value in the last iteration of the previous timestep (for example, $\dot{y}^{n}$). The motion solver is characterized by the continuously updated acceleration for each iteration. From this newly derived acceleration, the velocity and displacement were predicted/corrected by the Newmark scheme.

One of the findings here was that the Newmark scheme can only be used in the present research when the strongly-coupled solver was used. In case of the weakly-coupled scheme, where the structural solver is only being run once per timestep, the implicit character of the Newmark solver is lost. The 'predictor-corrector' feature in equations eq. 3.32 and eq. 3.33 is only using its predictions and corrections for the previous/next timestep instead of the previous/next iteration within one timestep when the explicit FSI scheme was used. This means the structural solver would already produce an intrinsic error for each timestep, which in turn would lead to energy unbalances at the fluid-structure interface. Various simulations have indeed shown poor energy conservation by using the Newmark scheme in combination with the weakly-coupled scheme of *OpenFOAM*. It has to be noted here that in general, it is not necessarily true that a weakly-coupled scheme with the Newmark's scheme would always lead to a poor energy conservation. In fact, when the structural solver is implemented separately from the fluid solver and if the Newmark solver can re-iterate its structural evaluation for each timestep, then the problem described here should be resolved. Yet, within *OpenFOAM*, the Newmark solver is only being used implicitly when the FSI coupling is implicit as well (they are integrated with each other). Besides the implicit structural Newmark solver, there is also an explicit solver available within *OpenFOAM* which is known as the Symplectic integrator [83]. This scheme is based on the leapfrog method. The explicit character of this solver leads to a constant structural displacement for each iteration within one timestep, while the acceleration and velocity may change each iteration. This is in line with the theoretical formulation as was pointed out by [81]. The structural displacement of the current timestep is only dependent on the acceleration found in the previous timestep (and not on the last iteration within the current timestep). This explicit character means that employing multiple subiterations does not lead to a strongly-coupled scheme since the displacement is constant over these subiterations. In other words, when the symplectic solver is being used in combination with the implicit FSI scheme of fig. 3.3, the mesh will only move one time for the first subiteration in each timestep. Therefore, the strongly-coupled scheme in

OpenFOAM only works as a truly strongly-coupled scheme when the implicit Newmark solver is selected as a structural solver. Based on these findings, the term 'weakly-coupled' scheme is from here referred to the explicit FSI solver combined with the explicit structural solver (symplectic scheme). The term 'strongly-coupled' scheme referred to the implicit FSI solver combined with the implicit structural solver (Newmark scheme).

One of the drawbacks of the explicit scheme (see left figure in fig. 3.4) is that the phase lag between the fluid and structural solver inherently leads to inconsistent solutions of the fluid and structure. Hence, conservation of the overall fluid-structure system might be lost. This is in turn, as described in the literature as negative numerical damping [64] or artificial added mass [62], could lead to divergence of the system. This problem of energy conservation is prevented by using the strongly-coupled implicit solver (see right figure in fig. 3.4). Pressure-momentum (and for turbulent flows, also k-ω) convergence indicates that the obtained structural solutions are converging as well. After all, within the implicit scheme, the mesh is moving for every subiteration. Hence, if the pressure, momentum (and k-ω) are showing very low relative errors after a couple of subiterations it may be concluded that the mesh is also not moving substantially over these subiterations (and thus reaching a converged solution). Yet, as was pointed out earlier in the *OpenFOAM* study of [84] (similar FSI solver), it is possible that the motion is converging to a different order since the overall convergence is only dependent on the fluid solver's tolerances. Hence, in the present research, the structural motion convergence has been monitored as well to ensure that energy conservation is obtained for every timestep. Hence, this solver is seen as a strongly-coupled scheme rather than a fully coupled scheme. Within a fully coupled scheme, the number of subiterations would always be adequate such that convergence has been reached to a monolithic solution (i.e. structural and fluid solver convergence and energy conservation between the two solvers). Yet, since the structural convergence has been monitored and controlled indirectly by the number of subiterations required for the fluid solver, the implicit scheme is deemed as very strong.

Mesh diffusion The mesh movements for the free-vibrations cases have been computed and performed by a spherical linear interpolation scheme (SLERP). The SLERP interpolates the displacement and rotation to compute the mesh deformation while taking the distance of the moving object into account. The benefit of the SLERP algorithm is that it was possible to specify a mesh region where the cells preserved their shape. From the cylinder body, up to a radius of $25D$, the mesh was kept rigid throughout the entire simulation. This rigidly defined region allowed the mesh to keep its initial high quality characteristics in the critical O-grid block (described in section 3.1.2) constant during the simulation. The mesh deformation was then applied to all cells in the region of $25D - 40D$ from the cylinder body. As the height of the domain was set to $50D$, it was argued that the radial distance of $40D$ was adequately far away from the far field which prevented awkward mesh deformation (i.e. inverted cells). The rigid mesh region option was not available for the forced-vibrations cases. In those cases, the mesh deformation started immediately from the cylinder wall.

3.2.3. Flux field correction

Regarding the reference frame for the FSI cases, the arbitrary Lagrangian Eulerian formulation has been used. In this description, the Lagrangian (where grid nodes are connected to the moving fluid particles) and Eulerian perspectives (where the grid nodes are fixed in which the fluid moves) are combined. The use of this framework has altered the convective term of the momentum equation (eq. 2.7) to cope for the relative velocity between the fluid and mesh velocity [62]. Hence, eq. 2.7 has changed to:

$$\frac{\partial \mathbf{u}}{\partial t} + \nabla \cdot (\mathbf{u}(\mathbf{u} - \mathbf{w})) + \frac{1}{\rho}\nabla p - \nabla \cdot (\nu \nabla \mathbf{u}) = 0 \tag{3.34}$$

where $\mathbf{w}$ is the mesh velocity field which was either computed by the SLERP algorithm or by Laplace's equation. This correction was thus performed for both the 1-way and 2-way coupled model.

3.3. Post-processing

In this section, all the important post-processing operations will be explained. It must be noted first that for all the results, the transient part of the time series was always filtered out in the post-processing. The amount of shedding cycles that were required before a steady-state solution was varied per simulation case. For example, it was noted that a coarse mesh usually showed larger transient time histories. The forced-vibration cases showed smaller transient time histories compared to the stationary cases.

3.3.1. Power Spectral Density

The vortex shedding frequency, f_{shed}, has been determined by extracting the power spectral density (PSD) diagram of the lift force time series. The shedding frequency was identified by taking the frequency from the PSD which corresponded to the dominant peak response where the magnitude was at its maximum. In the present report, the timestep was not fixed during the simulation as was explained in section 3.1.2. To ensure that the lift and drag data points were equally spaced along the filtered time series, the original signals have been interpolated by the obtained time-averaged timestep size. This means that the lift and drag force signals have been equally spaced and their distribution matched the time-averaged timestep size. After the interpolation, the sampling frequency for the extraction of the PSD of the lift/drag signals was based on the time-averaged timestep size. It must be noted that the interpolation has introduced a small post-processing error. The interpolation has been considered as a robust method of extracting the PSD of the lift and drag signal with originally a varying sampling frequency. As a sanity check, the sampling frequency for the PSD was decreased with 20%. Without interpolation, this yielded an increment of 23.7% of the dominant frequency. This would imply that without interpolation, the choice of the sampling frequency has a direct, big influence on the extracted shedding frequency, which would make the post-processing unreliable. However, with interpolation, decreasing the sampling frequency by 20% would lead to an increment of only 1% of the shedding frequency. The timestep varied around 4% peak-to-peak, yielding an acceptable (indicative) post-processing error of $< 0.3\%$ for the dominant frequency when interpolation was applied.

Besides the interpolation, the accuracy of the shedding frequency prediction was expected to depend on two other factors. The first factor was the amount of vortex shedding cycles over which the PSD has been taken (after the transient part). When more shedding cycles are obtained, more data points will be available for the PSD extraction which would reduce the standard deviation. It has been attempted to always minimize this variance by simulating an adequate amount of shedding cycles. The standard deviation of both aerodynamic forces has been monitored during all the simulations to see if the number of shedding cycles was indeed adequate. Furthermore, when the results of different cases were compared, the filtered steady-state timeframe was always kept equal (for grid convergence studies). The second factor was the timestep size. A smaller timestep size with the same amount of vortex shedding cycles means more data points and hence a finer signal for the PSD extraction. It was shown before that the spatial refinements lead to a smaller mean timestep size, see section 3.1.2. In the spatial refinement study, this would mean that a finer mesh inherently yields finer output signals of the aerodynamic forces. Hence, smaller post-processing errors were expected for the dominant shedding frequency prediction with finer meshes (besides the smaller expected truncation errors).

The usability of the Strouhal number as a metric for grid convergence studies has been troubled by the choice for an adjustable timestep scheme. Although the interpolation of the time signals was robust, it still yielded an (indicative) post-processing error of $< 0.3\%$ for the shedding frequency. The Strouhal number was used one time in the present research for the forced-vibration grid convergence study. It turned out that the grid was not converging based on the Strouhal number, while for the lift and drag coefficient convergence was observed (as will be shown in chapter 4). It was seen in this specific grid convergence study that the relative spatial error was found to reach values of $< 0.04\%$ for the drag coefficient for meshes m1.2 − 1.5 and $< 0.48\%$ for meshes m1.4 − 1.5 for the lift coefficient. The apparent relative spatial errors for the Strouhal number also reached $< 0.3\%$. Since these relative errors are reaching below the indicative post-processing error, the Strouhal number was excluded from the grid convergence study. For future work on VIV and on grid convergence studies it has been recommended to use a fixed timestep size to avoid the post-processing error caused by the interpolation. The Strouhal number could be a usable metric for grid convergence studies with a fixed timestep.

3.3.2. Force computation

The lift and drag force coefficient are defined as follow:

$$C_L = \frac{F_y}{0.5\rho U^2 DL} \tag{3.35}$$

$$C_D = \frac{F_x}{0.5\rho U^2 DL} \tag{3.36}$$

Where F_y is the transverse lift force in $[N]$, F_x is the in-line drag force in $[N]$, ρ is the air density in $[kg/m^3]$, U is the velocity magnitude in $[m/s]$, D the cylinder diameter in $[m]$ and L the spanwise length of the cylinder

in $[m]$. Both force coefficients have been computed at every timestep by one of the standard *OpenFOAM* post-processing tools.

3.3.3. Skin-friction coefficient

The skin-friction coefficient around the cylinder was evaluated by using the following relation:

$$C_f = \frac{\tau_w}{0.5\rho U^2} \tag{3.37}$$

where τ_{wall} is the shear stress at the cylinder wall in $[N/m^2]$. The wall shear stress has been computed by one of the standard *OpenFOAM* post-processing tools. The time-averaged wall shear stress was taken over the steady-state solution. Then, in the post-processing open-source programme *paraView* the wall shear stress was filtered for only at the cylinder wall. The wall shear stress is proportional to the velocity gradient in the boundary layer at the cylinder wall:

$$\tau_w = \mu \left(\frac{\partial u}{\partial y} \right)_{y=0} \tag{3.38}$$

where μ is the dynamic viscosity, u is the velocity component in x-direction and y is the distance in y-direction.

3.3.4. Pressure coefficient

The pressure coefficient was defined by this equation:

$$C_p = \frac{p - p_\infty}{0.5\rho_\infty U^2} \tag{3.39}$$

where p is the static pressure around the cylinder wall in Pa, p_∞ the static pressure in the freestream in Pa, ρ_∞ the freestream fluid density in kg/m^3 and lastly U the free stream velocity in m/s. The static pressure in the free stream was zero. The pressure around the cylinder wall was filtered from the computational domain by *paraView*, similar to the skin-friction coefficient. The time-averaged steady-state static pressure around the cylinder wall was used for the calculation of the pressure coefficient. The base pressure coefficient, $C_{p,b}$ is located at the most aft part of the cylinder, i.e. at $\theta = 180°$.

3.3.5. Standard deviation of pressure coefficient

The variance of C_p has been calculated according to the following, statistical relation:

$$\sigma^2 = \frac{\sum (X - \mu)^2}{N} = \overline{X'X'} \tag{3.40}$$

where X is a variable of interest, in this case C_p. The most right side of the above equation is similar to the Reynolds stress tensor which was reported in eq. 3.3. The standard function *Prime2Mean* within *OpenFOAM* has computed the variance of the pressure distribution over time in the steady-state part. Then, the standard deviation σ was easily derived by taking the square root of σ^2. The unit of the standard deviation σ has the same unit as the variable of interest X.

3.3.6. FSI metrics

In the 2-way coupled simulations, an output from the structural solver and an output from the fluid solver were evidently expected. As will be shown later in the results section, it was very useful to relate the aerodynamic quantities obtained with the motion trajectory observed for the cylinder body. These quantities have been related to each other in a similar fashion as was done in the doctoral thesis of [4]. Three methods have been explained in his thesis work: Fourier coefficient analysis (frequency domain), time lag analysis (time domain) and energy transfer analysis (time domain). These three methods will be recapitulated in this section. The lift force of 3.25 in steady-state equilibrium can be characterized by the following equation:

$$F_y = F_c sin(2\pi f_c t) + F_s sin(2\pi f_s t) \tag{3.41}$$

which has been decomposed into two sinus signals. One of these is a consequence of the cylinder motion dictating the wake (denoted with 'c' subscript in contrast to the earlier defined subscript 'cyl') and one sinus

signal is representing the Strouhal shedding frequency (denoted with 's' in the subscript in contrast to the earlier defined subscript 'shed'). Usually, only the cylinder component is present during lock-in. Further away from the lock-in region the Strouhal relation is valid again and the Strouhal sinus component is dominant. In between these regions, i.e. the moment when the wake is locking out or desynchronizing, both components are present of eq. 3.41. This phenomenon is usually referred to as *beating*, where two sinus signals can be observed in the time series of the lift coefficient. It was more convenient to assume the eq. 3.41 only consisted out of one component. Therefore, in the subsequent approach, the lift force signal only consisted out of one sinus signal. T

The harmonical motion of eq. 3.25 in steady-state can be described by the following sinus signal:

$$y^*(t) = y^*_{max} sin(2\pi f_c t) \tag{3.42}$$

of which the derivative leads to the transverse velocity:

$$\dot{y}^*(t) = 2\pi f_c y^*_{max} cos(2\pi f_c t) \tag{3.43}$$

It may be re-iterated that for the 1-way coupled model, the signal of eq. 3.42 is known a priori while for the 2-way coupled model the motion displacement has been calculated for every timestep. Still, the following theory is applicable for both models. In the literature, various attempts have been made to relate the aerodynamic excitation force to the left-hand side (LHS) of eq. 3.25, may it be for the development of analytical models or to obtain better insights from wind-tunnel experiments and numerical simulations. The comprehensive summary of some of the analytical models which have utilized the relation between the aerodynamic force and structural parameters has been given in the book of [3]. In the doctoral thesis of [4], the relation was used to investigate the fluid-structure interaction of his forced wind-tunnel experiment. The FSI analysis relies on the basic assumption that the harmonical lift force can be decomposed into a part which is in phase with the cylinder velocity and a part which is in phase with the cylinder displacement. The part that is in in phase with the cylinder velocity is referred to as the aerodynamic damping, the part in phase with displacement as the aerodynamic stiffness and then lastly the part in face with the acceleration is the added mass. Based on these assumptions, the lift force can be decomposed as follows [85]:

$$F_y = k_a y + c_a \dot{y} \tag{3.44}$$

From eq. 3.44, it is readily seen that when the aerodynamic damping term is moved to the LHS of 3.25, it has a negative effect on the overall system damping. Hence, *positive* values of c_a would mean that the fluid is exciting the structure (energy transfer from wake to the structural system). Respectively, when the sign of c_a is found to be negative, the wake is damping the structure (energy transfer from structure to wake).

First method: Fourier coefficient analysis Inspecting eq. 3.42, eq. 3.43 and eq. 3.44 leads to the conclusion that the aerodynamic force in phase with the velocity should be in phase with the cosine and for the displacement it should be the sine. The decomposition can be done by the Fourier coefficient analysis. A reference wave signal can be represented as the following Fourier series:

$$x(t) = a_0 + \sum_{n=1}^{\infty} a_n cos(\frac{2\pi nt}{T}) + \sum_{n=1}^{\infty} b_n sin(\frac{2\pi nt}{T}) \tag{3.45}$$

where a_0, a_n and b_n can be computed by:

$$a_0 = \frac{1}{T}\int_0^T x(t)dt \tag{3.46}$$

$$a_n = \frac{2}{T}\int_0^T x(t)cos(\frac{2\pi nt}{T})dt \tag{3.47}$$

$$b_n = \frac{2}{T}\int_0^T x(t)sin(\frac{2\pi nt}{T})dt \tag{3.48}$$

By applying this series to the earlier expression of the lift force in eq. 3.41 (with only one sinus signal which is in phase in this example with the cylinder frequency):

$$F_y = F_c cos(\phi_c) sin(2\pi f_c t) + F_c sin(\phi_c) cos(2\pi f_c t) \tag{3.49}$$

where $T = \frac{1}{f_c}$. Hence, the coefficients are $b_1 = F_c cos(\phi_0)$ and $a_1 = F_c sin(\phi_0)$. In non-dimensional form:

$$C_L = C_{L,max} cos(\phi_c) sin(2\pi f_c t) + C_{L,max} sin(\phi_c) cos(2\pi f_c t) \tag{3.50}$$

where the lift force coefficient in phase with the velocity is:

$$C_{L,\dot{y}} = C_{L,max} sin(\phi_c) \tag{3.51}$$

The lift force coefficient in phase with the displacement:

$$C_{L,y} = C_{L,max} cos(\phi_c) \tag{3.52}$$

The lift force amplitude of eq. 3.49 is then found by:

$$F_c = \sqrt{a_1^2 + b_1^2} \tag{3.53}$$

and the phase angle by

$$\phi_c = tan^{-1}(\frac{a_1}{b_1}) \tag{3.54}$$

The phase angle is the phase lag between the aerodynamic force vector ($F_y(t)$) and the motion displacement ($y(t)$) vector. Positive angles would mean that the lift force is being led by the cylinder displacement. The Fourier coefficient analysis is one way to determine the phase angle hence the part of the lift force which is in phase with the velocity, see eq. 3.49.

Second method: Time lag analysis The second approach to determine the phase angle by computing the time lag observed in the lift force signal and displacement signal between two successive peaks. For the 1-way coupled model, the displacement motion can simply be plotted against the lift force as the motion trajectory is known a priori. For the 2-way coupled model, the transverse displacement and velocity values have been obtained by the output log file of the FSI solver within *OpenFOAM*. Thus, for the 1-way and 2-way coupled simulations the lift force output and motion trajectory were plotted in the same figure. Within *MATLAB*, the time difference between two successive peaks was obtained. Knowing the period T for the lift and displacement signal was equal and equivalent to 360°, the phase angle can be determined. Then, the phase angle was computed for multiple peaks to see if the phase angle stayed constant over time during the steady-state or if there is a big variation for the phase angle over time. From the phase angle vector for all the peaks in the steady-state the time-averaged value was taken to minimize the numerical error.

Third method: Energy transfer analysis The third approach is based on the time-averaged power transfer between the fluid and the vibrating cylinder, which has been used by other studies as well [86] and [4]:

$$C_{L,\dot{y}} = \frac{\sqrt{2}\,\overline{C_L' \dot{y}'}}{\sqrt{\overline{\dot{y}^2}}} \tag{3.55}$$

The denominator of eq. 3.55 is also known as the root mean square (RMS) value. Similar expressions have been defined for the aerodynamic stiffness (lift proportional to cylinder displacement):

$$C_{L,y} = \frac{\sqrt{2}\,\overline{C_L' y'}}{\sqrt{\overline{y^2}}} \tag{3.56}$$

Then, similarly, the lift force in phase with the acceleration was taken by:

$$C_{L,\ddot{y}} = \frac{\sqrt{2}\,\overline{C_L' \ddot{y}'}}{\sqrt{\overline{\ddot{y}^2}}} \tag{3.57}$$

In the case of a pure sinusoidal signal, eq. 3.55 and eq. 3.56 are equivalent to eq. 3.51 and eq. 3.52, respectively. Hence, with the third approach, the phase angle can be computed by the formula defined before:

$$\phi_c = tan^{-1}(\frac{C_{L,\dot{y}}}{C_{L,y}}) \tag{3.58}$$

The benefit of the third approach, where the time-averaged power transfer is computed, is that lift force in phase with the velocity can always be computed, irrespective to the output signal. It was mentioned before, that for beating, two sinus signals can be expected. This also implies that there are two phase angles to be computed (for both sinus signals). It may be concluded that the first and second approach would have been cumbersome for this operation while the third approach is very suitable to deal with such signals. With the energy evaluation over the complete steady-state time signal of the lift force and structural motion, only one time-averaged phase angle was computed. This means that, the two phase angles observed for the beating signal, have been composed into one relative sinus signal with one phase angle. This 'composed' phase angle represents the relation between the lift force and motion displacement on average over time, which is more convenient for the FSI analysis compared to having two different phase angles. Furthermore, the dot product in the time-averaged power analysis yields a higher data resolution for estimating the lift force in phase with the velocity, since every element in the both output vectors are compared. For the second approach, only the peaks have been compared which might be more susceptible for numerical noise. Therefore, the third approach has been employed together with eq. 3.58 to obtain the 'time-averaged' phase angle in the present work. For purely sinusoidal signals, the phase angles were computed by the second and third approach to check if the phase angle of the two approaches agreed. It was observed that for all the harmonical signals that were checked, the phase angle of the second and third approach agreed well. This has proven that the time-averaged phase angle is a solid method of determine the relation between the lift force vector and cylinder motion displacement.

Vector diagram An illustration of the cylinder motion, displacement and lift force vector has been adopted from [4] in fig. 3.5. Firstly, it is evident that the cylinder velocity lags 90° behind the cylinder motion, because of the differentiation of the harmonical cylinder displacement. Then, the phase angle (defined in eq. 3.54 and eq. 3.58) is characterized by the phase lead of the cylinder motion compared to the lift force. This diagram shows that positive phase angles imply that the lift force is in phase with the velocity while negative values show an out of phase component. The fluid is exciting the cylinder when the lift force is in phase with the cylinder, while it is damping the cylinder when the lift force is out of phase with the velocity. These two regions are illustrated as well in fig. 3.5. In other words, a positive phase angle leads to a positive lift force coefficient in phase with the velocity (see eq. 3.51) which indicates the fluid is exciting the cylinder to oscillate.

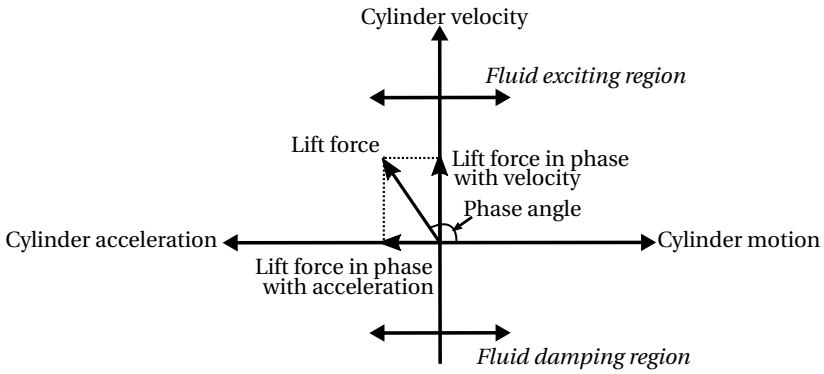

Figure 3.5. Vector diagram of cylinder motion and lift force, adopted from [4]

Added mass coefficient As was pointed out in the review of [87], a distinction can be made between the potential added mass coefficient (C_A) and the 'effective' added mass coefficient (C_{EA}). The former coefficient represents the added mass coefficient when a still fluid is exposed to an oscillation cylinder. Typically, the value for this coefficient is $C_A \approx 1$ for small transverse oscillations [87]. This coefficient is usually considered as the 'true' added mass. The other coefficient, the effective added mass, represents the lift force in phase with the cylinder acceleration when the fluid has an inflow speed higher than zero. Therefore, this latter coefficient also captures the fluid inertia effects caused by vorticity dynamics. The true added mass shows how much air is moved by the cylinder just as a consequence of the surrounding fluid mass being moved by the cylinder

body. Then, the effective added mass also takes the FSI effects into account leading to the additional fluid inertia.

To compute the effective added mass, the cylinder motion has to be taken into account. This approach has been adopted from [4]. The effective added mass can be computed by dividing the lift force in phase with the acceleration (eq. 3.57), divided by the cylinder's acceleration:

$$M_A = \frac{\frac{1}{2}\rho D U^2 C_{L,\ddot{y}}}{y^*_{max}(2\pi f_c)^2} \tag{3.59}$$

Then, the effective added mass coefficient is defined as the inertial fluid mass divided by the volume of the displaced fluid:

$$C_{EA} = \frac{M_A}{\rho V} = \frac{M_A}{\pi \rho D^2 L/4} \tag{3.60}$$

By rearranging these terms, the following relation can be obtained [4] [87]:

$$C_{EA} = -\frac{1}{2\pi^3} \frac{C_{L,\ddot{y}}}{y^*_{max} \frac{D^2 f_c^2}{U^2}} \tag{3.61}$$

4

Results

In this chapter, all the results will be reported on the laminar and turbulent flow cases. In line with the research plan illustrated in chapter 2, fig. 2.17 and tab. 2.1, all the different assessments and outputs will be covered in this chapter. The first section focuses only on the results of the laminar flow cases, while the section after that on the results of the turbulent flow cases. In the laminar section, most of the work is focused to assess the reliability and accuracy of the CFD model used in the present research. Some assessments are performed for the turbulent cases, which are mostly for the stationary cylinder. A lot of experimental results and some numerical results from the literature is available in the supercritical regime for the stationary cylinder to compare the present model against. This offered the opportunity to carefully assess the presently used URANS model. The results for the *forced-* and *free-vibration* cylinder in the supercritical regime were obtained to address the research question defined in chapter 1: *What is the fluid-structure interaction effect of a transversely oscillating cylinder exposed to VIV at supercritical Reynolds numbers?*

The following two questions will be emphasized in this chapter:

- *What do the results show?*
- *How do the results compare against other work in the literature?*

The latter question provides some room for discussion. Hence, some discussion on the modelling will be included in this chapter as well.

4.1. Laminar flow

In this section, all the numerical results and assessments in the laminar flow regime (defined in chapter 2 as $80 < Re < 200$) will be presented. The results for the stationary, forced- and freely-vibrating cylinder set-up will be treated respectively in this section.

4.1.1. Stationary cylinder

Grid refinement study In the present research, as was explained in the previous chapter and shown in tab. 3.3, four successively finer grids have been created to perform a grid convergence study for the laminar meshes. The discretization error is defined as the difference between the exact solution of the governing equations and the exact solution of the numerical approximation of the differential equations [42]. The goal of the grid refinement study was to evaluate if the grid was refined adequately such that the spatial discretization error asymptotically reached zero. The same study was performed for the temporal discretization, which is reported after this section. Since all the numerical schemes that have been adopted in the present simulation are of second order, the order of the overall solver can be considered as second order. The theoretical order of convergence was therefore equal to 2 [76]. When the higher-order terms are neglected, the relation between the observed order of convergence, spatial discretization error and mesh size is defined as follows:

$$log(E) = log(C) + p \cdot log(n) \tag{4.1}$$

where E is the spatial discretization error, C is a constant, p is the observed order of convergence and n is the mesh size in number of cells. Usually, the discretization error is estimated by comparing the obtained

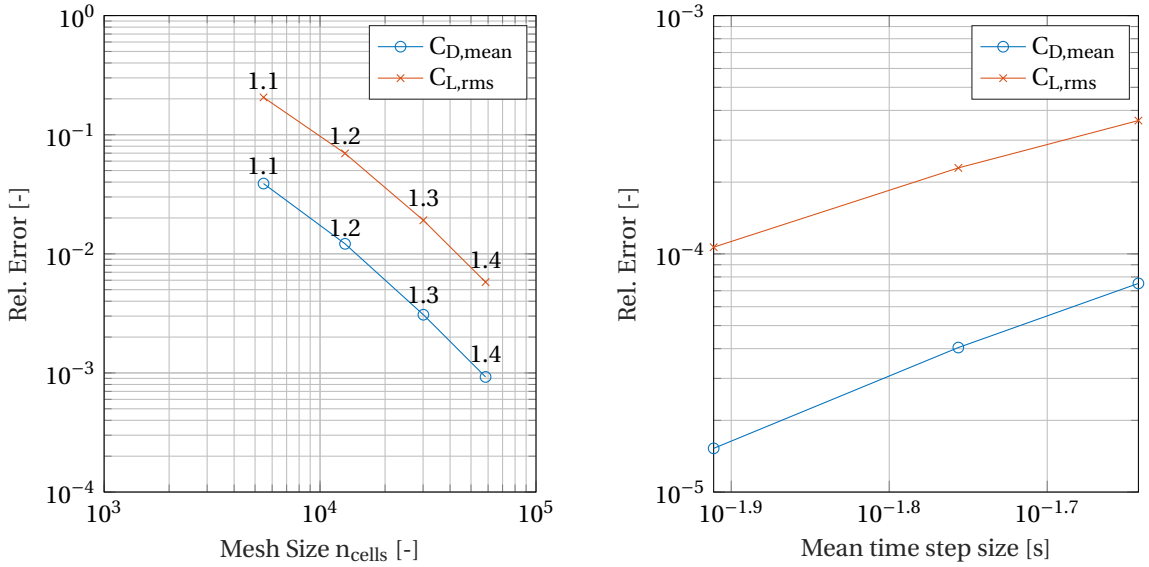

Figure 4.1. *Stationary* cylinder: log-log plot of the relative error of the mean drag coefficient and RMS of the lift coefficient compared to the finest mesh m1.5 of tab. 3.3 versus the number of mesh cells (left subfigure) and compared to the finest timestep scheme t1.4 of tab. 4.1 versus the time-averaged timestep size (right subfigure).

solution to an exact solution of the numerical problem from the literature. Yet, it has been observed that at this moment there is no exact solution available to flow problem of vortex-shedding in the literature. The analytical models are far from capable of computing the exact numerical solution. Therefore, the grid refinement study was compared to the finest mesh, mesh 1.4 in tab. 3.3. In the grid comparison, only the mesh was changed and all other parameters and settings were kept the same. The maximum Courant number for all these mesh refinement runs was $Co_{max} = 0.7$. It was believed that the effect of the timestep size on the truncation error would have been suppressed when the Courant number was kept equal in the grid convergence study. The results of the grid convergence study are shown in a log-log figure, see the left subfigure in fig. 4.1, which allowed the estimation of the observed order of convergence p of eq. 4.1. The numbers in the left subfigure of fig. 4.1 next to the data marks correspond the earlier defined mesh numbers in tab. 3.3.

The slope becomes more constant between mesh 1.2−1.4 compared to the slope between meshes 1.1−1.2. The convergence slope also increased after mesh 1.2. The estimated slope of mesh 1.2 – 1.4 is $p \approx 1.68$ for $C_{L,rms}$ and $p \approx 1.73$ for $C_{D,mean}$. Since the theoretical order of convergence was 2, it has been concluded that the meshes 1.2 – 1.4 Approach 2 fairly good. The reason why the observed order of convergence is a bit smaller compared to the theoretical order could be due to various factors. For example, grid quality, temporal discretization, post-processing and boundary conditions could always contribute to a discretization error. In fact, besides the finer spatial resolution the grid quality has increased considerably, see tab. 3.3. This could explain the fact why the observed order of convergence has increased somewhat during every refinement, as seen in fig. 4.1.

The observed slope between meshes 1.2 – 1.4 indicated that these meshes are in the asymptotic region, which was the goal of this grid refinement study. At the same time, it may be concluded that the meshes 1.1 – 1.2 are still in the non-asymptotic region, where higher-order terms are not negligible. Therefore, the slope is smaller than the slope observed between mesh 1.2 – 1.4. Considering meshes 1.2 – 1.5 are all in the asymptotic region, it is also important to see how close the meshes approaches a spatial discretization error of zero. The relative error for mesh 1.3 compared to the finest mesh is 0.31% for the $C_{D,mean}$ and 1.91% for the $C_{L,rms}$. These errors have been considered to fall within satisfactory accuracy. As the moving cases are expected to increase the computational cost, mesh 1.3 has therefore been chosen to pursue the verification and validation studies. This mesh has proven to be a good compromise between computational cost and adequate refinements.

It may be re-iterated that the convergence observed for the laminar stationary case in the above figure and table does not give any information if the obtained solution is converging to the correct, exact numerical value. The error was taken relative to the finest mesh rather than an exact numerical solution. Yet, the grid

refinement study showed that the flow solution obtained from the fine grid, is grid-independent and is in the asymptotic range. Moreover, as will be shown later in this report, the results of the fine grid have been verified to show that the present CFD simulation showed good agreement with the state-of-the art CFD simulations available in the literature.

Temporal refinement study Besides the grid-independent solutions found in the previous section, it was also important to make sure that the obtained solutions were timestep independent. In the present CFD model, the timestep was varying over time (adjustable) as explained before. The timestep has been varied indirectly by imposing a different maximum Courant number on the adjustable timestep scheme. The four timestep schemes for the temporal refinement study have been listed in tab. 4.1. All these schemes have been run with mesh 1.3. This mesh made sure that the contribution of the spatial error to the truncation error was at satisfactory low values, as was pointed out in the previous section.

Timestep scheme	Co_{max}	ΔT_{mean}
t1.1	1.3	0.0228
t1.2	1	0.0175
t1.3	0.7	0.0123
t1.4	0.4	0.0070

Table 4.1: The four timestepping schemes used for the laminar temporal refinement study

The evolvement of the four timestep schemes during steady-state are displayed in fig. 4.2. In the left figure, it is clear that the simulation did not violate the maximum Courant number constraint and stuck to the input values of tab. 4.1. In the right figure, the effect on the timestep size becomes clear. Indeed, the desired effect of the maximum Courant number on the timestep size has been achieved. For a smaller Courant number, the timestep size decreased accordingly (see eq. 3.22). Although variations of ΔT can be observed in fig. 4.2, they are rather small (variation peak-to-peak is < 3.5%) and hence the time-averaged value has been used for the temporal refinement study. The time-averaged timestep sizes for the four schemes have been listed in tab. 4.1.

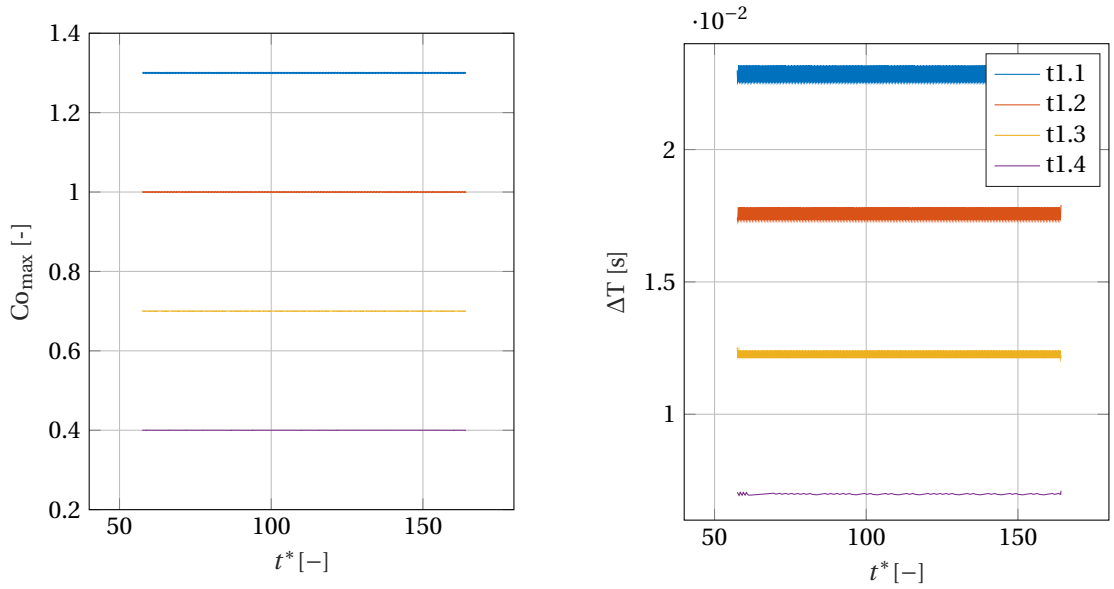

Figure 4.2. The maximum Courant number and the timestep size against the non-dimensional time $t^* = t/T_{shed}$

The effect of the temporal refinement on the error relative to the finest timestep scheme t1.4 has been plotted in the log-log form (similar to previous refinement study) in fig. 4.1. The average slope for $C_{D,mean}$ is 2.55 and for $C_{L,rms}$ is 1.95. The slope is fairly constant and therefore the relative errors have been considered

to be in the asymptotic range. The slopes are higher compared to the ones found in spatial refinement studies. In fact, for the drag force coefficient, it is noticeable that the observed order of convergence is higher than the theoretical order of convergence of 2. The relative temporal discretization error for timestep scheme t1.3 was found to be 0.0015% for $C_{D,mean}$ and 0.01066% for $C_{L,rms}$. The timestep scheme $t1.3$ has been chosen for the subsequent CFD simulations in the present research, based on the observed convergence and small relative temporal discretization error. A couple of comments have been made on these observations. First of all, the relative spatial discretization error is 0.31% for $C_{D,mean}$ and 1.91% for $C_{L,rms}$. Hence, the spatial error contribution should not be disregarded in the present temporal refinement study. In addition, the adjustable timestep scheme is more prone to post-processing errors. Not only the metrics of interest are varying with time now, but also the dependent variable (the timestep size). Since the observed relative temporal discretization errors have been found to be very small ($< 0.04\%$) for all the schemes $t1.1 - 1.4$, it is reasonable that these two effects could have affected the observed order of convergence (and explain why it is higher than 2 for $C_{D,mean}$). At the same time, the fairly constant observed slope in fig. 4.1 shows that these errors did not affect the convergence of the timestep refinement and are more likely to be of a systematic nature. Lastly, it was noted before that the mesh quality variations in the mesh refinement study might have led to inconsistent refinements and therefore to an overall improvement of the order of convergence. Yet, in the present temporal refinement study it is believed that the method behind the four timestep schemes is solid (no inconsistencies between the schemes $t1.1 - 1.4$) as was shown in fig. 4.2. Hence, this could be the reason why the observed order of convergence for the temporal refinement study is higher compared to the spatial refinement study, because the timestep refinements were more systematic.

Influence of cylinder wall cell height Although the non-dimensional wall distance y^+, defined earlier in eq. 3.19, is more often used for turbulent flows the metric has been used in the present research for the laminar flows as well. It was firstly used to see if the y^+ estimation was indeed accurate by post-processing the data and recalculating the real y^+. Secondly, since the flow around the cylinder was interpreted as very complex and highly dependent on the boundary layer, the effect of the wall cell height was considered to be very important. Hence, four different wall cell heights have been applied to the mesh while the same amount of mesh cells were used and the same Courant number. A wall cell height at the cylinder of $y = 0.057$ was needed to achieve a $y^+ = 1$ for $Re = 100$, as was stated before. All the wall cell height variations have been done with the fine mesh $m1.3$, with $N = 30.096$ and a Courant number of $Co_{max} = 0.4$. The only change that has been made in the mesh was the cell distribution in radial direction from the cylinder while keeping the total number of cells equal. The first mesh was based on a cylinder wall cell height of $y = 0.05$, which is somewhat below the desired value of $y = 0.057$. Then, the maximum wall cell height that was possible within the O-grid block, without disturbing the mesh quality too much, was $y = 0.0846$. This height was 1.7 times bigger compared to the mesh with $y = 0.05$. The cylinder wall cell height was decreased by this ratio as well. These different distributions have led to four meshes listed in tab. 4.2. The mesh with the highest wall cell height was expected to be the poorest performing mesh because the boundary layer was supposed to be solved for a smaller portion.

Timestep scheme	y_{wall}	**Cell Distribution**	y^+_{pred}	$y^+_{max,calc}$	$y^+_{mean,calc}$
y1.1	0.0846	Uniform	1.5	1.8	0.95
y1.2	0.0500	Exponential	1	1.1	0.55
y1.3	0.0295	Exponential	0.5	0.7	0.3
y1.4	0.0175	Exponential	0.3	0.4	0.19

Table 4.2: y^+ and y_{wall} variations for four different meshes

To achieve the highest cell distribution without affecting the mesh quality too much, a uniform cell distribution was required. This ensured that the cell size at the circumference of the O-grid block was kept at adequate small levels for the transition to the other grid blocks. Next to the cell distribution, the predicted y^+ value, the calculated maximum y^+ value and the calculated mean y^+ value were listed as well. The calculated values were evaluated after the simulation by the using the locally computed wall shear stress for each timestep. It is therefore shown that the predicted y^+ value is in good agreement with the actual y^+ value found after the simulation (although the formulas defined earlier in eq. 3.19 are generally not for laminar flow). Besides the fact that mesh y1.1 was expected to resolve a smaller part of the boundary layer, it was

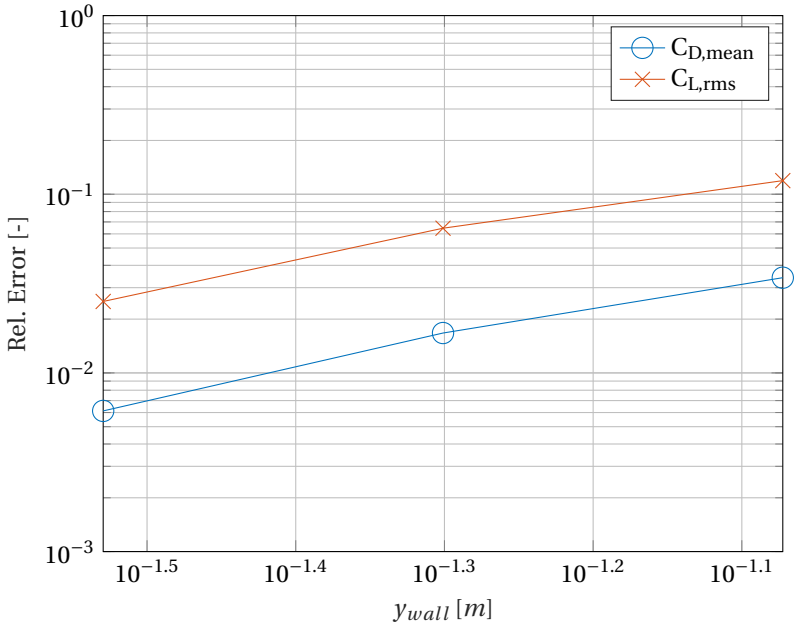

Figure 4.3. *Stationary* cylinder: log-log plot of the relative error of the mean drag coefficient and RMS of the lift coefficient compared to the smallest cylinder cell wall height y1.4 of tab. 4.2 versus the cylinder wall height y_{wall}.

also found that this mesh quality was the poorest. In fact, the mesh quality seemed to increase between the meshes y1.1 – 1.4. The cylinder wall height and the computed error relative to mesh y1.4 are displayed in a similar log-log plot as before, see fig. 4.3. The mean slope was found to be equal to $p = 1.6$ for $C_{D,mean}$ and $p = 1.5$ for $C_{L,rms}$. These results showed that the influence of the cylinder cell wall height is significant (considering that the mesh size was kept equal). The relative errors for mesh y1.2 were found to be 1.7% for the drag and 6.5% for the lift coefficient. Although this relative error is still quite large for the lift coefficient, this wall cell height has been chosen for the verification and validation studies. This wall cell height proved to be well below the desired y^+ value of 1 and showed results which agreed well with other numerical studies as will be reported later.

Verification and Validation As was stated before, there is no exact analytical solution available at this moment for the fluid around a stationary cylinder. Still, comparisons against other CFD studies available in the literature was considered as a good alternative to show the performance of the present CFD model. In the literature, plenty of CFD studies simulating VIV have been done at low Reynolds number (laminar flow). For example, see [88, p. 86, tab. 5] for a compilation of many CFD simulations at $Re < 3 \cdot 10^5$. Yet, not a lot of experimental studies have been found in the literature for laminar flow. It was argued in [88] that experiments for $Re < 6 \cdot 10^3$ requires a small test section width and a large aspect ratio. These requirements are both seen as a practical complication for laboratories. Only the experiment of Tanida et al. [89] relevant for the present study has been found which measured the lift force, drag force and Strouhal number at $60 < Re < 110$. The Strouhal number has been measured in more experimental studies in the laminar Reynolds range. The CFD work of O. Posdziech and R. Grundmann [72] was considered reliable as an extensive grid convergence study and domain size convergence study were both completed in their work. The numerical studies of Placzek et al. [64], Blackburn and Karniadakis [34], Shiels et al. [5] and the experimental study of Tanida et al. [89] also investigated either a forced- or free-vibration case. Hence, these results have been included here to observe how well the present CFD model agrees with these papers without the FSI features included. This comparison served as en extra verification to the moving results. The lift coefficient amplitude, mean drag coefficient and Strouhal number as a function of the Reynolds number are shown in fig. 4.4 and fig. 4.5, respectively. All the studies included in the figures were CFD studies, except for the ones which are denoted with (Exp.) in the legend. Simulations of the present work have been completed for $Re = 80, Re = 100, Re = 150, Re = 185$ and $Re = 200$.

The $C_{L,max}$ in the right subfigure of fig. 4.4 shows very good agreement with the other numerical studies.

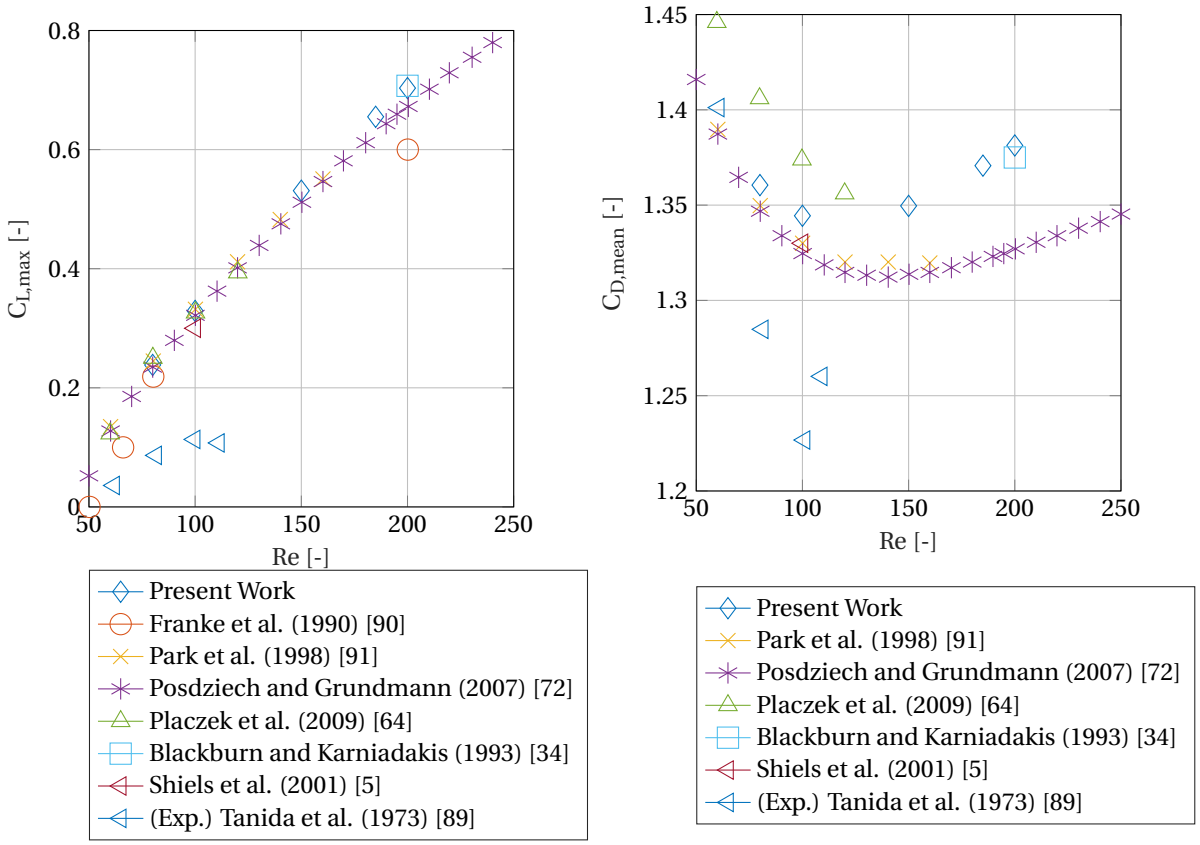

Figure 4.4. The lift coefficient amplitude (left subfigure) and mean drag coefficient (right subfigure) for $50 < Re < 250$ for a stationary cylinder

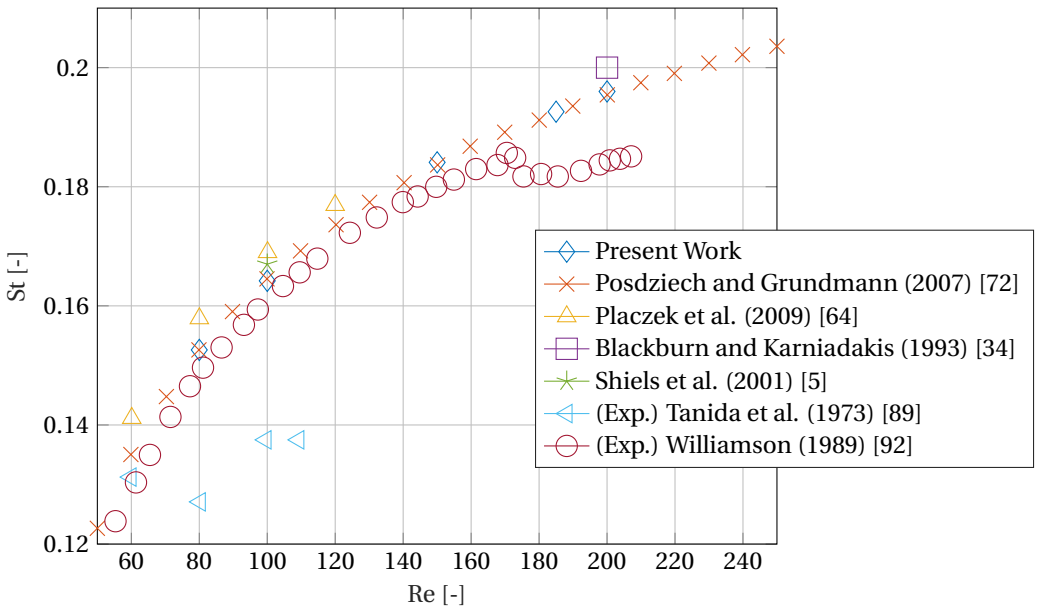

Figure 4.5. The Strouhal number for $50 < Re < 250$ for a stationary cylinder

For low Reynolds numbers, $Re < 150$, the lift amplitude is in good agreement with the results of [72] which was completed at a domain size of $70D$. For $Re >= 150$ the results of the present simulation seem to be higher than the lift amplitude predicted by Posdziech. At the same time, at $Re = 200$ the lift is nearly identical compared to the work of [34]. The study of [34] was done at a computational domain with $L_1 = 12.5D$ and $L_2 = 25D$. The results of [90] show an under prediction compared to most of the other numerical results. Their domain size was $20D$, yet their grid refinement might have been the cause of this underprediction, as was argued by [72].

At lower Reynolds numbers, $Re < 150$, the mean drag is again in the vicinity Posdziech and Grundmann's work. Although the mean drag increment for $Re > 150$ has been captured, the drag has been over-predicted slightly. In line with the observations made for the lift amplitude previously, the mean drag at $Re = 200$ compares well to the study of [34].

The predicted Strouhal number shows excellent agreement with the other numerical studies. It was expected that the Strouhal number would agree better with the other numerical studies as was pointed out earlier in section 3.1.2. For all the flow metrics, it may be concluded that the experiment results of Tanida et al. [89] show big deviations compared to the numerical studies. It was already stated by [88] that their experiment was conducted at an aspect ratio of only 10, no end plates were used and oil was used as working medium. Therefore, these results should be interpreted with caution. However, the Strouhal number of Williamson's experiment [92] approaches the numerical results very close for $Re < 170$. His work was done with endplates, a large aspect ratio and negligible cylinder vibrations. Hence, the experimental study of [92] is more reliable compared to the one of [89]. For $Re > 170$, the results of Williamson's work fall under the numerically predicted curve of the other studies. This difference could be attributed to the fact the free shear layer starts to transition to a turbulent vortex street (see fig. 2.6 and fig. 2.7) which impacts the wake and hence the vortex shedding frequency component in the Strouhal relation. It is plausible that the CFD model was not able to capture these secondary flow features located more downstream in the wake, where the mesh resolution decreases.

4.1.2. Moving cylinder: 1-way coupling

Non-dimensional form of 1-way coupled VIV system In the forced-vibrations cases, the cylinder motion was prescribed and known a priori. This type of experiments gives the ability to exactly define the motion trajectory of the cylinder and to investigate the effect of these tightly controlled cylinder vibrations on the wake. No feedback of the fluid forces on the wake is therefore included the forced-vibration simulations. Referring to eq. 3.23, two additional input parameters were required compared to the stationary cylinder: f_{cyl} and the oscillation amplitude y_{max}. The cylinder frequency was made non-dimensional by the stationary shedding frequency:

$$f^* = \frac{f_{cyl}}{f_{shed,stat}} \tag{4.2}$$

The cylinder amplitude by the cylinder diameter:

$$y^*_{max} = \frac{y_{max}}{D} \tag{4.3}$$

and the non-dimensional time is given by (unless stated otherwise in the report):

$$t^* = t/T_s \tag{4.4}$$

The frequency ratio defined in 4.2 is typically used for forced oscillation studies to give an indication of how close the cylinder vibration frequency is to the stationary shedding frequency. The cylinder has no mass in this simulation and is purely a geometry which affects the wake. Therefore, the closest situation to lock-in for a forced-vibration experiment is reached when $f^* = 1$, when the cylinder is moving at same frequency for vortex shedding observed for a stationary cylinder.

Besides the non-dimensional motion parameters, the Reynolds number should be kept constant as well when comparing to other numerical studies. Hence, to ensure similarity between two forced-vibration experiments these three non-dimensional parameters should be constant: f^*, y^*_{max} and Re. When inspecting eq. 4.2, besides the non-dimensional frequency f^*, f_{shed} is also required to compute f_{cyl} as a dimensional input for the CFD model. It is not always the case forced-vibration studies present their stationary results in the same work as well. In addition, it could be argued that since in the stationary and forced-vibration nearly

the same computational set-up has been used, it would be more consistent to also use earlier obtained stationary results from the same CFD model for the moving cases. Hence, in the forced-vibrations studies, f_{shed} from the stationary runs of before are used. However, one can imagine that when the used f_{shed} differs significantly from the numerical study to be compared, the comparison does not hold up any-more. In light with that, it is therefore important that the stationary results of the moving studies is also compared in the present research. This has been done previously in fig. 4.4 and fig. 4.5.

Grid refinement study Similar to the grid refinement study of the stationary cylinder results, a grid refinement study was performed for the forced-moving cylinder. The same (laminar) meshes have been used as for the stationary case. The details of these meshes can be found in tab. 3.3. The same method as before has been used to determine the order of convergence, see eq. 4.1. The log-log plot for spatial convergence for the forced-moving cylinder can be seen in the left subfigure of fig. 4.6. Again, as was observed for the stationary cylinder, it seems that relative error between mesh 1.1 – 1.2 is still in the non-asymptotic region, indicating the presence of higher-order terms. Inspecting meshes 1.2 – 1.4 may lead to the conclusion that these relative errors are located in the asymptotic range, where the slope in fig. 4.6 and therefore the observed order of convergence is more constant. The average slope for meshes 1.2 – 1.4 is found to be 1.91 for $C_{L,rms}$ and 1.37 for $C_{D,mean}$. This indicates that the observed order of convergence for the lift coefficient is very close to the theoretical order of convergence, while for the drag coefficient this is rather far away. Although deviations from the theoretical order of convergence were expected, it is unclear how the observed order of convergence deviated from the theoretical order of convergence. Especially since the grid quality improved going from mesh 1.2 to mesh 1.5, it was expected that the slope would increase towards 2 like with the lift coefficient. The relative spatial discretization error for mesh 1.3 was found to be 0.011% for $C_{D,mean}$ and 1.78% for $C_{L,rms}$. These errors have been deemed as satisfactory accurate and therefore mesh 1.3 has been used for the validation and verification cases. While the relative error for $C_{L,rms}$ is similar to the one found before for the stationary case, the relative error for $C_{D,mean}$ is an order of magnitude smaller for the forced cases.

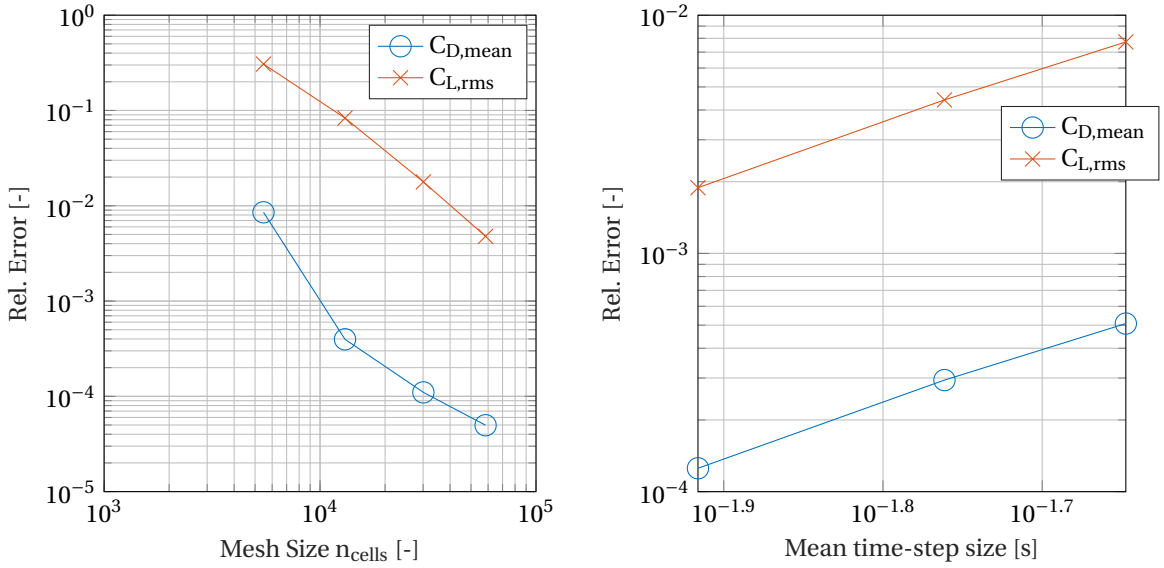

Figure 4.6. *Forced*-vibration: log-log plot of the relative error of the mean drag coefficient and RMS of the lift coefficient compared to the finest mesh m1.5 of tab. 3.3 versus the number of mesh cells (left subfigure) and compared to the finest timestep scheme t1.4 of tab. 4.1 versus the time-averaged timestep size (right subfigure).

As part of understanding the convergence behaviour of the two aerodynamic metrics, their fluctuating signal has been plotted in fig. 4.7 for one period. The first observation is that for both the lift and drag force coefficients, mesh 1.1 shows the largest deviations from the other results which confirms that higher-order terms are probably still present. In addition, the drag coefficient peak shows small oscillatory behaviour for mesh 1.1. These oscillatory results seem to disappear away with increased mesh size. The lift force coefficient does not show these small fluctuations around the peak. Fig. 4.7 also indicates that meshes 1.2 – 1.5 are

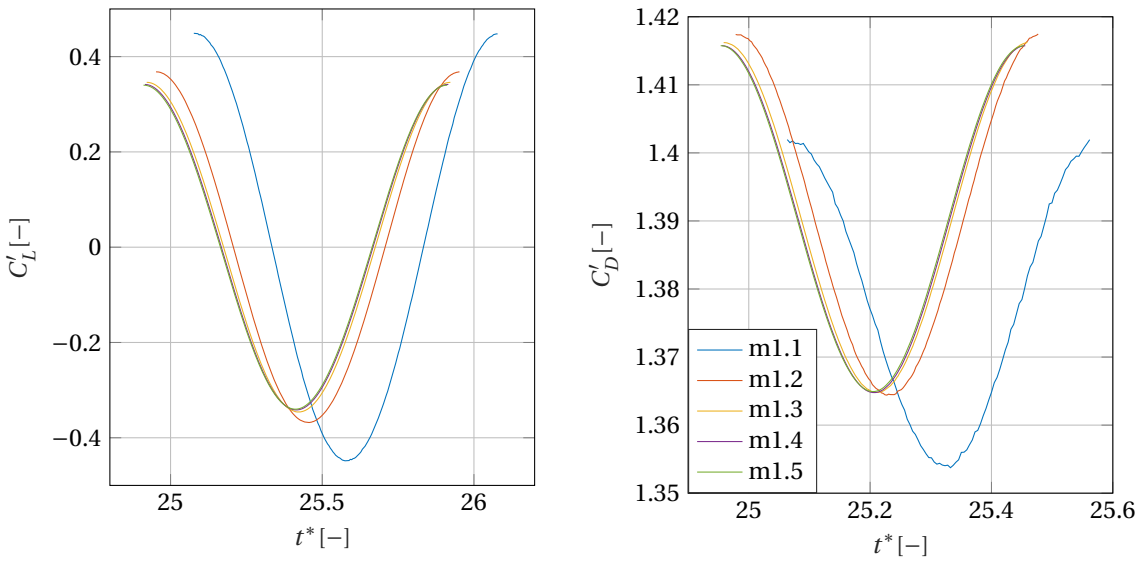

Figure 4.7. Fluctuating lift coefficient (left) and fluctuating drag coefficient (right) for one shedding period

converging and are located in the asymptotic region.

The presence of the small peak oscillations for the drag coefficient implies that it was harder for the drag coefficient to reach convergence compared to the lift coefficient. This would explain why the observed order of convergence for $C_{D,mean}$ is found to be somewhat lower compared to the one for $C_{L,rms}$. The observed slope for lift is found to be higher and for drag lower relative to the stationary grid refinement study. The higher expected flow fluctuations locally around the cylinder body are possible additional error sources compared to the stationary case. It was believed that the dynamic mesh preserved the initial mesh quality of the stationary mesh well, this is shown in Appendix C. Another aspect that must be taken into account is the energy balance in the 1-way coupled FSI model. The grid convergence may have been troubled by the fact that the oscillations were *forced*. By prescribing the cylinder motion, energy has been added to the wake continuously. This makes it harder for the system to reach an equilibrium, where the energy input is equal to the energy dissipation in the wake. In contrast to forced-vibrations, the two-way coupled FSI in free-vibration would allow the energy transfer to develop in such a way that equilibrium is reached. The (artificial) reached steady-state in forced-vibration cases could affect the observed order of convergence.

Temporal refinement study Like the temporal refinement study for the stationary cylinder, the temporal discretization error for the forced-moving cylinder was also studied. Mesh 1.3 was adopted again for this study. The timestep schemes are identical to the previous one used for the stationary cylinder, they have been summarized in tab. 4.3. The mean timestep size was computed in the same manner as before and their values are very close to the time-averaged timestep sizes found for the stationary cylinder.

Timestep scheme	Co_{max}	ΔT_{mean}
t1.1	1.3	0.0225
t1.2	1	0.0173
t1.3	0.7	0.0121
t1.4	0.4	0.0069

Table 4.3: Forced-cylinder: timestep size variations

The results of the temporal refinement study has been plotted in the log-log form in the right subfigure of fig. 4.6.

As fig. 4.6 shows, the slope is very constant and temporal convergence has been reached. The average slope was found to be 2.26 for $C_{L,rms}$ and 2.24 for $C_{D,mean}$. The relative temporal discretization error for timestep scheme t1.3 was 0.013% for $C_{D,mean}$ and 0.19% for $C_{L,rms}$. These errors were both considered to be very accurate and hence timestep scheme t1.3 has been chosen for all the forced-moving simulations. Again, the observed order of convergence is higher than the theoretical value of 2. This was also observed for the temporal refinement study of the stationary cylinder simulations. The same reasoning why this observed order of convergence turned out higher than 2 holds up for the forced-moving cases.

The relative errors seem to be an order of magnitude higher compared to the stationary cylinder while the order of convergence is in better agreement. The higher relative error is likely not caused by the contribution of the spatial discretization error, since the same mesh was used and the relative spatial errors were found to be smaller for the forced-vibration case. It is possible that the higher relative error is caused by the mesh deformations, imposing higher local Courant numbers in the regions where high flow fluctuation are expected. This could have led to a higher truncation error, however this was not checked in the present study.

Verification and Validation The verification of the forced-moving cylinder has been done against the numerical study of [64]. Their results for a stationary cylinder have been included before in the results. From the stationary results, it turned out that the drag coefficient of the present work was somewhat lower compared to their predicted drag coefficient. The lift coefficient amplitude agreed well with the lift coefficient predicted by the presently used model for the stationary cylinder. All the simulations have been done at constant Reynolds number of $Re = 100$ and non-dimensional amplitude $y^*_{max} = 0.25$. The reduced frequency, $f^* = \frac{f_{cyl}}{f_{shed}}$, has been varied between $0.5 < f^* < 1.5$. According to the experiment of [93] for forced VIV at low Reynolds numbers, lock-in was established for $0.87 < f^* < 1.18$ (see [93, fig. 8, p. 508]). Therefore, it is expected that the operating points which fall outside this region leads to different vortex shedding behaviour.

The results of the forced-vibration simulations are presented in fig. 4.8 for the aerodynamic coefficients. Similar to the stationary cylinder, the drag coefficient was a bit lower compared to the results of [64]. The lift coefficient agreed well with the predicted lift coefficient found in the study of [64]. The lift amplitude seems to be a bit lower compared to the verification study for $f^* = 1.5$. It is noticeable that the lift coefficient for $f^* > 1$ kept on increasing. For $f^* < 1$ it decreased and came closer to the stationary value. This trend was also predicted by the numerical studies of [64] and [94]. This contrasts with the typical lock-in response, where the lift and drag forces only show a magnification for a certain band-with around $f^* = 1$ (also called the lock-in band with). At one point, the lift coefficient would decrease and approach the stationary lift coefficient value again (see for example [2, fig. 21, p. 35]). Also, the mean drag force appeared to increase a bit for $f^* > 1$ but closer to the stationary mean drag force compared to the lift force. The added mass of the fluid is the suspected cause of the continuous increment of the aerodynamic forces after the critical frequency, as will be explained in section 4.2.2.

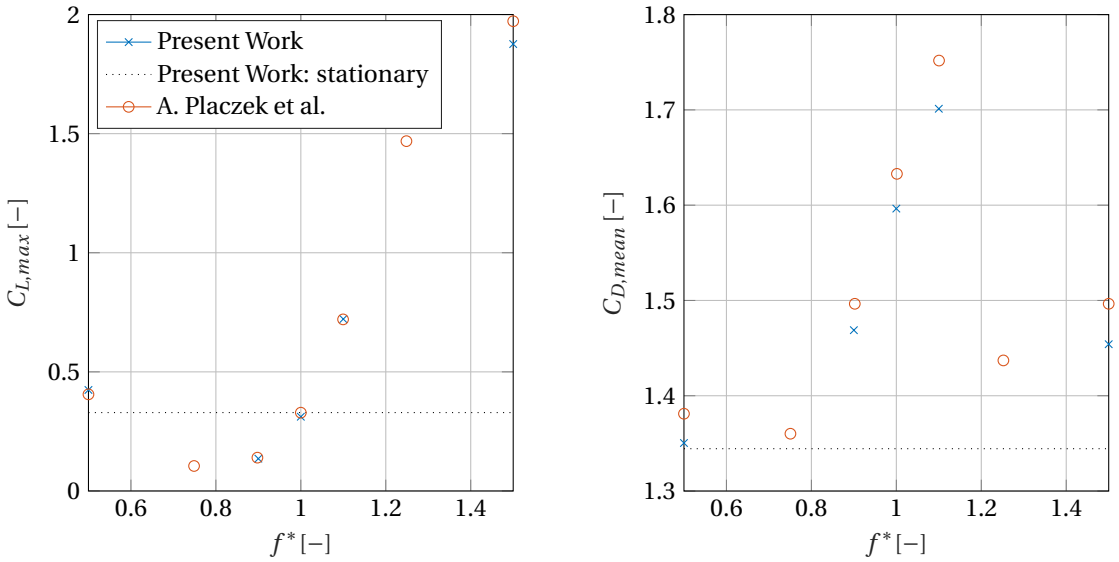

Figure 4.8. The lift coefficient amplitude (left) and mean drag coefficient (right) for $0.5 < f^* < 1.5$

Force time series inside the lock-in region The time series of the lift (left subfigure), motion (left subfigure) and drag coefficients (right subfigure) for $f^* = 1$ are plotted in fig. 4.9. The drag and lift force coefficients showed a harmonical response. Only two shedding cycles are shown because the signal remains like this throughout the full steady-state simulation. The drag coefficients fluctuated around two times the shedding cycle period, which is clearly shown in fig. 4.9, right subfigure. Based on fig. 4.9, it may be concluded that the

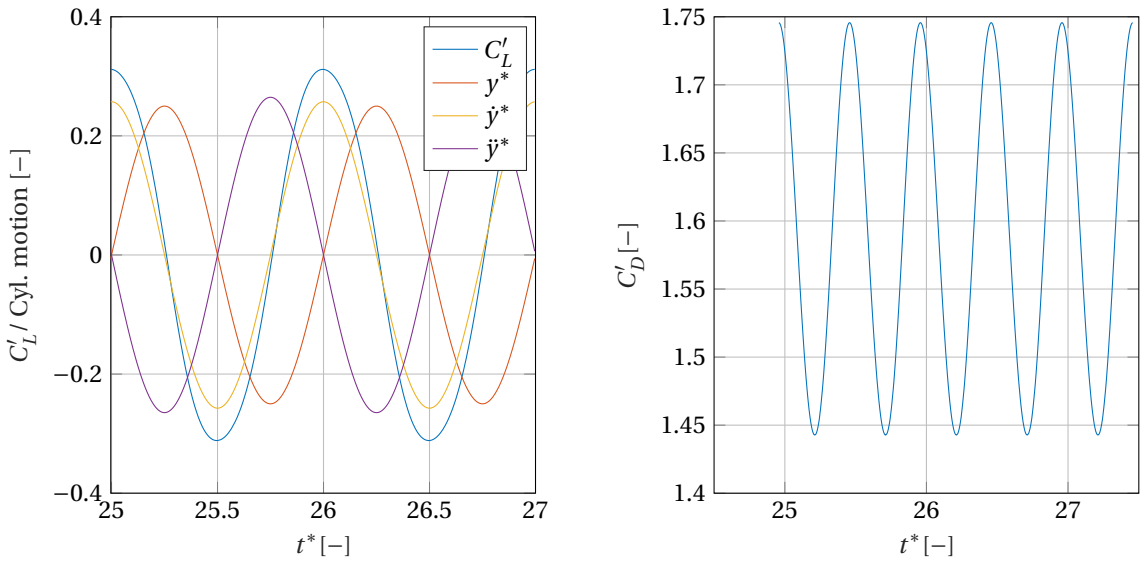

Figure 4.9. Fluctuating lift coefficient (left) and fluctuating drag coefficient (right), both in steady-state and for a multiple of 2 shedding cycles at $f^* = 1$

transverse velocity of the cylinder body was in phase with the lift coefficient, while the cylinder displacement and acceleration were out of phase.

Indeed, the phase portrait on the left subfigure of fig. 4.10 shows an ovoid trajectory. When the cylinder has reached its maximum non-dimensional displacement, the lift force coefficient is equal to zero and vice versa. This would confirm that the lift force is out of phase with the cylinder displacement. The non-dimensional FSI coefficients were found to be: $C_{L,y} = 0.0134$, $C_{L,\dot{y}} = 0.3228$ and $C_{L,\ddot{y}} = -0.0134$ compared to an amplitude of $C_{L,max} = 0.3117$. From these numbers it may be stated that the lift force is very strongly in phase with the transverse cylinder velocity. Since the lift force in phase with the velocity is positive, the fluid is supplying energy on average to the structure. Hence, in this state with $f^* = 1$, the FSI is contributing to the cylinder vibrations.

Force time series outside the lock-in region The lift and drag time history differed significantly for the operating points outside the lock-in region. The time series of C_L' and C_D' are shown in fig. 4.11, which was outside the lock-in region at $f^* = 1.5$. In contrast to the harmonical drag and lift history found before inside the lock-in region, fig. 4.9, the time series now show a more chaotic behaviour and the signal is far from a pure harmonical one. This phenomenon is known as *beating* within structural dynamics [95]. The beating signal can be decomposed into multiple sinus signals, all operating at different frequencies. The occurrence of multiple signals is caused by the prescribed cylinder frequency being too far away from the stationary shedding frequency. Most of the time, the wake was dictated by the cylinder motion (lock-in). Yet, sometimes the wake was characterized by the Strouhal relation (lock-out). When the driving frequency f_{cyl} is prescribed even further away from the stationary frequency, the wake would probably adapt even more to the Strouhal relation and hence the flow is dominated by lock-out. These two wake frequencies have been reflected in the time series of the lift time series, fig. 4.11, where multiple periodic signals can be seen.

It must be noted that the more chaotic nature of the lift and drag signal made the verification outside the lock-in harder. Usually, in the literature, the lift amplitude and time-averaged drag has been reported. Especially the lift amplitude may be very instantaneous during the beating phenomenon, as can be seen in fig. 4.11. This could lead to different interpretations of the results. The harmonical signals found inside the lock-in region have a constant lift and drag amplitude over time, which makes the verification more reliable. For example, the slight under prediction of the $C_{L,max}$ at $f^* = 1.5$ could very well be caused by different post-processing, see fig. 4.8.

The phase portrait and PSD of the lift time series are shown in fig. 4.12. In contrast to the unique, ovoid shape found previously in fig. 4.10 for $f^* = 1$, the phase portrait is more chaotic now and multiple trajectories can be identified. This phase portrait shows that the evolvement of the lift coefficient and non-dimensional amplitude is rather chaotic and varies from vortex shedding cycle-to-cycle. The wake pattern is therefore not

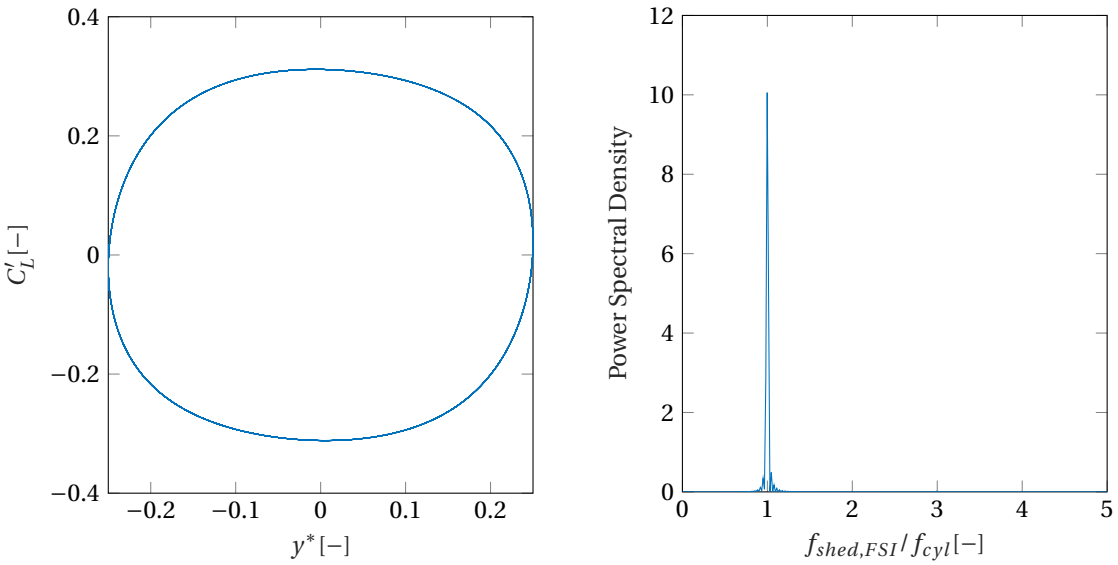

Figure 4.10. Phase portrait of non-dimensional cylinder motion amplitude against fluctuating lift coefficient (left) and PSD of the lift coefficient time series (right), both at $f^* = 1$

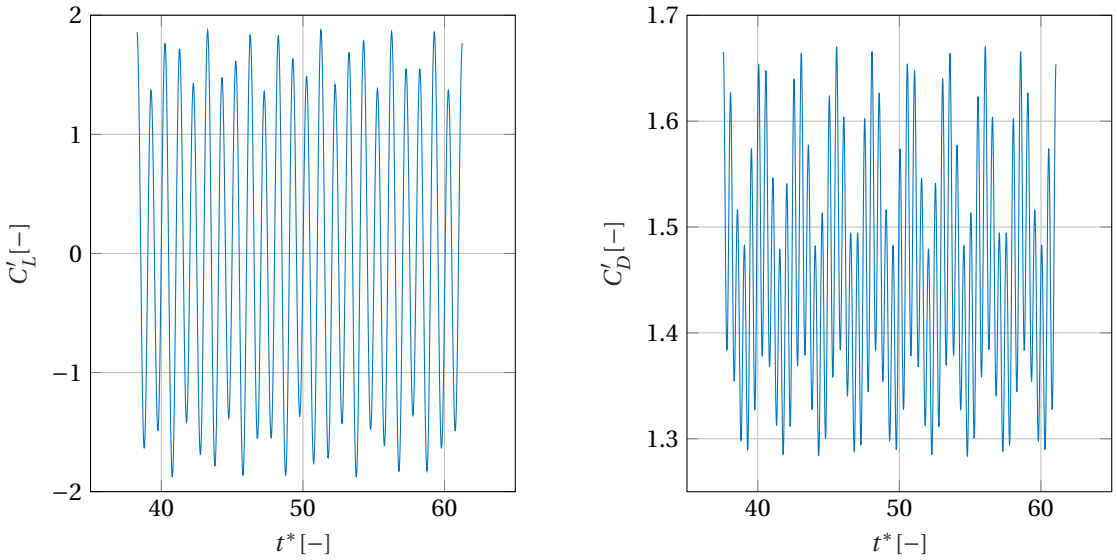

Figure 4.11. Fluctuating lift coefficient (left) and fluctuating drag coefficient (right), both in steady-state and for a multiple of 23 shedding cycles at $f^* = 1.5$

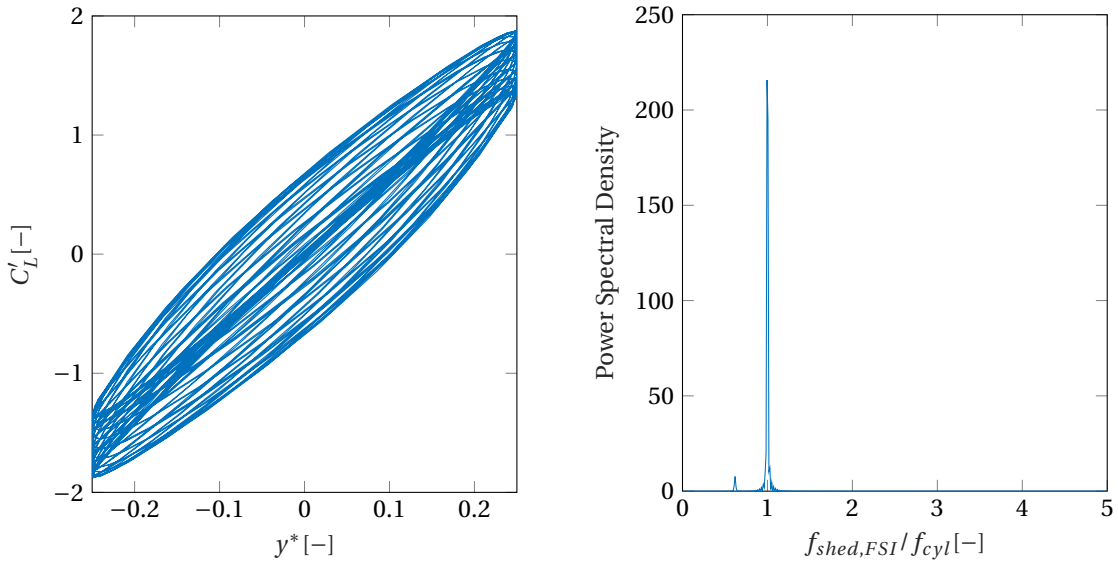

Figure 4.12. Phase portrait of non-dimensional cylinder motion amplitude against fluctuating lift coefficient (left) and PSD of the lift coefficient time series (right), both at $f^* = 1.5$

stable and changes continuously. Again, it is believed that the intermittent stages where the wake follows the Strouhal relation (lock-out) or the cylinder frequency (lock-in) is causing this chaotic behaviour in the wake. On the right subfigure of fig. 4.12, the PSD of the lift coefficient indeed shows two peaks. The dominant peak is reflecting the cylinder frequency and the second, smaller peak is located near the stationary shedding frequency. These results are in line with the time series and phase portraits presented in the numerical study of [64]. Because of the beating phenomenon, the wake changed continuously. This has shown that the CFD model was able to capture more complex flow fields as well.

It was observed that the computed aerodynamic damping and other FSI metrics for the case of $f^* = 1.5$ were not reliable. As a sanity check, the coefficients computed for only one shedding period were compared against the computed coefficient for a multiple of at least 10 periods. This comparison showed that these quantities differed by > 10%. The presented FSI quantities before for $f^* = 1$ differed by less than 1% which is deemed to be reliable.

4.1.3. Moving cylinder: 2-way coupling

Non-dimensional form of 2-way coupled VIV system Eq. 3.25 has been non-dimensionlized in appendix B. This has led to the following equation:

$$\frac{d^2y^*}{dt^{*2}} + 2\zeta\frac{dy^*}{dt^*} + y^* = U^{*2}\frac{C_L}{m^*} \tag{4.5}$$

Based on this equation, it has become common practice to use the non-dimensional parameters U^*, m^* and ζ to scale the system of eq. 3.25 [5], [85]. Solving the Navier-Stokes equations would lead to the pressure field and velocity field in the computational domain. Once the pressure distribution around the cylinder is obtained, *OpenFOAM* is able to calculate the aerodynamic forces exerted on the cylinder body. According [16], dynamic similarity is achieved between different CFD simulations when the Reynolds number is equal and when the geometry is similar. The derivation of the Reynolds number scaling for the Navier-Stokes/URANS equations is shown in in appendix A. Hence, inspecting eq. 4.5, this would mean that $C_L = f(Re)$ when the geometry is preserved. This means that the 2-way coupled problem scales with four non-dimensional parameters: U^*, m^*, ζ and Re. In the present research, when validation and verification studies were performed, these parameters will always be matched to the non-dimensional values used in the study that is compared. This will ensure that the 2-way coupled system in the present model is operating under the same circumstances as the studies which are used for comparison.

There are multiple definitions of the non-dimensional parameters which represent VIV, although they are usually very similar and relatable. The first numerical study that has been used for verification was the one from [65]. The amplitude and frequency response of their study was used as a comparison. Since the present

research aimed to capture the aerodynamic forces, an additional verification study of the CFD model was performed to two other papers which included the forces in their results. The studies of [5] and [64] both predicted the lift and drag forces for a 1DOF transverse freely-vibrating cylinder. Their studies were found to be reliable and were incorporated in the present research to verify the accuracy of the present CFD model to predict the fluid forces. The non-dimensional parameters that have been used in all the incorporated studies next to definitions used in the present research have been listed in tab. 4.4.

Non-dimensional parameter	Present Work	Williamson and Govardhan [29]	Shiels et al. [5]
m^*	$\frac{m}{\pi\rho D^2 L/4}$	$\frac{m}{\pi\rho D^2 L/4}$	$\frac{m}{0.5\rho D^2 L}$
k^*	–	–	$\frac{k_s}{0.5\rho U^2 L}$
ζ	$\frac{c}{2\sqrt{km}}$	$\frac{c}{2\sqrt{k(m+m_A)}}$	$\frac{c}{0.5\rho UL}$
U^*	$\frac{U}{f_{nat}D}$	$\frac{U}{f_{nat}D}$	$\frac{U}{2\pi f_{nat}D}$
f^*	$\frac{f_{cyl}}{f_{nat}}$	$\frac{f_{cyl}}{f_{nat}}$	$\frac{f_{cyl}D}{U}$

Table 4.4: Non-dimensional parameter definitions

The non-dimensional values in tab. 4.4 are in slightly different format than previously defined in eq. 4.5 and in appendix B. Still, these non-dimensional values have proven to be reliable. The dimensionless numbers used in [29] have appeared in many free-vibration studies. In fact, the study of [65] used the same non-dimensional values as the ones defined in [29], except that the damping ratio was slightly different. In [29], the damping ratio was augmented with the added mass of the fluid m_A. Regarding the two verification studies reported in the present chapter, the definitions used were identical to the ones defined in the referred study. After the verification studies, all the results of the present research have been expressed in the non-dimensional parameter definitions of [29] without the added mass, as can be seen in tab. 4.4.

Verification of the cylinder motion prediction In the study of [65] of freely-vibrating 1-DOF structure was coupled to a 2D CFD model. In their study, simulations have been performed of two circular cylinders in tandem arrangement. Before the tandem arrangement, the 2D flow around a single cylinder was simulated by employing DNS. Their FSI model was loosely-coupled, meaning an explicitly partitioned approach. The non-dimensional parameters that have been used in their study were according to the non-dimensional parameters that were used in the present work as well (see tab. 4.4). The simulations have been carried out at $Re = 150$, $m^* = 2$, $\zeta = 0.007$ for a reduced velocity sweep of $2.5 < U^* < 16$. The amplitude and frequency response are displayed in fig. 4.13.

The non-dimensional amplitudes agree well with the results of [65], as is shown in fig. 4.13. The lock-in region is clearly identified by the increased y^*_{max} for the range of $4 < U^* < 7$. All the results lead to fully developed harmonical steady-state solutions. Hence, the verification is deemed as reliable, since y^*_{max} was taken over a multiple of periods rather than taking an instantaneous value. The results for y^*_{max} seem to agree even better outside the lock-in region, where inside the lock-in region some of the results fall a little bit below the results computed by [65]. Since their structural model also only involves an one-degree-of freedom system, it is believed that no significant differences in the structural solver were present. No results of their stationary cylinder have been included in their paper, which makes it harder to compare the fluid solver's performance. The further away from the lock-in region, the closer the aerodynamic forces would reach the stationary cylinder wake. This will be shown later, in the verification of the aerodynamic forces during free-vibration. This means the better agreement outside the lock-in implies that the fluid solver is comparing well against the fluid solver of [65]. The small under prediction inside the lock-in region is probably caused by the fluid-structure interaction modelling. The study of [65] also used a weakly-coupled FSI scheme and the Newmark scheme for the solving structural motion. These settings are similar to the presently used weakly-coupled scheme for the laminar flow cases. Yet, as was pointed out earlier in section 3.2, within *OpenFOAM* the im-

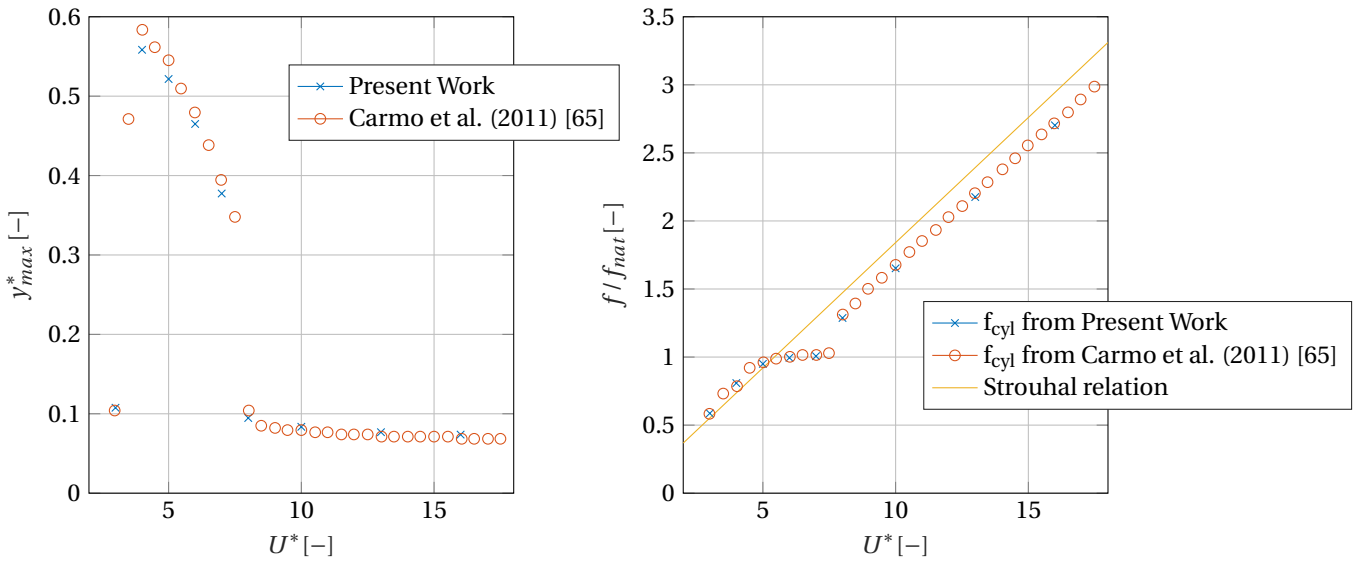

Figure 4.13. Non-dimensional amplitude (y^*_{max}) (left subfigure) and frequency ratio (right subfigure) against the reduced velocity at $Re = 150$, with $m^* = 2$ and $\zeta = 0.007$

plicit character of the Newmark scheme might be lost by using the explicit FSI algorithm. At this point during the research, this complication related to the Newmark solver in *OpenFOAM* was not known. Therefore, the simulations have been run under the assumption that the Newmark solver would solve the motion as how the solver usually operates according to [82]. It is possible that this complication has caused the difference in results inside the lock-in region. This has not been checked in retrospect by re-running the simulations with a strongly-coupled solver.

Fig. 4.13 again demonstrates that the present model captures the motion response of the cylinder well. The frequency response is in line with the earlier observed lock-in region of $4 < U^* < 7$, where it has become clear now that the cylinder frequency f_{cyl} tags along to the natural frequency of the system f_{nat} (i.e., $f_{cyl}/f_{nat} = 1$). Outside this region, the cylinder frequency has followed the (linear) Strouhal relation according to eq. 2.2. It has been noted that before the lock-in region, the cylinder frequency tends to follow the Strouhal relation very tight, while after the lock-in region there is a systematic deviation. Although the linear relation was nicely predicted by the present CFD code and [65], the absolute values are a little below the theoretical values obtained from the Strouhal relation.

These verified free-vibration cases show that the present weakly-coupled FSI model is capable of capturing the motion response of light cylinder bodies exposed to VIV. All the simulations have been operated successfully and no numerical instability has been observed. The next step was to verify the accuracy of the aerodynamic force predictions.

Verification of the aerodynamic forces prediction In the numerical study of [5] a new non-dimensional parameter was introduced to collapse the non-dimensional mass m^* and spring-stiffness k^* into one effective parameter k^*_{eff}. This parameter was defined by the following relation:

$$k^*_{eff} = k^* - 4\pi^2 f^{*2} m^* \tag{4.6}$$

It has appeared that this parameter collapses the structural parameters well for undamped systems, even when the mass was set to zero [5]. The study of [64] also supported the good representation of k^*_{eff} for multiple response branches. Hence, for the verification of the aerodynamic forces, the effective elasticity parameter was used. Typically in VIV studies, the amplitude and force responses are plotted against the reduced velocity U^* or reduced frequency f^* as defined in tab. 4.4. Yet, as it turned out, the effective elasticity parameter k^*_{eff} produced similar lock-in shapes as the frequency ratio f^* or reduced velocity U^*. To give an indication of how this new parameter worked out in terms of the non-dimensional parameters used in the present work, the k^*_{eff} parameter from [5] was translated to the reduced velocity and mass ratio found

in the second column of tab. 4.4. Relating to those non-dimensional parameters, the reduced velocity in this verification analysis was varied between $0 < U^* < 7$, the mass ratio between $0.5 < m^* < 10$ while the damping ratio was equal to zero ($\zeta = 0$). The Reynolds number (same definition for all cases) was in this verification analysis equal to $Re = 100$. When comparing these relatable non-dimensional parameters with the previous study, it may be concluded that the mass ratio of this analysis has the same order of magnitude as in the previous verification analysis. In addition, the non-dimensional damping was set very low in the previous analysis and this time it is even set to zero. The reduced velocity sweep is very similar and the Reynolds number is very close compared to the previous analysis. Hence, the computed structural motion was expected to be in the neighbourhood of the previous computed amplitude.

The amplitude response is shown in fig. 4.14 and the aerodynamic force responses in fig. 4.15.

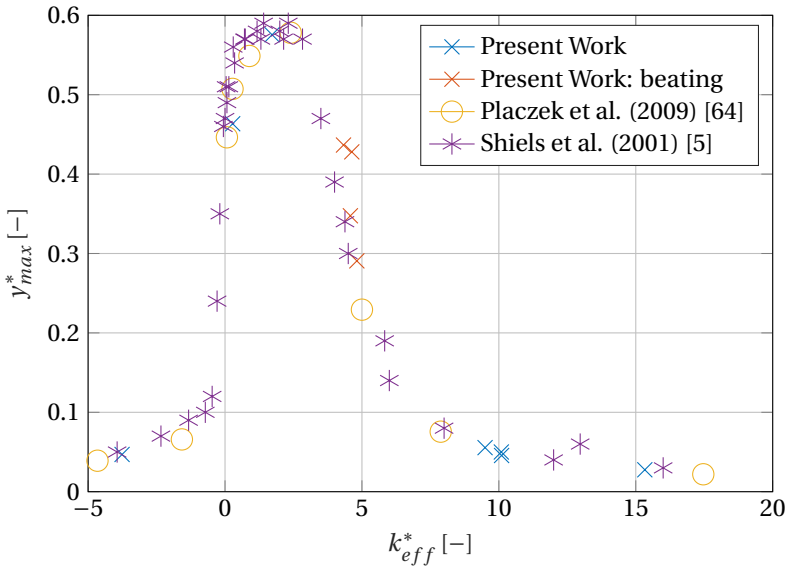

Figure 4.14. Non-dimensional amplitude (y^*_{max}) against the effective elasticity [5] (k^*_{eff}) at $Re = 100$

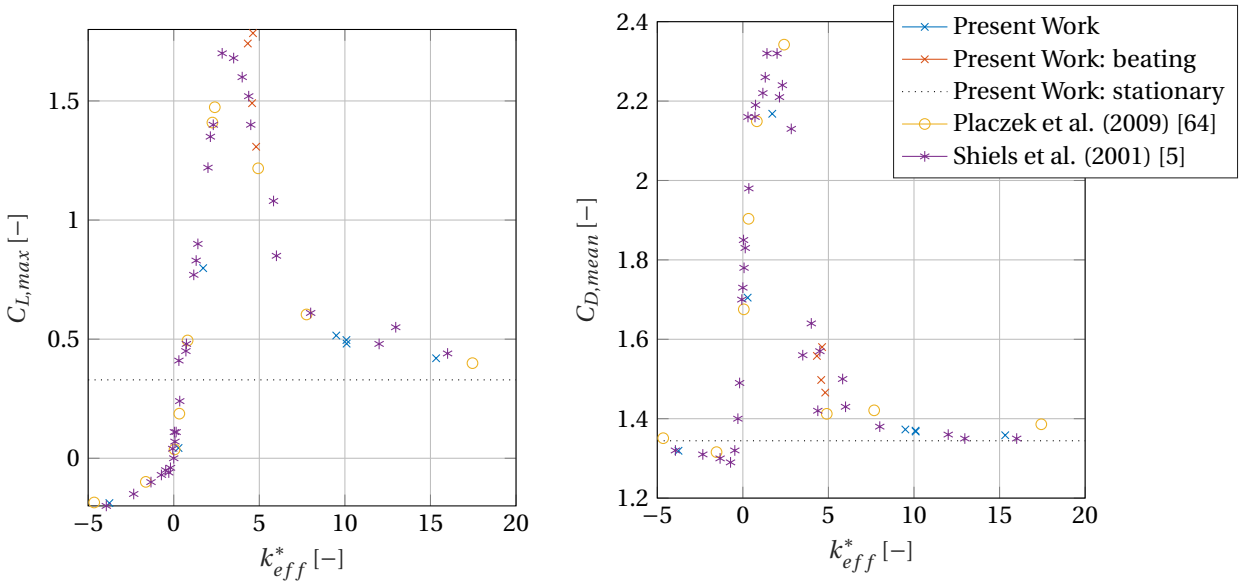

Figure 4.15. Lift coefficient amplitude $C_{L,max}$ and mean drag coefficient $C_{D,mean}$ against the effective elasticity (k^*_{eff} [5]) at $Re = 100$

The first observation from fig. 4.14 and fig. 4.15 is the fine agreement of the presently obtained results with the two numerical studies of [5] and [64]. Based on these figures, the lock-in region can be identified in the range of $0 < k^*_{eff} < 6$, where the oscillation amplitudes and aerodynamic forces experience a clear magnification. The maximum observed displacement amplitude was $y^*_{max} = 0.58$ at $k^*_{eff} = 1.72$. The simulations in the outer lock-out regions all reached steady-state and positive cylinder displacement. The observed amplitudes for $k^*_{eff} < 0$ and for $k^*_{eff} > 8$ are relatively low: $y^*_{max} < 0.05$. In these ranges, the mean drag coefficient tends to vary closely around the stationary mean drag coefficient found before. The lift amplitude shows the same trend for a positive k^*_{eff}, however, for negative values of the effective elasticity this does not hold up. This reason for this difference is that Shiels et al. [5] assumed $C_{L,max}$ to be negative for $k^*_{eff} < 0$, caused by the observed phase shift of π between the cylinder displacement and fluctuating lift.

Self-limiting mechanisms As was explained before in section 2.2.4, the vortex-induced vibrations are self-limiting at higher amplitudes. It was stated that this response is not caused by the structural damping but by the fluid-structure interaction. The self-limiting fluid-structure interaction was mostly observed at lower values of S_G in fig. 2.10, which means lower values of m^* or ζ. At these smaller values of the structural parameters, the cylinder was more susceptible to oscillations caused by the wake. The CFD model that has been used in the present research was verified under the circumstances of a relatively low mass ratio and damping ratio to see if the CFD model was able to reproduce these more challenging FSI cases. The self-limiting property of VIV has proven to be a very interesting feature which might appear at higher Reynolds numbers as well.

Previous investigations of the self-limiting effect show that various flow mechanisms come into play to limit the cylinder motion. It was found by Mittal and Kumar [96] that the self-limiting response is caused by the reduction in aerodynamic forces, the development of multiple frequency peaks rather than one and by having a *soft* lock-in [96]. Soft lock-in was defined in [96] as the operating range of the cylinder where the dynamic shedding frequency is not exactly equal to the natural frequency of the cylinder, while y^*_{max} and the aerodynamic forces are still considerably higher compared to the stationary case. It was stated by [96] that this phenomenon is so far only observed for light structures.

The results of the present simulation for free-vibrations have shown the three mechanisms limiting the cylinder motion amplitude, described by [96]. Fig. 4.16 (left subfigure), at $K^*_{eff} = 0.28$ (where $y^*_{max} = 0.46$), shows a second high-frequency PSD peak which has a smaller magnitude compared to the dominant peak. This second peak is located at exactly three times the dominant shedding frequency. The second PSD peak can also be observed in the lift coefficient time series in fig. 4.17. It seems that during every real period (which corresponds to the dominant peak) three secondary, weaker vortices are being shed. Two of these secondary vortex shedding periods are clearly shown. It is possible that the third high-frequency shedding period falls within the dominant shedding period which is why it is not shown in fig. 4.17. It was observed that the second high-frequency peak was not observed for the cylinder motion, which showed a fine harmonical trajectory. This second shedding peak was also seen in the numerical study [64, fig. 16, p. 96] for free-vibration and [64, fig. 13b, p. 92] for forced-vibrations when the oscillation amplitude in both cases was high. The study of [64] suggested that high amplitude oscillations can lead to additional high-frequency peaks. The periodicity within one real period (cycle-to-to cycle periodicity) is not affected by these components, while the shape is. Yet, it was found in the present study that this additional frequency component did not appear in all the free-vibration simulations were high values of y^*_{max} were observed. In fact, the process of multiple shedding peaks and the reduction of the aerodynamic forces appeared to go hand in hand. The detuning mechanism because of the soft lock-in was not always coherently present with the two other mechanisms described earlier. For example, the results of the two cases shown in tab. 4.5 and in fig. 4.16 and fig. 4.17 show this contradiction. The non-dimensional parameters used in tab. 4.5 and for the analysis of these results are based on the definitions of Shiels et al. [5], displayed in tab. 4.4.

Although both cases show considerably high steady-state amplitudes (y^*_{max}) and their operating conditions are close to each other (k^*_{eff}), the three self-limiting mechanisms are not present in both cases. Case 1 in fig. 4.16 shows a clear second frequency component in the power spectral density of the lift time series which agrees with one of the proposed self-limiting mechanisms of [96]. Case 2, right subfigure of fig. 4.16 does not show this second PSD peak. In fig. 4.17 the right subfigure clearly shows that the lift has reached a fine harmonical steady-state solution, with no additional shedding. Indeed, the lift amplitude for $k^*_{eff} = 1.72$ is found to be significantly higher compared to the case 1 with $k^*_{eff} = 0.28$. So far these observations would lead to the conclusion that case 1 has experienced a self-limiting structural feedback on the wake. This would also

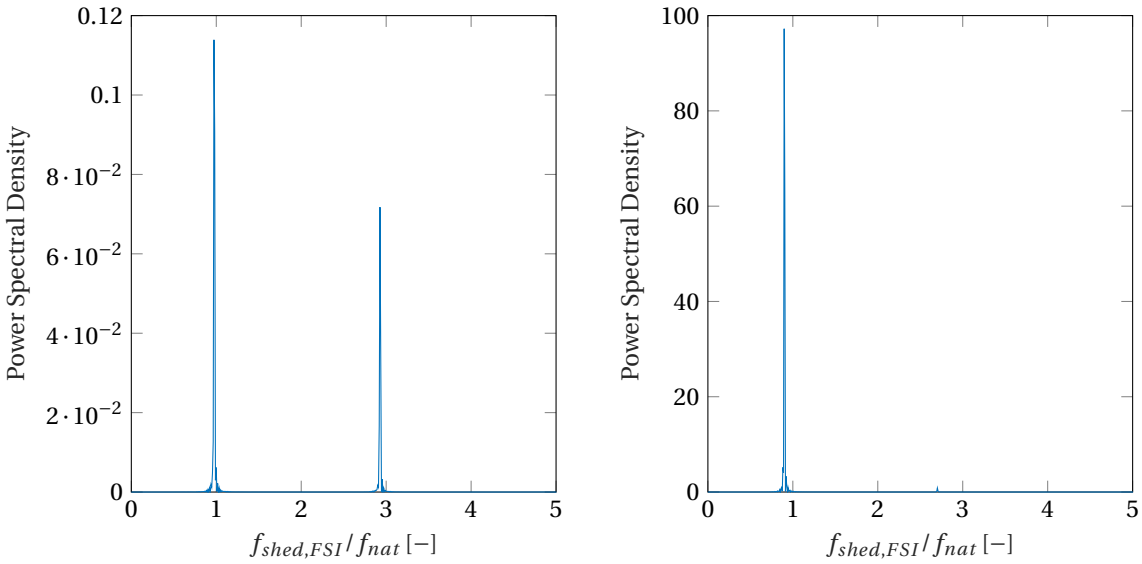

Figure 4.16. PSD of the lift coefficient time series, left for $k^*_{eff} = 0.28$ and right for $k^*_{eff} = 1.72$

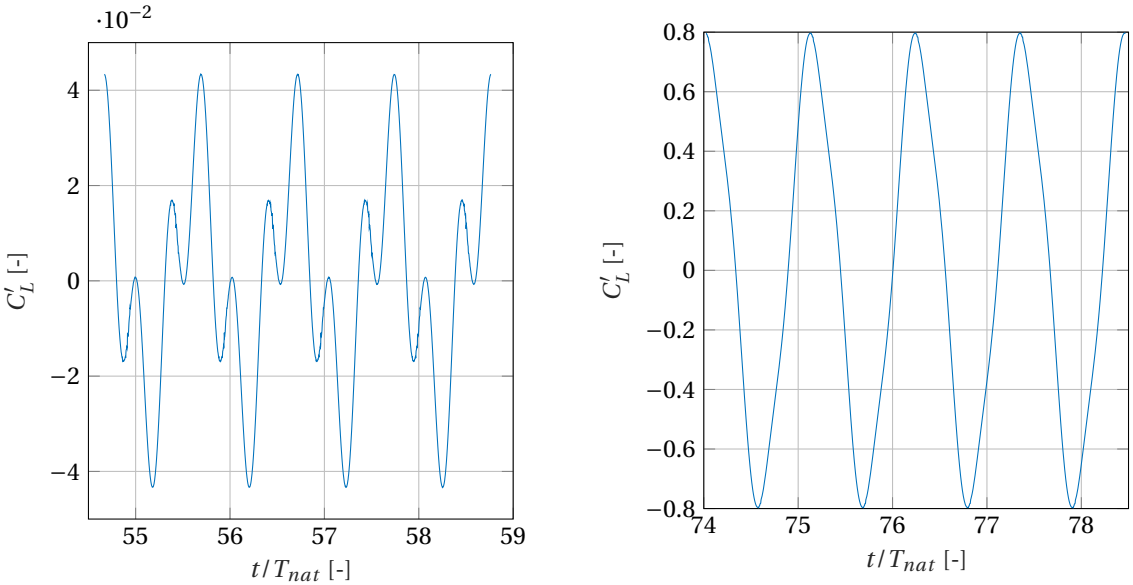

Figure 4.17. Steady-state fluctuating lift coefficient for four periods, left for $k^*_{eff} = 0.28$ and right for $k^*_{eff} = 1.72$

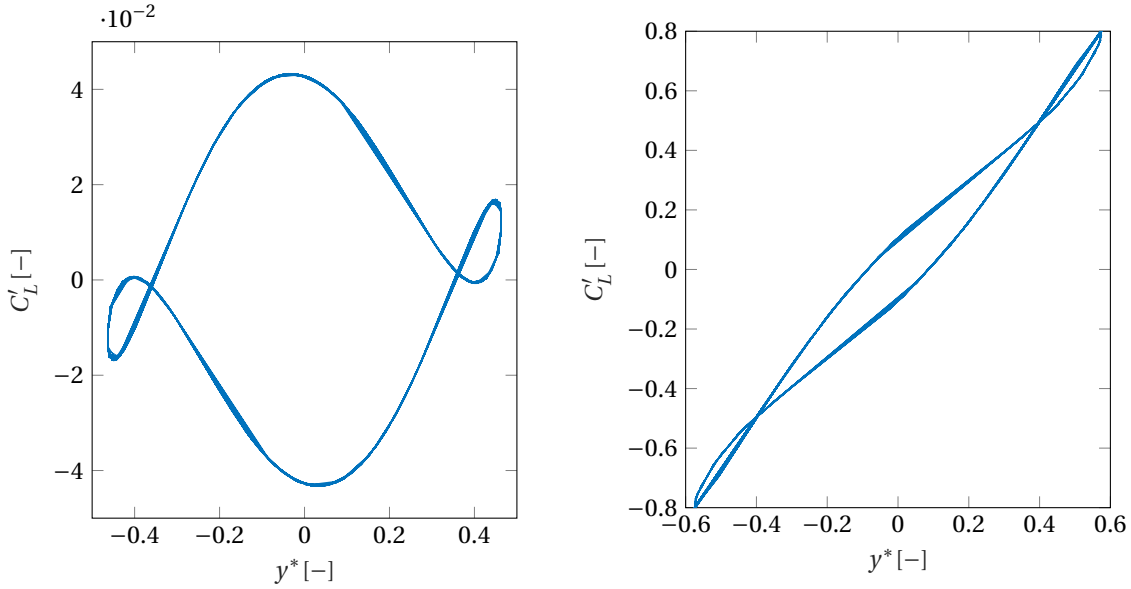

Figure 4.18. Phase portrait of non-dimensional cylinder motion amplitude against fluctuating lift coefficient, left for $k^*_{eff} = 0.28$ and right for $k^*_{eff} = 1.72$

imply that case 1 suffers from a soft lock-in. Yet, the frequency ratio f^* in tab. 4.5 proves that this assumption is not true. The detuning in case 2 has led to a softer lock-in compared to case 1. It is possible that this softer lock-in suppressed the magnification of the lift force from going to even higher values than currently seen in fig. 4.17 (right subfigure). It means that the proposed mechanisms of [96] causing the self-limiting property of VIV are not necessary false. It shows that in every case the wake and the structural response is rather unique and that the presence of the self-limiting mechanisms depends on the operating circumstances and how the fluid-structure interaction develops until it has reached the steady-state solution. Hence, the three self-limiting mechanisms described before are not always present simultaneously.

Parameter	**Case** 1	**Case** 2
U^*	1.03	0.76
m^*	5	5
ζ	0	0
k^*	4.74	8.74
k^*_{eff}	0.28	1.72
y^*_{max}	0.46	0.58
$C_{D,mean}$	1.71	2.17
$C_{L,max}$	0.04	0.80
$C_{L,y}$	0.0055	0.7125
$C_{L,\dot{y}}$	−0.0262	−0.06
$f^* = \frac{f_{shed,FSI}}{f_{nat}}$	0.97	0.90
$f^* = \frac{f_{shed,FSI}}{f_{shed,stat}}$	0.92	1.15

Table 4.5: Results for two free-vibration cases in lock-in

Lastly, when inspecting the phase portraits of both cases in fig. 4.18 the secondary vortex shedding is seen back in Case 1. The two additional, smaller ovoid figures around the maximum non-dimensional displacement show the secondary vortex shedding well. The phase portraits have been obtained over a multiple of 60 periods, which supports that both cases have reached equilibrium as their periodicity (and the trajectory of the phase portraits) is constant over time. The phase portrait of Case 1 implies that the cylinder displacement and lift force are out of phase while for case 2 the typical Lissajou figure shows that these two quantities are in phase. Furthermore, the estimated aerodynamic damping is relatively higher for Case 1 when compared against the lift force amplitude. This would imply that relatively more energy has been dissipated in the wake for Case 1 compared to Case 2.

Beating phenomenon The red cross-marks in fig. 4.14 and fig. 4.15 have been marked with a different colour than the other operating points because their time series of the aerodynamic forces and motion trajectory showed a beating phenomenon. The cylinder body showed a considerable motion amplitude during the beating, $0.29 < y^*_{max} < 0.4$. Moreover, the lift coefficient amplitude is also found to be relatively high for the beating range, as seen in fig. 4.15. Only the drag coefficient seems to fall within lower values, which are closer to the stationary results. The fluctuating lift and the PSD of the lift signal of one of the beating operating points have been shown in fig. 4.19. The reduced frequency was found to be $f^* = f_{shed,FSI}/f_{nat} = 0.74$ (see also right subfigure of fig. 4.19) and the other frequency ratio was $f_{shed,FSI}/f_{shed,stat} = 1.13$. The dominant peak in the PSD figure corresponds to one single lift period, i.e. the time after which the signal reaches the same magnitude of C'_L again, independent of the varying amplitude. Yet, the left subfigure of fig. 4.19 would suggest that the lift signal consists of multiple time periods. These other time periods have not been picked up by the PSD extraction. The numerical study of [97] faced a similar situation. It was argued in their study that the occurrence of an additional PSD peak depends on the degree to which the amplitude varies. The amplitude variation would be an indication of the beating energy. When this variation is stronger the PSD will more likely capture these secondary flow features. The amplitude variation of C'_L of the present results was not strong enough to yield additional PSD peaks. For more explanation on the decomposition of the lift signal into multiple periods, the reader is referred to the study of [64].

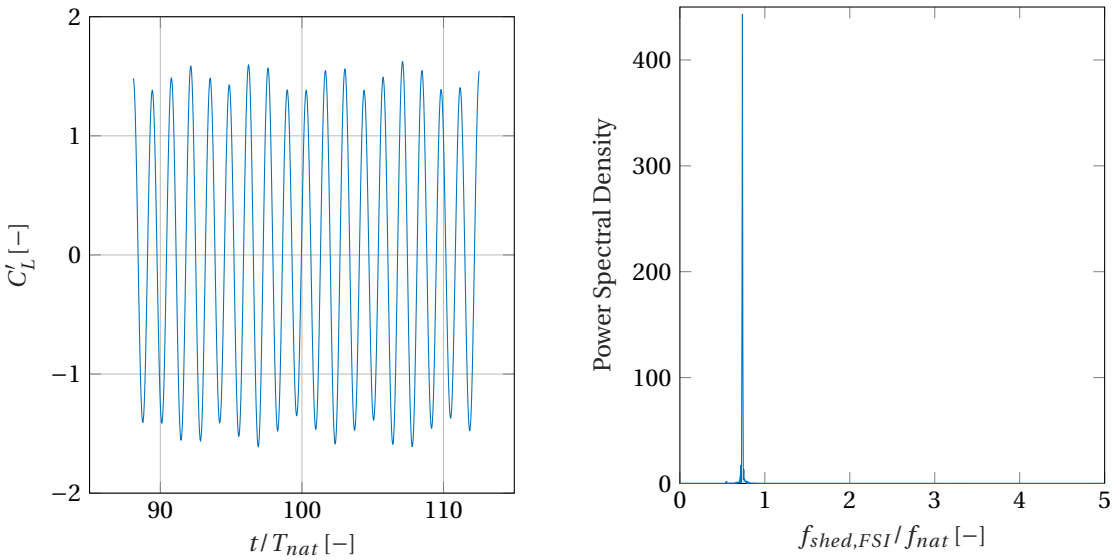

Figure 4.19. Beating phenomon for $k^*_{eff} = 4.58$, left subfigure is the fluctuating lift coefficient for a multiple of 18 periods and right subfigure is the PSD of the fluctuating lift coefficient

The frequency ratios $f^* = f_{shed,FSI}/f_{nat} = 0.74$ and $f_{shed,stat} = 1.13$ show that wake is neither following the natural frequency nor the stationary shedding frequency. The other operating points, the blue cross-marks in fig. 4.14 showed that the wake either tagged along with the natural frequency (lock-in, $0 < k^*_{eff} < 6$) or with the stationary shedding frequency ($k^*_{eff} > 8$ and $k^*_{eff} < -2$). In fact, it was observed that when the beating was more pronounced in the time series, that the shedding frequency of the moving cylinder deviated more from both the natural frequency and the stationary shedding frequency. This would suggest that

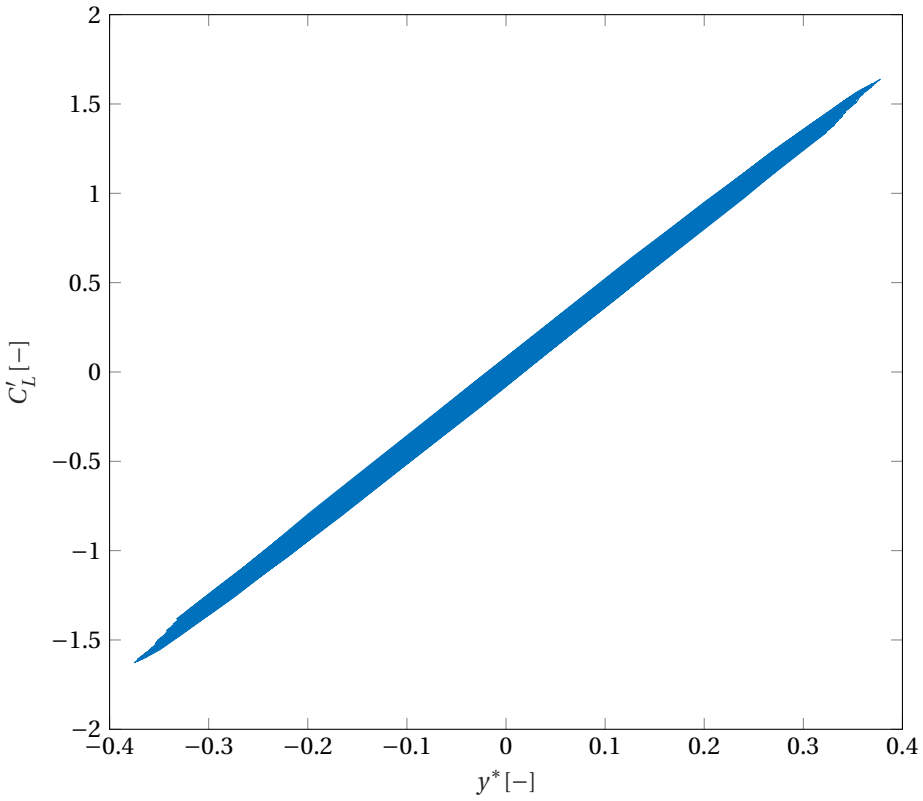

Figure 4.20. Phase portrait of non-dimensional cylinder motion amplitude against fluctuating lift coefficient when the cylinder is experiencing beating at $k^*_{eff} = 4.58$

the beating phenomenon can be described as a phase where nor the natural frequency nor the stationary shedding frequency dictates the vortex-induced vibrations. The operating range of k^*_{eff} was established by varying the natural frequency of the system. It can be concluded that during the beating, the natural frequency reached a value where it is still close enough to the stationary shedding frequency to trigger cylinder oscillations while at the same time not close enough to dictate the shedding process. This reasoning is in line with the earlier explanations found in the literature for the beating phenomenon [95]. According to [98] and [68], the beating phenomenon is related to intermittent stages of wake synchronization and desynchronization. After the wake is disordered, the lift force drops which also reduces the oscillations amplitude. Then, at a lower oscillation amplitude, the wake would become more stable again and more periodic. This would lead to a positive interaction between fluid and structure where both the cylinder amplitude and lift force rise again. These intermittent stages led to a non-harmonical time series of the lift and cylinder amplitude time series. It can be seen as a continuous 'battle' where the shedding frequency either favours the natural frequency or the stationary shedding frequency. This explanation of continuous (de)-synchronization during the beating was also given in the numerical study of [64].

Fig. 4.20 demonstrates the irregularity caused by the beating in the phase portrait of the fluctuating lift coefficient against y^*_{max}. For example, the phase portrait in fig. 4.18 (right subfigure) shows only one, unique trajectory while during the beating multiple trajectories have occurred during steady-state. These different trajectories are the consequence of the earlier observed changing behaviour of the lift force and cylinder motion for every period. Evaluating the aerodynamic damping or stiffness with eq. 3.55 and eq. 3.56 was therefore troublesome. In fact, the estimated $C_{L,\dot{y}}$ differed as much as $\approx 65\%$ when comparing the evaluation over just one period to a multiple of periods. Still, based on the phase portrait in fig. 4.20, the cylinder displacement was overall in phase with the lift force which yielded the increased $C_{L,max}$ and y^*_{max} in fig. 4.14 and fig. 4.15 of the beating operating points.

The beating phenomenon tends to show more chaotic behaviour in the time series which makes the verification of the time-dependent metrics harder. Typically, the peak amplitude of the lift coefficient and peak amplitude of the cylinder displacement are reported in VIV studies. These two quantities are therefore in-

stantaneous and more susceptible to vary compared to a periodic RMS values or time-averaged value. It is still possible to verify the outcome under such circumstances when comparing the time series directly. Yet, it is first hard to reproduce the conditions of a certain time series. Secondly, not many time series figures are available in numerical VIV studies. In the present report, the main goal of the laminar CFD cases is to verify the CFD model and to build up confidence for the more complex cases. Hence, these beating operating points might be more susceptible to false verification. Hence, the amplitude of the lift coefficient and cylinder displacement was deduced by taking the time-averaged value of all the minima and maxima observed in the time series. This has eliminated part of the arbitrariness nature of the beating signal. Although it is unknown how the results have been post-processing in the studies of [5] and [64], the beating points seem to match with their results in fig. 4.14 and fig. 4.15.

Lastly, two cases seemed to yield unstable conditions and lead to divergent results. These cases have not been included in the present report. The suspected cause of these operating points was in fact the weakly-coupled scheme, where the negative numerical damping resulted in an unstable coupling. Still, by manipulation of the structural parameters it was possible to reproduce stable coupling simulations for the complete range of k^*_{eff} that was used in the other numerical studies of [64] and [5]. This might be another benefit of the effective elasticity parameter. The same k^*_{eff} was reached while using different structural parameters. This gave more freedom to parametrize the VIV problem compared to for example the reduced velocity U^*, which does not collapse the non-dimensional spring-stiffness or mass. Furthermore, the reason why these operating points eventually diverged was most likely caused by the complication of the Newmark implementation within *OpenFOAM*, which was earlier explained in section 3.2. When the explicit symplectic structural solver was used in combination with the weakly-coupled FSI scheme, the cases did not diverge. Similarly, when the implicit Newmark structural solver was used in combination with the implicit FSI scheme, the cases did not diverge either.

The preliminary conclusion based on the 2-way weakly coupled simulations of the present work is that for a large part of the operating range, the VIV has been simulated accurately. In fact, it seems the model was able to capture the beating phenomenon an some of the self-limiting mechanisms adequately. Since the beating phenomenon is also expected for higher m^*, the verification of these operating points was important to show that the weakly-coupled solver is capable of capturing this more challenging phenomenon as well. Yet, the 'beating results' must treated with caution because of their more chaotic nature. Furthermore, the FSI model was able to capture the operating points inside lock-in and further outside lock-in well, compared to the literature. Lastly, it was noticed that some of the FSI scheme/structural solver combinations lead to divergence. These combinations were avoided in the turbulent moving simulations.

Non-dimensional analysis The non-dimensional parameters that were used are tabulated before in tab. 4.4. It was noticed during the research that when the non-dimensional values (of the study to be compared) were transformed into dimensional values, there was usually one degree of freedom left over. To see the effect of this on the solution, two Approaches have been performed to acquire the dimensional values. In the first Approach, the value of the inflow fluid velocity was assumed and was kept constant during the reduced velocity sweep. In the second Approach, the value of natural frequency was assumed and was kept constant during the reduced velocity sweep. These two assumptions can be seen as a starting point for obtaining all the dimensional values required to run the simulations. Four simulations have been performed to determine the reliability of the non-dimensional values and to see if there are differences in the results between the two Approaches. These four simulations have been denoted as Cases 1.1, 1.2, 2.1 and 2.2, see tab. 4.6. Case 1.1 and Case 1.2 represented the first Approach and Case 2.1, 2.2 represent the second Approach. All the four cases have been simulated before as well for the verification of the freely-moving model with the study of [65], see fig. 4.13. This time, the Approaches have been cross verified to see if the two Approaches affect the aerodynamic and structural response.

In the first Approach it was assumed that: $U = 1$ = constant. This led to a variation of the structural parameters of k and c while U^* was varied. Consequently, the natural frequency varied accordingly. The other relevant input parameters for *OpenFOAM*, m and ν were constant during the U^*-sweep. Case 2.1 and 2.2 have been used for the second Approach, where the natural frequency was assumed and kept constant in contrast to the first Approach. The natural frequency was chosen to match the stationary Strouhal frequency obtained earlier for $Re = 150$ (see fig. 4.5). In this Approach, all the structural parameters remained constant during the sweep (c, k, m). On the other hand, the inflow velocity U and the kinematic viscosity ν did vary for every U^* in this Approach.

Parameter	**Case** 1.1	**Case** 1.2	**Case** 2.1	**Case** 2.2
U^*	5	16	5	16
m^*	2	2	2	2
ζ	0.007	0.007	0.007	0.007
Re	150	150	150	150
$f_{nat}[Hz]$	0.2001	0.0625	0.1841	0.1841
$m[kg]$	1.57	1.57	1.57	1.57
$k_s[N/m]$	2.481	0.242	2.1	2.1
$c[N \cdot s/m]$	0.0276	0.0086	0.0254	0.0254
$U[m/s]$	1.0	1.0	0.9202	2.9456
$\nu[m^2/s]$	0.0066667	0.0066667	0.006134	0.01963733
$C_{D,mean}[-]$	2.05	1.28	2.06	1.27
$C_{L,RMS}[-]$	0.10	0.17	0.11	0.16
$y^*_{max}[-]$	0.52	0.07	0.53	0.07
$f_{cyl}/f_{nat}[-]$	0.95	2.70	0.94	2.65
$f_{cyl}/f_{shed}[-]$	1.03	0.92	1.02	0.90

Table 4.6: Results for two free-vibration cases inside (Case 1.1/2.1) and outside (Case 1.2/2.2) the lock-in band

The two Approaches can be summarized as follows:

1 In the Approach 1, the dimensional values are obtained by starting in the fluid domain and assuming a constant value for the free stream velocity. Hence, the structural parameters must vary to cope with the desired U^* sweep. In this Approach, the natural frequency is varied around the stationary Strouhal frequency. Lock-in was obtained when the natural frequency was close enough to the stationary Strouhal frequency.

2 In Approach 2, the dimensional values are obtained by starting in the structural domain and assuming a constant value for the natural frequency. This time, the fluid parameters must change for every U^* variation. In this Approach, the Strouhal frequency is varied around the natural frequency by changing the freestream velocity. If the Strouhal frequency is in the vicinity of the natural frequency, lock-in occurred.

Both methods in theory should produce the same results if the non-dimensional values are equal. This is one of the upsides of CFD: it allowed easy variation of different input parameters. In reality, it would be very hard for example to vary the kinematic viscosity in a wind tunnel. The results have shown that indeed the two Approaches yielded the same results. There are small differences observed but these seem to be acceptable. This supports the reliability of the non-dimensional values listed in tab. 4.4. This non-dimensional analysis is performed for the turbulent flow as well.

4.2. Turbulent flow

In this section, the results for the supercritical regime $Re > 3.5 \cdot 10^6$ will be presented. Similar to the previous section, the results of the stationary, forced- and freely-vibrating cylinder will be treated respectively in this section.

An important note must be made on the definition of 'turbulence' regarding the next section of this report. From a fluid dynamics perspective, turbulence is characterized as the flow which is highly unsteady, 3D, has fluctuations on a broad range of length and time scales and contains considerable vorticity levels [42]. Nevertheless, the term 'turbulence' has been used in the present report to identify the supercritical Reynolds number simulations which have been performed. In the present research only two Reynolds regimes have been investigated in which one of them the flow was mostly laminar (laminar regime) and one of them the flow mostly turbulent (supercritical regime). In that sense, the term was *turbulence* was used sometimes in this report merely to distinguish the 'turbulent' simulations performed at the supercritical Reynolds number and the 'laminar' simulations performed before at $Re < 200$.

4.2.1. Stationary cylinder

Firstly, a spatial and temporal refinement study was performed. The meshes m2.1 – 2.4 in tab. 3.3 have been used for the spatial refinement study. The temporal convergence study was done by using four timestepping schemes, which are reported after the spatial convergence study. There is no 'perfect' solution or benchmark case in this Reynolds regime both experimentally and numerically, as was noted by [54]. Hence, the convergence studies were performed relatively to the finest mesh or finest timestepping scheme. After the refinement studies, the results obtained with the present k-ω SST turbulence model were compared against the experimental and numerical work found in the literature. A compilation of the experimental and numerical work in the supercritical Reynolds regime is tabulated in tab. 4.12.

Study	**Re**	**Turb. Model/Exp.**	**Ti %**
Roshko, 1961 [25]	$1.5 \cdot 10^5 - 9 \cdot 10^6$	Exp.	?
Achenbach, 1968 [52]	$4 \cdot 10^5 - 5 \cdot 10^6$	Exp.	0.7
Jones et al., 1969 [2]	$5 \cdot 10^5 - 17 \cdot 10^6$	Exp.	0.2
Schewe, 1983 [99]	$2.3 \cdot 10^4 - 7.1 \cdot 10^6$	Exp.	0.4
Travin et al., 2000 [54]	$5 \cdot 10^4 - 3 \cdot 10^6$	3D DES	?
Catalano et al., 2003 [48]	$0.5 \cdot 10^6 - 4 \cdot 10^6$	3D k-ϵ	?
	$0.5 \cdot 10^6 - 2 \cdot 10^6$	3D LES	?
Ong et al., 2009 [49]	$1 \cdot 10^6 - 3.6 \cdot 10^6$	2D k-ϵ	0.8
Squires et al. [100]	$8 \cdot 10^6$	3D DES	?
Present Work	$3.6 \cdot 10^6$	2D k-ω SST	0.061

Table 4.7: Overview of experimental and numerical studies at supercritical Reynolds number.

Grid refinement study As was explained before in section 3.1.2, no wall functions have been used in the present turbulent simulations to predict the boundary layer. The flow field was resolved up to the viscous sublayer. For this reason, y^+ must be located within the inner layer, i.e. $y^+ < 5$ [101]. Increasing the Reynolds number makes the viscous sublayer thinner. Hence, in order to keep $y^+ < 5$ at even higher Reynolds numbers, the cell height at the wall had to be decreased. The present grid convergence study was performed at a constant Reynolds number of $Re = 3.6 \cdot 10^6$ and therefore the estimated $y_{wall} = 7 \cdot 10^{-6}$ was kept constant in all the meshes. This cell wall height aimed for a $y^+ = 1$.

Mesh	Grid Size	Co_{max}	ΔT_{mean}	t	y^+_{mean}
m2.1	69.069	0.7	0.00425	150 – 350	0.399
m2.2	98.730	0.7	0.00381	150 – 350	0.401
m2.3	176.635	0.7	0.00303	150 – 350	0.404
m2.4	314.186	0.7	0.00228	150 – 260	0.407

Table 4.8: Timestep size and y^+ variations for the four turbulent meshes

The mesh properties, the time discretization settings and other relevant CFD properties are summarized in tab. 4.8. As was explained earlier in section 3.1.2, the meshes were refined by a factor of $r = 1.33$ applied to the mesh edges. This led to roughly a doubling in the amount of grid cells. Like the laminar grid refinement study, the timestep was set adjustable and was constrained to a maximum Courant number of $Co = 0.7$. Except for the simulation with mesh m2.4, the other simulations have been carried out until $t = 350[s]$. Yet, it was observed that the effect of this on the aerodynamic quantities obtained with mesh m2.4 was negligible. Since in all four meshes the cylinder cell wall height was kept constant, the time-averaged mean y^+ value was also nearly identical in all four cases in tab. 4.8. This tabulated y^+ value was calculated after the simulation. The value was obtained by taking first the mean value of the y^+ distribution around the cylinder. Then, this mean value was time-averaged over the steady-state part of the simulation. It was thus concluded that the wall cell height at the cylinder estimated before yielded a sufficiently low y^+ value.

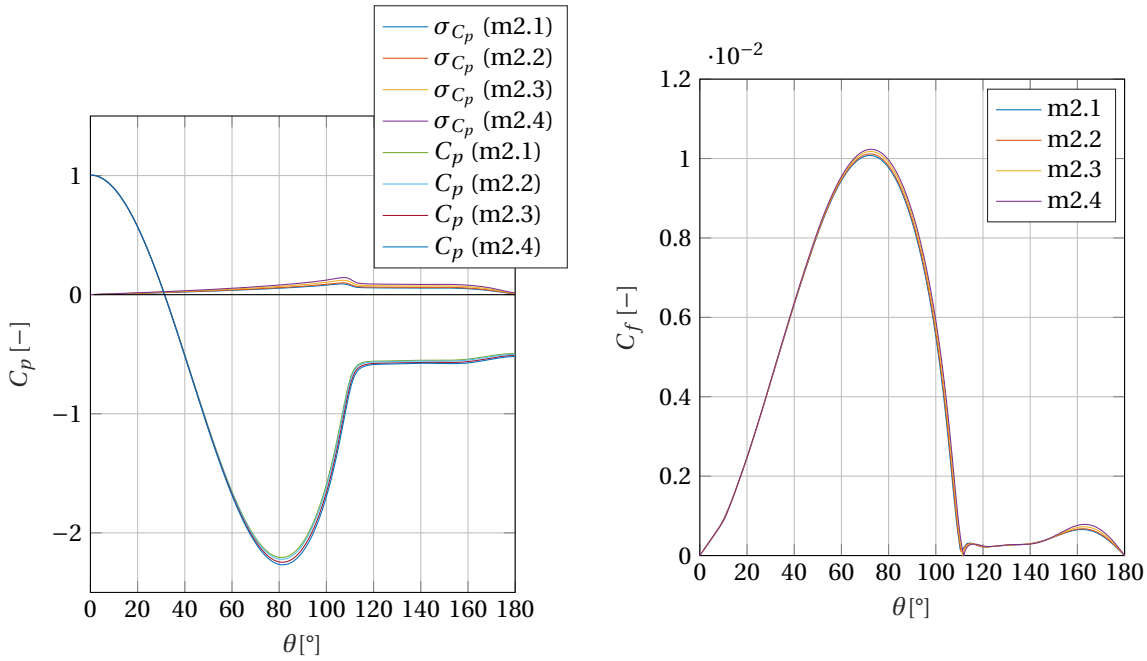

Figure 4.21. Pressure (left) and skin-friction distribution (right) for the meshes m2.1 – 2.4

The pressure coefficient distribution and skin-friction distribution for the meshes m2.1 – 2.4 around the cylinder wall are shown in fig. 4.21. The corresponding aerodynamic quantities have been tabulated in tab. 4.9. All the pressure and skin-friction curves around the cylinder wall show a nearly identical beginning part for $0° < \theta < 60°$. The curves start to deviate more around the minimum pressure peak/maximum velocity peak located at $\theta = 70 - 80°$. The pressure recovery shows a similar curve for all four meshes. Both the skin-friction and pressure distribution indicated that with every mesh refinement, the separation point was predicted more aft. This indication has been confirmed by the obtained separation angle, see tab. 4.9. Furthermore, the solution seems to converge to a more negative base-pressure coefficient. The standard deviation of the pressure coefficient (see eq. 3.40) shows that most of the cycle-to-cycle pressure fluctuations have been expe-

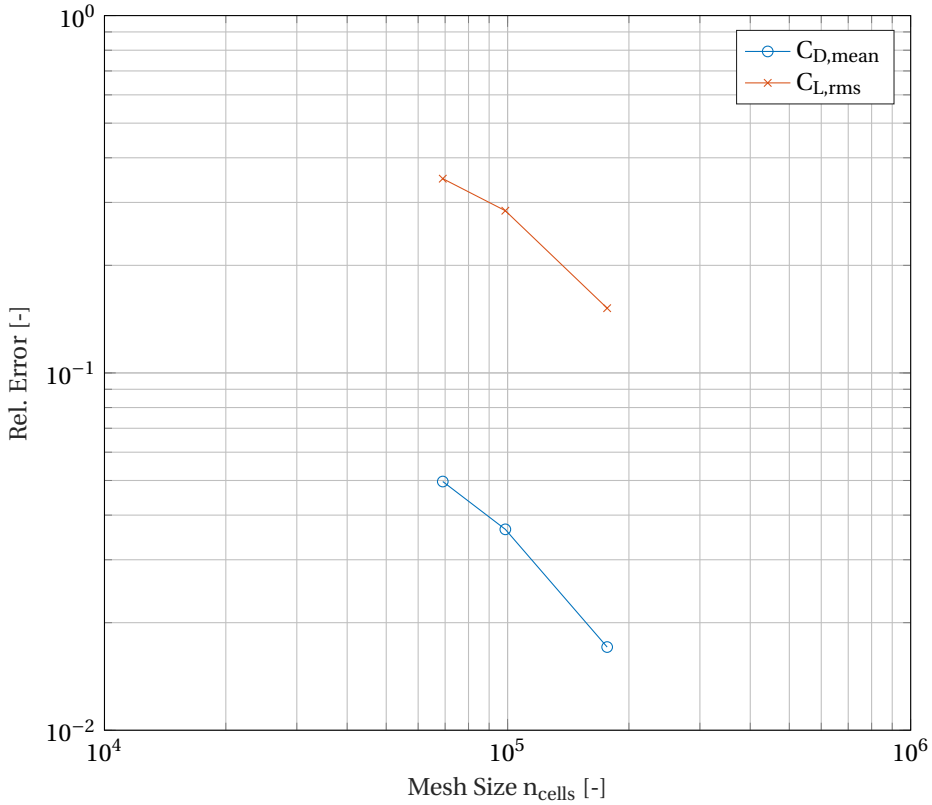

Figure 4.22. Log-log plot of the relative error of the mean drag coefficient and RMS of the lift coefficient compared to mesh 2.4 of tab. 3.3 versus the number of mesh cells

rienced around the separation point. It is interesting to note that with every mesh refinement, the standard deviation of the pressure coefficient increased. This can be explained by the fact that a finer mesh is able to resolve the flow field better and is therefore better capable of capturing the fluctuations of the flow around the cylinder wall. These variations in turn can lead to predictions of a varying separation angles over time and hence to different pressure distributions over time.

Mesh	$C_{L,rms}$	$C_{D,mean}$	St	$-C_{P,b}$	θ_{sep}
m2.1	0.0917	0.4114	0.323	0.4937	110.3
m2.2	0.1009	0.4171	0.324	0.5009	110.7
m2.3	0.1196	0.4255	0.323	0.5110	111.4
m2.4	0.141	0.4329	0.322	0.5195	111.8

Table 4.9: Aerodynamic quantities obtained for all four meshes

The RMS of the fluctuation lift coefficient and the mean drag coefficient have been used to perform the grid convergence study for the meshes m2.1 – 2.4. This study was done by the same approach as for the laminar grid convergence studies. The log-log plot is shown in fig. 4.22. Again, since no 'perfect' solution has been found in the literature to use as a reference value for the grid convergence study, the errors were taken relative to results obtained with mesh m2.4.

It was observed that the grid convergence slopes for the base-pressure coefficient $C_{P,b}$ was identical to the one shown for the mean drag coefficient $C_{D,mean}$ in fig. 4.21. This is in line with earlier observations in the literature where the base-pressure coefficient was found to have a considerable correlation with the mean drag coefficient [54]. The slope between meshes m2.2 – 2.3 are found to be $p = 1.30$ and $p = 1.08$ for

the drag and lift, respectively. Although the theoretical order of convergence might be a little bit smaller than $p = 2$ because of the first order convective turbulence discretization scheme used (see section 3.1.2), the found slopes are still considerably lower than was desired. The lower slope for the lift compared to the drag is in line with the earlier observations for the grid refinement study for the stationary laminar case. Unfortunately, after many attempts, higher convergence slopes were not obtained. Yet, as has been reported later, the obtained results do fall within the range of numerical data found in the literature. It might have been worth to pursue an even finer mesh with a size of around $\approx 1.5 \cdot 314.186$ to see if the mesh would eventually reach the asymptotic range. However, because of computational cost, mesh m2.2 has been chosen to pursue the research. The implied relative discretization error for this mesh is 3.65% and 28.44% for the drag and lift force, respectively. These high errors show as well that the asymptotic range was not reached with the grid refinement study.

Discussion on grid refinement study In this paragraph, a few modelling aspects are reported which could possibly explain why the grid convergence was not as good as desired. Based on decades of research it was stated in [101] that resolving the flow field up to the viscous sub layer could lead to grid-dependent solutions. It was argued that between the inner region and the outer (turbulent) region the flow field tends to fluctuate severely. These flow fluctuations require a very dense grid. In addition to that, the near-wall flow in the viscous sublayer is very viscous and therefore a wall damping function is required to model this correctly. These two modelling constraints imply a numerically stiff set of equations to be solved. This could lead to divergence of the linear pressure-momentum solvers or lead to grid dependent solutions. In the present flow problem, the flow separation had a very big impact on the flow field around the cylinder which has most likely introduced even more numerical difficulties for the turbulence model. All these imposed challenges made the model more susceptible to (discretization) errors which affected the grid convergence slope.

In the numerical study of [77], the accuracy of the RANS model with *OpenFOAM* was compared against the turbulent benchmark cases of NASA [71]. It has been concluded in their study that the grid convergence observed for the *OpenFOAM* simulations was slightly outperformed by the benchmark cases of other CFD solvers.

In the study of [102], values for the turbulent flow quantities reaching the cylinder wall were recommended to enhance the performance of the two-equation turbulence model. It was not expected that by achieving these recommended values the performance of URANS would have been enhanced significantly, since the presently observed ambient turbulent values at the cylinder wall were already close to the recommended values in the study of [102]. These ambient values and also the effect of the turbulence intensity on the aerodynamic forces will be addressed further ahead in section 4.2.1.

CFD studies in the literature (see tab. 4.7) on vortex shedding also experienced difficulties in obtaining grid convergence at these Reynolds numbers. In the study of [54], no grid convergence was achieved for their DES, even when the mesh was refined with a factor of 2 in all directions. It was argued in their study that they were running a 'complex numerical-physical system with numerous sources of error'. With refining the grid not all these errors were reduced which implied grid-dependence. Although the present URANS does not resolve the larger turbulence scales as with the LES part in the DES, it is still likely that turbulence modelling introduced additional discretization errors [76]. This could explain why the results are non-diverging but not as good as with the laminar cases before. Other numerical studies, [100], [56] were also not able to demonstrate a grid-independent solution for this complex flow problem. One study, [49], was actually able to produce grid convergence with an URANS $k-\epsilon$ model simulating vortex shedding at $Re = 3.6 \cdot 10^6$. Their computational domain had dimensions of $27Dx14D$ and consisted out of 48.706 cells, according to [49]. In the study of [49], wall models were used to predict the boundary layer flow. Since the Reynolds number is very high it is plausible to use wall functions instead of resolving the flow field up to the boundary layer, as the log-law layer extends far enough to be predicted by a model. Yet, it is known that wall functions do not predict flow detachment correctly. It was therefore maybe possible that their grid convergence was obtained because of the more robust wall functions (which are probably less susceptible to grid refinement). However, it is the question whether these results have converged to the right solution. Hence, it is still believed that it is the right choice not to use wall models for the present complex flow problem. The challenge should be to achieve the grid convergence while resolving the boundary layer up to the wall. Two recommendations will be suggested in the next paragraph which could be used in future work to overcome this challenge.

Recommendations for improving the grid convergence The first recommendation is regarding the eddy viscosity limitation in the URANS model. For vortex-shedding fluid problem, it is possible that the RANS model might lead to larger errors when the eddy viscosity is too high. It was specifically mentioned in the study of [102] that free vortices are a typical flow phenomenon where the accuracy might be affected by having a too high eddy viscosity value. One way to deal with this is to include an eddy viscosity limit. Currently, in *OpenFOAM* the eddy viscosity is unbounded. It was also noted by [102] this limitation should be done carefully, as it scales with the Reynolds number proportionally. It was observed in the present simulations for $Re = 3.6 \cdot 10^6$ that the eddy viscosity ratio can become as large as $\nu_t/\nu > 1 \cdot 10^5$. The option of a eddy viscosity limiter has not been pursued in this research and is therefore marked as a recommendation for other studies to look into.

Furthermore, it was believed that the mesh characteristics at the cylinder wall can be improved. Considering the mesh characteristics it was believed that the y^+ value was equal in all four meshes and always below 1. Yet, besides the cylinder wall cell height the cell growth rate at the wall is also an important characteristic in the present flow simulation. This ratio was equal to 1.2 in the present mesh, which was chosen such that the gradients in the sublayer were adequately resolved. Especially since the boundary layer flow in the present flow problem had such a severe impact on the overall solution, it makes sense to decrease this ratio to even closer values of 1 to enhance the accuracy at the wall even more. This is an idea for future CFD work on this complicated flow matter.

Domain Size The reason why this domain size has been used was explained before in the present report in section 3.1.2. Where the domain size chosen before was based on a study for laminar flows, it was of interest in the present research to investigate the effect of a smaller domain size on turbulent flow. For this reason, a smaller computational domain was created with the same mesh topology as was present in mesh m2.3. The same O-grid and mesh spacing was still in place in the smaller domain.

After inspection of the results obtained for the grid convergence studies, it became clear that the turbulent flow fields stopped to develop after $L2 \approx 25D$. After this, the wake field became constant. The eddy viscosity, μ_τ, was most critical in the estimation of the wake length and took the longest distance to fully develop. An outflow length of $L2 = 20D$ was chosen such that the wake had a reasonable distance to develop. This time, a second order scheme was used for the turbulence convective discretization which is in contrast to the earlier settings for tab. 4.9. The results of this comparison are tabulated in tab. 4.10.

Domain size ($L1xL2xL3$)	Grid Size	$C_{D,mean}$	$C_{L,RMS}$
$50Dx50Dx100D$	176.635	0.4551	0.2176
$10Dx20Dx20D$	176.635	0.4672	0.2393

Table 4.10: Effect of domain size on aerodynamic forces

Firstly, before the smaller domain was compared with the larger domain, it was already noticed that the mean drag and lift RMS have differed from the previous case in tab. 4.9 while the domain size and the grid size was equal to mesh m2.3. The reason for this difference is purely because of the turbulence discretization scheme, since all other CFD settings were kept the same. When inspecting the results of the different domain size in tab. 4.10, it was seen that the differences are considerable between the domain sizes. The mean drag increased by 2.7% and the lift RMS by 10%. It is not expected that change of the discretization scheme would change these increments. It is possible that an outflow length of $L2 = 20D$ was not adequate for the turbulent wake to develop as it did for the case where $L2 = 50D$. However, it is hard to explain how this has affected the overall solution of the aerodynamic forces around the cylinder. In addition, as was explained in section 3.1.2 that a boundary condition was used which should prevent reversed flow. Nevertheless, it was concluded that the domain size of $100Dx100D$ ensured the flow fields to fully develop. No further domain size studies were performed as this was already done in the literature for laminar flows, see section 3.1.2.

Temporal refinement study The effect of the timestep size on the results was investigated and reported on the turbulent case, with the same approach that was used for the temporal refinement study in the laminar case, see section 4.1.1. This meant that the timestep size was varied indirectly by changing the maximum Courant number. Four timestep schemes have been evaluated, i.e. $Co = 1.3, Co = 1, Co = 0.7$ and $Co = 0.4$.

Mesh m2.2 has been used for the temporal refinement study. The resulting (mean) timestep sizes are tabulated in tab. 4.11.

Timestep scheme	Co_{max}	ΔT_{mean}
t2.1	1.3	0.00706
t2.2	1	0.00544
t2.3	0.7	0.00381
t2.4	0.4	0.00218

Table 4.11: The four timestepping schemes used for the turbulent temporal refinement study

The effect on the RMS of the fluctuating lift coefficient and the time-averaged drag coefficient were plotted in the log-log format in fig. 4.23. The mean slopes are $p = 1.87$ and $p = 1.79$ for the lift and drag, respectively. These slopes are located close to the theoretical order of convergence which should be a little bit below $p = 2$. For the scheme t2.3, the relative errors are found to be 4.34% and 0.41% for the lift and drag, respectively. This scheme is still computationally feasible while the implied errors are considered as acceptable. Therefore, t2.3 has been chosen as the standard timestep scheme for all the turbulent runs (moving and stationary).

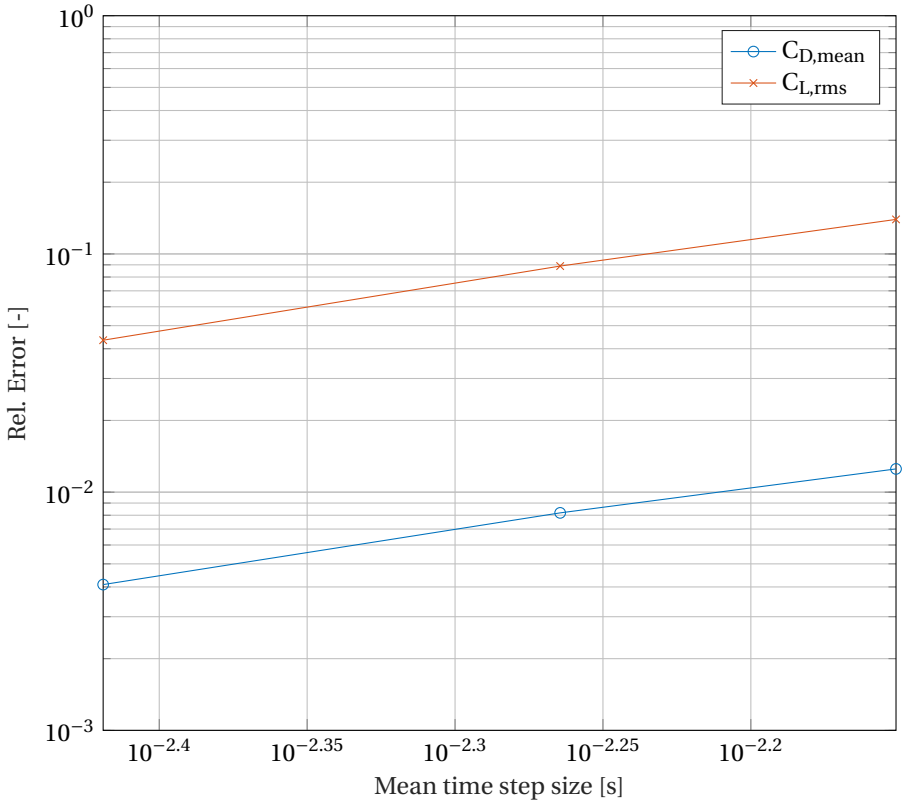

Figure 4.23. Stationary cylinder: log-log plot of the relative error of the mean drag coefficient and RMS of the lift coefficient compared to the finest timestep scheme t2.4 of tab. 4.11 against the time-averaged timestep size

As the slope is approaching $p = 2$ and as the relative errors are starting to stagnate, it may be concluded that these errors are in the asymptotic range and hence temporal convergence was obtained. This converging trend is in contrast with the outcome of the spatial refinement study before on the turbulent case. Although in the laminar cases spatial convergence was obtained, it is interesting to note that the temporal refinement in all cases (laminar and turbulent) showed a stronger convergence. These observations may imply that the

designed mesh was not perfectly suitable for the vortex shedding fluid problem. As the slope of spatial convergence in the laminar cases fell behind the temporal slopes, it is likely that this trend became more pronounced in the turbulent cases as more sources of error were introduced affecting the spatial convergence. Hence, in line with the earlier recommendations in section 4.2.1, it has been suggested for future research to carefully pay attention to the mesh generation and be very critical about the details as the fluid problem tends to be very sensitive. An example of the sensitiveness can be found in the previous section, where it became apparent that after only changing the turbulent discretization scheme, the lift and drag coefficient differed significantly. Also the change of these forces when the domain was made smaller was substantial.

Verification and Validation of Turbulence Model The experimental and numerical work used for verification and validation are listed in tab. 4.7. The obtained results have been compared quantitatively and qualitatively against the numerical and experimental work tabulated in tab. 4.12. In the quantitative part, typical aerodynamic quantities for vortex shedding have been evaluated. Differences between the present CFD simulation and the experimental work was expected a priori. Yet, it was deemed as important to see how big these differences are and to obtain an understanding how the URANS k-ω SST model would fall within the available state-of-art studies in the literature. Concerning the qualitative analysis, the skin friction coefficient and the pressure coefficient are evaluated around the cylinder body to analyze the boundary layer development. These two parameters have provided better insights to spot turbulence modelling differences or modelling errors between CFD and experiments. Besides the distinction between quantitative and qualitative analysis, the simulations have been performed at two Reynolds numbers: $Re = 3.6 \cdot 10^6$ and $Re = 8 \cdot 10^6$. These two Reynolds numbers have been evaluated because the operating range of the turbulent freely-moving case started in the supercritical Regime ($Re > 3.5 \cdot 10^6$) and extended up to a Reynolds numbers of $Re > 10 \cdot 10^6$. It was therefore deemed as necessary to assess the CFD turbulence model at two Reynolds numbers in the supercritical Reynolds regime. In the literature, it was believed, the highest Reynolds number for a CFD simulation on vortex shedding was $Re = 8 \cdot 10^6$ (see tab. 4.7). This has motivated to run an in-depth analysis at $Re = 8 \cdot 10^6$. Besides the assessment, it was indicated before that the supercritical regime is a rather novel CFD research area because of its large implied computational cost. Hence, the detailed analysis allowed to offer new insights in to the complex flow features present in these Reynolds numbers. For example, the effect of the Reynolds number on the boundary layer in the super critical regime has been addressed. The observed boundary layer development has been related back to trends postulated earlier by other studies or to classical boundary layer theory.

The most relevant studies and their results are tabulated in tab. 4.12:

Study	Re	St	$C_{D,mean}$	$C_{L,rms}$	$C_{P,b}$	θ_{sep}
Exp. [52]	$3.6 \cdot 10^6$	0.25	0.76	?	≈ -0.81**	115°
Exp. [2]	$3.5 \cdot 10^6$	0.24	0.58	0.07	≈ -0.65**	≈ 125**
	$8.27 \cdot 10^6$	0.29	0.58	0.08	≈ -0.57**	≈ 106**
2D k-ϵ URANS [49]	$3.6 \cdot 10^6$	0.31	0.46	0.08	≈ -0.54**	114°
DES [54]	$3 \cdot 10^6$	0.35	0.41	0.06	-0.53	111°
DES [100]	$8 \cdot 10^6$	0.37	0.37	?	≈ -0.48**	114°
Present Work	$3.6 \cdot 10^6$	0.32	0.42	0.1	-0.5	111°
	$8 \cdot 10^6$	0.34	0.36	0.08	-0.45	114°

Table 4.12: Measured and predicted results by most relevant studies of tab. 4.7. The values marked with ** have been estimated indirectly based on the available pressure distribution where the constant pressure plateau was reached.

From a first observation it is shown in tab. 4.12 that the obtained results from the present work are in good agreement with the numerical studies. Especially with the two DES studies, the present URANS k-ω SST simulation compared well. The Strouhal number and lift RMS quantities differed slightly. The reason why

the two DES studies agreed better with the present URANS model rather than the other URANS model will be explained in the subsequent section by visualizing the pressure distribution and skin friction coefficient. With regards to the experimental studies, the measured Strouhal number was generally lower, the measured mean drag coefficient higher while the lift RMS agreed fairly well. As the turbulent freely moving cases were constrained to only move in the transverse direction, it was more important that the lift force had good agreement with the experimental and numerical work. Besides the lift coefficient, the Strouhal number was also of interest for the moving cylinder cases. The Strouhal number resembles the frequency of the lift force that would excite the cylinder body to vibrate. It must be taken into account that this Strouhal number is lower in reality, which could initiate different structural responses. The correlation between the base-pressure coefficient and mean drag becomes clear again in tab. 4.12. Because of a lower base-pressure, the drag tends to go up proportionally. The separation angles are all within an acceptable range, meaning the location of flow separation was predicted well by the numerical simulations.

Skin-friction Distribution at Re = $3.6 \cdot 10^6$ The skin-friction coefficient distribution at $Re = 3.6 \cdot 10^6$ is displayed in the left graph of fig. 4.24, together with the numerical studies of [54], [49], [48] and experimental work of [52]. In [54], the flow field was predicted by a detached-eddy simulation. The one-equation Spalart-Allmaras model was used as turbulence model for their URANS modelling (with wall functions). The S-A model is known for its good prediction of boundary layer flows exposed to a pressure gradient. The results of [48] were obtained by a 3D large-eddy simulation (LES) and by a 2D URANS model for the study of [49]. The latter simulation was based on the two-equation k-ϵ turbulence model. It has appeared that the skin-friction coefficient obtained with the present URANS model fell below the obtained values with the DES and the LES. Also, the skin-friction coefficient does not reach negative values implying URANS did not simulate a reversed boundary layer flow where all other simulations did predict negative values after separation. The skin-friction coefficient showed an increment for $\theta > 140°$ which the DES did not predict. The same increment was predicted by the other LES and URANS model. Except for the other URANS of [49], the present URANS model agreed qualitatively well with the LES and DES results. It seems that the LES simulation is closer to the DES simulation in terms of magnitude, but it seems the LES predicted the separation phenomenon better. Nevertheless, the present URANS model and the other numerical simulations predicted a similar separation location as the one seen in the experiment of [52](see tab. 4.12). The separation phenomenon has been predicted similar with the present URANS model compared to the DES study.

One of the modelling errors, caused by a wrong modelling assumption, immediately comes to light when inspecting the left graph of fig. 4.24. The predicted skin friction coefficient by all the numerical studies is significantly higher compared to the measured values by the experiment for $\theta = 0-90°$. The problem with the present turbulence modelling is that all the flow is assumed to be turbulent (laminar flow or transition was not considered in the model). The absence of the laminar flow prediction in the numerical studies is causing the skin friction coefficient to be significantly higher compared to the real flow. In fact, it is well established (see [16] and [103]) that for laminar boundary layers the skin friction coefficient is lower compared to turbulent flow. This difference is caused because in laminar flow the velocity gradient at the wall tends to be lower while the vortices in the boundary layer of turbulent flow lead to a higher velocity gradient and hence more shear stress at the wall. It was also argued before by [54] and [48] that the over-prediction of the friction coefficient is caused by the fact that laminar flow at the beginning part of the cylinder wall was not taken into account in the modelling at all.

In contrast to URANS and DES, the transition point was captured by the experiment of [52] at $\theta = 65°$, 'indicated by a small rise and a following retarded drop of the skin friction distribution'. The small jump is caused by the added vorticity caused by the transition to turbulence while after transition the coefficient still drops because of the favourable pressure gradient. This transition point is located rather far from the stagnation point, indicating a large modelling error for URANS. It must be noted that the relatively low inlet turbulence intensity used in the experiment of [52] might have contributed to transition point being located rather far away from the stagnation point ($Ti = 0.7\%$, see tab. 4.7). The transition point was not given in the other experimental studies listed in tab. 4.7.

The skin-friction coefficient predicted by the URANS of [49] is about half the magnitude of the other simulations before separation which is surprisingly. Their results seem to have performed as best compared to the experimental data. Yet, it is questionable whether this agreement is a good sign as in their modelling the flow was assumed to be fully turbulent as well. The k-ϵ turbulence model is known for its poor performance when predicting fluid separation and strong pressure gradients. This could explain why the URANS results of [49] under-predicted the skin-friction coefficient for the turbulent flow which in fact enhanced the agreement

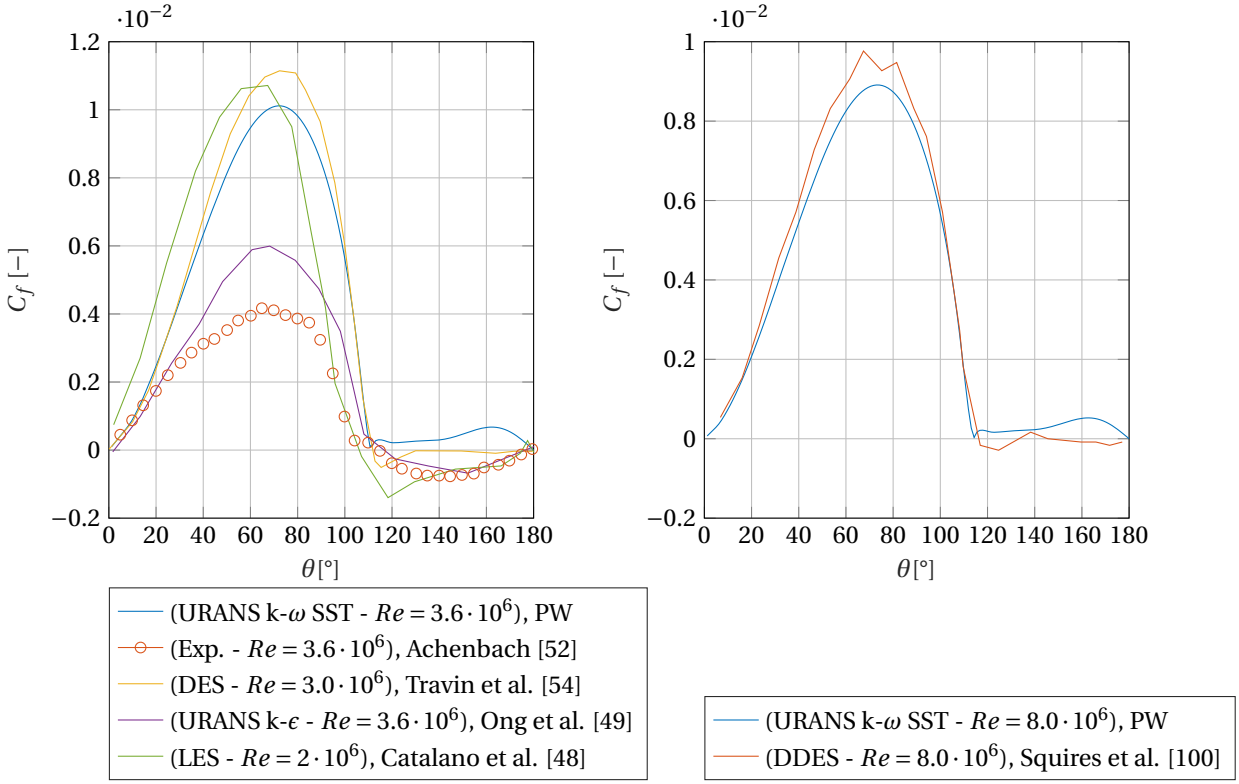

Figure 4.24. Time-averaged skin-friction distribution around the cylinder compared to various numerical and experimental work of tab. 4.7

with the experiment. Their predicted separation angle is closer to one measured by [52], see tab. 4.12. Nevertheless, the S-A model (even with wall functions) and the present k-ω turbulence model are better suitable for boundary layer prediction and hence the predicted skin-friction distribution of [54] was interpreted as more reliable for comparison. Tab. 4.12 shows that the predicted separation angle was equal to the one found with the DES. It is believed that, although deviations with the experiment are present, the presently used URANS $k-\omega$ SST model without wall functions was reliable. The numerical results of the DES and LES simulation shown in the left graph of fig. 4.24 support this argument.

The numerical study of [53] investigated the usability of a transition model coupled to the k-ω SST model for the flow prediction around a circular cylinder in the transitional Reynolds regime ($Re = 8.5 \cdot 10^6$). In their study, it was shown that the augmented CFD model indeed predicted the skin-friction coefficient better than the standard k-ω SST model. On the other hand, the LES model in the study of [48] predicted the flow separation and recirculation region rather well while their upstream skin-friction was over-predicted as shown in fig. 4.24. This shows that the upstream modelling errors did not have a significant impact on the flow separation prediction.

Skin-friction Distribution at Re = 8.0 $\cdot 10^6$ In the right graph of fig. 4.24, the skin-friction coefficient at $Re = 8 \cdot 10^6$ was plotted together with the numerical work of K. Squires et al. [100]. In an attempt to asses a new DES version, known as delayed detached-eddy simulation, [100] performed multiple simulation on a circular cylinder at $Re = 8 \cdot 10^6$. In their numerical study, the original DES version was based on the Spalart-Allmaras eddy-viscosity turbulence model in URANS. The skin-friction coefficient was only computed for the newer DES model. The skin-friction coefficient was overall higher predicted by [100] than the present URANS k-ω SST simulation. The predicted separation angle again agreed well with the predicted one by [100], i.e. $\theta_{sep} = 114°$. This shows again that the present k-ω SST model is performing similar as the DES model with the S-A URANS implementation. The rise and fall of the skin-friction coefficient seems to be in good agreement as well. After the separation it seems that reversed flow has been simulated by the LES part in the DES of [100] while with the present simulation this was not captured.

Effect of Reynolds number on Skin-friction Coefficient With a higher Reynolds number, the air flow has more momentum. This would lead to two effects [103]:

1 The higher momentum leads to a thicker boundary layer and hence the velocity gradient tends to decrease. This in turn would lower the skin-friction coefficient. When comparing the skin-friction distribution for $Re = 8 \cdot 10^6$ to $Re = 3.6 \cdot 10^6$, there is indeed a decrement of the skin-friction coefficient.

2 At the same time, a higher Reynolds number would lead to earlier transition and more turbulence. Hence, the boundary layer is more dominated by turbulent flow which would increase the skin friction. Yet, in the present simulation this effect is not captured and therefore the skin friction coefficient only decreased.

The decrement of the skin-friction coefficient with increasing Reynolds number was also observed in the numerical studies of [49] and [48]. Yet, these decrements of the skin-friction coefficient are relatively small and therefore it was deemed as plausible to compare the friction data found in [48] at $Re = 2 \cdot 10^6$ with the present results at $Re = 3.6 \cdot 10^6$ as long as the drag crisis does not start to play a role in the simulation.

Pressure Distribution at Re = $3.6 \cdot 10^6$ The pressure distribution for $Re = 3.6 \cdot 10^6$ has been plotted in the left graph of fig. 4.25, together with the experimental work of [2], [52] and the numerical work of [54] and [49]. The standard deviation of the pressure coefficient from the present work is shown as well in fig. 4.25. At $\theta = 0°$ the pressure coefficient was found to be $C_p = 1$, which was expected at the stagnation point where the dynamic pressure is equal to zero. When comparing the results to the numerical work of Travin et al., the agreement is good. The predicted pressure distribution agreed better with the DES results of [54] compared to the skin-friction coefficient. A small under-prediction is observed for the first 90° and after that for $\theta = 90-110°$ a small over-prediction is observed. The same deviations between the URANS of [49] are present when comparing to the DES. Flow separation is shown by the constant pressure plateau for $\theta > 110°$. For the last part of the cylinder body ($\theta = 110-180°$), the pressure plateau is nearly identical to the one of Travin et al. except for the very last part of the cylinder (the base-pressure coefficient). There, the pressure increased slightly obtained with the present simulation while the other numerical simulations showed a constant plateau. The measured base-pressure coefficient at $\theta = 180°$ is $C_{p,b} = -0.5$ for the present simulation and $C_{p,b} = -0.53$ was obtained by [54], as show in tab. 4.12. This difference is caused by the pressure increment at the very last part of the cylinder. It was not expected that this error was caused by the time filter or by the interpolation method for obtaining the C_p-distribution. A time-averaged value during steady-state was taken and the obtained standard deviation shows that at this part of the cylinder no significant deviation was present. The pressure coefficient at the stagnation point was equal to 1 which supported that the interpolation method was right. In fact, it might be an error which is more related to the turbulence model. The small pressure bump at the base of the cylinder was also observed in the study of [54], see [54, fig. 8b, p.304]. The URANS of [49] predicted a more constant pressure plateau after separation. Nevertheless, the three numerically obtained base-pressure coefficients are close to each other (especially when the constant plateau value is compared). This shows again that the obtained results from the present URANS model fall within the range of numerical data at $Re = 3.6 \cdot 10^6$.

Compared to the experimental work of [2] [52], the numerically predicted pressure coefficient agrees well in the front part of the cylinder for $\theta = 0-63°$. After that, the numerical values show an earlier pressure recovery at $\theta \approx 80°$ and a less negative C_p peak. It was shown before that the transition point of the boundary layer was identified at $\theta = 65°$ for $Re = 3.6 \cdot 10^6$ by [52]. It seems that the pressure distribution started to deviate around this point, which could indicate that the transition had an impact on the pressure distribution. The boundary layer in the experiment of [2] continued to decelerate further aft (at $\theta = 90°$) which explains why the separation also occurred later in their measurements. The numerically predicted base-pressure coefficients were slightly higher than the experimental values and therefore they fell outside the range of experimental data. This is also seen back in tab. 4.12 where the measured base-pressure coefficients by the experiments were overall more negative. This also explains why the mean drag coefficients were overall higher for the experimental measurements compared to the numerical studies in tab. 4.12. This might indicate the numerical models still fall short in predicting the detached flow accurately. This in line with the observations made in the study of [73]. There it was shown URANS failed to capture the separation phenomenon correctly, while their LES results were more promising. Comparing their study must be done with caution, as their simulation was performed at a Reynolds number of $Re = 48.000$ which is a different regime. The LES of [48] was performed in the transitional regime and also in their study the LES predicted the separation phe-

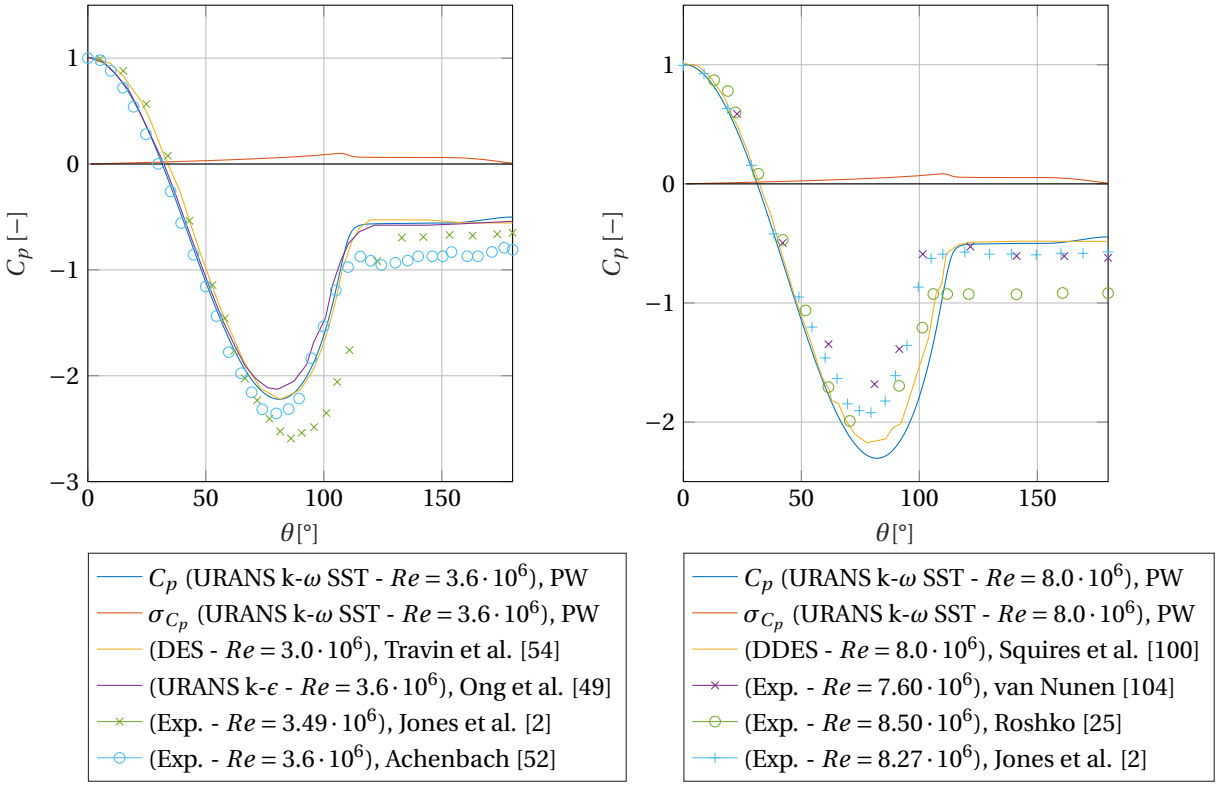

Figure 4.25. Time-averaged pressure distribution around the cylinder compared to various numerical and experimental work of tab. 4.7

nomenon better compared to URANS. Their predicted drag coefficient agreed better with the experimental values, showing promising results for LES.

Although the flow was assumed to be fully turbulent, it was suspected URANS did not predict some of the crucial larger turbulent detached eddies in the near-wake region. This possibly lead to a predicted wake which was too thin for its Reynolds number (compared to the experiments). This in turn lead to a lower drag coefficient (together with the larger base-pressure coefficient) and to a smaller bulk of recirculating flow in the low-pressure wake. This latter effect could have led to a higher vortex shedding frequency, enhancing the Strouhal number. The thinner wake predicted by URANS would explain the overall lower drag coefficients and larger Strouhal numbers for the numerical studies compared to the experimental values in 4.12. The suspected thinner wake has not been confirmed by comparing the flow field in the wake region between the CFD results and the experiment.

Pressure Distribution at Re = 8.0 ·10^6 Inspecting the right graph of fig. 4.25, the predicted pressure distribution agreed well with the DES of [100]. Except the negative pressure peak and the base-pressure coefficient differed slightly. The deviation found around $\theta = 80 - 90°$ was found before for the skin-friction coefficient as well. Again, the pressure decay predicted with the CFD simulations for the front part of the cylinder is similar to the experimental data, as was for $Re = 3.6 \cdot 10^6$.

It seems that the base-pressure coefficient of the numerical simulations did not fall within the range of experimental data. For $Re = 8.0 \cdot 10^6$ it appeared that the pressure plateaus observed for the experimental data at the most aft part of the cylinder remained more constant compared to the experimental data at $Re = 3.6 \cdot 10^6$. In the latter case, the pressure coefficient seemed the increase slightly at the aft part of the cylinder. The numerical data at $Re = 8.0 \cdot 10^6$ show a slight increment at the most aft part of the cylinder, in contrast to the experimental data. This could explain why the base-pressure coefficients were overall higher for the numerical studies compared to the experimental results at $Re = 8.0 \cdot 10^6$. This might indicate that URANS was not able to predict the more chaotic detached flow accurately, leading to a slightly inaccurately predicted pressure-distribution at the aft part of the cylinder.

It has been argued before in chapter 2 that the accuracy of the URANS model would improve with higher Reynolds numbers. The portion of turbulent boundary layer flow around the cylinder becomes bigger when the Reynolds numbers is increased. Yet, when comparing the left and right graph in fig. 4.25 it is difficult to draw a conclusion on how well both cases agree with the experimental work. While separation was predicted rather early compared to the experiments at $Re = 3.6 \cdot 10^6$, the opposite was true for $Re = 8 \cdot 10^6$. In this case, the separation point was predicted more aft compared to the experimental work. Because there is still laminar flow present in the experimental studies, it is possible that this made the boundary layer more prone to separate compared to the fully turbulent flow in the CFD simulations. Yet, this effect was not present at $Re = 3.6 \cdot 10^6$.

Standard Deviation of Pressure Coefficient The cycle-to-cycle variation was mostly present around the separation point, which was expected. It means that every cycle, the fluid separation angle slightly shifts front and backwards on the cylinder which yields a slightly different pressure distribution. It has also been noted that the standard deviation before separation generally seems smaller compared to after the fluid separation. The flow field inside the wake has a more chaotic nature because of the low-pressure region which attracts reversed flow and also because the larger eddies start to form here to trail aft. This flow field here is more random over time, although the URANS equations inherently averages out these more fluctuating quantities and models the complete turbulence spectrum. Hence, the output signals of the lift and drag force are still harmonical.

Conclusion on Turbulence Model Although there is no prefect agreement with the experimental data in the literature, the turbulence model was considered to be reliable. The pressure and skin-friction distributions have shown that the presently obtained results agree well with the other state-of-the art numerical studies in the supercritical regime. Only the skin-friction results obtained with the k-ϵ model differed considerably with the presently obtained distribution. It was expected that these deviations are caused by the turbulence modelling differences. The present URANS model agreed well with two different DES studies in the supercritical regime and agreed fairly well with one LES study found in the transitional regime. So far, it therefore seems DES is not able to provide more accurate results compared to URANS. When a higher fidelity approach is desired than URANS, LES would be the recommended model. The LES of two different studies indeed demonstrated this approach was better able to predict the separation phenomena, leading to more accurate results for the vortex-shedding problem. No LES studies have been found in the supercritical regime (the study of [48] was in the transitional regime).

Since the moving domain was only dedicated to the transverse degree-of-freedom, the lift force and Strouhal number were considered to be the most important quantities. The predicted lift coefficient and separation angle agreed well with the experimental values, while the drag coefficient and Strouhal number deviated considerably. The Strouhal number predicted by the URANS model should therefore be treated with caution in the moving domain. Overall, it was concluded the present turbulence model was reliable to pursue further simulations in the moving domain.

Wake analysis The vortex wake pattern observed in fig. 4.26 is known as the 2S wake pattern, as defined by the study of [15]. The 2S wake pattern compromises two single vortices, both being shed from the cylinder for each oscillation cycle or shedding period T_s. This pattern is also known as the classical Von Kármán street.

The instantaneous wake vorticity has been plotted in fig. 4.26 for one shedding period T_s. It can be observed that the top left subfigure is the mirror image of the bottom left subfigure and the same holds for the top right and bottom right subfigure. Hence, there is a clear vortex pattern visible in these figures. Fig. 4.26a is in good agreement with the vorticity contour shown in the numerical study of [49] at $Re = 3.6 \cdot 10^6$, obtained with a 2D URANS k-ϵ model, see [49, p. 149, fig. 6]. Fig. 4.26c is in good agreement with the vorticity contours shown in the numerical study of [48] obtained with a 3D URANS k$-\epsilon$ model at $Re = 1 \cdot 10^6$, see [48, p. 466, fig. 4]. In the latter study, instantaneous vorticity contours obtained with a LES was also shown. It was observed, although some coherent structures were visible, that the LES simulated a more chaotic wake with no clear vortex pattern. This was because the LES captures more of the realistic flow features typically present in the transitional regime $1.5 \cdot 10^5 < Re < 3.5 \cdot 10^6$. Yet, since all the turbulence is modelled within URANS, these rather complex flow features were not captured by URANS. It is for this reason that URANS predicts a more coherent vorticity structure in the wake, both in the transitional and supercritical regime. In other words, URANS is not sensitive to the drag crisis (which leads to large modelling errors). The numerical study of [100] presented an instantaneous vorticity plot by their DES approach. The wake structure seen in the latter study

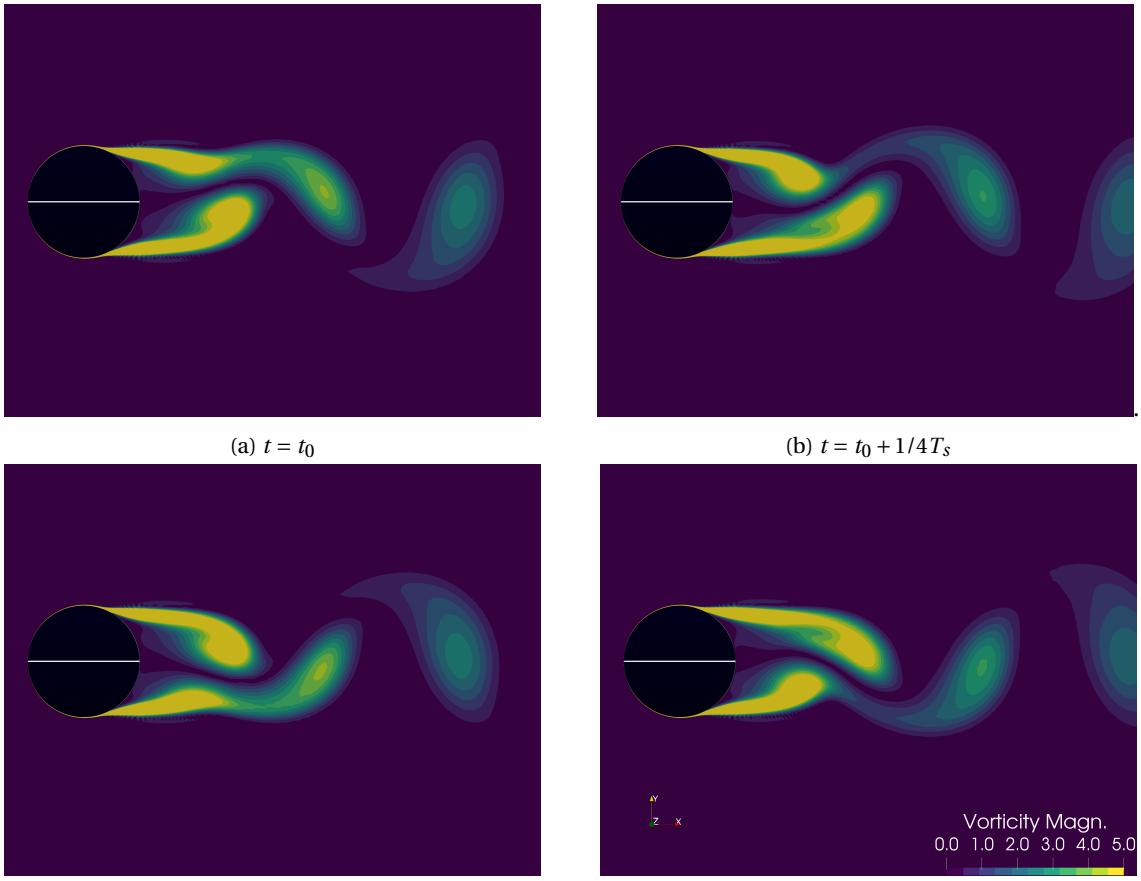

(a) $t = t_0$ (b) $t = t_0 + 1/4T_s$

(c) $t = t_0 + 2/4T_s$ (d) $t = t_0 + 3/4T_s$

Figure 4.26. Instantaneous (non-dimensional) vorticity magnitude ($\left|\frac{\xi D}{U_\infty}\right|$) for one shedding period starting from top left to top right, bottom left and ends at bottom right. Vorticity range has been filtered to $\frac{\xi D}{U_\infty} = 0-5$. The white line inside the cylinder indicates the zero-line (origin) of the computational domain. Time t_0 is taken at the instant where the lift coefficient is approximately zero and T_s is the reciprocal of the shedding frequency.

was considered to be more coherent compared to the chaotic wake captured in the transitional regime by the LES approach of [48]. This quick comparison would indeed imply that the supercritical regime is potentially suitable for the URANS approach since the vortex street becomes stable again in this regime and the unstable features typical for transcritical regime are less likely to occur. However, this suggestion should be further crystallized by employing more of these higher fidelity CFD studies in the super critical regime.

Effect of turbulence intensity In the present CFD simulations, the inflow turbulence was assumed to be $Ti = 3\%$ and the eddy viscosity ratio $\mu_\tau/\mu = 10$. One of the issues regarding the turbulence inflow quantities is the decay of these quantities over the inflow length $L1$ (see fig. 3.1), as was rightly pointed out by the study of [102]. In other words, the turbulent inflow quantities which have been set up at the inlet may be significantly lower at the cylinder as they decay over the distance travelled. This decay has been evaluated briefly in the present research, from a theoretical point of view and from the CFD data obtained with one of the simulations. The theory has been explained well in the study of [102] and their formulas have been adopted to estimate the decay rate. These formulas are as follows:

$$k = k_{FS}\left[1 + (C_{\epsilon 2} - 1)\left(\frac{\epsilon}{k}\right)_{FS}\frac{L1}{U}\right]^{\frac{-1}{C_{\epsilon 2}-1}} \tag{4.7}$$

$$\epsilon = \epsilon_{FS}\left[1 + (C_{\epsilon 2} - 1)\left(\frac{\epsilon}{k}\right)_{FS}\frac{L1}{U}\right]^{\frac{-C_{\epsilon 2}}{C_{\epsilon 2}-1}} \tag{4.8}$$

$$\omega = \omega_{FS}\left[1 + \omega_{FS}\beta\frac{L1}{U}\right]^{-1} \tag{4.9}$$

$$\epsilon_{FS} = C_{\mu}\frac{\rho k^2}{\mu}\frac{\mu_{\tau}}{\mu}^{-1} \tag{4.10}$$

Where $\beta = 0.09$, $C_{\epsilon 2} = 1.92$, $C_{\mu} = 0.9$. Although the k-ω SST model was used for the turbulence in the simulations, the k-ϵ equations have been 'borrowed' to estimate all the decay ratios. The other turbulence inlet quantities were estimated by the equations stated before, eq. 3.17 and eq. 3.18. The estimated turbulence quantities according to eq. 4.7 - eq. 4.10 at the cylinder wall (defined as ambient levels) for an assumed inlet turbulence of $Ti = 3\%$ and $\frac{\mu_{\tau}}{\mu} = 10$ at $Re = 4 \cdot 10^6$ have been listed in tab. 4.13. In addition to the theoretical data, data obtained directly from a CFD simulation at $Re = 4 \cdot 10^6$ with the same assumed turbulent inlet properties were listed in the same table. The values obtained from a CFD simulation were taken at a probe located at $x, y = (-4D, 0)$. The turbulent quantities, k and ω remained constant over time during the steady-state time frame at the probe location of $x, y = (-4D, 0)$, since the inflow turbulent inflow values were constant throughout the entire simulation and evidently the flow was not impacted before reaching the cylinder.

	Variable	**Free stream**	**Decay ratio**	**Ambient**
Theory	k	$1.02e-03$	$2.5e-04$	$2.56E-07$
	ω	470	$4.86e-04$	0.228
CFD Simulation	k	$1.02e-03$	$3.97e-04$	$4.06E-07$
	ω	470	$6.02e-04$	0.283

Table 4.13: Estimated ambient turbulent quantities compared against actual CFD data.

As can been seen from tab. 4.13, the data from the simulation corresponds well with the estimated values. The turbulence intensity Ti and eddy viscosity ratio μ_{τ}/μ have been calculated backwards with eq. 3.17 and eq. 3.18, which yielded ambient values of $Ti_a = 0.061\%$ and $\mu_{\tau}/\mu_a = 6.6$. These are indeed significantly lower than the assumed inlet quantities, $Ti = 3\%$ and $\mu_{\tau}/\mu = 10$. The most likely cause of this decrement is the large inflow distance $L_1 = 50D$ of the computational domain. The impact of the turbulent inflow quantities on the aerodynamic coefficients have been tabulated in tab. 4.14.

	Study	**Case** 1 **(Standard Case)**	**Case** 2	**Case** 3
(Assumed) input	$Ti(\%)$	3	15	30
	$\frac{\mu_{\tau}}{\mu}$	10	25	50
Output from CFD	$C_{L,RMS}$	0.0984	0.0996	0.101
	$C_{D,mean}$	0.4096	0.4105	0.4114
	St	0.3247	0.3288	0.3288

Table 4.14: Impact of turbulent inlet quantities on aerodynamic quantities

The lift coefficient increased by $\approx 1.4\%$ and drag coefficient by $\approx 0.3\%$ between case $1-2$ and $2-3$. The Strouhal number increased slightly in case 2 and remained constant between case $2-3$. It is possible that the effect of the turbulence intensity on the Strouhal number did not became as apparent as for the aerodynamic forces due to possible post-processing errors (these have been pointed out before in section 3.3). The numbers in tab. 4.14 illustrate that with such a large inflow size, it is hard to do a proper investigation of the turbulence inflow quantities. The only way to deal with such a large inflow distance is to use floor values, as was suggested in the study of [102]. These floor values ensure that the inflow quantities will reach the cylinder front edge as desired, by enforcing a minimum limit. In the present research the turbulence intensity $Ti_a = 0.061\%$ can be considered as relatively low when looking back to other researches listed in tab. 4.7. However, the study of [102] suggested to use an ambient turbulence intensity $Ti_a \approx 0.1\%$ and an eddy viscosity ratio of $\frac{\mu_{\tau}}{\mu}_a \approx 2 \cdot 10^{-7} \cdot Re = 0.8$ for external aerodynamical applications simulated with two-equation

turbulence models. The presently observed eddy viscosity ratio at the cylinder wall might be a little bit higher (μ_τ/μ_a = 6.6 compared to 0.8), the turbulence intensity ratio is nicely matched with the one suggested by the study. A more thorough analysis on the effect of the turbulence intensity on the aerodynamic forces and the vortex shedding fell outside the research scope of the present research. It is shown here that the ambient values were reasonably close to the recommended values of [102]. It was therefore believed that the assumed turbulent inlet quantities have facilitated the k-ω SST model to perform as desired.

4.2.2. Forced-vibrations: 1-way coupled

The results in this section are obtained to address the research question defined in chapter 1. The resulting aerodynamic forces are presented first. Then, the obtained phase angles are analyzed. One specific case, where *beating* occured, was analyzed into more detail. It appeared, as was expected, that the phase angle varied over time for the beating case. Then, as a result of the phase angle development, the aerodynamic damping results are shared. After that, the effect of the true and effective added mass coefficient on the aerodynamic response is discussed. By a detailed wake analysis, the 'switching mechanism' is shown which is known from the literature. Furthermore, a validation study was performed by comparing the CFD results to only wind-tunnel experiment found in the supercritical regime for a forced-vibrating cylinder. Lastly, the contour map, extracted from the aerodynamic damping, is presented. This contour map illustrated the practical use of the aerodynamic damping and the link between CFD and a phenomenological model.

Operating Grid The forced-vibration model has been used extensively to simulate the aerodynamic responses for a broad operating range of different cylinder amplitudes and oscillation frequencies. The operating *grid* for the 1-way coupled model is defines as follows:

Parameter	Value
$\mathbf{y}^*_{max}$	(0.0035 0.015 0.025 0.05 0.1 0.175 0.25)
$\mathbf{f}^*$	(0.58 0.74 0.89 0.95 1.01 1.07 1.23)
Re	$3.8\cdot10^6 - 7.4\cdot10^6$

Table 4.15: Non-dimensional parameters and values for the mass coefficient sensitivity study

It may be re-iterated that the frequency ratio used here is equal to: $f^* = \frac{f_{cyl}}{f_{shed,stat}}$. Hence, seven different prescribed oscillation amplitudes together with seven different frequency ratios are evaluated by the 1-way coupled model. This broad operating grid gave the opportunity to obtain insights about the lock-in region, force magnifications and aerodynamic responses under non-equilibrium operating conditions. Moreover, as was argued in section 2.3.2, the generated data from CFD for the specified grid in tab. 4.15 is potentially useful for calibration purposes regarding the development of phenomenological models. The aerodynamic results of this section are all displayed in a 3D figure, where f^* is on the x-axis, y^*_{max} on the y-axis and the aerodynamic quantity of interest on the z-axis.

Aerodynamic forces In fig. 4.27, the RMS of the lift force coefficient has been plotted against the frequency ratio f^* and non-dimensional amplitude y^*_{max}. For every increment in y^*_{max} and f^*, the lift force increased. For the motion frequency sweep, it can be seen that in general, a higher cylinder motion frequency leads to a higher lift coefficient. Based on the trend in fig. 4.27, the relation between cylinder frequency and lift force almost looks linear, except around the critical frequency ratio of $f^* = 1$.

Especially after $f^* > 1$, the lift coefficient takes substantial values at $y^*_{max} > 0.1$. It was shown before that the stationary RMS of the lift coefficient was found to be in the range of $C_{L,rms} = 0.08 - 0.1$. This would imply that at the operating point of $y^*_{max} = 0.25$ and $f^* = 1.2$, the forced-vibration simulations yielded a magnification factor of 19. The continuation of the lift coefficient increment after $f^* = 1$ was also observed for the laminar forced-vibrations, see fig. 4.8. Hence, it was not expected that the turbulence model was causing these high lift magnifications under certain conditions. It was believed that the force magnification was caused by the added mass effect of the fluid, which will be reported further ahead in this section. This is line with the earlier explanation of [4], where a lift coefficient rise for $f^* > 1$ was also observed.

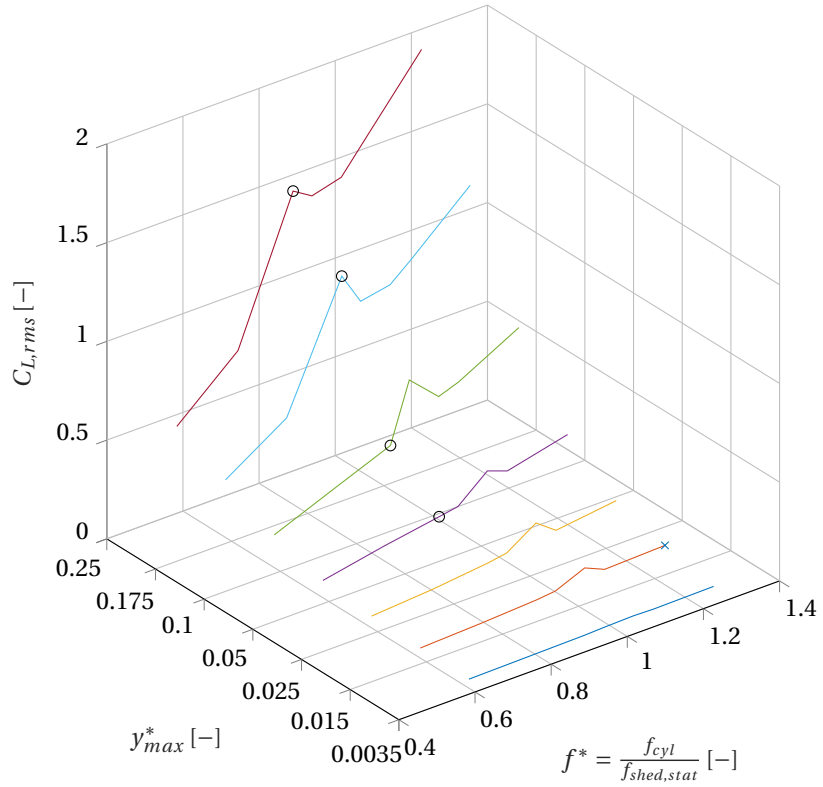

Figure 4.27. Forced-vibration lift coefficient (RMS) results for the specified operating grid

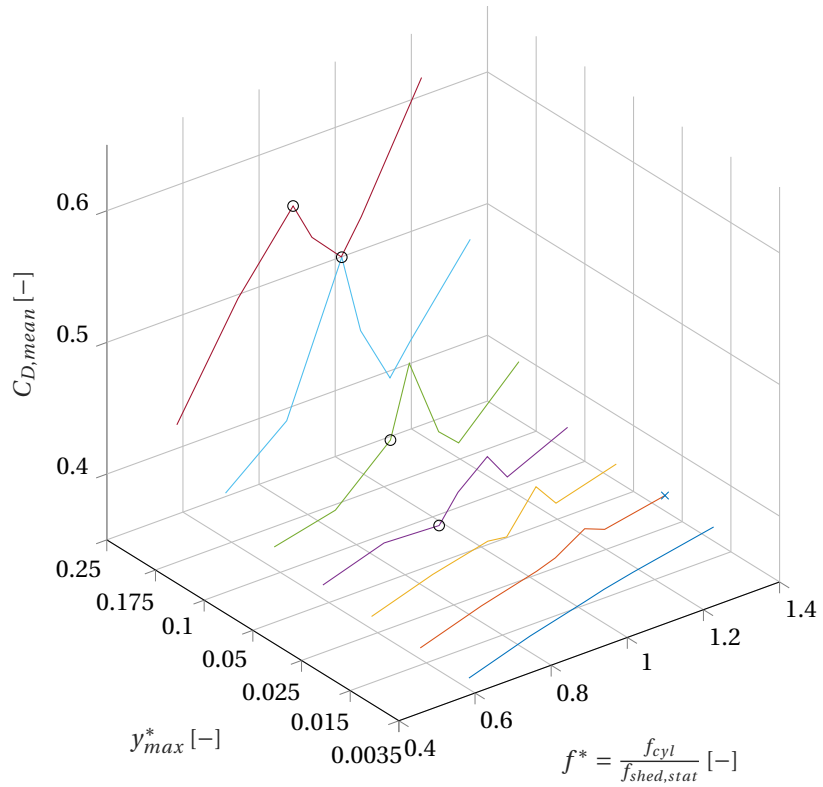

Figure 4.28. Forced-vibration mean drag coefficient results for the specified operating grid

The mean drag coefficient (see fig. 4.28) reached less substantial magnifications factors. For $y^*_{max} = 0.25$ and $f^* > 1.2$, the magnification factor was found to be 1.5. When comparing the lift and drag coefficient directly, it seems that the lock-in effect on the drag coefficient is more apparent compared to the lift coefficient. There is a clear increment and small decrement for the drag coefficient, after which it starts increasing again. The same trend was observed in the forced-vibration results for laminar flow. As will be shown later, the drag coefficient was not impacted by the added mass coefficient since the cylinder was only forced to move in the transverse direction. Yet, at higher frequencies the drag coefficient still seemed to rise as shown in the results of fig. 4.28. This trend concerning the drag coefficient has not been investigated in to more detail. The increased values of the lift coefficient RMS and mean drag coefficient around $f^* = 1$ were believed to be a consequence of the wake lock-in on to the cylinder motion, which is in line with the literature (see the second effect described back in section 2.2.4). Based on these (non-linear) force magnifications in fig. 4.27 and fig. 4.28, the following lock-in regimes were estimated: $y^*_{max} = 0.015, 0.05, 0.10 : 0.9 < f^* < 1.1$ and $y^*_{max} = 0.175, 0.250 : 0.75 < f^* < 1.05$. It must be noted that a denser operating grid could have given a better estimation of the lock-in boundaries. These estimated lock-in boundaries firstly show that the lock-in band increases with increasing amplitude, which is typical for VIV. The boundaries also show that the lock-in region starts to move to lower frequency ratios for higher oscillation amplitudes. It seems for higher oscillation amplitudes the flow field tends to lock-in relatively earlier at lower frequency ratios.

Phase angle In fig. 4.29, the phase angle between the lift force and the cylinder motion was plotted for the entire grid.

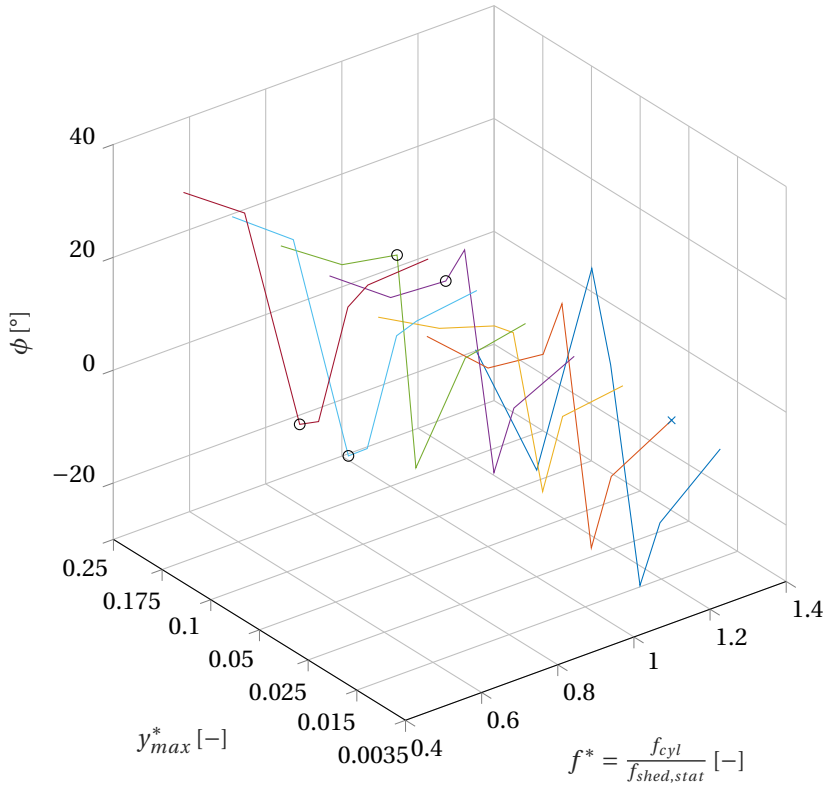

Figure 4.29. Phase angle results for the specified operating grid

The following observations are made based on the phase angle results displayed in fig. 4.29:

- For the complete amplitude spectrum considered here, it seems that the phase angle showed more agreement for either high or low frequency ratios. At lower frequency ratios, the phase angle is positive in the range of $20° < \phi < 30°$. Then, the phase angle dropped significantly and switched sign to a range of $-22° < \phi < 8°$. For $f^* > 1$ the phase angle raised again and approached a value of approximately zero.
- It seems that the general trend of the phase angle to drop by from a positive value to a negative value around the critical frequency is more pronounced at higher oscillations amplitudes ($y^*_{max} > 0.10$). The

phase angle shows a larger drop for larger oscillations displacements and also the drops occurred earlier. Whereas the phase angle drop for $y^*_{max} = 0.10$ became apparent at $f^* = 1.01$, for $y^*_{max} > 0.10$ this drop already became apparent at $f^* = 0.89$.

- It has appeared that the frequency bandwidth where the phase angle fell and rose again corresponded to the earlier defined lock-in ranges by the non-linear force magnification. Similar to the trend observed for the aerodynamic forces, it appeared for higher oscillation amplitudes the phase angle switch occurred relatively faster (i.e. at lower frequency ratios) indicating the flow field locked in earlier as well.

It has been noticed for some of the simulations, the phase angle was found not to be constant over time. An explanation to this can be found in the beating phenomenon. It was explained before in section 3.3.6 that the beating signal usually consists out of multiple sinus signals. Under such circumstances, for each signal a different phase angle can be identified. This means that the periodicity of the beating yielded a 'harmonical' varying phase angle over time. An example of a beating case is given in fig. 4.30 to illustrate the phase angle development. This case was run under $y^*_{max} = 0.015$ and $f^* = 1.23$, which was marked by the 'x'- symbol in fig. 4.27, 4.28, 4.29, 4.32, 4.33. In the left subfigure of fig. 4.30, the obtained fluctuating lift coefficient and the prescribed (non-dimensional) displacement motion was plotted. In the right subfigure, the computed phase angle in the time-domain was plotted for each shedding cycle observed in the left subfigure.

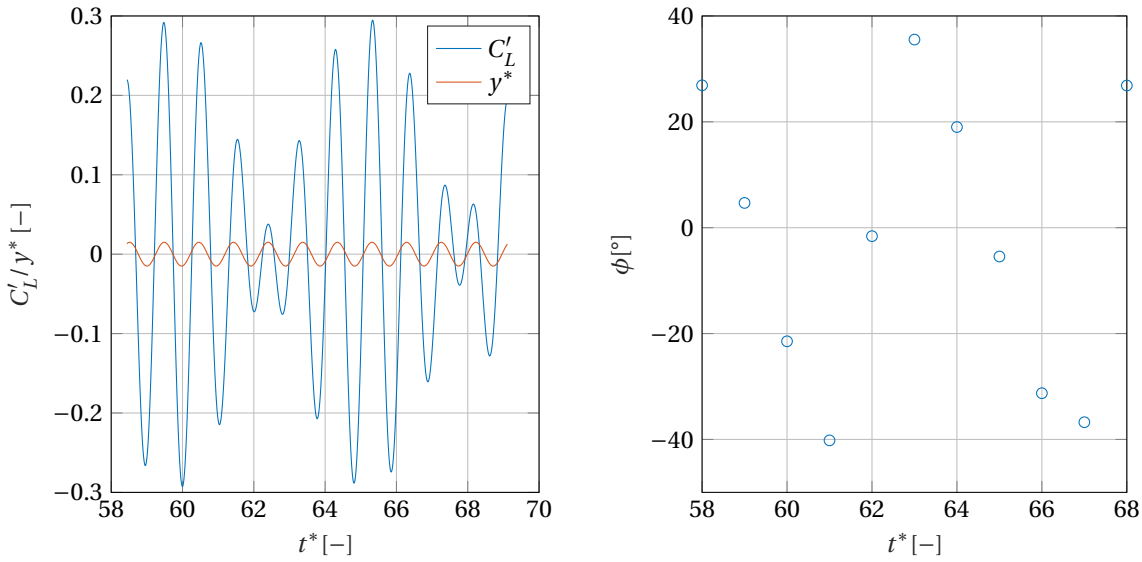

Figure 4.30. Fluctuating lift coefficient and (non-dimensional) displacement motion (left) and corresponding fluctuating phase angle (right), both in steady-state for the prescribed motion of $y^*_{max} = 0.015$ and $f^* = 1.23$

The following observations have been made:

- While the prescribed motion is evidently harmonical, the lift force shows a varying frequency which is therefore fluctuating relatively to the cylinder motion for every cycle.
- This can be seen back in the phase angle evolvement, which varied between $35° < \phi < -40°$.
- This implies the fluid is continuously changing from a damping source to an exciting source and vice versa.

When looking towards the PSD plot of the complete lift time-series in steady-state, in fig. 4.31, two main responses can be identified. These two peaks resemble the continuous 'battle' between the stationary shedding frequency and the natural frequency both trying to dictate the wake behaviour. This is in line with earlier observations in the laminar regime, see section 4.1.3.

In the present research, for convenience, it was decided to take the time-averaged phase angle of the complete steady-state time signal. This phase angle describes the time-averaged relation between the lift force vector and motion displacement. For example, the case of fig. 4.30 showed a time-averaged phase angle of: $\phi = -2.5°$. Overall, the wake was then considered to be damping the cylinder motion.

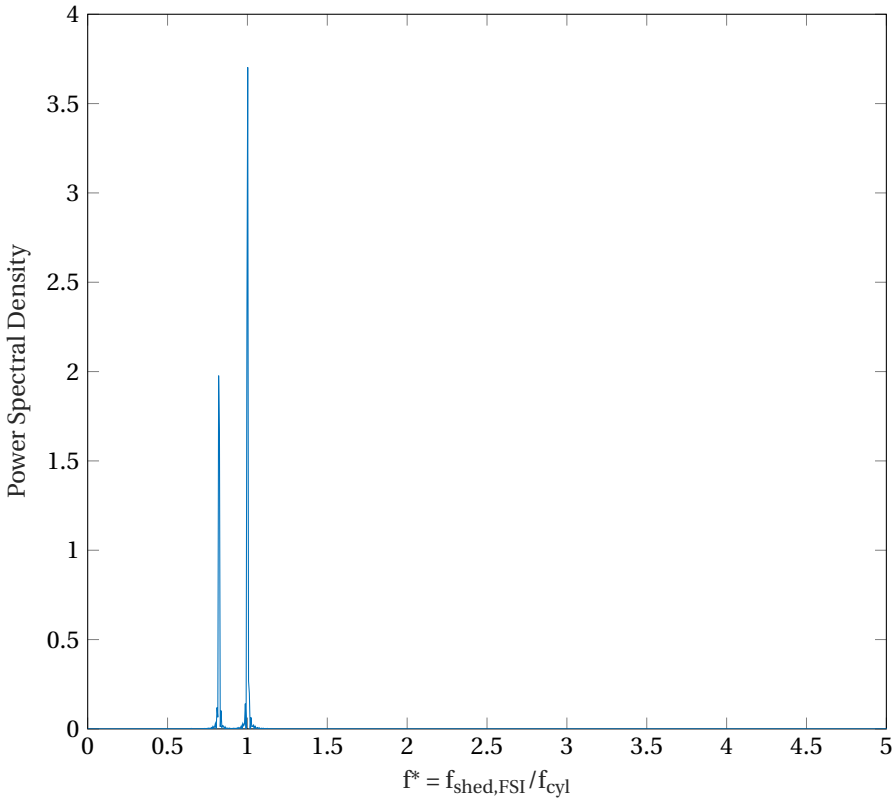

Figure 4.31. Power-spectral density of the fluctuating lift coefficient in steady-state for the case with prescribed motion $y^*_{max} = 0.015$ and $f^* = 1.23$.

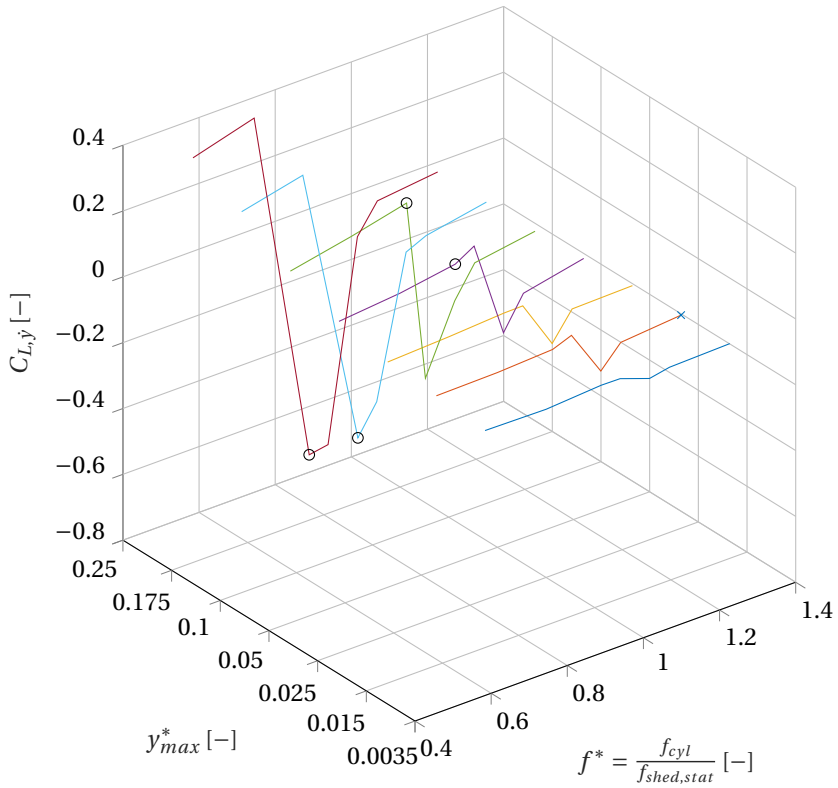

Figure 4.32. Aerodynamic damping results for the specified operating grid

Aerodynamic damping In fig. 4.32, the results on the aerodynamic damping are shown. Similar to the development of the phase angle, the aerodynamic damping showed a sudden drop and rise around the critical frequency ratio. For $f^* < 1$, the aerodynamic damping was found to be within the range of $0 < C_{L,\dot{y}} < 0.3$. For larger frequency ratios, $f^* > 1.1$, the aerodynamic damping was approaching a value of zero for all amplitudes considered here. When the non-dimensional amplitude was increased, the aerodynamic damping inside the lock-in range showed a decrease while just before the lock-in range an increase. The former trend is deemed as stable and resembles the self-limiting behaviour earlier observed and described in section 4.1.3. Considering a free-vibrating system where the shedding frequency is close to the natural frequency, the cylinder would inherently start to show a transverse displacement. The cylinder would start to move towards even higher non-dimensional values, until the operating circumstances have led to a wake which starts to damp this motion. In a free-vibrating system, it would depend also on the structural damping at which non-dimensional amplitude equilibrium would have been reached. Stability is considered when the aerodynamic damping goes to even lower values when the oscillation amplitude grows. It provides a stable feedback system to prevent the system oscillating towards infinity large displacements, regardless of the structural damping. The unstable character is the exact opposite and can be spotted at $f^* \approx 0.7 - 0.8$. This would imply that, for every larger cylinder displacement, the aerodynamic damping started to excite the cylinder even more.

True added mass coefficient Firstly, the true added mass coefficient (section 3.3.6) has been evaluated. This has been done by simulating the prescribed motion in a still fluid. Under such circumstances, the vortex effects should be minimized [87] and only the amount of surrounding air actually being displayed is measured. Typically, this coefficient (as explained in section 3.3.6) was found to be close to one for small transverse oscillations. It was not clear what the effect of the cylinder frequency on the true added mass coefficient would be. While the effective added mass coefficient is a function of the frequency andf the amplitude, the true added mass coefficient is a different metric which should not be measured during flow-induced vibrations [87]. Therefore, the effect of the prescribed frequency and motion amplitude of a cylinder body was investigated when surrounded by an initially still fluid (i.e. the inflow velocity is equal to zero). The results of these cases are tabulated in tab. 4.16. It must be noted that with a zero-inflow velocity, a Reynolds number of zero and lift coefficient of zero may be expected. Yet, for convenience the inflow velocity was assumed to be equal to the one which allowed a proper comparison between the cases.

Parameter	**Case** 1	**Case** 2	**Case** 3
Re	$5 \cdot 10^6$	$5 \cdot 10^6$	$4.5 \cdot 10^6$
f^*	0.89	0.89	1.01
y^*_{max}	0.025	0.10	0.10
$C_{D,mean}$	$-3.4 \cdot 10^{-8}$	$-5.9 \cdot 10^{-9}$	$-2.3 \cdot 10^{-9}$
$C_{L,max}$	0.139	0.548	0.697
$C_{L,\ddot{y}}$	-0.138	-0.544	-0.692
$C_{L,\dot{y}}$	-0.012	-0.014	-0.018
C_A	1.019	1.005	1.006

Table 4.16: Results for forced-vibration cases with zero inflow velocity

Based on the results in tab. 4.16, the following conclusions have been drawn:

- The true added mass coefficients was found to be very close to one, which is in line with the classical values taken in the literature [4]. Hence, without any vortex dynamics, the added mass is equal to the displaced air volume by the cylinder motion.
- This was supported by the fact that the lift coefficient in phase with the acceleration was nearly equal to the lift coefficient amplitude, implying that the cylinder displacement (or acceleration) was almost entirely responsible for the resultant lift force vector.
- Evidently, since the true added mass coefficient is 1, the lift force caused by the air volume displacement linearly scaled with the acceleration: $y_{max} cos(2\pi f_{cyl})^2$. The cases with increased amplitude and frequency therefore both shown an increment of the lift force.
- No effect was found on the mean drag coefficient by the transverse cylinder displacement.

Effective added mass coefficient Regarding the 1-way coupled cases, where there is an incoming wind speed, the 'effective' added mass coefficient (rather than the true added mass coefficient) is introduced to capture the additional inertial effects caused by the FSI (apparent vortex dynamics for example) [87]. In contrast to the case with a still fluid, the 1-way coupled cases with incoming wind speed have an unsteady vortex-street trailing aft behind the cylinder. Because of the cylinder movement, this vortex street might be affected. Some air molecules could in turn phase out with the cylinder's acceleration while other fractions of the air wake could synchronize with the cylinder's acceleration. Therefore, it can be imagined that the total apparent inertial component of the fluid force is different compared to the inertial component only caused by the displaced air volume around the cylinder body. This latter effect is then captured with the effective added mass coefficient, C_{EA}. To summarize:

- $C_{EA} > 1$ means that the vortex dynamics as a result of the FSI effects are causing the fluid inertia to effectively increase.
- On the other hand, when the coefficient is lower than 1, it would imply that the FSI effects are reducing the effective inertial effect of the fluid.
- A coefficient of 1 implies that the inertial effect is only a consequence of the displaced volume of the fluid by the cylinder body (similar to the true added mass coefficient).

The reader is referred to section 3.3.6, [4] or [87] for a more detailed explanation on the added mass coefficients.

The effective added mass coefficient, C_{EA}, has been computed for all the simulations (see fig. 4.33). Based on the results in fig. 4.33, the following observations were made:

- As f^* increases, the added mass coefficient shows an overall trend of growth. Especially in the lock-in region, the FSI effects become apparent. Around $f^* \approx 1$, there is a peak of the added mass coefficient.
- Outside the lock-in region, the FSI still has an additional effect on the effective added air mass. For $f^* > 1$, the added mass coefficient is still higher than 1, although slowly decreasing. This is in contrast for the operating regime of $f^* < 1$, where the added mass coefficient tends to be a bit below 1. It may be concluded, that at higher frequencies, the vortex dynamics are increasing the additional inertial component of the fluid while at lower frequencies they tend to reduce this inertial component.
- With increasing y^*_{max}, the effective added mass coefficient did not necessarily show an increment. The development of the coefficient for a varying frequency ratio remained quite similar over the entire amplitude spectrum. The highest peak of the effective added mass coefficient was found inside the lock-in region for $y^*_{max} = 0.015$. For higher amplitudes, it can be seen that the frequency range of increased added mass coefficient became larger. This corresponds to the earlier observed lock-in regions.

It was argued before that the increased lift coefficient was caused by the added mass coefficient. This reasoning was based on the following observations:

- Firstly, it was seen that the true added mass coefficient remained close to one for some of the operating points in the grid: $y^*_{max} = 0.025, 0.10; f^* = 0.89$ and $y^*_{max} = 0.10; f^* = 1.01$. For the entire operating range of $0.0035 < y^*_{max} < 0.25$ and $0.75 < f^* < 1.23$ it was expected that the true added mass coefficient would stay close to one.
- The effective added mass coefficient, except inside the lock-in region, stayed in the range of $0.9 < C_{EA} < 1.14$ for the entire operating grid. Hence, outside the lock-in region, it was not the effective added mass M_A (from eq. 3.60) that caused a magnification factor of $M \approx 19$ of the lift forces. In fact, it was the increment of the prescribed cylinder displacement amplitude and frequency that caused these high magnification factors for $f^* > 1$ and $y^*_{max} > 0.1$ in fig. 4.27.
- The benefit of using the effective added mass coefficient to evaluate the FSI effects compared to the lift force in phase with the cylinder displacement (or acceleration), is that this coefficient is a function of the body acceleration (see eq. 3.61). This filters out the inertial effects caused by simply moving the air volume around the cylinder body and shows the apparent inertial effects caused by the FSI.
- Inside the lock-in regime, the added mass of air increased significantly compared to outside of the lock-in region. Therefore, in fig. 4.27 you see a small bump around the critical frequency ratio which disrupts the earlier spotted linear trend.

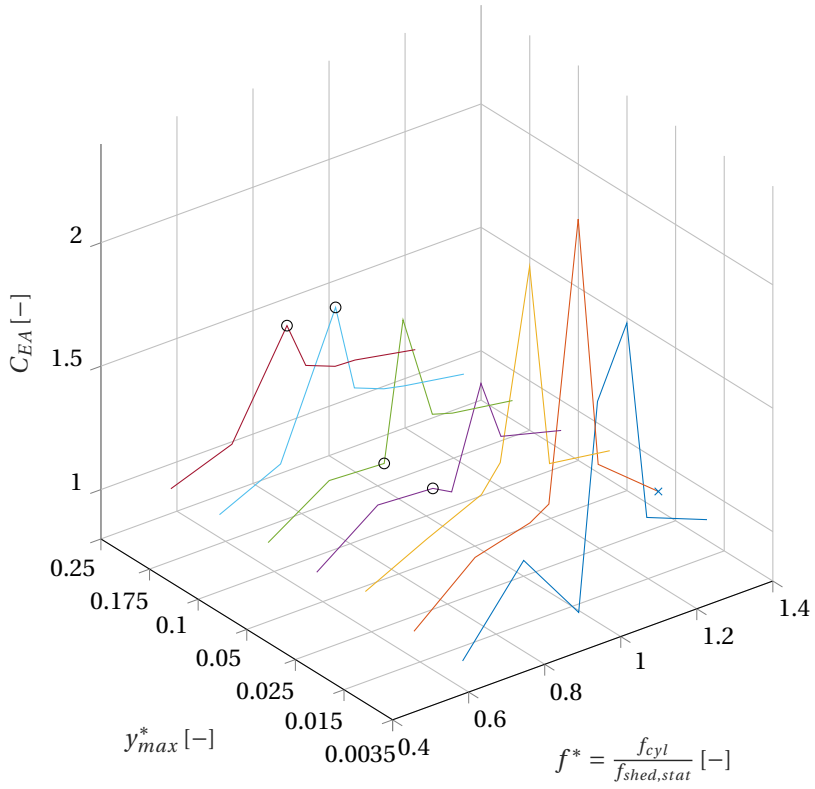

Figure 4.33. Effective added mass coefficient results for the specified operating grid

Wake analysis To further investigate the phase angle drop, the vorticity field has been investigated of the following four cases: $y^*_{max} = 0.05, 0.10, 0.175, 0.25$, all at $f^* = 0.89$. These four cases have been detonated in fig. 4.27, 4.28, 4.29, 4.32, 4.33 with the 'o'-symbol. These four cases were picked because the phase angle shows a clear drop when the non-dimensional amplitude was increased from $y^*_{max} = 0.10$ to $y^*_{max} = 0.175$. In addition, the lift RMS, the effective added mass coefficient seemed to increase significantly between these two operating points. The aerodynamic damping decreased substantially between these amplitudes. Hence, the vorticity analysis has been performed to provide a more detailed insight in what is happening in the wake between these operating points. The (non-dimensional) vorticity magnitude has been plotted for the four selected cases in fig. 4.34. All the instantaneous vorticity plots were taken when the cylinder was at or very near to its maximum displacement during their motion trajectory. The zero line of the cylinder motion trajectory (or the origin) has been illustrated by the white line inside the black cylinder.

The following insights were obtained from the vorticity plots:

- For lower amplitudes, $y^*_{max} = 0.05 - 0.10$, the vortices were more stretched horizontally. For these smaller amplitudes it was observed that the vortices separated from the cylinder body at the lower side when the cylinder was at its positive amplitude. This can be seen best in the second subfigure of $y^*_{max} = 0.10$, where the lower vortex is about to trail aft and separate from the vortex attached to the cylinder body.
- When the amplitude was increased from $y^*_{max} = 0.05$ to $y^*_{max} = 0.10$, the vortex started to 'roll up' more towards the cylinder body. This effect is most likely because of the higher acceleration of the cylinder body, causing the fluid particles to rotate more in the transverse direction.
- At the cylinder amplitude of $y^*_{max} = 0.175$, the vortex pattern changed completely. The vortices are less stretched than before and the vortices are more 'rolled up', leading to denser vortices close to the cylinder body. The pattern is similar between the cases of $y^*_{max} = 0.175$ and $y^*_{max} = 0.25$, although the magnitude of the vortices increased in the latter case.
- In these higher amplitude cases, the timing of the vortex shedding has changed. In these cases, when the cylinder is moving upwards, the vortices trailed aft from the upper side of the cylinder body rather

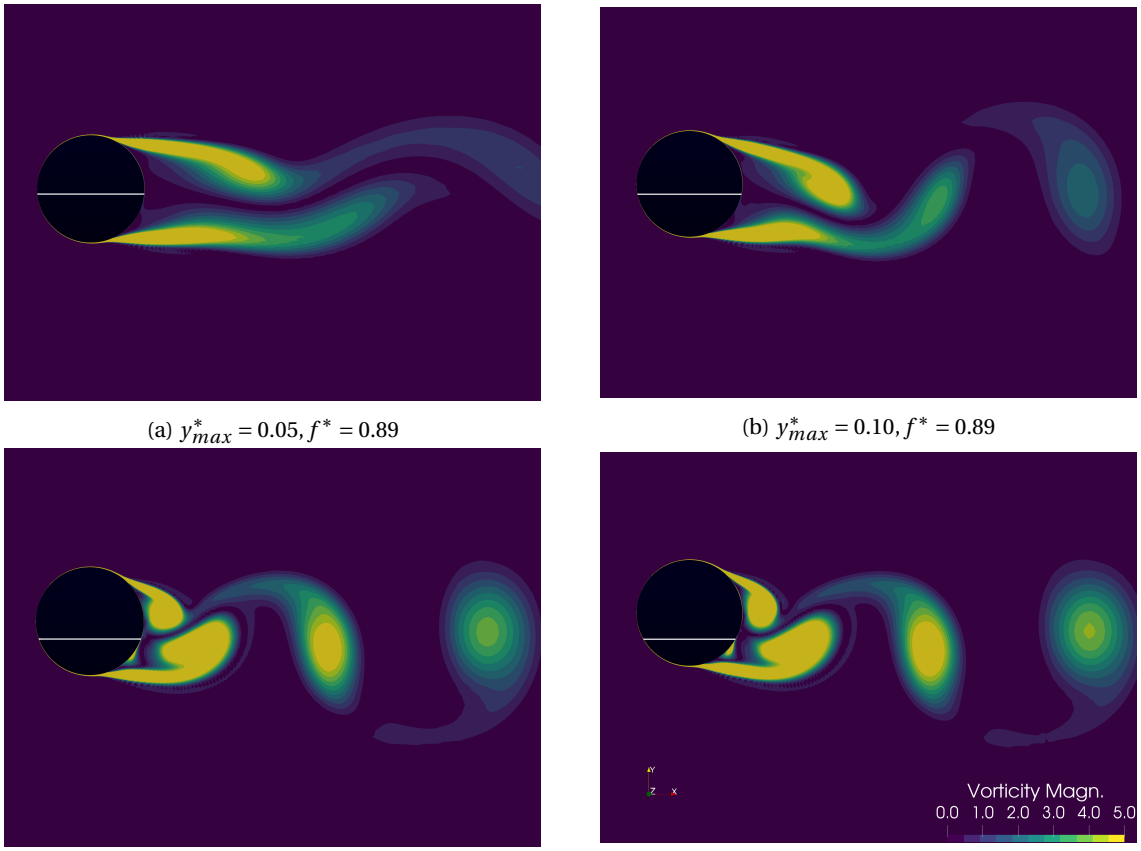

(a) $y^*_{max} = 0.05, f^* = 0.89$

(b) $y^*_{max} = 0.10, f^* = 0.89$

(c) $y^*_{max} = 0.175, f^* = 0.89$

(d) $y^*_{max} = 0.25, f^* = 0.89$

Figure 4.34. Instantaneous (non-dimensional) vorticity magnitude ($\left|\frac{\xi D}{U_\infty}\right|$) at the maximum, positive displacement. From top left to bottom right, the following displacement amplitudes were prescribed: $y^*_{max} = 0.05$, 0.10, 0.175, 0.25, all four cases operating at $f^* = 0.89$. Vorticity range has been filtered to $\frac{\xi D}{U_\infty} = 0 - 5$.

than the lower side. It is believed that the change of vortex shedding pattern caused the phase angle to drop.

- Compared to the stationary vortex wake pattern, the vorticity patterns in the wake presented here for $y^*_{max} = 0.05$ and $y^*_{max} = 0.10$ looked similar to one seen in fig. 4.26 for the stationary cylinder. The wakes observed for $y^*_{max} = 0.175$ and $y^*_{max} = 0.25$ looked different than the stationary vortex pattern. This can be explained by the fact that for lower displacements, the wake is more dictated by the Strouhal relation and hence the stationary wake pattern while for higher y^*_{max} the wake is more dictated by the cylinder motion because of the FSI effects.
- It can be seen that in all these four cases the 2S wake pattern mode is active in the wake, similar to the stationary wake of fig. 4.26.

As has been explained in chapter 2, section 2.2.4, the phase angle behaviour during lock-in has been related before to the change of vortex shedding timing by numerous studies. Several numerical studies have shown the relation between the vorticity patterns observed in the wake and phase angle jump around the critical frequency, [29] mentioned some of these. The switch was typically related to the side of the cylinder where the vortices shedded from. For lower frequency ratios, that is before the critical frequency ratio, the shedding occurred when the cylinder is at its maximum displacement and it occurs on the opposite side compared to the position of the cylinder [14]. Then, after the critical frequency has been surpassed and when the phase angle 'jumped' or switched sign, the vortex started to shed from the same side as the cylinder's position when the maximum displacement is reached. Therefore, the present simulations have clearly captured the vortex shedding timing switch associated with the phase angle jump. Although in fig. 4.34 it is not the frequency ratio that has been varied, but the amplitude ratio, the same trend was observed when the frequency ratio was varied for a constant amplitude. As shown in fig. 4.29, the two middle operating points

representing the cases in fig. 4.34 ($y^*_{max} = 0.1, f^* = 0.89$,; $y^*_{max} = 0.175, f^* = 0.89$) show a similar phase angle drop compared to for example when the frequency ratio is increased from $f^* = 0.89$ to $f* = 1.01$ at a constant amplitude of $y^*_{max} = 0.1$. The change of vortex patterns in the latter two operating points was found to be identical to the latter two operating points when the amplitude was increased. This is in fact caused by the larger lock-in range observed for higher amplitudes. Therefore, two causes have been observed for the phase angle to drop:

- Around the critical frequency, the phase angle drops. This drop is related to an observed change of vortex shedding timing in the wake and is in line with several other numerical/experimental studies [29], [14]. Because the phase angle has dropped, the aerodynamic damping also decreases substantially inside the lock-in region. This latter effect causes the fluid to damp the cylinder motion.
- If close enough to the critical frequency, an increment of the amplitude can lead to a phase angle drop as well. Again, this was related to an observed vortex pattern switch in the wake. This phase angle drop caused the aerodynamic damping to become more negative as the amplitude was increased, as shown in fig. 4.32. The latter trend was deemed as a stable operating path for the dynamic system. As [4] suggested, this phase-flipping behaviour might therefore be one of the causes of the self-limiting nature of vortex-induced vibrations.

Comparison with wind-tunnel experiment In the NASA wind-tunnel experiment of [2] a forced-vibration experiment was performed at supercritical Reynolds numbers for the amplitudes of $0.0035 < y^*_{max} < 0.025$. This was the only forced-vibration experiment found at supercritical Reynolds. No forced-vibration CFD studies at supercritical Reynolds numbers have been found. The lift magnification factor and aerodynamic damping of the wind-tunnel experiment have been compared to the results of the present CFD model in fig. 4.35 and fig. 4.36. Based on the results in fig. 4.35, the following observations were made:

- It was firstly hard to identify the curve-fit in the number of data points incorporated from [2], especially at $y^*_{max} = 0.0035$ and $y^*_{max} = 0.0139$. It seemed there was some agreement for $y^*_{max} = 0.015$ and $y^*_{max} = 0.025$ mostly before the critical frequency ratio of $f^* = 1$. This showed the CFD model predicted the effect of the transverse motion amplitude on the lift magnification factor well.
- The lift magnification factor in the lock-in region for the lowest non-dimensional amplitude of $y^*_{max} = 0.0035$ was under-predicted by the CFD model. The wind-tunnel experiment predicted a higher magnification there.
- It seemed the wind-tunnel experiment also predicted the continuation of the lift force increment after lock-in, although slightly below the results obtained from the CFD model. This continuation was earlier explained by the effective added mass in section 4.2.2.

Regarding the aerodynamic damping results, see fig. 4.36, the following conclusions have been drawn:

- Before the critical frequency, the aerodynamic damping appeared to rise from a non-zero value towards a even higher positive value. In addition, this rise was even larger when the prescribed motion amplitude increased, implying instability just before the critical frequency. These trends were observed for the wind-tunnel results and the CFD model results.
- The magnitude of the predicted aerodynamic damping by the CFD model agreed well with the wind-tunnel experiment before lock-in and after lock-in. Both the experiment and the CFD model predicted positive values for the aerodynamic damping before lock-in (except for $y^*_{max} = 0.0035$) and values approaching zero after lock-in.
- The experiment predicted the rise of the aerodynamic damping considerably sharper leading to higher peak damping values compared to the CFD results. The CFD model did predict a rise of the damping coefficient just before the critical frequency, however, it was not as large as the experiment measured. It is either possible the CFD model was not able to capture this sharp damping rise or the specified operating grid was not dense enough and the peak was missed.
- Both the wind-tunnel experiment and the CFD model showed the 'switching' mechanism (see previous section) to be present in the supercritical regime. The predicted timing of this aerodynamic damping 'switch' agreed well with the wind-tunnel experiment. Hence, the overall behaviour of the aerodynamic damping under varying frequency ratio measured by the experiment was found to be similar to the predicted behaviour by the CFD model.

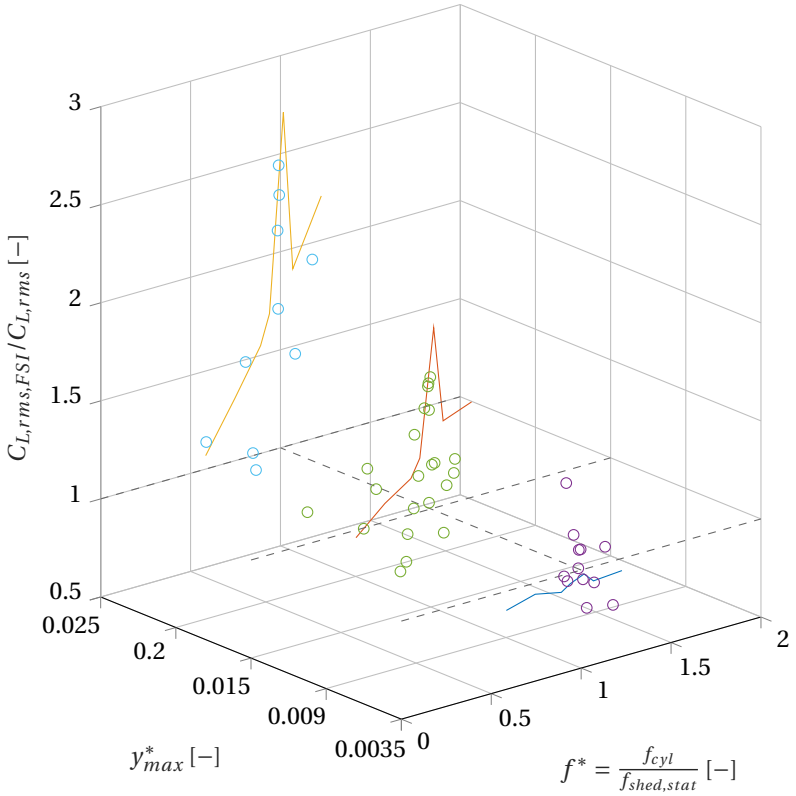

Figure 4.35. Lift magnification factor (RMS) caused by FSI. The bulllets represent the wind-tunnel data from [2], at $\mathbf{A}^* = [0.0035 \quad 0.0139 \quad 0.0278]$ for the purple, green and blue coloured-bullets , respectively.

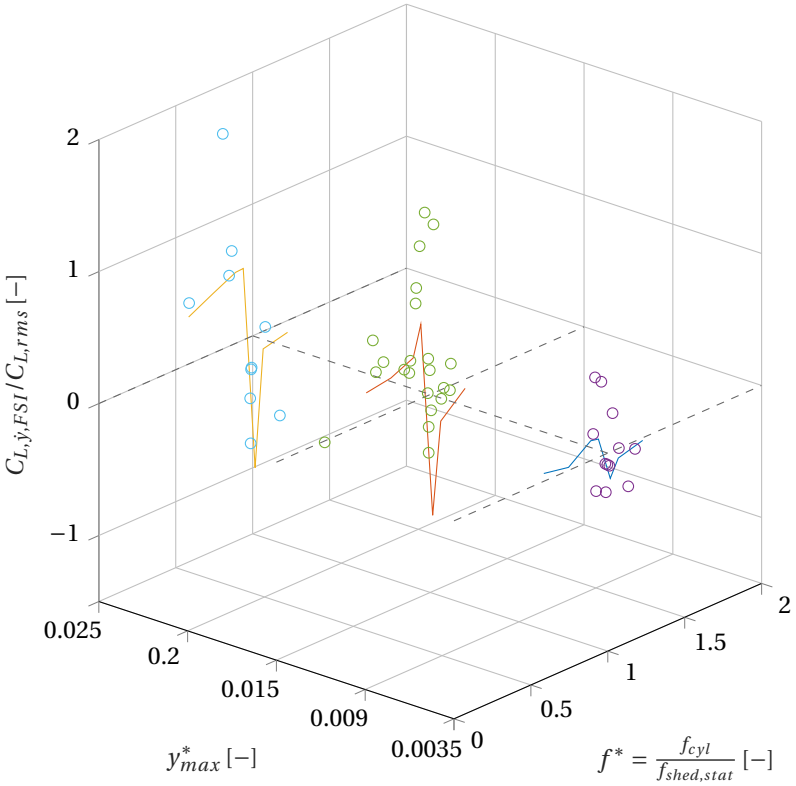

Figure 4.36. Aerodynamic damping magnification caused by FSI. The bulllets represent the wind-tunnel data from [2], at $\mathbf{A}^* = [0.0035 \quad 0.0139 \quad 0.0278]$ for the purple, green and blue coloured-bullets, respectively.

Contour map The 3D plot of the aerodynamic damping for the specified operating grid has been converted to a contour map, in fig. 4.37, by extracting the overlapping contour lines from fig. 4.32. In line with the earlier observed trend for the aerodynamic damping, it can be observed in fig. 4.37 that the aerodynamic damping is generally positive before the critical frequency and becomes negative afterwards. The 'zero' contour line clearly illustrates the frequency ratio where the aerodynamic switched sign. This zero-contour line again shows that the lock-in of the flow field occurs relatively quicker at lower frequency ratios for higher oscillation amplitudes, as the contour line curves towards the left at higher oscillation amplitudes.

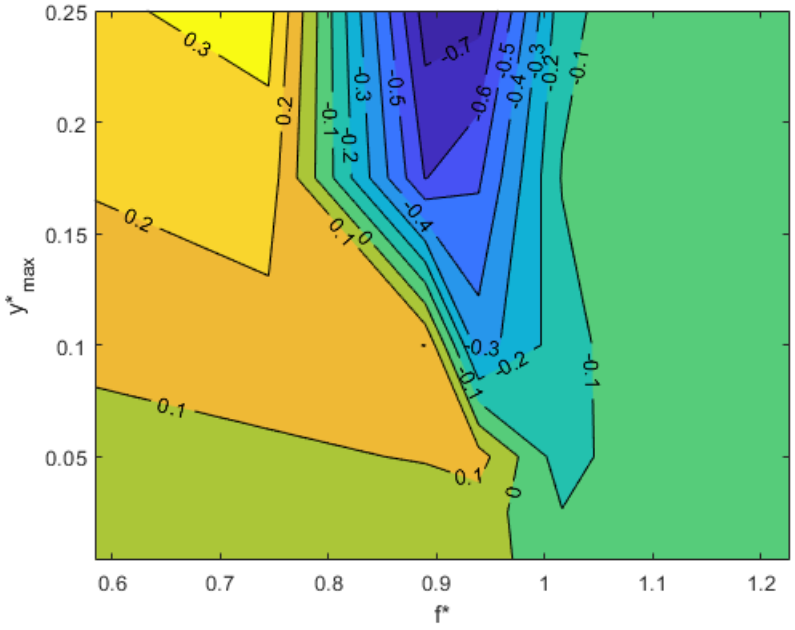

Figure 4.37. Contour map of $C_{L,\dot{y}}$

It appeared the results at higher oscillation amplitudes showed more coherence over the grid. Hence, the contour lines are denser around higher oscillations amplitudes. It has been reasoned that for lower non-dimensional amplitudes, $0.0035 < y^*_{max} < 0.1$ the aerodynamic damping curves (see fig. 4.32) showed bigger changes for each increment of the amplitude. In this region, where the oscillations amplitudes are relatively low, the flow field is still party following the Strouhal relation and partly impacted by the structural motion. Then, at larger oscillations amplitudes the flow field is dominated more strongly by the structural motion, suppressing the Strouhal relation. Hence, the probability of the flow field of changing wake patterns starts to decay and the relation between fluid and motion starts to become more coherent. It must be noted that the specified oscillation amplitudes were located relatively closer to each other at higher y^*_{max}, while the increments between the amplitudes of $0.0035 < y^*_{max} < 0.1$ were larger. This effect must not be ignored and it is likely this has contributed to the observed coherences. Ideally, a denser operating grid at lower frequencies and amplitudes could have been analyzed to see if indeed the coherence of the fluid-motion relation at lower amplitudes decreases.

Assuming a structural damping of zero, the stable reduced frequencies can be deduced from fig. 4.37 as well. The reduced frequency of $f^* = 0.75$ would imply an unstable operating point for the system. When there would be no structural damping, the oscillation amplitude would grow because of the stationary vortex shedding. When the cylinder has reached a sufficiently high oscillation amplitude, a positive aerodynamic damping would excite the cylinder to even higher amplitudes. Because the aerodynamic damping only seemed to increase for this frequency ratio when the transverse amplitude rises (at least based on current data set and fig. 4.37), it could lead to a continuous self-exciting system potentially growing to very large amplitudes. Besides the assumed structural damping of zero, it would also require a low mass coefficient m^* which allows the vortex shedding to initiate and eventually resonate the cylinder because the frequency ratio is 25% off from the critical frequency. The effects of the structural damping and mass coefficients are addressed in the next section of this chapter in the *free-vibration* set-up.

In contrast to the frequency ratio of $f^* = 0.75$, a stable system can be identified at $f^* = 1$. For this operating point, the aerodynamic damping becomes even more negative for every oscillation amplitude increment leading to enhanced aerodynamic damping. Especially around the frequency ratio of $f^* = 1$ this self-limiting property becomes very important. As has been shown in the next section, around a frequency ratio of $f^* = 1$, a broader range of mass-damping system's would be susceptible to resonate since the frequencies of the vortex shedding and structure match so well. This means systems with a relatively low mass and damping coefficient would most likely still reach a stable maximum amplitude around these stable frequencies.

These two trajectories, one stable and one unstable, illustrate the practical use of the aerodynamic damping. As was argued in the study of [4], the aerodynamic damping is capable of collapsing and summarizing most of the FSI behaviour into one parameter. By taking the mass-spring-damper system described in eq. 3.25 and assuming the lift force consists out of two in-phase components as in eq. 3.44, the following relation can be obtained [4]:

$$2S_G y^*_{max} \iff C_{L,\dot{y}} \tag{4.11}$$

where S_G is the Skop-Griffin parameter defined in eq. 2.5. By using the obtained dependency of $C_{L,\dot{y}}$ on the cylinder oscillation amplitude and frequency in fig. 4.37, the resulting equilibrium points where eq. 4.11 holds can readily be found. Eq. 4.11 shows the relation between the structural properties (collaped by S_G), the FSI effects (lift force in phase with velocity) and the resulting cylinder displacement amplitude. This may be seen as a simple method for utilizing the aerodynamic damping. Nevertheless, the study of [105] for instance has demonstrated the usability of the aerodynamic damping in a more comprehensive phenomenological model where the results were promising.

4.2.3. Free-vibrations: 2-way coupled

In this section the results have all contributed to addressing the research question defined in ch. 1. First, the non-dimensional values used for the Standard Batch are presented. Then, the typical lock-in maps are shown for the Standard Batch. After that, the results of the Standard Batch are categorized based on their aerodynamic and motion responses. In some of these Categories, the wake of are analyzed into more detail by displaying the vorticity contours. The effect of two structural parameters on the VIV response is addressed as well: of the mass coefficient m^* and the damping coefficient ζ. Lastly, similar to the laminar results section, a non-dimensional analysis is presented for the turbulent cases.

Non-dimensional parameters for the Standard Batch In the laminar cases the mass ratio was kept relatively low in both verification studies, to $m^* = 2$ and $0.5 < m^* < 10$. The damping ratio was also very low or even set to zero in the laminar free-vibration simulations: $\zeta = 0.007$ and $\zeta = 0$. In the turbulent free-vibration studies, both these parameters have been increased for two reasons. The first reason was based on estimation of a realistic mass and damping ratio, based on the modal mass and damping values of a wind turbine tower, assuming that only the first mode of response would be relevant to vortex-induced vibrations. Without going into further detail regarding these values, it was found that a non-dimensional mass of $m^* = 29.6$ and damping $\zeta = 0.003$ would be a good first approximation of the realistic values. These values represent the Standard Batch for the analysis of the free-vibration phenomenon for turbulent flows. Yet, as will be reported later, the effect of varying the mass ratio and damping ratio has been studied as well (relative to the Standard Batch). The parameters have been varied according to Approach 1 in section 4.1.3, meaning that the dimensional inflow velocity was assumed to be $U = 1[m/s]$ and from there the other (structural) parameters were obtained. The reduced velocity has been varied from $U^* = 1.88$ until $U^* = 10.74$ such that the entire lock-in regime was covered. The Reynolds number has been varied from $2.90 \cdot 10^6 < Re < 10.74 \cdot 10^6$, which corresponds to the reduced velocity sweep. All the non-dimensional values for the Standard Batch are summarized in tab. 4.17.

Non-dimensional parameter	Value
U^*	$1.88 - 10.74$
Re	$2.80 \cdot 10^6 - 1.60 \cdot 10^7$
m^*	29.6
ζ	0.003

Table 4.17: Non-dimensional parameters and values for the Standard Batch

Results of the Standard Batch Similar to the results in the laminar case, the RMS of the lift coefficient, the mean drag coefficient, the non-dimensional amplitude and the frequency ratios are shown for the turbulent free-vibration simulations. The lift RMS coefficient amplitude and mean drag coefficient for a varying reduced velocity and Reynolds number is shown in fig. 4.38. As will be demonstrated in the next sections, in some of the cases a non-harmonical lift/motion response is observed. In these cases, for comparison, it is deemed better to deduce the RMS of the lift coefficient rather than the lift force amplitude. The maximum lift RMS was found to be $C_{L,rms} = 0.985$ at $U^* = 3.22$, compared to the stationary value this yielded a magnification factor of $M_{C_L} \approx 10$. The maximum mean drag coefficient was $C_{D,mean} = 0.588$ which only lead to a magnification factor of $M_{C_D} \approx 1.5$ compared to the stationary drag coefficient. This latter magnification factor was expected to be lower since the in-line DOF was suppressed in the present analysis.

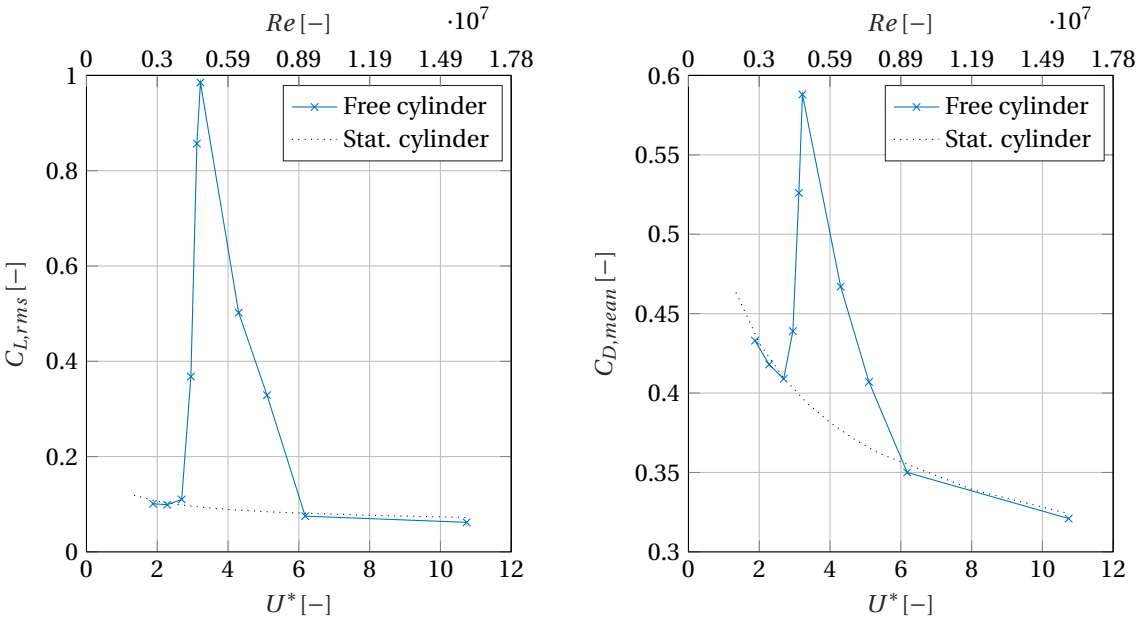

Figure 4.38. RMS of lift coefficient (left) and mean drag coefficient (right), both for the standard batch defined in 4.17

In fig. 4.39, the amplitude and frequency response are shown against the reduced velocity and Reynolds number. The maximum non-dimensional displacement was found to be $y^*_{max} = 0.519$ for $U^* = 4.30$ and corresponding Reynolds number of $Re = 6.40 \cdot 10^6$. The frequency response figure has been shown in a similar fashion as was done previously for the laminar free-vibrating case in fig. 4.13. The bandwidth of the lock-in region, illustrated by the frequency ratio of $f^* \approx 1$, was considered to be quite large. It was concluded that the observed lock-in region (by the classical definition) based on the frequency response corresponded well with the region where an increased oscillation amplitude was found. Yet, when comparing the amplitude response with the lift force, the curves were considered to be slightly different. The maximum RMS value of the lift coefficient was found for a lower reduced velocity compared to the maximum displacement amplitude. In line with that, the lock-in curve based on the lift coefficient seems to be located for a somewhat lower range of reduced velocities compared to the motion amplitudes curve. Hence, it seems the higher oscillation amplitudes have been achieved by a lower lift coefficient. The aerodynamic damping is the suspected cause for this, meaning that a bigger portion of the lift force was in phase with the velocity for the reduced velocity range of $4 < U^* < 6.5$. Therefore, relatively more energy was transferred from the wake to the cylinder. This is supported by the observations for the *forced-vibration* simulations, as will be shown in the next section.

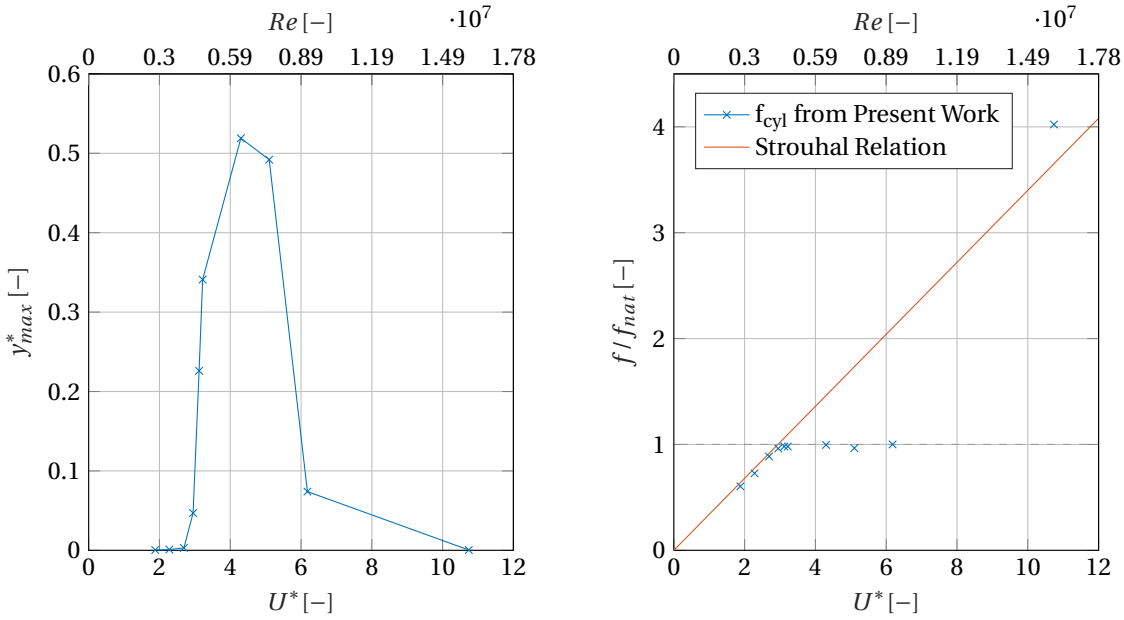

Figure 4.39. Non-dimensional displacement amplitude (left) and frequency response (right), both for the standard batch defined in 4.17

Results categorized Where for the laminar flow all the cases reached steady-state relatively fast (in 60 vortex shedding cycles), this did not hold up for all the turbulent flow simulations. The turbulent simulations, in some cases, required more than 200 shedding cycles until steady-state was reached. In some of the cases, a periodic signal was obtained, but over a very long period.

The following four Categories are defined, based on the different VIV responses observed for the Standard Batch:

1 Harmonical lift and transverse displacement signal with constant amplitude and a constant phase angle, all reached within 40 – 50 shedding cycles. The results have been observed either before the lock-in region or after the lock-in region. Both cases were located quite far away from the lock-in region such that only the stationary shedding frequency (from the Strouhal relation) was dominant.

2 An eventually harmonical lift and transverse displacement signal with constant amplitude and constant phase angle, reached after 125 – 250 vortex shedding cycles. These cases were located just before the lock-in region (or in the transformation phase), the shedding frequency was lower than the natural frequency, although closer compared to the previous Category.

3 A periodical lift and transverse displacement signal, both with varying amplitude over time. In these cases the phase angle varied as well over time, although a stable behaviour was found. The 'periodicity' of these signals amounted to ≈ 40 vortex shedding cycles. These cases were typically located inside the lock-in region.

4 A beating lift and transverse displacement signal, with multiple frequency responses and a varying amplitude. These cases were located close to the lock-in region, but for higher reduced velocities, where the shedding frequency was higher compared to the natural frequency. In these cases, the beating eventually transformed into a diverging behaviour of the cylinder motion. This Category showed an unstable response, leading to divergence.

In these Categories, harmonical should be interpreted as a periodical signal with only one constant frequency over time (for example, like a sinus signal). Still, although the frequency of the signal was constant over time, the amplitude of the signals was observed to vary in some cases. These subtle differences between the four type of results are shown in more detail in this section.

Cat. 1: Outside the lock-in region In the first Category, the Strouhal frequency is located far away from natural frequency. Hence, in this Category it is evident that the shedding frequency has been dominated by the (stationary) Strouhal frequency. Although the frequency of the lift force was relatively far away from the natural frequency, a structural motion was still observed. The peak amplitude only reached $y^*_{max} = 4.29 \cdot 10^{-4}$. This motion is caused by the 'stationary' fluid forces acting on the cylinder which moved the cylinder slightly at the Strouhal frequency. Since the Strouhal frequency and natural frequency are located too far-off each other, no lock-in or resonant response was observed. The mean drag coefficient and lift force amplitude were found to be very close to the stationary values found before, as shown in fig. 4.38.

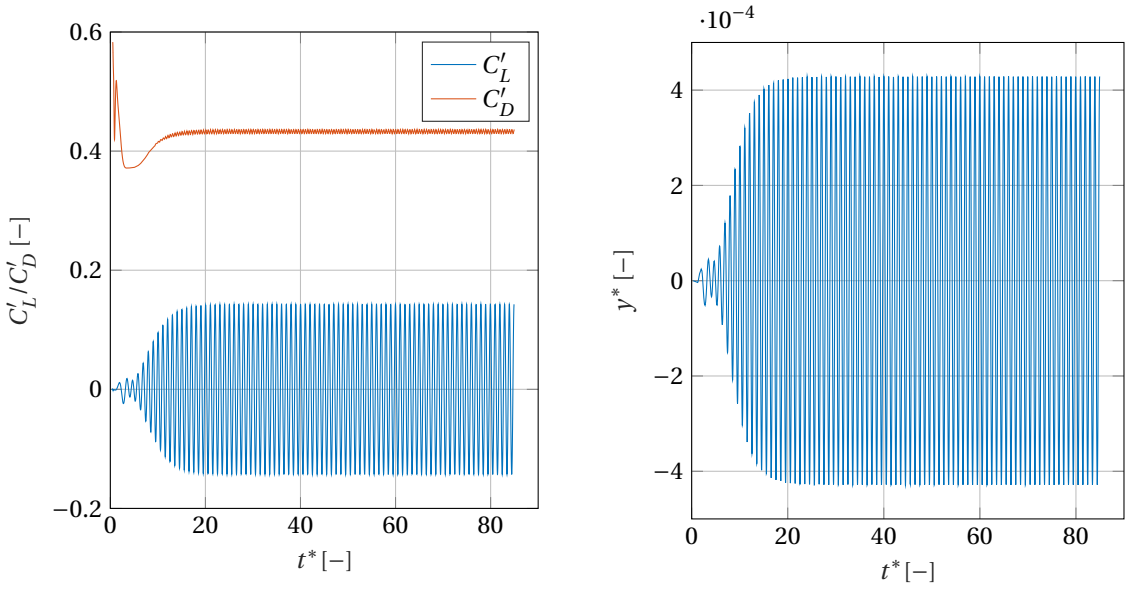

Figure 4.40. Fluctuating aerodynamic forces (left) and (non-dimensional) displacement motion (right), both for the non-dimensional values of $U^* = 1.88$, $m^* = 29.6$, $\zeta = 0.003$ and $Re = 2.80 \cdot 10^6$

The phase angle development for each cycle and the phase portrait are shown in fig. 4.41. Besides the initialization of the flow field and the transient part, the phase angle appeared to be constant: $\phi = 0°$. This constant phase angle is also reflected in the phase portrait, which showed just one fluid-motion trajectory for the entire steady-state part (for the phase portrait, the transient part was filtered out). In addition, as seen in the phase portrait, when the displacement showed a peak the lift force also showed a peak. The same holds for when the displacement was near zero. In other words, the fluid and displacement are in phase with each other. It is not surprising that a phase angle of $\phi = 0°$ was observed here. Since the wake was only governed by the Strouhal frequency, it only makes sense that the structural motion (although very small) simply tags along to this Strouhal relation assuming there is no fluid-structure interaction. The latter assumption should be valid since no signs of lock-in were observed for this case in the phase angle development, wake or force time-series. Hence, because of the Strouhal relation dictating both the wake and the cylinder motion, the fluid and motion were found to be in phase. This statement was supported by the PSD plots of the fluid and motion trajectory as well. Both the PSD's of the lift and motion displacement time series yielded only one dominant frequency peak at the (stationary) Strouhal frequency. The motion peak of the lift time series showed a higher magnitude, implying that the lift force showed a stronger periodical behaviour corresponding to the Strouhal relation.

The vorticity wakes for two cases outside the lock-in regime are presented in fig. 4.42. Both subfigures in fig. 4.42 represent the Category 1. The left subfigure was taken before the lock-in (smaller U^*) band while the right subfigure after the lock-in band (larger U^*). The angle for fig. 4.42a was constant over time and close to zero, i.e. $\phi \approx 0°$ as shown in fig. 4.41. The phase angle for fig. 4.42b showed a similar development over time but had a different magnitude: $\phi \approx 180°$.

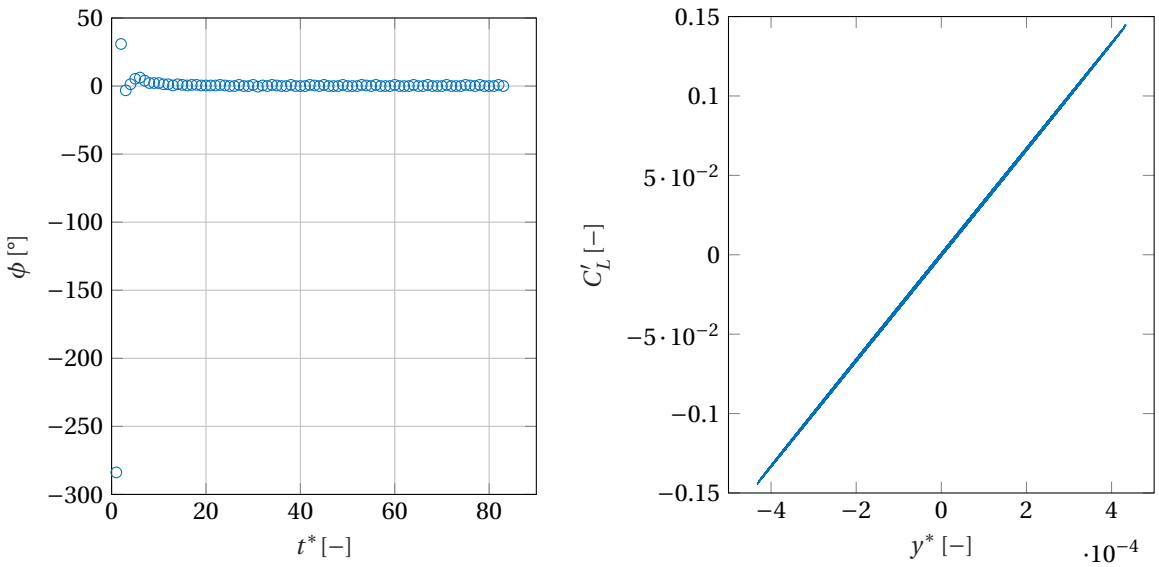

Figure 4.41. Phase angle development over time (left) and (non-dimensional) phase portrait of the steady-state signal (right), both for the non-dimensional values of $U^* = 1.88$, $m^* = 29.6$, $\zeta = 0.0033$ and $Re = 2.80 \cdot 10^6$

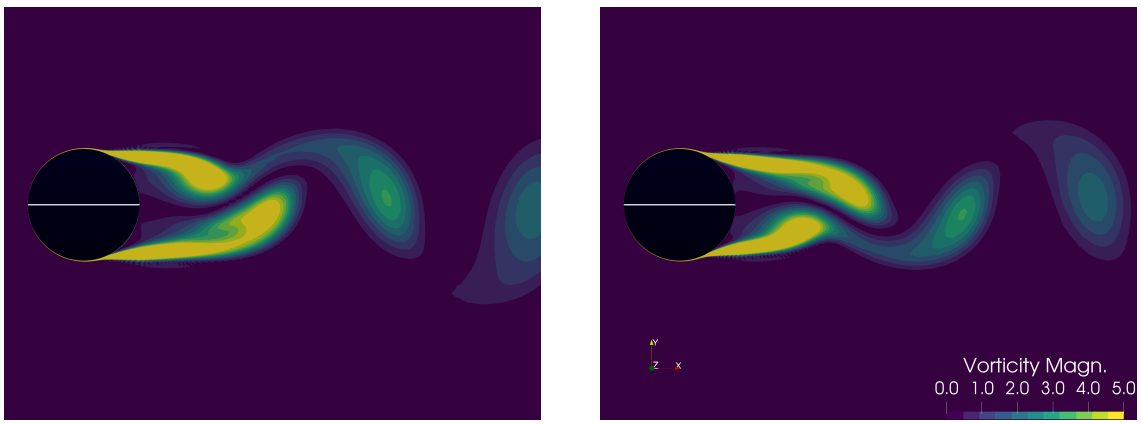

(a) $U^* = 1.88$, $m^* = 29.6$, $\zeta = 0.0033$ and $Re = 2.80 \cdot 10^6$

(b) $U^* = 10.7$, $m^* = 29.6$, $\zeta = 0.003$ and $Re = 1.6 \cdot 10^7$

Figure 4.42. Instantaneous (non-dimensional) vorticity magnitude ($|\frac{\xi D}{U_\infty}|$) outside the lock-in band at the maximum, positive displacement. Vorticity range has been filtered to $\frac{\xi D}{U_\infty} = 0 - 5$.

Based on fig. 4.42, the following observations were made:

- Both wake patterns look similar to the patterns of the stationary wake from fig. 4.26. In fact, the timing of the vortex shedding relative to the computed *lift forces* was found to be identical to the stationary cylinder case. In addition, the 2S wake pattern is present in this vorticity plot as well.
- Fig. 4.42a corresponded well with fig. 4.26b and fig. 4.42b with fig. 4.26d.
- While the timing of these wake patterns relative to their *lift forces* was the same, the timing relative to the *cylinder motion* was not the same.
- Both images were taken when the cylinder was at its maximum displacement and appeared to be a mirror image of each other. This mirror image confirms the phase angle difference of $\phi \approx 180°$.
- The trend of a positive phase angle corresponding to a vortex being shed at the opposite side of the cylinder oscillation's side is again confirmed in this case. The phase angle of $\phi \approx 180$ corresponding to fig. 4.42b shows that the vortices indeed depart from the lower side of the cylinder while the cylinder is at its positive maximum. Vice versa happened for the case with a phase angle of $\phi = 0°$.

It seems that the phase angle has switched to the typical positive value of $\phi > 100°$ found in the literature [106], [30] and [15] after the lock-in band is passed. The two former studies yielded a phase angle of around $\phi \approx 180°$. Yet, other studies have also shown a different phase angle behaviour for the lock-in range, for example [4] yielded a negative phase angle for higher U^*.

Cat. 2: Closely before lock-in Just before lock-in, the lift and cylinder displacement time series showed a different response compared to the previous Category. In this Category, the motion displacement is substantially higher. Furthermore, the wake and cylinder motion showed two dominant frequency responses in contrast to only one dominant peak in the previous Category. In fig. 4.43, the force (left subfigure) and displacement history (right subfigure) are shown.

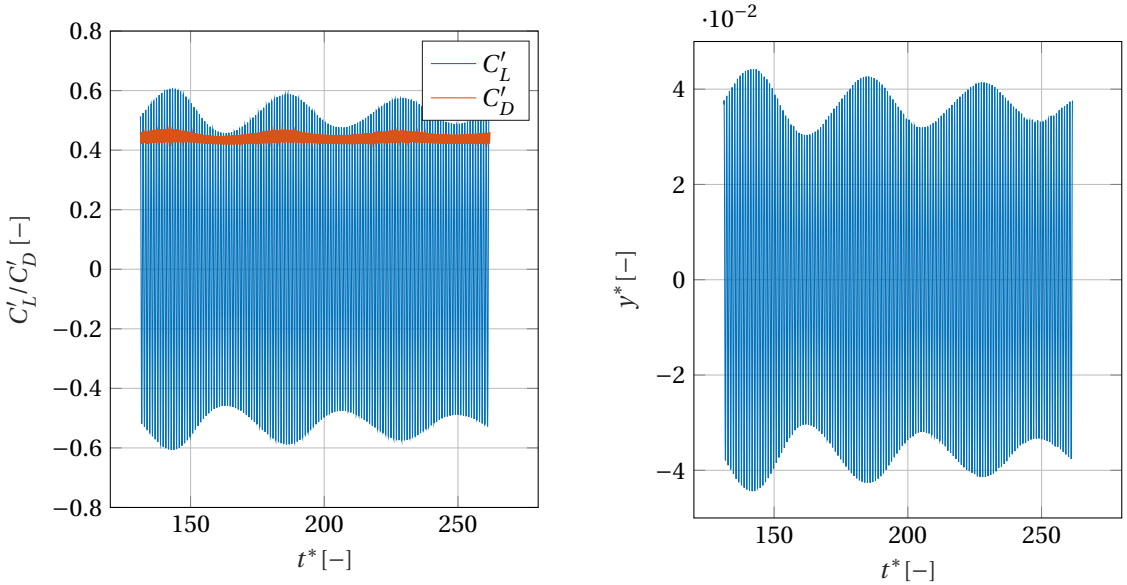

Figure 4.43. Fluctuating aerodynamic forces (left) and (non-dimensional) displacement motion (right), both for the non-dimensional values of $U^* = 2.95$, $m^* = 29.6$, $\zeta = 0.003$ and $Re = 4.40 \cdot 10^6$

The lift force became around 7 times larger compared to the previous Category, which was outside the lock-in band. The motion amplitude increased by two orders of magnitude compared to the previous case. These two increments already show a glimpse of how this Category is approaching the lock-in regime more closely compared to the previous Category. The increased reduced velocity brought the natural frequency closer to the shedding frequency (Approach 1 of section 4.1.3). These operating conditions enhanced the energy transfer from the fluid to the structure, which in turn increased the motion response. Still, the two PSD plots extracted from the lift and motion time series yielded only one dominant peak at the Strouhal frequency and hence the wake was governed by the Strouhal relation. A very small, second frequency peak

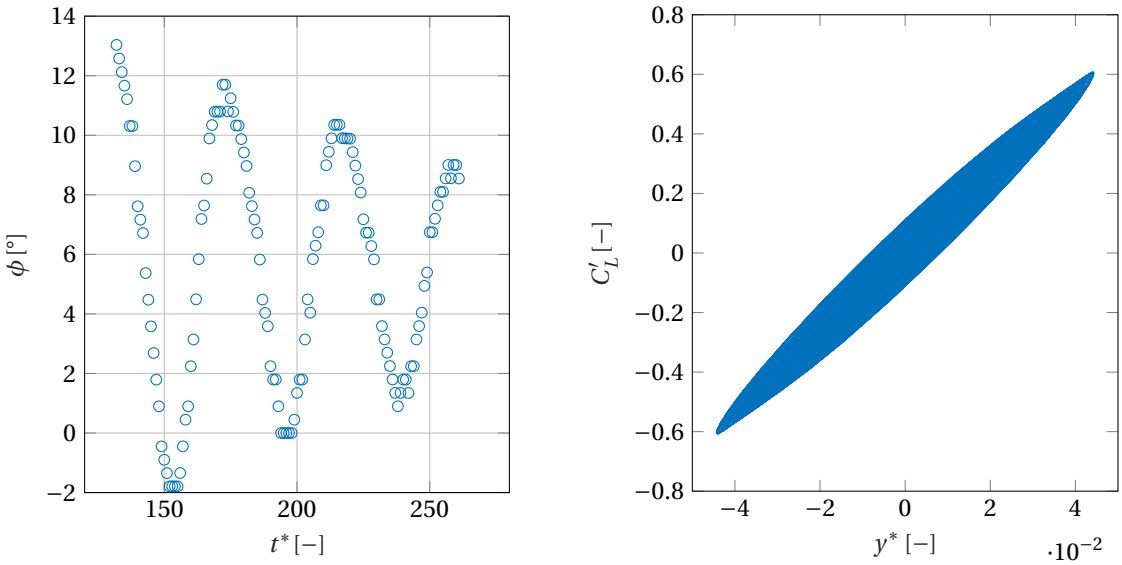

Figure 4.44. Phase angle development over time (left) and (non-dimensional) phase portrait of the steady-state signal (right), both for the non-dimensional values of $U^* = 2.95$, $m^* = 29.6$, $\zeta = 0.003$ and $Re = 4.40 \cdot 10^6$

was found in the motion PSD around the natural frequency. This relatively small natural frequency response was already enough to increase the cylinder motion by two orders of magnitude.

The development of the lift force coefficient and cylinder displacement over time in fig. 4.43 also differed compared to the previous Category. In these time series, the lift coefficient and non-dimensional amplitude are showing a varying amplitude over time. The amplitudes showed a continuous alteration of increment and decrement while slowly converging towards a constant amplitude. Because of the limited computational resources, these simulations were not finished. Yet, it was expected that the amplitude would reach a constant level at a certain t^* for $t^* > 250$. When this latter condition is reached, equilibrium may be expected between the fluid and structure. In the timeframe of fig. 4.43, the energy transfer between the fluid and the structure is still varying over time. When there was a net energy transfer from the fluid to the structure, the non-dimensional amplitude started to increase and vice versa.

The corresponding phase angle development and phase portrait of fig. 4.43 is displayed in fig. 4.44. The phase angle seemed to fluctuate periodically around a mean phase angle of $\phi_{mean} \approx 5°$. When the phase angle was above the mean phase angle, the aerodynamic damping was higher and the fluid was exciting the cylinder more. Contrary, when the phase angle was below the mean value, the fluid was damping the cylinder motion. Therefore, the oscillations observed in the phase angle development in fig. 4.44 were found to be in line with the earlier lift force and cylinder motion oscillations shown in fig. 4.43. Each peak of the phase angle in fig. 4.44 was found to be located around the steepest lift force/cylinder displacement increment (largest positive slope) in fig. 4.43. Similar to the expected equilibrium conditions of the lift force and motion amplitude stated before, it was expected for $t^* > 250$ the phase angle would reach a constant plateau as well at a certain time instant (similar to the plateau observed in fig. 4.41). The phase portrait does not show one unique cycle as was observed in the previous Category. This means that the lift force and structural displacement are changing continuously over time and do not show a unique relative trajectory. Still, the overall shape of the phase portrait indicated that lift force and cylinder displacement should be in phase with each other, or at least close to that. Indeed, the estimated mean phase angle of $\phi_{mean} = 5°$ demonstrated that the lift force and structural motion are nearly in phase with each other. It may be expected once the phase angle becomes constant and equilibrium is reached, the phase portrait would also show a unique trajectory similar to the one plotted in fig. 4.41.

Cat. 3: Inside the lock-in region Inside the lock-in region, the aerodynamic forces and structural motion showed a periodical behaviour but with varying amplitude over time, as shown in fig. 4.45. While in the previous Category, the lift coefficient reached a maximum of $C_{L,max} = 0.69$, in this Category inside the lock-in band the lift coefficient reached a maximum of $C_{L,max} = 2.22$. Increasing the reduced velocity from $U^* = 2.95$ to $U^* = 3.12$ lead to a substantial lift magnification of $M_{C_L} \approx 3.2$. The motion amplitude showed an even more

impressive increment; one order of magnitude compared to the previous Category. Hence, the transition from Category 2 (at the border of the lock-in band) to Category 3 (inside lock-in band) particularly impacted the structural displacement.

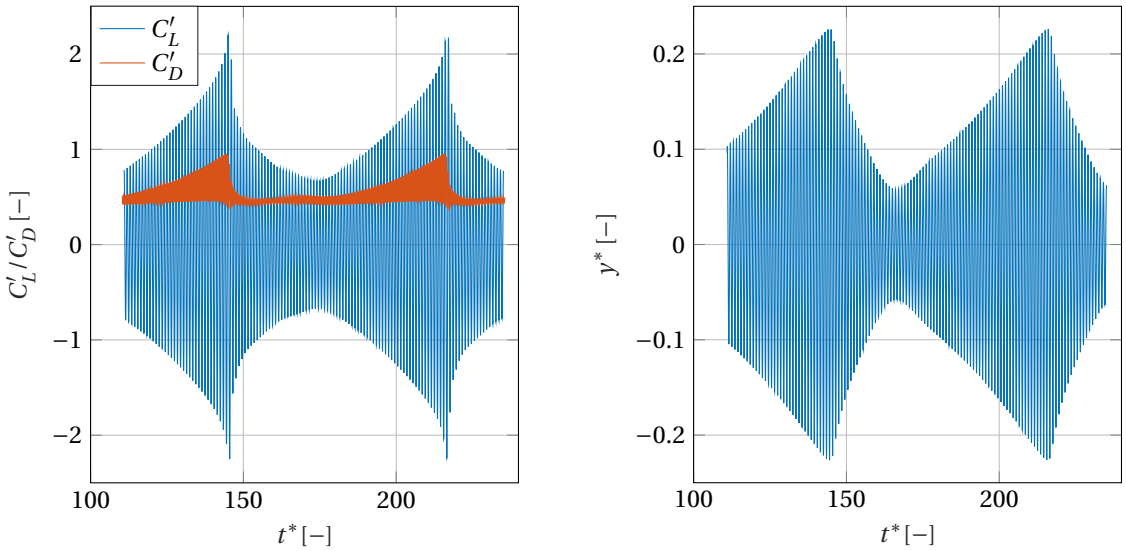

Figure 4.45. Fluctuating aerodynamic forces (left) and (non-dimensional) displacement motion (right), both for the non-dimensional values of $U^* = 3.1$, $m^* = 29.6$, $\zeta = 0.003$ and $Re = 4.60 \cdot 10^6$

The PSD plots of the lift and motion trajectory both showed one dominant peak around the natural frequency. This is the first case where the wake was governed by the structural oscillations rather than the Strouhal relation. A secondary, smaller frequency peak was observed for both the lift and motion PSD's. Interestingly, the smaller peak for the lift time series was located further away from the Strouhal frequency while for the motion PSD the opposite was true. The fact that the secondary lift frequency peak is not located closer to the Strouhal frequency compared to the secondary motion frequency peak can be explained by two factors. Firstly, the Reynolds number has been varied accordingly to the reduced velocity sweep as was shown in tab. 4.17. The Strouhal number is dependent on the Reynolds number and therefore varied for each case with a different reduced velocity. For some of the operating conditions, the Strouhal number has been interpolated between two different cases. This interpolation might have introduced an error. Secondly, the Strouhal number for the stationary cylinder has been evaluated with loose fluid solver settings in contrast to the tight settings for the moving cases (see tab. 3.7). This difference might have caused a difference in the Strouhal number between the stationary and moving case. These two factors could have affected the Strouhal number evaluation. Hence, it is possible that the secondary frequency peak of the lift time series was located closer to the Strouhal number than the secondary motion frequency peak.

The overall phase angle development and phase portrait of this Category is shown in fig. 4.46. The phase angle variation is in line with the lift force and motion development over time. When the lift force coefficient and transverse displacement increased, the phase angle was typically positive. Vice versa when the lift force and transverse displacement were decreasing. Especially around the peaks of the lift force coefficient and transverse displacement in fig. 4.45, the phase angle dropped significantly. This drop will be explained in the subsequent sections. The phase portrait indicates that the lift force and transverse displacement tended to move generally in phase with each other. The mean phase angle was found to be $\phi_{mean} = 9°$ and supports this latter observation. Yet, there is no unique cycle, as was the case for Cat. 1 in fig. 4.41. This is caused by the continuous amplitude variation of the aerodynamic forces and structural motion.

The time series are presented again fig. 4.47, but for a smaller timeframe around the first lift/motion peak observed in 4.45 around $t/T_s = 145$. The corresponding, varying phase angle for each shedding cycle was plotted in the same figure. In this timeframe, the lift force and motion displacement showed an alternation of growth and decay. This alternation was related to a phase angle drop (see right subfigure of fig. 4.47) and wake pattern change. While for the earlier shedding cycles the phase angle was observed to be positive, it suddenly dropped to a negative value when the 146th cycle started. This phase drop is causing the aerodynamic damping to change of sign. Where the aerodynamic damping was positive for the cycles 142 – 144 it became

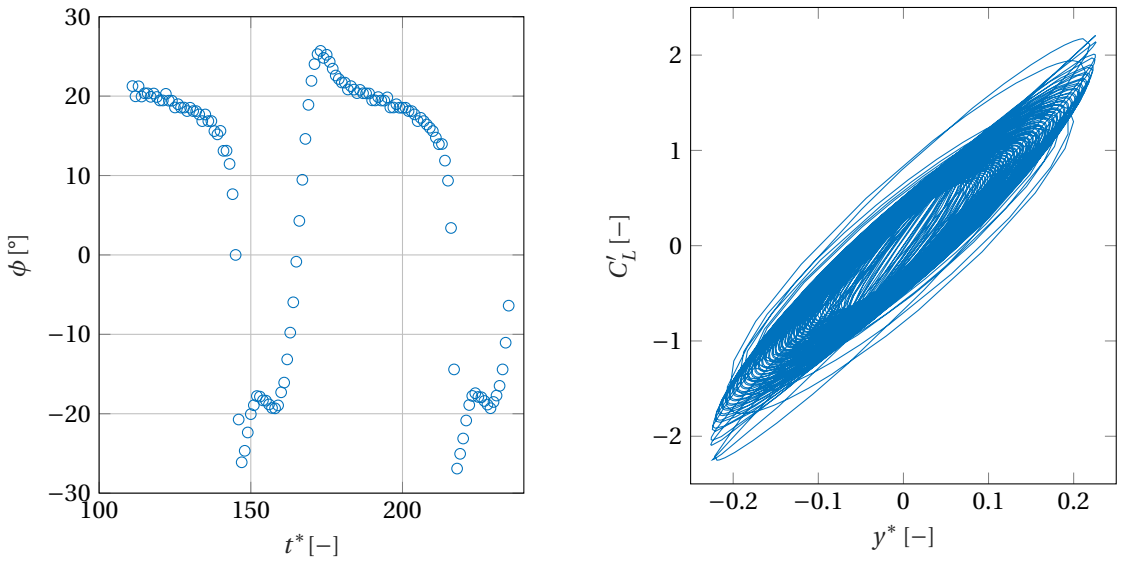

Figure 4.46. Phase angle development over time (left) and (non-dimensional) phase portrait (right), both for the non-dimensional values of $U^* = 3.1$, $m^* = 29.6$, $\zeta = 0.003$ and $Re = 4.60 \cdot 10^6$

negative for the cycles 146 – 147. Hence, in the former cycles the fluid was exciting the cylinder and during the latter cycles the fluid was damping the cylinder's motion. The phase angle evolvement can be seen back in the time series in fig. 4.47 by the relation between the lift coefficient and non-dimensional amplitude. In the earlier cycles, the lift force coefficient is *leading* the displacement which corresponds to a positive phase angle. In the last couple of cycles, the lift force starts to fall behind the motion displacement and is then said to be *lagging* behind the displacement vector. In the latter case, the phase angle was indeed negative.

Beside the relation between the lift force and motion displacement, the amplitude development is also related to the phase angle development. Where in the cycles 142 – 144 the lift force grew and the transverse displacement as well, they both started to decay once the phase angle switched sign. When the wake is exciting the cylinder, it makes sense that the cylinder vibrations would grow. Apparently, with the stronger oscillations, the lift force also tended to increase (self-excitation). Yet, at one point this self-exciting effect stopped when the phase angle switched sign. In the last couple of cycles, the amplitudes of both the lift coefficient and displacement started to decay. Apparently, a change in the wake has caused the VIV to go from a self-exciting nature to a self-limiting one.

The phase angle drop can be related to the wake pattern development shown in fig. 4.48, as was done for the forced-vibration cases. The left subfigure corresponds to the positive phase angle at $t/T_s = 143.5$ and the right subfigure to the negative phase angle at $t/T_s = 146.5$ of fig. 4.47.

When the phase angle was positive, the vortices were shed from the bottom side of the cylinder when the cylinder reached its maximum positive displacement, see fig. 4.48a. The opposite was true for when the phase angle turned negative, then the vortices shed from the same side as where the cylinder was oscillating to. It seems that at one point the cylinder motion became too big which reorganized the wake in such a way that the wake started to damp the cylinder motion. Hence, the self-exciting behaviour observed for the positive phase angles changed to a self-limiting behaviour when the wake was reorganized and the phase angle became negative. This continuous alteration between self-excitement and self-limitation is reflected in the lift force times series of fig. 4.45. No steady-state equilibrium was therefore found, where the transverse displacement amplitude and lift coefficient amplitude stayed constant (and hence the energy transfer between the fluid and the structure stayed constant).

This trend, the relation between the vortex shedding and the phase angle, was found to be in line with the observations for the forced-vibration simulations before in section 4.2.2. In fact, fig. 4.48b looks similar to the observed wake pattern in fig. 4.34c and 4.34d. Yet, the wake pattern for 4.48a does not correspond with the 'positive phase angle' wake patterns observed for the forced-vibration simulations in fig. 4.34a and fig. 4.34b. This might have to do with the fact that those latter wake patterns corresponded to a phase angle of $\phi = 19 - 20°$ while the ones presented here to a phase angle of $\phi = 10 - 14°$. Where in the forced-vibration cases the phase angle dropped directly from $\phi = 19°$ to $\phi = -22°$ when the amplitude was increased from

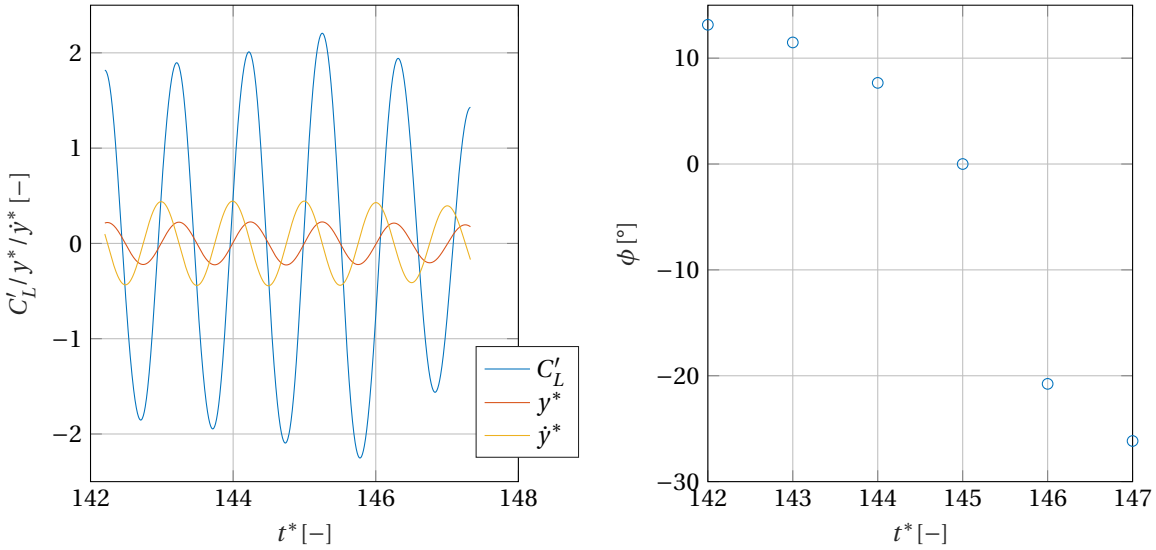

Figure 4.47. Fluctuating lift coefficient and (non-dimensional) displacement/velocity (left) and corresponding fluctuating phase angle (right) around a peak in the lift force development under the operating conditions of $U^* = 3.1$, $m^* = 29.6$, $\zeta = 0.003$ and $Re = 4.60 \cdot 10^6$

$y^*_{max} = 0.1$ to $y^*_{max} = 0.175$, for the free-vibration case the phase angle development was more gradual over time. Therefore, it may be concluded that the vortices shown in fig. 4.48a compromised a wake pattern development in between the wakes of fig. 4.34b and fig. 4.48b.

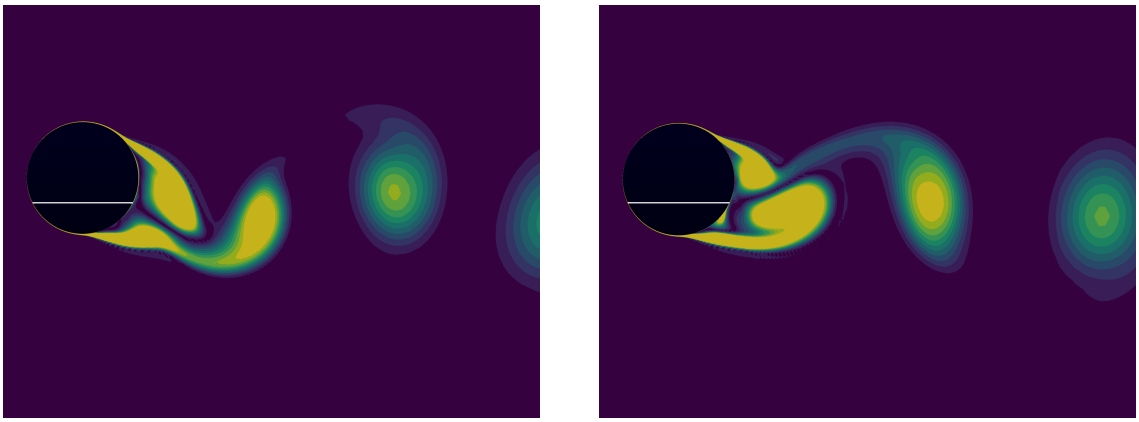

(a) $t/T_s = 143.5$ (b) $t/T_s = 146.5$

Figure 4.48. Instantaneous (non-dimensional) vorticity magnitude ($\left|\frac{\xi D}{U_\infty}\right|$) at the maximum, positive displacement. Vorticity range has been filtered to $\frac{\xi D}{U_\infty} = 0-5$. Cases obtained under following non-dimensional operating conditions: $U^* = 3.1$, $m^* = 29.6$, $\zeta = 0.0033$ and $Re = 4.64 \cdot 10^6$.

Cat. 4: Closely after lock-in Closely after lock-in, in contrast to the previous three Categories, the wake and structure did not reach a stable equilibrium. In fig. 4.49, the lift force, drag force and transverse displacement are shown. As can be seen from these figures, the fluctuating forces and structural motion were still developing when the simulation was stopped. In fact, prior to this simulation a lower oscillation amplitude and lift coefficient were expected. This Category is in the reduced frequency range of $0.5 < f^* < 0.7$ compared to the range of $1.2 < f^* < 0.9$ for Category 2 and 3. Because these latter two Categories were located more closely to the critical frequency, it was expected these Categories would show the highest oscillations amplitudes and lift forces. Nevertheless, it has been reasoned the simulations for Category 4 were not experiencing numerical divergence. In fact, the transverse velocity error of the last PIMPLE loop has been monitored closely

(right subfigure in fig. 4.50). As can be seen from this figure, the velocity error stayed well below the desired threshold of 10^{-5}. One 'peak' error is shown in fig. 4.50, however it is expected this peak was caused by a post-processing error. The fluid solver converged each timestep and the specified non-linear tolerance criteria of 10^{-6} was reached every timestep for the fluid. The fluid convergence (and indirectly structural convergence) was typically reached after $3-4$ subiterations. Because of the motion solver's implementation within *OpenFOAM* (see section 3.2.2), the structural convergence observed the right subfigure of fig. 4.50 also guarantees that the FSI coupling has been solved adequately. Furthermore, an additional identical case with 10 subiterations has been run. It appeared this even more strongly coupled case did not prevent the divergence from happening, which also supports there was no numerical divergence. It was believed the divergence was feasible and this has been explained by the following steps:

- The Category 4 cases are located around a frequency ratio of $0.5 < f^* < 0.7$ which initially triggered a beating phenomenon where the wake was continuously switching between following the Strouhal relation or the cylinder motion (for $225 < t/T_S < 350$ in fig. 4.49, beating further explained in section 4.1.3).
- It was known from the *forced-vibration* simulations of before that the operating range of $0.5 < f^* < 0.7$ yielded potentially unstable trajectories for the system (shown in fig. 4.37). In this bandwidth, the aerodynamic damping keeps on increasing with growing oscillation amplitudes. Therefore, the relatively small rise of the transverse oscillations as a result from the beating opened the possibility of undergoing an unstable trajectory where the aerodynamic damping would only excite the cylinder even more.
- Eventually, the beating phenomenon stopped and the wake fully adapted to the cylinder's natural frequency: one dominant PSD peak was observed located at the natural frequency for the lift force signal (for $t_T/s > 350$ only one sinus signal can be seen in fig. 4.49 and fig. 4.50 shows indeed one dominant peak in the PSD of the lift signal).
- The self-excitation is expected to continue until the cylinder reaches an amplitude where the aerodynamic damping starts to become negative again. The simulation was stopped when the oscillation amplitude reached $y^*_{max} > 0.5$. Since the contour map of the forced-vibration simulations considered an operating grid up to $y^*_{max} = 0.25$, it is not known if (and when) a negative aerodynamic damping would occur somewhere along the trajectory. The simulation was stopped because of the considerable amount of computational time and power required to further continue this run, while not knowing if an equilibrium would be reached after all.
- It may be concluded the damping coefficient ζ was not large enough to suppress the aerodynamic excitement of the wake. Even though at lower amplitudes, as shown in fig. 4.37, when the aerodynamic excitement was still relatively low the system's damping was not able to phase out the oscillations. Ideally, the damping coefficient should be matched to at least the value of the positive aerodynamic damping reached at the first isoline in the contourmap.

It may be questioned if the contour map obtained by the *forced-vibration* experiments can be considered as a reliable source of information. The predicted aerodynamic damping coefficients have been compared against the results from a supercritical wind-tunnel experiment before in fig. 4.35 and 4.36. Although in some cases the magnitude might differ, the behaviour of the aerodynamic damping for a varying frequency ratio was considered to be similar. In fact, the wind-tunnel experiment of [2] also observed an unstable trajectory at a frequency ratio of $f^* = 0.965$. In addition, in fig. 4.36 it was shown that the CFD results agreed well with the experiment before the lock-in band (except for the lowest amplitude). Hence, the observed aerodynamic behaviour in the contour map was deemed as a reliable source of information to explain observed divergence here for the *free-vibration* experiment.

Another aspect of the above reasoning which might attract some discussion is the plausibility of the cylinder vibrating at a frequency ratio of $f^* = 0.7$. Various numerical and experimental studies in the literature showed similar broad lock-in ranges, where the non-dimensional amplitude reached values of $y^*_{max} > 0.5$ as well for these low frequency ratios. For example, the numerical study of [106] also yielded a broad lock-in map. Yet, the latter study was performed at a lower mass ratio and Reynolds number. The 2-DOF experimental study of [107] showed a similar broad lock-in band as [106]. The wind-tunnel study of [30] also showed a lock-in region extending to a frequency ratio of $f^* = f_{nat}/f_{shed,stat} = 0.6$. The DPIV experiment of [108] observed a distinction between a two-branch and three-branch response, based on the non-dimensional amplitude versus reduced velocity response. The distinction was related to the mass-damping parameter,

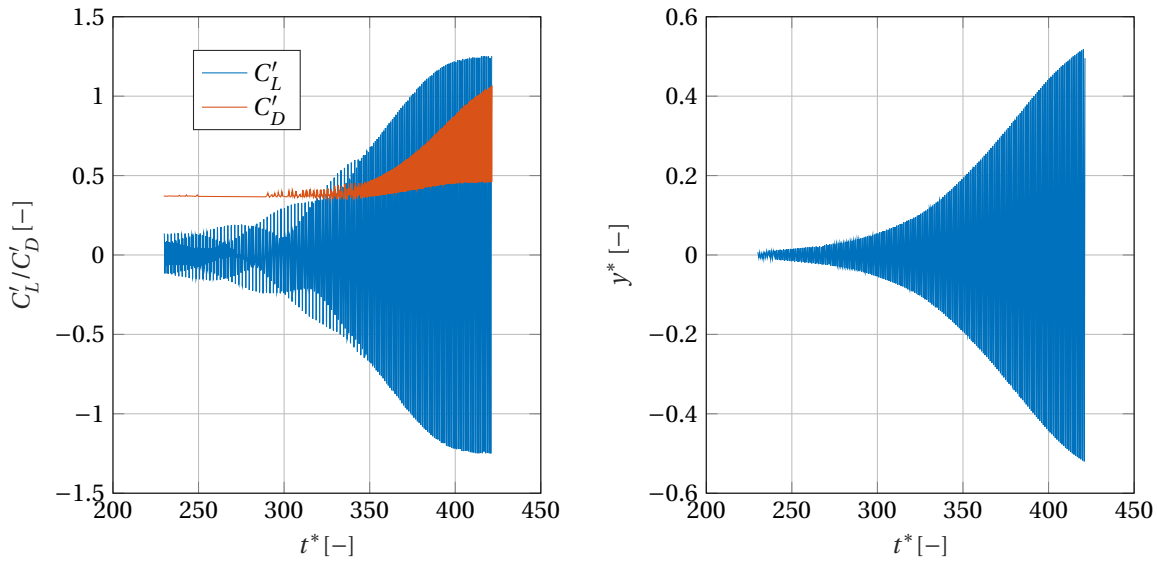

Figure 4.49. Fluctuating aerodynamic forces (left) and (non-dimensional) displacement motion (right), both for the non-dimensional values of $U^* = 4.30$, $m^* = 29.6$, $\zeta = 0.003$ and $Re = 6.40 \cdot 10^6$

where a low value typically leads to the three-branch response with a significantly broader lock-in range and also the 2P wake mode. The latter wake mode has been observed in the present research as well and has been shown in the next section which considered the mass coefficient effect. Hence, although usually at lower Reynolds numbers and mass-damping values, plenty of VIV studies found in the literature showed similar broad lock-in ranges as was found in the present research. In fact, the book of [3] noted the vortex-shedding frequency might shift towards the natural frequency 'by as much as ±40%', when the oscillation amplitudes are large. Hence, it is highly possible the stationary wake was strong enough to initialize and trigger the cylinder movement, although the operating conditions were 30% off the critical frequency. Eventually, the cylinder oscillations became strong enough (partly because of the aerodynamic excitation) such that the shedding frequency started to follow the natural frequency (lock-in).

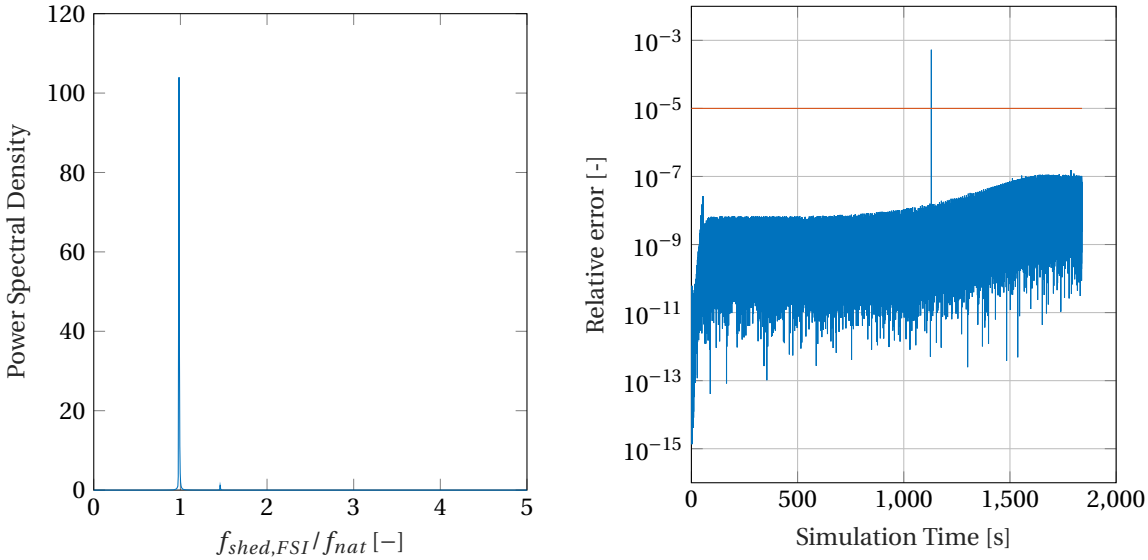

Figure 4.50. Power-spectral density of the fluctuating lift coefficient (left) and relative velocity error (right) for the following operating conditions: $U^* = 4.30$, $m^* = 29.6$, $\zeta = 0.003$ and $Re = 6.40 \cdot 10^6$

Effect of mass coefficient on VIV The Standard Batch of CFD cases was defined before in section 4.2.3 in tab. 4.17. The first sensitivity analysis on the Standard Batch has been dedicated to investigate the effect of the mass coefficient on the lift forces and transverse displacement. This resulted into four additional cases analysed for three different reduced velocities. Because of the large computational cost, only three operating points of the previous batch have been analysed for a different mass coefficient: $\mathbf{U}^* = (2.95 \quad 3.12 \quad 3.22)$. These three operating points corresponded to the previously defined Categories 2 and 3 and are therefore either located closely before the lock-in band or are inside the lock-in band. Out of all the operating points it was deemed as most interesting and relevant to the present research to further analyse the sensitivity of certain parameters when lock-in was present (or at least starting to become present). When the simulations were started for this sensitivity analysis, it was expected Category 2 and 3 would entail the lock-in region as best. However, as the simulations of Category 4 appeared to eventually yield higher oscillation amplitudes it would have been relevant as well to conduct the sensitivity study for this Category. No sensitivity analysis has been done for Category 4.

For the sensitivity analysis, the standard mass coefficient of $m^* = 29.6$ has been multiplied by $\mathbf{M}_{m^*} = (8.6 \quad 2 \quad 0.5 \quad 0.085)$ which yielded the following mass coefficients: $\mathbf{m}^* = (254.6 \quad 59.2 \quad 14.8 \quad 2.5)$. The idea was to investigate one very large and one very small mass coefficient, while also investigating some cases in between to see if there is a relation between the mass coefficient and the results. Similar to tab. 4.17, the mass-sensitivity cases have been tabulated in tab. 4.18 for a clear overview. In total, 9 additional cases have been run compared to the Standard Batch.

Non-dimensional parameter	Value
$\mathbf{U}^*$	$(2.95 \quad 3.12 \quad 3.22)$
Re	$4.4 \cdot 10^6 - 4.8 \cdot 10^6$
$\mathbf{m}^*$	$(2.5 \quad 14.8 \quad 29.6 \quad 59.2 \quad 254.6)$
ζ	0.003

Table 4.18: Non-dimensional parameters and values for the mass coefficient sensitivity study

The results of the mass sensitivity study have been shown in fig. 4.51. Regarding the effect of the mass coefficient on the displacement amplitude, the results were as expected. Each time the mass coefficient was lowered, the non-dimensional amplitude increased. This can be explained by the fact that a lower mass ratio leads to a lower structural inertia compared to the fluid inertia. This in turn made the cylinder more susceptible to oscillations and possibly lock-in. In the present sensitivity study, the effect on the lock-in band has not been investigated because of the large computational power required to compute the full lock-in curve again for different mass ratios. Based on fig. 4.51, it may be concluded increasing the mass coefficient would at one point lead to a motion-fluid response which is similar to the one of a stationary cylinder. This reasoning was supported by the fact the lowest two mass coefficients did not lead to a major difference in response. In other words, there is a critical mass ratio which prevents the system of undergoing an enhanced fluid-structure interaction.

The middle two curves, for $m^* = 29.6$ and $m^* = 14$ both showed an increasing trend with increased reduced velocity, while the curve for $m^* = 2.5$ implied a ceiling. As will be shown further ahead in this section, it appeared the highest mass coefficient led to a different type of response for some of the operating points. This different response might have led to a different lock-in curve as well. The sensitivity of the motion amplitude to the mass coefficient was not linear at all. The sensitivity was different for each of the operating conditions and is therefore hard to generalize.

The effect of the mass coefficient on the lift force is a bit different compared to the effect on the motion amplitude. The curve for $m^* = 2.5$ was different. In fact, where the motion amplitude grew when the mass coefficient was lowered from $m^* = 14.8$ to $m^* = 2.5$, the lift coefficient showed a different trend. For $U^* = 2.95$ the lift force indeed increased, but for $U^* = 3.12$ it barely increased and for $U^* = 3.22$ it decreased. It turned out the aerodynamic damping relative to lift coefficient magnitude for both mass ratios $m^* = 14.8$ and $m^* = 2.5$ at $U^* = 3.2$ was quite low, which means the aerodynamic damping could not have caused this counter intuitive result. Yet, it was believed the counter intuitive result was caused by the dynamic state which was reached for both mass ratios. The mass ratios of $m^* = 29.6$ and $m^* = 14.8$ led to a more dynamic fluid-structure interaction, where the lift coefficient was able to reach higher peak values. This effect is clearly visible in fig. 4.52 between the responses for $m^* = 14.8$ and $m^* = 2.5$. Besides the lift RMS curve for $m^* = 2.5$

which differed slightly, the other curves agreed well with the curves observed for the motion amplitude in fig. 4.51.

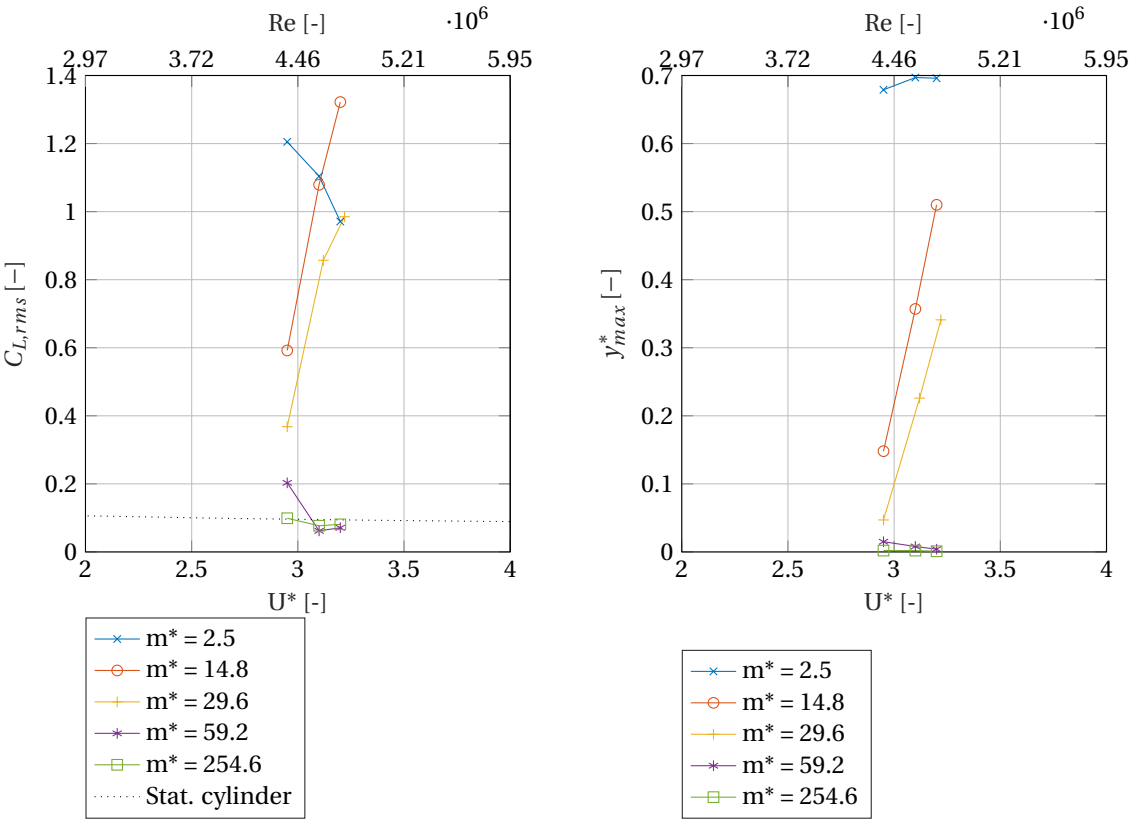

Figure 4.51. RMS of lift coefficient (left) and (non-dimensional) transverse motion amplitude (right), both results for the mass sensitivity study of tab. 4.18

For $U^* = 2.95$, the lift coefficient and motion displacement time-series are shown in fig. 4.52. The following observations were made:

- A larger mass coefficient leads to a smaller lift coefficient and non-dimensional displacement, as was earlier shown in fig. 4.51.
- A larger mass coefficient also leads to a steadier, harmonical signal. The only exception to this observation is the case with the lowest mass coefficient of $m^* = 2.5$ where a stable amplitude is reached after the transient part.
- It seemed the cylinder was more inclined to stick to its dynamic equilibrium (steady-state) at higher mass coefficients. The beating phenomenon or other non-harmonical behaviour were less likely to occur as the larger inertia prevented the cylinder from changing to a different dynamic state. In other words, the energy transfer between the cylinder and the fluid remained more constant for a higher mass coefficient.

Similar to fig. 4.52, the time series for the lift coefficient and transverse displacement are displayed in fig. 4.53 for $U^* = 3.10$. The results for $U^* = 3.20$ were quite similar to the results for $U^* = 3.10$, therefore these results have not been plotted here (note that both operating points were from Category 3).

Comparing fig. 4.53 ($U^* = 2.95$) with fig. 4.52 ($U^* = 3.10$) lead to the following observations:

- When the mass coefficient was $m^* = 2.5$, the force time series and dynamic state does not seem to vary much when the reduced velocity was varied between $\mathbf{U}^* = (2.95 \quad 3.10)$. This could indicate the lock-in band has increased with a lower mass coefficient, leading to indifferent results when the reduced velocity is only varied slightly. Also quantitatively, the non-dimensional transverse displacement amplitudes and lift coefficient amplitudes were found to be in the vicinity of each other at $m^* = 2.5$ (see fig.

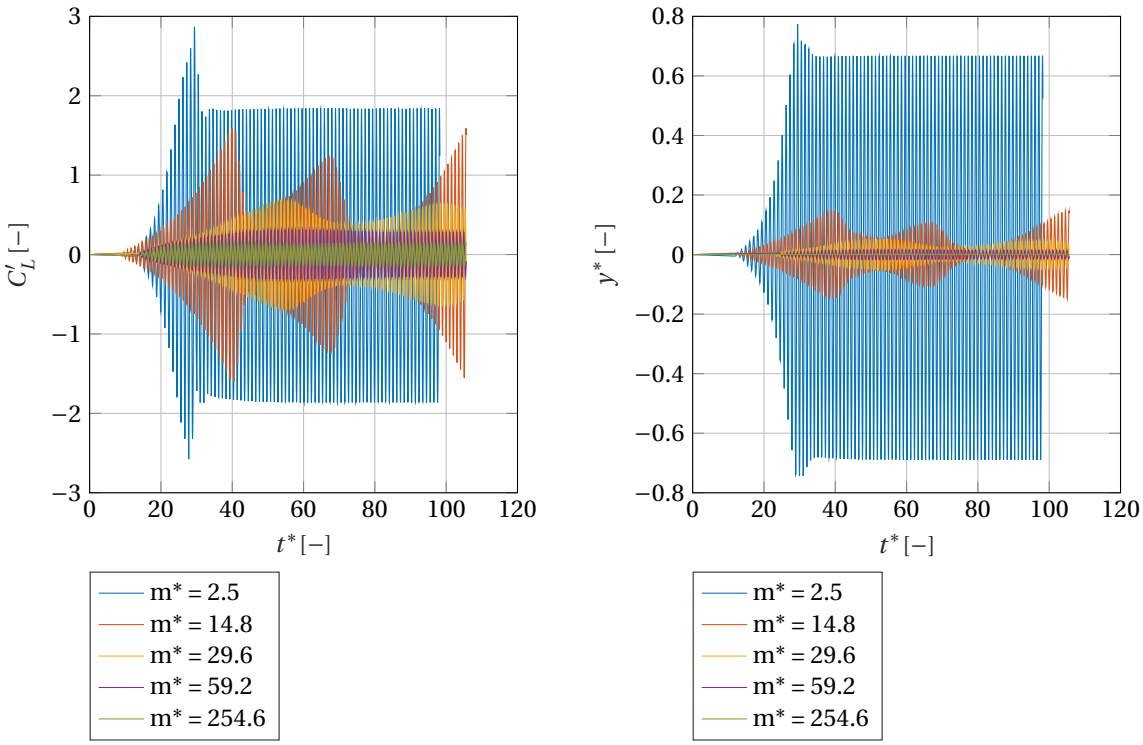

Figure 4.52. Fluctuating lift coefficient (left) and (non-dimensional) displacement (right), under the operating conditions of $U^* = 2.95$, $\mathbf{m}^* = (2.5 \quad 14.8 \quad 29.6 \quad 59.2 \quad 254.6)$, $\zeta = 0.003$ and $Re = 4.4 \cdot 10^6$

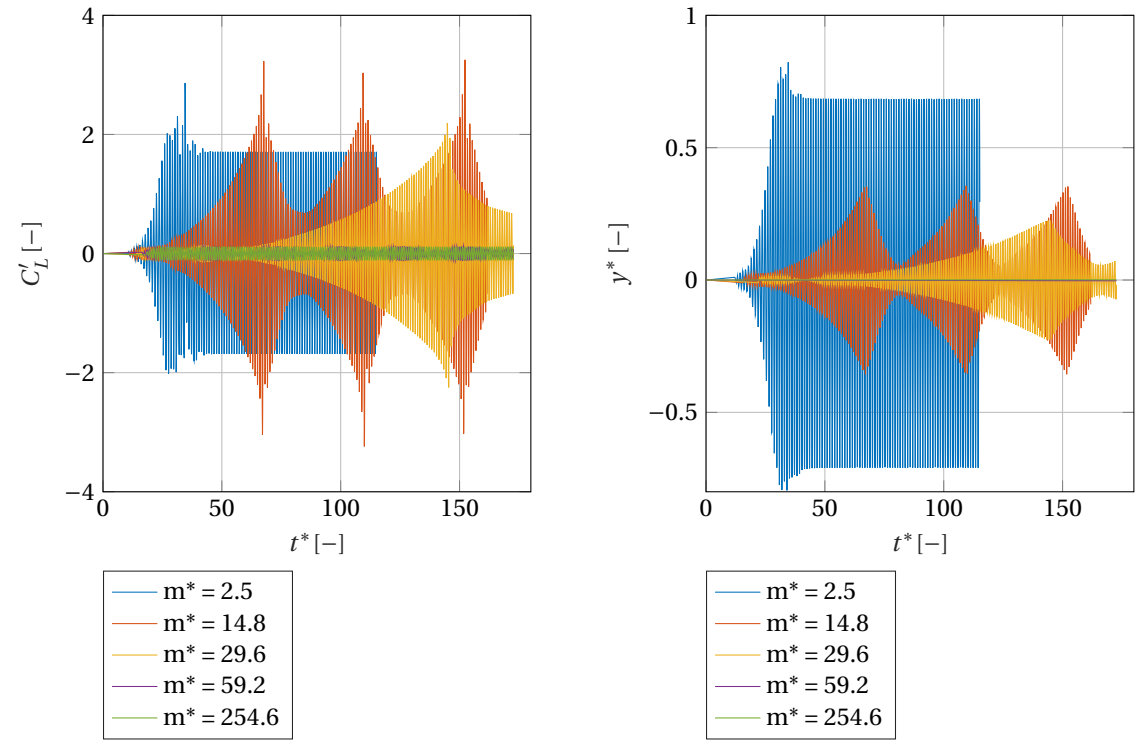

Figure 4.53. Fluctuating lift coefficient (left) and (non-dimensional) displacement (right), under the operating conditions of $U^* = 3.10$, $\mathbf{m}^* = (2.5 \quad 14.8 \quad 29.6 \quad 59.2 \quad 254.6)$, $\zeta = 0.003$ and $Re = 4.4 \cdot 10^6$

4.51). With such a low mass coefficient, lock-in was established fairly quickly. The shedding frequency showed a strong response close to the stationary shedding frequency instead of close to the natural frequency. This would imply the cylinder was not in lock-in mode according to the definition stated in section 2.2.4.

- When the mass coefficient was $m^* = 254.6$, the aerodynamic forces and dynamic state seemed to be insensitive as well to the change of the reduced velocity between $\mathbf{U}^* = (2.95 \quad 3.10)$. This time, the shedding frequency showed a weak response (compared to the lower mass coefficients) and followed the stationary shedding frequency very closely $f_{shed,FSI}/f_{shed,stat} \approx 1$ rather than the natural frequency $f_{shed,FSI}/f_{nat} = 0.98$. The higher mass coefficient yielded a very stiff system which the fluid forces could not initiate to move significantly and therefore the wake tended to follow the stationary Strouhal relation.
- For both reduced velocities of $\mathbf{U}^* = (2.95 \quad 3.10)$, it was reasoned that the mass ratios of $m^* = 14.8$ and $m^* = 29.6$ allowed the fluid-structure system to develop in a more dynamic way where energy transfer between fluid and structure was not constant.
- It has appeared the Categories defined earlier in section 4.2.3 are no longer applicable for either very high or very low mass coefficients. It seemed the aerodynamic forces and dynamic state converged to a similar solution over the range of reduced velocities investigated here: $\mathbf{U}^* = (2.95 \quad 3.12 \quad 3.22)$ when the mass coefficient is either very high (which approaches a stationary cylinder) or very low (which approaches a cylinder supposedly strongly in lock-in mode although the frequency response did not show this).

Interesting wake patterns have been identified for the lowest mass coefficient cases with $m^* = 2.5$. The phase angle and phase portrait of one of these cases at $U^* = 2.95$ have been shown in fig. 4.54 (corresponding to the case with $m^* = 2.5$ in fig. 4.52). Similar to earlier findings, the phase angle was found to be positive when the lift coefficient was still growing in the beginning, transient part of the simulation. Then, when the equilibrium was found, the phase angle dropped to a lower, more constant value of around $\phi \approx 3°$. The phase portrait in fig. 4.54 indeed shows a steady-state condition with one unique lift-motion trajectory, implying a more constant phase angle.

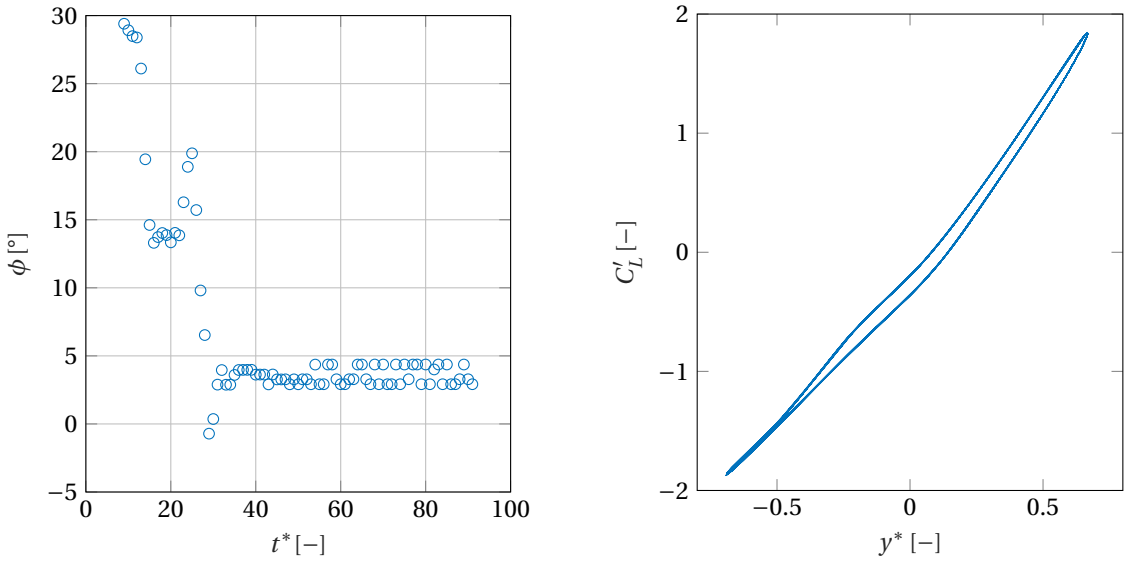

Figure 4.54. Phase angle development over time (left) and (non-dimensional) phase portrait (right), under the operating conditions of $U^* = 2.95$, $m^* = 2.5$, $\zeta = 0.003$ and $Re = 4.4 \cdot 10^6$

Only the 2S wake pattern was identified from the defined wake patterns of [15] in the vorticity contours shown before. In this specific case, with $m^* = 2.5$, the wake patterns 2P and P+S also appeared to be active. The 2P pattern was found at the $t/T_s = 27^{th}$ shedding cycle, still when the lift and displacement amplitude was growing. The phase angle was found to be $\phi \approx 19°$ there. The P+S pattern was found in the steady-state regime.

The 2P pattern, in which two vortex pairs are formed each cycle, can be identified in fig. 4.55a. First one strong vortex separates from the cylinder body and then quickly after that a smaller vortex separates as well and follows the larger vortex. The vortices lose their strength as they trail further aft from the cylinder body in the wake. It was shown in the review of [14] that some of the experiment/numerical works done before were able to show 2P/2S modes for $Re > 1000$ and some not. In fact, in the study of [106], two of the known vortex patterns (2S and 2P) have been identified in the wake by a RANS approach. It must be noted the mass ratio was only $m^* = 2.4$ in their study which is nearly the same as the presently used mass coefficient in fig. 4.55 (although the damping was one order of magnitude higher than the one used in [106]). Before, when the mass coefficient was larger, only the 2S mode was found in the wake. It is possible that the lower mass coefficient, in line with the findings of [106], made the 2P formation possible. This might be caused by the higher, transverse displacement amplitudes which were reached with the lower mass coefficient.

In the fig. 4.55b another vortex mode was seen. This vortex mode looked much alike the P+S pattern of [15], in which a vortex pair and a single vortex are being shed each cycle. First, a large vortex sheds from the cylinder body and after that three smaller vortices quickly shed as well from the body. The middle vortex of these three smaller vortices fades out relatively quick. When this happens, the P+S pattern becomes visible in the wake. Before the P+S pattern becomes apparent, it is unclear which pattern the wake with 4 vortices would resemble of the study of [15]. Although the cylinder in both subfigures of fig. 4.55 showed a similar transverse displacement, the wake pattern was different. It has been reasoned that this difference was caused again by the phase angle (and hence the state of the system).

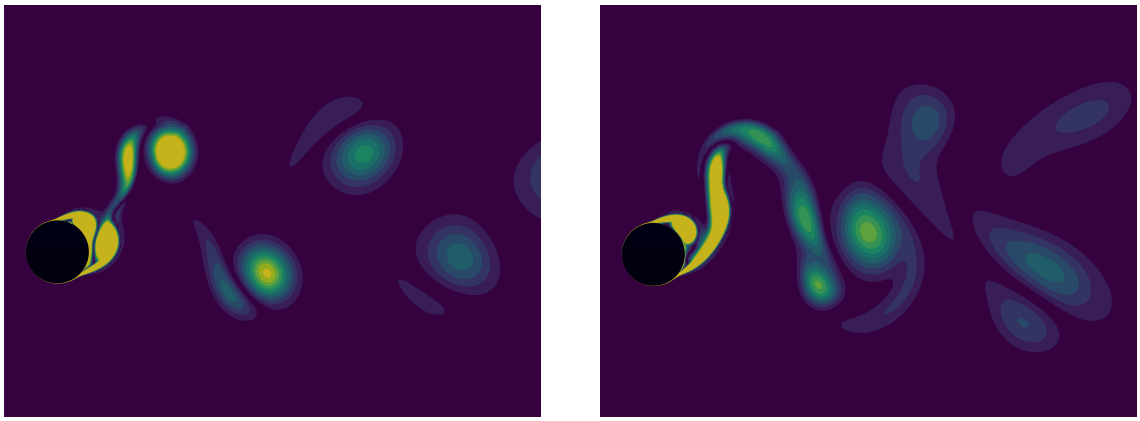

(a) $t/T_s = 27.0, y^* = -0.66, \phi \approx 19°$ (b) $t/T_s = 95.6, y^* = -0.69, \phi \approx 3°$

Figure 4.55. Instantaneous (non-dimensional) vorticity magnitude ($\left|\frac{\xi D}{U_\infty}\right|$) at the maximum, negative displacement. Vorticity range has been filtered to $\frac{\xi D}{U_\infty} = 0-5$. Cases obtained under following non-dimensional operating conditions: $U^* = 2.95$, $m^* = 2.5$, $\zeta = 0.003$ and $Re = 4.4 \cdot 10^6$.

Effect of damping coefficient on VIV Like the previous section, a sensitivity analysis has been performed on the (structural) damping coefficient. The input parameters have been tabulated in tab. 4.19. The mass coefficient corresponds to the one used for the Standard Batch. The reduced velocities are identical to ones used in the analysis on the mass coefficient, which is in the lock-in band (or close to).

Non-dimensional parameter	Value
$\mathbf{U}^*$	(2.95 3.12 3.22)
Re	$4.4 \cdot 10^6 - 4.8 \cdot 10^6$
m^*	29.6
ζ	(0.002 0.003 0.007)

Table 4.19: Non-dimensional parameters and values for the damping coefficient sensitivity study

The results for the damping sensitivity study have been shown in fig. 4.56. The lock-in curves for $\zeta = 0.002$

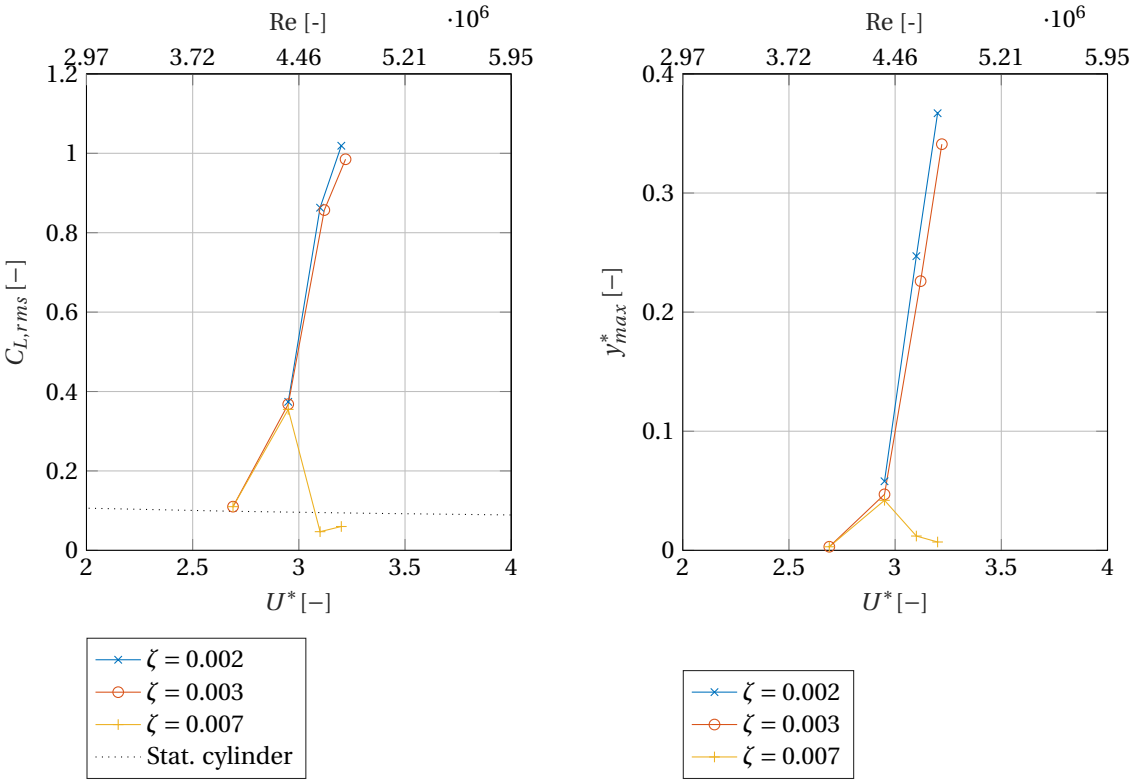

Figure 4.56. RMS of lift coefficient (left) and (non-dimensional) transverse motion amplitude (right), both results for the damping coefficient sensitivity study of tab. 4.19

and $\zeta = 0.003$ are similar. The main effect of the damping coefficient observed in these curves is on the magnitude, where a lower damping leads to a slightly larger lift coefficient RMS and motion amplitude. The results for $\zeta = 0.007$ show a different trend over the range of reduced velocities. For $U^* < 3$ it seemed the curve for $\zeta = 0.007$ agreed well with the other damping curves. Yet, for $U^* > 3$, the lock-in curve started to deviate for $\zeta = 0.007$ compared to the curves of $\zeta = 0.003$ and $\zeta = 0.002$. It has appeared, as will be shown further ahead in this section, the damping coefficient was sufficiently large to almost completely phase out the motion and wake responses observed for the lower damping curves.

Whereas the Categories defined earlier did not seem to be applicable when the mass coefficient was changed significantly, the Categories remained applicable when the damping coefficient as varied. The effect of the damping coefficient on Category 2, which is just before lock-in, is shown in fig. 4.57. The damping coefficient did not change the time series qualitatively, in contrast to the observed responses for the mass coefficient sensitivity analysis. It was found that the eventual harmonical signal that was reached in Category 2 was reached faster when the damping coefficient was higher. This can be seen back in fig. 4.57 by the less oscillatory transient part when the damping coefficient was higher.

With regards to Category 3, the effect of the damping coefficient on the aerodynamic forces and cylinder motion is shown in fig. 4.58. In contrast to Category 2, this time the damping coefficient does have a qualitative effect on the aerodynamic forces and cylinder motion. When the damping coefficient was increased from $\zeta = 0.002$ to $\zeta = 0.003$ the amplitude decreased slightly and the initialization of VIV took longer, but the trajectory was similar. For $\zeta = 0.007$ the trajectory changed significantly. The structural damping was most probably too large to allow the cylinder body and the wake to initialize the 'strong' trajectory observed for the other damping cases. The energy transfer from the wake to the cylinder body was overruled by the energy dissipation of the structural damper. This finding demonstrated that the 2-way FSI coupled cases, in contrast to the 1-way coupled and stationary cylinder cases, are hugely dependent on the transient part of the simulation. It matters how the wake and the cylinder motion develop and how they interact with each other before equilibrium is reached. If the interaction is suppressed it can prevent a strong trajectory from occurring, while if the configuration is more susceptible it can lead to significant lift forces and transverse displacements.

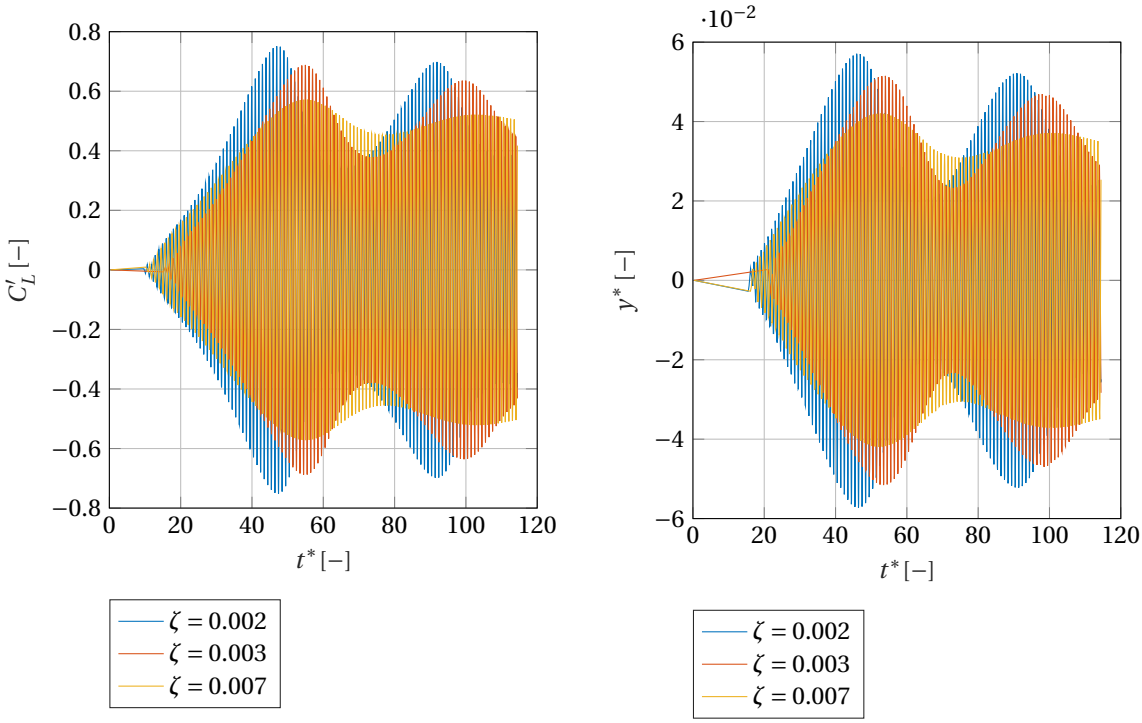

Figure 4.57. Fluctuating lift coefficient (left) and (non-dimensional) displacement (right), under the operating conditions of $U^* = 2.95$, $\mathbf{c}^* = (0.002 \quad 0.003 \quad 0.007)$, $m^* = 29.6$ and $Re = 4.4 \cdot 10^6$

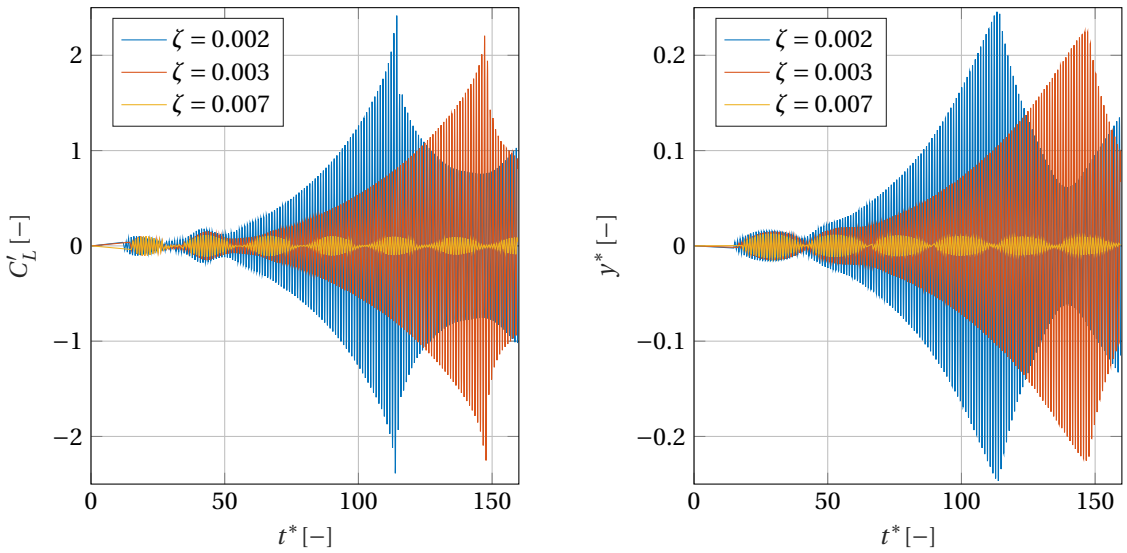

Figure 4.58. Fluctuating lift coefficient (left) and (non-dimensional) displacement (right), under the operating conditions of $U^* = 3.10$, $\mathbf{c}^* = (0.002 \quad 0.003 \quad 0.007)$, $m^* = 29.6$ and $Re = 4.4 \cdot 10^6$

Non-dimensional analysis: Two Approaches In the free-vibration studies for laminar flow it was shown before that these four non-dimensional parameters adequately describe the 2-way coupled problem (see section 4.1.3): m^*, ζ, U^* and Re. It was deemed as important to see if these four non-dimensional parameters worked as good in the supercritical Reynolds regime as they did in the laminar regime. Therefore, similar to section 4.1.3, multiple cases have been simulated where the non-dimensional values were equal but their dimensional values slightly changed. The non-dimensional and dimensional input parameters and results have been shown in tab. 4.20.

Parameter	**Case** 1.1	**Case** 1.2	**Case** 2.1	**Case** 2.2
U^*	4.3	4.3	3.2	3.2
m^*	3446.9	3446.9	29.6	29.6
ζ	0.003	0.003	0.003	0.003
Re	$3.2 \cdot 10^6$	$3.2 \cdot 10^6$	$4.8 \cdot 10^6$	$4.8 \cdot 10^6$
$f_{nat}[Hz]$	0.23	0.324	0.31	0.324
$U[m/s]$	1.0	1.4	1.0	1.04
$m[kg]$	2707.2	2707.2	23.2	23.23
$k_s[N/m]$	5835.5	11219.5	88.3	96.3
$c[N \cdot s/m]$	25.3	35.1	0.30	0.31
$\nu[m^2/s]$	$3.13E-07$	$4.33E-07$	$2.1E-07$	$2.18E-07$
$C_{D,mean}[-]$	0.42	0.42	0.58	0.58
$C_{L,RMS}[-]$	0.09	0.09	1.0	1.0
$C_{L,y}[-]$	-0.13	-0.13	1.31	1.31
$C_{L,\dot{y}}[-]$	0.001	0.001	0.25	0.25
$y^*_{max}[-]$	$1.36E-05$	$1.35E-05$	0.34	0.34
$St[-]$	0.322	0.321	0.30	0.30
f_{shed}	0.322	0.444	0.304	0.317

Table 4.20: Results of turbulent free-vibration cases inside (Case 1.2/2.2) and outside (Case 1.1/2.1) lock-in band

The same two Approaches from section 4.1.3 have been used to simulate identical non-dimensional cases while their dimensional values may differ. As can be observed, Case 1.1 has the same non-dimensional values as Case 1.2. The same holds for Case 2.1 and Case 2.2. Case 1.1 and Case 2.1 used Approach 1 while Case 1.2 and 2.2 used Approach number 2. In the first Approach (Case 1.1 and 2.1), the dimensional velocity was assumed to be constant and the value was assumed as well. From there on, the other dimensional parameters were deduced. In the second Approach (Case 1.2 and 2.2), the value of the natural frequency was assumed constant during the U^*-sweep. In the latter Approach, only the dimensional velocity was varied while the other dimensional values were kept constant. As shown in tab. 4.20, both Approaches have yielded identical results for the aerodynamic forces which is in line with the earlier findings in the laminar analysis.

The mass and spring-stiffness used for Cases 1.1 and 1.2 was considerably higher. In addition, Cases 1.1/1.2 were outside the lock-in band while Cases 2.1/2.1 were inside the lock-in band. These four Cases have been analyzed to see if the non-dimensionalization would work under different operating conditions. Tab. 4.20 shows that both Approaches arrive at the same results. The results confirmed that the non-dimensional values are usable for turbulent flows as well. It must be noted that for the comparison of Cases 1.1-1.2 and 2.1-2.2 it was deemed as important to deduce the aerodynamic quantities from an equal non-dimensional timeframe. If the latter was not done, larger deviations between the results were observed. Knowing that $t = t^* / f_{shed}$, it may concluded that a smaller shedding frequency leads to a longer simulation time. Tab. 4.20 shows that Approach 1 leads to a smaller shedding frequency. Therefore, to save computational time it has been recommended to adopt Approach 2 for VIV analysis rather than Approach 1.

Non-dimensional analysis: Cylinder Size In addition to the verification of the two proposed Approaches before, the effect of the cylinder diameter on the results has been evaluated as well. The aim of this additional parameter study was to see if the size of the cylinder is taken into account well by the four non-dimensional parameters. These Cases have been listed in tab. 4.21.

Parameter	**Case** 3.1	**Case** 3.2	**Case** 4.1	**Case** 4.2
U^*	2.95	2.95	3.1	3.1
m^*	14.8	14.8	29.6	29.6
ζ	0.003	0.003	0.003	0.003
Re	$4.4 \cdot 10^6$	$4.4 \cdot 10^6$	$4.6 \cdot 10^6$	$4.6 \cdot 10^6$
$f_{nat}[Hz]$	0.34	0.085	0.32	0.08
$U[m/s]$	1.0	1.0	1.0	1.0
$D[m]$	1.0	4.0	1.0	4.0
$m[kg]$	11.6	185.8	23.2	371.7
$k_s[N/m]$	52.5	52.5	94.5	94.5
$c[N \cdot s/m]$	0.163	0.65	0.31	1.24
$\nu[m^2/s]$	$2.3E-07$	$9.1E-07$	$2.16E-07$	$8.6E-07$
$C_{D,mean}[-]$	0.47	0.47	0.57	0.57
$C_{L,RMS}[-]$	0.59	0.59	0.97	0.98
$C_{L,y}[-]$	0.80	0.80	1.30	1.31
$C_{L,\dot{y}}[-]$	0.05	0.05	0.35	0.28
$y^*_{max}[-]$	0.15	0.15	0.23	0.23
$St[-]$	0.32	0.32	0.32	0.31

Table 4.21: Results of turbulent free-vibration Cases for a varying diameter under different operating conditions

Case 3.1 and Case 3.2 have equal non-dimensional parameters. The same is true for Case 4.1 and Case 4.2. The main difference between Cases $3.1-3.2$ and $4.1-4.2$ is the diameter of the cylinder. For Cases 3.1 and 4.1 the diameter was set equal to $D = 1[m]$. For Cases 3.2 and 4.2 the diameter was increased to $D = 4[m]$. To keep the non-dimensional values equal while increasing the cylinder diameter, other dimensional values needed to be tweaked to cope with the change of cylinder size. Therefore, the other dimensional values are tabulated as well in tab. 4.21 to show the effect on them.

Cases 4.1 and 4.2 belonged to the Standard Batch, while Cases 3.1 and 3.2 were used in the analysis on the mass/spring-stiffness variation before. As shown in tab. 4.21, the results are in good agreement between Cases $3.1-3.2$ and $4.1-4.2$. Similar to the previous non-dimensional analysis, this shows that the classical four non-dimensional parameters adequately describe the VIV problem (even when the diameter was changed). Even the aerodynamic stiffness and damping terms show good agreement, except for the aerodynamic damping term found for Cases $4.1-4.2$. Considering that these aerodynamic quantities are more prone to fluctuations because they depend on both the fluid forces and cylinder motion, it was concluded that the non-dimensional method was reliable.

To illustrate the effect of the change in diameter on the absolute values on the time and cylinder displacement, the lift force coefficient and (dimensional) cylinder displacement are shown in fig. 4.59 for Cases 4.1 and 4.2 of tab. 4.21. The time t was dimensional on the x-axis of both subfigures. The first observation from these two subfigures is the fact that Case 4.2 needs a larger simulation time to reach the same conditions as Case 4.1. This is a direct consequence of the larger diameter used for Case 4.2. In fact, knowing the Strouhal number remains constant between Cases $4.1-4.2$ (see tab. 4.21), a larger diameter inherently leads to a smaller shedding frequency according to eq. 2.2. This in turn resulted in a four times larger shedding period T_s for Case 4.2. In other words, a four times larger diameter requires a four times larger simulation time. Therefore, to save computational time, it is recommended to run VIV simulations with a smaller diameter.

It can be seen in fig. 4.59 the lift coefficient reaches the same maximum amplitude (which confirms the

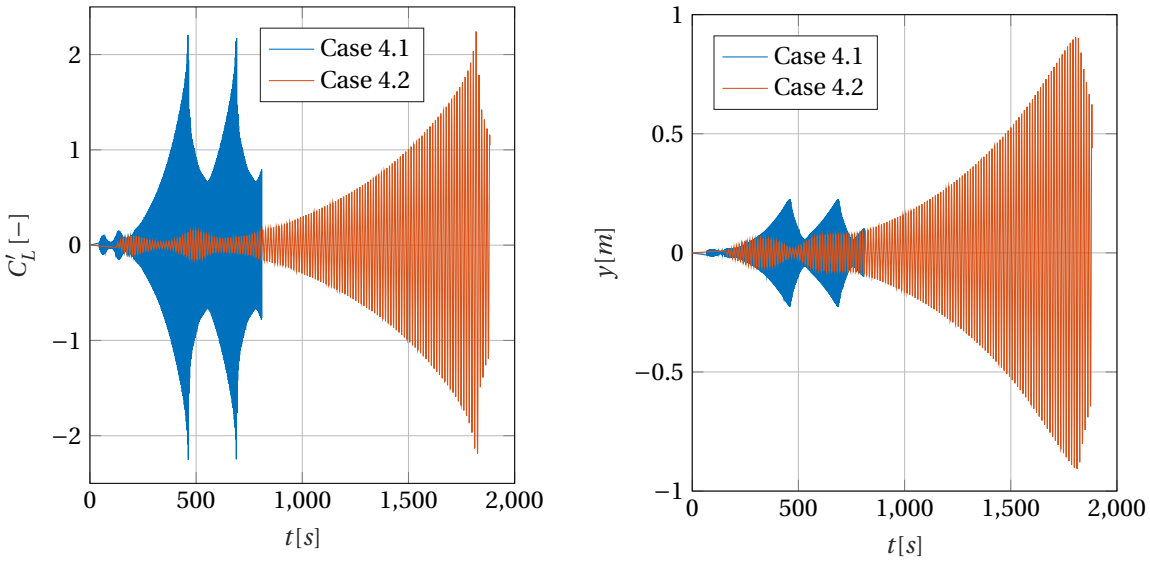

Figure 4.59. Fluctuating lift coefficient (left) and transverse cylinder displacement (right) of Case 4.1 and 4.2 in tab. 4.21

results in tab. 4.21). At the same time, the difference in diameter is seen back in the (dimensional) transverse cylinder displacement. For Case 4.2, the maximum amplitude is four times larger compared to Case 4.1. For the comparison of the results in tab. 4.21, an equal non-dimensional timeframe was taken for all the Cases. The aerodynamic damping, stiffness and to a smaller degree the aerodynamic force coefficients would show a larger deviation when the non-dimensional timeframe was not set equal between any of the two compared Cases.

Stability of FSI solver in supercritical regime In the laminar free-vibration cases, only two simulations lead to numerical divergence, which was mentioned in section 4.1.3. After the complication was found inside the code regarding the Newmark solver, it was concluded that it was not necessary the weakly-coupled FSI solver that caused the divergence in those two simulations. In fact, it was observed that the strongly-coupled solver did not change the results for the laminar free-vibration cases compared to the weakly-coupled results. Hence, initially, all the turbulent free-vibration cases have been run with the same weakly-coupled scheme as for the laminar cases with the symplectic structural solver. This latter solver suited the weakly-coupled scheme better than the Newmark solver in *OpenFOAM*, was was explained in 3.2.

In fact, it was believed that the weakly-coupled scheme would perform even better for the turbulent free-vibration cases compared to the laminar cases. It was mentioned earlier in section 2.3.2 that weakly-coupled schemes can introduce some artificial or numerically added mass under certain operating conditions [64] [62] [63] [109]. Referring to the section, the following effects on the stability on the weakly-coupled FSI system (in combination with an incompressible fluid) were expected for the turbulent free-vibration cases compared to the laminar free-vibration cases:

- The higher mass ratio was expected to increase the stability.
- The increased spring-stiffness was expected to increase the stability.
- The decreased fluid viscosity was expected to increase the stability.
- The decreased timestep size was expected to decrease the stability.

Based on these four statements, it was overall indeed expected that the weakly-coupled scheme would have been at least as stable as for the laminar cases. In this reasoning, the effect of the modelled turbulence fluctuations within URANS (the Reynolds stress tensor) by the eddy-viscosity model on the stability of the coupling was not taken into account.

Yet, it has turned out the turbulent free-vibration cases were more sensitive to divergence. This sensitivity was not caused by the weakly-coupled FSI scheme, it was rather caused by the fluid solver. In all the laminar cases only two outer correction loop was employed for the fluid solver. This appeared to be insufficient for the

turbulent freely-vibrating cases. The PIMPLE settings were explained in more detail in section 3.1.3. Even for the turbulent *stationary* case, the loose PIMPLE settings with only 1 outer correction was deemed as a fine set-up for resolving the flow field. In those cases, convergence of pressure-momentum and turbulence quantities was only assessed by enforcing linear tolerances rather by also including the outer tolerances. This was done because the Courant number was enforced to be $Co_{max} \leq 0.7$ which was considered to yield low timestep continuity errors, without the need for additional, computational costly outer corrector loops. In fact, it was observed the poor grid convergence shown before for the turbulent stationary cases did not improve at all by using tighter PIMPLE settings. Nevertheless, these tighter PIMPLE settings turned out to be a necessity for the turbulent moving cases. In contrast to the laminar *free-vibration* simulations, the loose PIMPLE settings did not yield stable results for the turbulent *free-vibration* simulations. In fact, the results did not change when tighter PIMPLE settings were applied for some of the laminar free-vibration cases in retrospect.

For the turbulent free-vibrating cases, the difference between loose fluid solver settings and tight fluid solver settings had a significant impact on the results. In some cases, the tight settings prevented divergence. In other cases, where stability did not seem to be an issue, the results still changed significantly. Therefore, the turbulent moving results obtained with the loose PIMPLE settings were disregarded in the present research. With this knowledge, all the turbulent moving cases of interest have been re-run with tighter fluid solver settings. As was described in section 3.2, it was readily possible within *OpenFOAM* to re-run the structural solver within each of the additional fluid outer loops (i.e. strongly-coupled FSI scheme). Indeed, the strongly-coupled sovler has been used for all of the turbulent *free-vibration* cases especially because the structural solver did not require much additional computational time. All the turbulent free-vibration cases have been run again with the implicit structural solver Newmark in combination with the implicit FSI scheme and tight fluid solver settings. Although the effect of the fluid solver settings on the 1-way coupled simulations was not investigated, the 1-way turbulent cases have been simulated as well with tight fluid solver settings.

The additional settings available for the strongly-coupled scheme were evaluated. These evaluations, in combination with the earlier observations shared for the turbulent free-vibration cases, have been summarized as follows:

- The effect of the relaxation factor ψ (eq. 3.31) was marginal on the force and motion results. It was observed that a lower relaxation factor required more outer corrector loops and hence the fluid solver sometimes had to be run more times than needed. This increased the computational time significantly. A standard relaxation factor of $\psi = 0.9$ was applied for all the strongly-coupled simulations.
- It was observed that an explicit FSI/implicit structural solver lead to unstable, divergent behaviour for $U^* = 2.95$. The combination of an explicit FSI/explicit structural solver (referred to as weakly-coupled scheme) lead to a stable steady-state solution for $U^* = 2.95$. Lastly, the combination of an implicit FSI/implicit structural solver (referred to as strongly-coupled scheme) lead to a stable solution as well. These findings were also observed before for one of the laminar cases, see section 4.1.3. The associated complication of the explicit/implicit combination implemented in *OpenFOAM* was pointed out before in section 3.2. Based on these findings, it was concluded that the weakly-coupled FSI solver was sufficient to predict the turbulent free-vibration cases, similar to the laminar free-vibration cases.
- Increasing the number of subiterations (with constant relaxation factor) did not lead to significant changes in the results. Typically, the amount of subiterations were found to be $i = 3-4$ for the Standard Batch, depending on how fast the outer criteria of the fluid solver were reached. When $i = 10$, it was indeed observed that the velocity residuals for each timestep decreased compared to when $i = 3-4$ but the results were identical in both simulations.
- As was stated before, the effect of using tighter fluid solver settings and by making sure that the pressure-momentum/$k-\omega$ coupling converged well, had a big impact on the turbulent-moving results.

It must be noted that the above-mentioned effects have only been evaluated for one case inside the lock-in regime where $U^* = 2.95$, except for the 'loose' fluid solver setting. The latter setting has been employed initially for all the turbulent free-vibration cases, as was explained before. Regarding the other items, the observations must be treated with caution because they might not be true for the entire operating range of $1 < U^* < 11$. For example, it could very well be that the weakly-coupled scheme would have led to divergent behaviour for other cases than $U^* = 2.95$. Regarding the tight and loose fluid solver settings, it has been argued that the loose fluid solver settings most likely lead to problems at the fluid-structure interface [110]. Although the energy conservation was respected at the fluid-structure interface, the problems on the fluid solver's side lead to a different, more unrealistic equilibrium.

It was found that if the aim is to reach accuracy, then the maximum number of iterations should be set to $i_{max} = 100$. Such a high number of iterations for the fluid solver would usually lead to satisfying the specified tolerances within each timestep and hence lead to small continuity errors. The outer tolerances were typically reached after $i = 3-4$ subiterations as was stated earlier. If stability is of the interest, it might be interesting to remove the additional fluid solver tolerances and to enforce a desired number of iterations (lower than $i_{max} = 100$). By removing the tolerances, the fluid solver will always complete all the number of iterations until the specified maximum is reached. Since it was not possible to specify structural tolerances within *OpenFOAM*, reaching the additional fluid solver tolerances may not automatically lead to a low relative error for the structural solver. It was found that these two tolerances can of be different orders of magnitude, even if the additional fluid tolerances are considered as tight ($1e-06$). For this reason, it was found to be better to remove the residuals and enforce a maximum number of iterations on the FSI solver. If this maximum number of iterations is higher than the number of iterations that were actually required for fluid convergence, the timestep continuity errors should be adequately low. For example, when only 3-4 iterations were required to reach convergence for the fluid solver, then with 10 iterations this should be the case as well. Then, the more challenging part is to find a number of subiterations which would lead to convergence on the structural solver while keeping an eye on the computational time. Ideally, the number of iterations should not be too high. As the fluid is being solved for each subiteration (for each timestep), increasing the number of iterations evidently leads to higher computational cost. It was found in the literature that introducing a structural convergence criteria in the FSI solver would prevent the need of estimating the number of subiterations required to reach convergence for both the fluid and structural solver [84]. This would be more convenient and could also lower the computational time, especially if the required number of subiterations varies per timestep throughout the simulation. In the study of [84] a dynamic relaxation factor ψ was implemented in the standard *OpenFOAM* FSI solver. This led to a $70-80\%$ reduction of simulation time while the coupled solver's stability was guaranteed as well.

5

Discussion, recommendations and conclusions

In this last chapter of the thesis report, the reliability of the model will be evaluated first. Then, a critical review on the FSI modelling will be reported. After that, the research question will be addressed and the progress towards the research objective will be evaluated in the conclusion of this MSc thesis.

This chapter focuses on the following three aspects of the thesis research:

- *How does the model perform?*
- *What can be done better for future work?*
- *What are the main outcomes of the results?*

5.1. Discussion and recommendations

5.1.1. Turbulence modelling

Regarding the accuracy and reliability of the presently used model, the following conclusions were drawn before by the grid convergence, verification and validation studies:

- All of the of the planned assessments in tab. 2.1 for the *laminar* flow regime have been completed successfully.
- Most of the *turbulent* assessments in tab. 2.1 have been completed successfully. Grid convergence was not achieved and the validation could have been better for the (turbulent) stationary cylinder.
- The results fell within the range of numerical data available at supercritical Reynolds numbers: drag, lift and Strouhal number. Furthermore, the predicted lift coefficient and separation angle agreed fairly well with the experimental studies. The Strouhal number was over predicted, which was experienced by other numerical studies as well.
- The *forced-vibration* model showed reasonable agreement with a wind-tunnel experiment found in the supercritical regime [2].

Although grid convergence was not obtained, the pressure and skin-distribution showed good agreement with the numerical studies found in the supercritical regime. The present work showed good agreement with two different DES studies performed in the supercritical regime and with one LES study in the transitional regime [54], [100] and [48]. Other numerical studies in the literature simulating VIV also faced problems with their grid convergence [54] [100] and [56]. Although convergence should be aimed for, the results obtained with the present URANS model were deemed as satisfactory for a qualitative analysis of the fluid problem as they agreed with the numerical data found in the literature. For future attempts to achieve grid convergence, a couple of recommendations were made in section 4.2.1. Carefully enforcing a maximum to the eddy viscosity ratio and decrease the cell growth ratio at the cylinder wall to even closer values to 1 (in the present mesh a ratio of 1.2 was used) were the most important recommendations. In addition, it was not recommended to

use wall functions for future work with URANS in the supercritical regime, such that the boundary layer is resolved up to the wall.

Regarding the accuracy of the model compared to experiments, some differences were observed. It was shown that the fully turbulent flow assumed by URANS impacted the skin-friction coefficient, which deviated from the experimental results. Nevertheless, the LES study of [48] demonstrated in the transitional regime that the boundary layer separation and the recirculation region were captured well, while their upstream skin-friction coefficient was also over-predicted due to inadequate modelling of the laminar boundary layer before separation. This showed the upstream errors did not have a large impact on the important flow features around and after flow separation. Therefore, although the numerical study of [53] indicated otherwise, the implementation of a transition model within URANS is not considered as a necessary next step for future research.

Based on comparisons of the pressure distribution with experimental data at $Re = 3.6{\cdot}10^6$ it was suspected that URANS was not able to capture the flow directly after separation accurately. This caused a higher base-pressure coefficient which led to a smaller drag coefficient compared to the experiments. The larger Strouhal number was expected to be caused by the incorrectly predicted detached flow. Besides the drag coefficient and the Strouhal number, it appeared the that lift coefficient and the separation angle were predicted fairly well by the present URANS approach compared to the experimental values. It is possible LES would be a better approach for predicting the detached flow compared to URANS, as was suggested by [48] and [73].

These observations are in line with the study of [73] were comparisons were made between URANS and LES for a vortex-shedding fluid problem. URANS was able to predict the main features of the flow qualitatively. Yet, LES has performed better in their study because of the direct resolution of large scales and the modelling of the interaction between the different scales. The boundary layer separation was argued to play an important role in vortex shedding, which turned out to be predicted well by LES. The study of [48] also showed LES was better able to capture the separation phenomenon compared to URANS. The two DES studies found in the supercritical regime seemed to yield similar accuracy compared to the present URANS results. LES is therefore recommended to be the preferred approach for future work when higher fidelity than URANS is desired. The challenge of the LES study in the supercritical regime is on one side the modelling choice regarding to which extend (potentially important) smaller sized eddies are resolved and on the other side to meet with the very fine grid resolution requirements for supercritical Reynolds numbers. In fact, when very small sized eddies in the near-wall region are desired to be resolved, the LES could readily become a DNS-alike approach. A LES study in the supercritical regime could indeed demonstrate if LES shows a better agreement with the experimental values than URANS.

In hindsight, URANS (and the CFD model) has proven its reliability throughout the successful completion of most of the assessments in tab. 2.1. The lift coefficient and Strouhal number were considered to be the most important aerodynamic parameters for the *transverse* oscillating simulations. The obtained lift coefficient of the turbulent stationary cylinder in the supercritical, which agreed fairly well with the experimental studies, may be seen as a good starting point for the turbulent moving simulations. The predicted shedding frequency for the moving simulations by the present FSI model should be interpreted with more caution, as the Strouhal number was over predicted for the stationary cylinder. Comparison against the supercritical FSI study [2] showed reasonable agreement between the present results and the wind-tunnel results. This comparison in fig. 4.35 and fig. 4.36 demonstrated URANS predicted the magnitude of the aerodynamic forces and the FSI response well. Regarding the FSI response, it was observed the CFD model predicted the aerodynamic 'switch' phenomenon well for the supercritical flow as was supported by the wind-tunnel data. The switch mechanism has been explained carefully in section 4.2.2.

In addition to the quantitative aspects, URANS was able to simulate some of the qualitative aspects of the vortex street at supercritical Reynolds numbers. In the first place, the present model predicted coherent vortex structures in the wake. This is in line with the anticipations in the literature, where a re-esthablished vortex street is present in the supercritical regime [25].

Near all turbulent simulations showed the 2S wake pattern. In a few cases the $2P$ or $P+S$ pattern was observed. These patterns have been defined in the study of [15]. The 2S wake pattern was visible in for example fig. 4.26, fig. 4.34 and fig. 4.48. Yet, the question is whether these obtained vortex structures are sufficiently reliable because they were obtained by URANS. It was believed in the present study the most important vortex characteristics in the wake can still be captured by URANS. In the first study on the vortex wake patterns of [111] by using PIV the switching mechanism of the wake was showed to still be present for turbulent flows at $Re = 5000$. Small-scale Kelvin-Helmholtz vortices were found to be present in the wake by the study of [111] and in some of the shedding cycles the large-scale vortices were more disorganized by

the near-wake turbulence. Nevertheless, when ensemble averaging was applied to multiple images under the same operating conditions, the vortex switching mechanism was similar to the one observed for lower Reynolds numbers. This averaging was possible, it was reasoned, since the smaller coexisting vortices and the turbulence distortion showed high fluctuations while the larger vortices were steadier. Relating these observations back to the presently obtained vorticity pattern by URANS, it may be assumed that neither the turbulence distortion nor the small-scale Kelvin-Helmholtz vortices have been captured by URANS. Yet, as the ensemble averaging of the PIV study of [111] showed, the vortex patterns can still be deducted from the mean flow for turbulent flows. In fact, the study of [73] demonstrated that the main wake patterns predicted by URANS agreed well with PIV and LES (by using only the mean field and two major Proper Orthogonal Decomposition). In other words, their study supported that URANS was able to predict the major modes. It is not known what the effect of the smaller vortices or turbulence distortion is on the mean vortex pattern in the wake. The effects of these latter two phenomena would be relevant to address in future numerical research by DNS. In addition, it would be relevant to investigate the effects the uncaptured turbulence by URANS on the FSI response as well in future work.

Additional higher fidelity numerical studies (preferably LES) can offer more reliable results and hence wake patterns predicted by LES may serve as good a comparison against URANS results. The inclusion of 3 dimensions instead of 2D would be an important next step as well. These more sophisticated models would shed more light on the possible wake patterns present in the supercritical regime (versus the transitional regime) and if indeed the patterns typically observed at lower Reynolds numbers ([15]) are present as well for large Reynolds numbers. Where it is difficult and costly to capture the wake patterns in an experiment, let alone at supercritical Reynolds numbers. The numerical studies might be able do this rather well.

5.1.2. FSI modelling

The standard *OpenFOAM* FSI solver has been verified in the laminar regime extensively. The solver has been compared against three other numerical VIV-FSI studies. The beating phenomenon, which could be interpreted as a complex type of fluid-structure interaction, was captured accurately as well. In addition, some of the features discussed in the literature on the self-limiting mechanism of VIV were also captured and treated. All these successfully completed assessments have proven the reliability and accuracy of the standard *OpenFOAM* FSI solver. While the FSI solver was unconditionally stable for the laminar regime, it appeared the solver had stability issues for some cases in the supercritical regime. Yet, eventually it has turned out these instability issues were not caused by the FSI solver but by the fluid solver. The convergence of the k-ω and pressure-momentum coupling was considered to be important for the stability of the turbulent moving cases, as was explained in section 4.2.3. Based on the experiences in the present research, the following settings have been recommended for the CFD-FSI model:

- 'Tight' fluid solver settings have been employed for the turbulent moving cases according to section 3.1.3.
- Strongly-coupled scheme has been used for FSI (implicit FSI solver with implicit structural solver Newmark).
- A high relaxation factor of $\psi = 0.9$ since the number of subiterations was typically found to be small: $i = 3-4$ (depending on outer tolerance criteria of fluid solver).

It was believed the sharp oscillating amplitude and lift coefficient rise for the Fourth Category in the turbulent *free-vibration* simulations (see fig. 4.49) were not caused by *numerical* divergence. These large increments were suspected to be plausible, since the specified operating conditions opened up the possibility for an unstable trajectory as was shown by the *forced-vibration* simulations. Fig. 4.50 supports this argument by showing the structural motion (and hence FSI-coupled) convergence for each timestep. In fact, increasing the number of subiterations or lowering the relaxation factor did not prevent the divergence observed in the Fourth Category.

Implementation of a structural tolerance and dynamic relaxation factor in the standard *OpenFOAM* FSI solver is recommended for future research. These implementations were carried out before by the study of [84]. Both these features could reduce the computational time significantly (while guaranteeing stability), which would be beneficial for the costly turbulent simulations.

It was aimed to include a comparison of the 1-way and 2-way coupled models to contribute on the on-going debate how well the *forced-vibration* and *free-vibration* canonical cases match (at supercritical Reynolds number). This comparison has not been done and it is therefore recommended for future research to address this comparability.

5.2. Conclusion

The following three canonical VIV cases have been investigated in the present research: stationary, forced-vibrating and free-vibrating cylinder. All these three cases have been analyzed for both the laminar regime (which was defined as $80 < Re < 200$) and supercritical Reynolds regime ($Re > 3.5 \cdot 10^6$). The results and the comparison in the laminar regime mostly demonstrated the accuracy and reliability of the CFD model. Some fundamental insights have been obtained in the laminar regime, but the results obtained in this regime mostly served to build up the confidence in the CFD model.

The results for the stationary cylinder in the supercritical Reynolds regime provided a challenging playing-field to assess the turbulence modelling capabilities of URANS within *OpenFOAM*. The model was compared both against numerical and experimental work. Based on these comparisons, it was concluded that the URANS k-ω SST model has proven its reliability as the results agreed well with two independent DES studies. Furthermore, most of the assessments defined in tab. 2.1 have been completed successfully by the model. The obtained lift force was predicted well, also compared to the experimental work in the supercritical regime. The obtained Strouhal number should be interpreted with caution for the turbulent moving cases. The accurate prediction of the lift force and Strouhal number was considered to be important, since in the present research the cylinder was only allowed to move in the *transverse* direction.

The *forced-vibration* and *free-vibration* simulations in the supercritical regime were aimed to address the research question: *What is the fluid-structure interaction effect of a transversely oscillating cylinder exposed to VIV at supercritical Reynolds numbers?*

Regarding the *forced-vibration* model, the following conclusions were drawn:

- The results demonstrate a lock-in band, phase angle switch coinciding with a change of the wake pattern around the critical frequency, aerodynamic damping contour map and enhanced effective added mass and lift magnification inside the lock-in band. All these phenomena describe the FSI effects at the supercritical Reynolds number.
- The *forced-vibration* simulations allowed to simulate the wake for behind a cylinder prescribed to oscillate for a wide range of motion amplitudes and frequencies. It gave the possibility to also run more unorthodox, non-equilibrium operation points in contrast to the *free-vibration* model. The aerodynamic damping contour map predicted by the *forced* model therefore offered great insights into the stable and unstable oscillation trajectories for the grid of $0.6 < f^* < 1.2$ and $0.0035 < A^* < 0.25$.
- The data from the aerodynamic contour map can be utilised to calibrate phenomenological models predicting VIV. This potential application of the CFD data was deemed useful for the research objective, to help Siemens to enhance their existing model.
- Furthermore, the aerodynamic damping contours offered useful insights to explain some of the phenomena occurring in the *free-vibration* simulations. Unstable trajectories observed in the *forced-vibration* results indeed led to divergence in the results for the *free-vibration* cases when the damping coefficient was too low. The damping coefficient was not able to suppress the aerodynamic excitement. Vice versa, stable trajectories observed in the *forced-vibration* results did not lead to divergence in the results of the *free-vibration* cases, even when the damping coefficients were very low. These strong correlations between the results of the *forced-* and *free-vibration* results support the potential of phenomenological models.
- The only FSI study found in the literature at supercritical Reynolds numbers was a forced-vibration wind-tunnel experiment which was useful to validate the turbulent-moving results. In fact, reasonable agreement was found between the wind-tunnel experiment and the present CFD model results. With further enhancements and an optimized fluid solver, the *OpenFOAM* URANS-FSI can be used to capture circular bluff bodies exposed to VIV in the supercritical regime.
- It may therefore be concluded the *forced-vibration* model provided a great intermediate modelling step in between the stationary and *free-vibration* cylinder. This latter statement also holds for the modelling aspect.

The main focus of the research was the *free-vibration* set-up, which was considered to be the most realistic set-up modelling VIV in this research. The results from the 2-way coupled model addressed the research question. In addition, the *free-vibration* model gave the opportunity to investigate the FSI effects of some of the structural parameters of the cylinder, which was not possible with the *forced-vibration* model. First, before the effect of the structural parameters was evaluated, a Standard Batch of cases was simulated. This Standard Batch entails the following operating conditions: $1.9 < U^* < 10.7$, $2.8 \cdot 10^6 < Re < 1.6 \cdot 10^7$, $m^* = 29.6$

and $\zeta = 0.003$. The results on this Standard Batch clearly rejected the **H0** hypotheses. The results showed a lift force magnification and a critical wind speed range around the lift force magnification (i.e. lock-in band). This means the typical characteristics of VIV found for lower Reynolds number in the literature are also present for supercritical Reynolds numbers. In fact, three of the five main VIV effects compiled by [3] have been observed for supercritical Reynolds numbers in the present research (all five effects were explained in section 2.2.4):

- Lock-in/synchronization: fig. 4.39 clearly shows the extended range where the wake adapted to the natural frequency.
- The strength of the shedded vortices increase: fig. 4.38 demonstrates a lift magnification within the lock-in band.
- The phase, sequence and pattern of vortices in the wake is affected: fig. 4.42 and fig. 4.48 illustrate this. The 'switch' mechanism has been captured for both the *forced*- and *free*-vibration simulations.

A lift magnification factor of $M_{C_L} \approx 10$ and drag magnification factor of $M_{C_D} \approx 1.5$ were both found to be the largest magnifications for the Standard Batch. The drag coefficient magnification was expected to be lower, since the cylinder was only allowed to vibrate in the transverse direction. The maximum non-dimensional oscillation amplitude was found to be $y^*_{max} = 0.52$. The results for the Standard Batch have been categorized into four Categories, based on their time series and FSI behaviour. Especially the third and fourth Category were interesting, as these Categories revealed the lock-in nature of VIV. In the Third Category, the fluid was no longer dominated by the Strouhal relation. The natural frequency was close enough to start dictating the wake, which led to lock-in. Yet, the aerodynamic force signals did not show a constant amplitude over time. In fact, it was demonstrated by the phase angle behaviour and changes in the wake pattern that this Category yielded a continuous alteration between self-excitation and self-limitation of the FSI. The wake restructuring was found to be in line with the 'switching mechanism' found earlier for the forced-vibration results. Because of the alteration, no steady-state equilibrium was found where the energy transfer between the structure and fluid remained constant over time. In the last Category, divergence was observed. It was believed the divergence was mathematically plausible and not a consequence of a numerical problem. This was supported by the convergence of the relative transverse (cylinder) velocity error. The divergence was believed as realistically possible. The results from the forced-vibration cases from the present work and the wind-tunnel data from [2] showed that unstable trajectories can occur under the operating conditions where divergence was observed.

An additional non-dimensional analysis has been performed for the supercritical *free-vibration* set-up to see if the four classical non-dimensional parameters used to describe VIV (see [85]) represent VIV adequately. The analysis indeed showed the four parameters capture the VIV problem rather well. In fact, two approaches have been proposed which can be used to parameterize VIV. One of these approaches yields a smaller shedding period T_S (while the non-dimensional values are kept the same). With a smaller shedding period, more shedding cycles can be analyzed in an equal timeframe. Hence, this approach offers the benefit of taking less computational time. The same holds for a smaller cylinder size (while bearing in mind that the non-dimensional values should be kept equal).

Regarding the effect of the structural parameters on the FSI, the sensitivity of the aerodynamic and structural response to varying both the mass and damping coefficient was studied. It was suggested that a sufficiently large critical mass coefficient would lead to nearly a stationary response (say $m^* > 59$). It seemed the FSI interaction was suppressed by the structural inertia. For a very low mass ratio ($m^* < 3$), the cylinder supposedly showed a stronger lock-in response. Interesting wake patterns like the 2P and P+S mode were identified for the lowest mass ratio ($m^* = 2.5$) corresponding to earlier URANS findings in the literature. It appeared the lowest mass ratio yielded a steady-state equilibrium with a constant amplitude for the aerodynamic forces and motion response. For very large mass ratios or very low mass ratios, it seemed that the response of the system did not vary significantly when the reduced velocity was varied. It was reasoned that a high mass ratio leads to a stationary response, which appeared to be quite indifferent for a varying reduced velocity. The small mass ratio might have increased the lock-in bandwidth which also yielded a somewhat indifferent response after varying the reduced velocity. When the mass ratio was in between the critical mass ratio and the very small mass ratio ($10 < m^* < 40$), it appeared the system yielded a more dynamic FSI response where the energy transfer between the structure and the fluid varied over time. These cases yielded high aerodynamic peak forces and were the most susceptible to changes in response when the reduced velocity was varied.

The effect of the damping coefficient was considered to be less severe compared to the effect of the mass coefficient as the time series remained more similar when the damping was varied. For some of the operating conditions an increased damping coefficient led to a significantly different response, in magnitude and qualitatively in the time series signal. Under these latter operating conditions, the damping coefficient proved to be useful to almost entirely phase out the motion response. It appeared the damping coefficient overruled the energy transfer from the wake to the cylinder by dissipation in the structural damper. The mass and damping sensitivity study showed the importance of the transient phase in the 2-way coupled simulations in contrast to the 1-way coupled and stationary results. The impact of the damping coefficient and mass coefficient on the time series of the aerodynamic forces and motion response demonstrated the importance of how the fluid and structure interact with each other before equilibrium has been reached for the free-vibration model. The damping coefficient or the mass coefficient could in fact determine whether the cylinder will follow a more unstable or stable trajectory defined earlier in the *forced-vibration* results.

In conclusion, this research has aimed to open up the relative new research area for supercritical Reynolds numbers by demonstrating the current CFD infrastructure (*OpenFOAM*, URANS and FSI coupling) is suitable for engineering work. Since no other numerical study has been found in the literature which has performed a similar combination of supercritical Reynolds numbers with FSI, the present research has delivered new insights and numerical data for this novel research area. Various typical VIV characteristics, known from the literature, have been observed in the supercritical regime. In addition, the FSI at supercritical Reynolds numbers has been investigated thoroughly by analyzing the aerodynamic damping, phase angle and wake patterns. All these results have addressed the research question. These insights have served to reach the research objective defined in chapter 1: *To help Siemens Gamesa define a more physically representative VIV model accounting for the large-scale effects by analyzing the critical parameters influencing VIV*. From a practical perspective, relevant data was obtained by the CFD model for potential optimisation of a phenomenological model predicting VIV. At the same time, more importantly, the insights obtained regarding the fluid-structure interaction at supercritical Reynolds numbers have contributed to a better understanding of the VIV phenomenon for Siemens Gamesa. The addressed research question has provided a fundamental analysis of how the phenomenon originates and how it is influenced by two of the main influencing parameters. Although no effort has been undertaken in the present research to investigate the phenomenological models in more detail, this theory-oriented thesis indeed showed that the Reynolds number and the fluid-structure interaction effects should be modelled carefully in a phenomenological model. Further practical improvements of the phenomenological model are within the capabilities of the CFD infrastructure as has been demonstrated in the present research. This research has deliberately shared its modelling experiences and possible recommendations for future work to further exploit the potential of CFD to improve phenomenological models.

A

Non-dimensional form of URANS

The incompressible Navier-Stokes equation for Newtonian fluids were given in chapter 2 in vector format:

$$\frac{\partial \mathbf{u}}{\partial t} + \nabla \cdot (\mathbf{uu}) + \frac{1}{\rho}\nabla p - \nabla \cdot (\nu \nabla \mathbf{u}) = 0 \tag{A.1}$$

$$\nabla \cdot \mathbf{u} = 0 \tag{A.2}$$

Considering only 2 dimensions, eq. 2.7 and eq. 2.8 are written in the cartesian coordinates (x,y) as follows:

$$\frac{\partial u}{\partial t} + u\frac{\partial u}{\partial x} + v\frac{\partial u}{\partial y} + \frac{\partial p}{\partial x}\frac{1}{\rho} - \nu\left(\frac{\partial^2 u}{\partial x^2} + \frac{\partial^2 u}{\partial y^2}\right) = 0 \tag{A.3}$$

$$\frac{\partial v}{\partial t} + u\frac{\partial v}{\partial x} + v\frac{\partial v}{\partial y} + \frac{\partial p}{\partial y}\frac{1}{\rho} - \nu\left(\frac{\partial^2 v}{\partial x^2} + \frac{\partial^2 v}{\partial y^2}\right) = 0 \tag{A.4}$$

$$\frac{\partial u}{\partial x} + \frac{\partial v}{\partial y} = 0 \tag{A.5}$$

After using the non-dimensional values listed in tab. A.1, eq. A.3 becomes:

$$\frac{U_\infty^2}{D}\frac{\partial u^*}{\partial t^*} + \frac{U_\infty^2}{D}\left(u^*\frac{\partial u^*}{\partial x^*} + v^*\frac{\partial u^*}{\partial y^*}\right) + \frac{U_\infty^2}{D}\frac{\partial p^*}{\partial x^*}\frac{1}{\rho^*} - \frac{\nu_\infty U_\infty}{D^2}\nu^*\left(\frac{\partial^2 u^*}{\partial x^{*2}} + \frac{\partial^2 u^*}{\partial y^{*2}}\right) = 0 \tag{A.6}$$

Dividing all the terms by $\frac{U_\infty^2}{D}$ leads to the following equation:

$$\frac{\partial u^*}{\partial t^*} + \left(u^*\frac{\partial u^*}{\partial x^*} + v^*\frac{\partial u^*}{\partial y^*}\right) + \frac{\partial p^*}{\partial x^*}\frac{1}{\rho^*} - \frac{\nu_\infty}{DU_\infty}\nu^*\left(\frac{\partial^2 u^*}{\partial x^{*2}} + \frac{\partial^2 u^*}{\partial y^{*2}}\right) = 0 \tag{A.7}$$

Where $\frac{\nu_\infty}{DU_\infty} = \frac{1}{Re}$. This derivation is also valid for the y-direction and therefore the scaling may be related to the vector equation of before:

$$\frac{\partial \mathbf{u}}{\partial t} + \nabla \cdot (\mathbf{uu}) + \frac{1}{\rho}\nabla p - \frac{1}{Re}\nabla \cdot \nabla \mathbf{u} = 0 \tag{A.8}$$

It is possible to derive the Reynolds-averaged Navier-Stokes equations by substituting the following relation in eq. A.8:

$$\mathbf{u}(\mathbf{x}, t) = \overline{\mathbf{u}}(\mathbf{x}, t) + \mathbf{u}'(\mathbf{x}, t) \quad \text{with} \quad \overline{\mathbf{u}'} = 0 \tag{A.9}$$

where $\mathbf{x} = (x\,y)^T$ is the position vector. Hence, the non-dimensional URANS equations are defined as follows:

$$\frac{\partial \overline{\mathbf{u}}}{\partial t} + \nabla \cdot (\overline{\mathbf{u}}\overline{\mathbf{u}}) + \frac{1}{\rho}\nabla \overline{p} - \frac{1}{Re}\nabla \cdot \nabla \overline{\mathbf{u}} = -\nabla \cdot \overline{\mathbf{u}'\mathbf{u}'} \tag{A.10}$$

$$\nabla \cdot \overline{\mathbf{u}} = 0 \tag{A.11}$$

Non-dimensional parameter	Relation
x^*	$\frac{x}{D}$
y^*	$\frac{y}{D}$
u^*	$\frac{u}{U_\infty}$
v^*	$\frac{v}{U_\infty}$
t^*	$\frac{t}{D/U_\infty}$
p^*	$\frac{p}{\rho_\infty U_\infty^2}$
ρ^*	$\frac{\rho}{\rho_\infty}$
ν^*	$\frac{\nu}{\nu_\infty}$

Table A.1: Non-dimensional parameters used for the non-dimensional URANS equations

The non-dimensional terms used for deriving the non-dimensional URANS are tabulated in tab. A.1.

B

Non-dimensional form of EOM

The equations of motion for a 1 degree-of-freedom structural system with an aerodynamic excitation force can be described by the following equation:

$$m\ddot{y} + c\dot{y} + k_s y = F_y \tag{B.1}$$

The natural frequency of this system is:

$$\omega_n = \sqrt{k_s/m} \tag{B.2}$$

and the critical damping coefficient:

$$c_c = 2\sqrt{k_s m} = 2m\sqrt{k_s/m} = 2m\omega_n \tag{B.3}$$

The damping coefficient can then be defined as the ratio of the actual damping against the critical damping:

$$\zeta = c/c_c = \frac{c}{2\sqrt{k_s m}} \tag{B.4}$$

Looking back to eq. B.1, the damping coefficient c can be expressed in the natural frequency and damping ratio by the following relation:

$$c = c_c \cdot \zeta = 2m\omega_n\zeta \tag{B.5}$$

And the spring stiffness constant by:

$$k_s = \omega_n^2 m \tag{B.6}$$

Finally, combining these last two expressions with eq. B.1 and dividing all terms by the mass yields:

$$\frac{d^2y}{dt^2} + 2\zeta\omega_n\frac{dy}{dt} + \omega_n^2 y = F_y/m \tag{B.7}$$

The following non-dimensional terms are introduced to form the non-dimensional equations of motion:

Non-dimensional parameter	Relation
y^*	$\frac{y}{D}$
t^*	$f_n t$
C_L	$\frac{F_y}{\frac{1}{2}\rho U^2 DL}$
m^*	$\frac{2m}{\rho D^2}$
U^*	$\frac{U}{\omega_n D}$
p^*	$\frac{p}{\rho_\infty U^2}$
ρ^*	$\frac{\rho}{\rho_\infty}$
ν^*	$\frac{\nu}{\nu_\infty}$

Table B.1: Non-dimensional parameter definitions

After substituting these non-dimensional parameters in eq. B.7, the following relation is obtained:

$$D\omega_n^2\left(\frac{d^2y^*}{dt^{*2}}\right)+D\omega_n\left(2\zeta\omega_n\frac{dy^*}{dt^*}\right)+D\left(\omega_n^2y^*\right)=C_L\frac{1}{2}\rho U^2DL\frac{1}{\rho D^2m^*\frac{1}{2}} \tag{B.8}$$

By processing all terms the following equation is obtained:

$$D\omega_n^2\frac{d^2y^*}{dt^{*2}}+D\omega_n^2 2\zeta\frac{dy^*}{dt^*}+D\omega_n^2y^*=C_LU^2\frac{1}{Dm^*} \tag{B.9}$$

Dividing all the terms by $\omega_n^2 D$ yields:

$$\frac{d^2y^*}{dt^{*2}}+2\zeta\frac{dy^*}{dt^*}+y^*=\frac{1}{\omega_n^2D}C_LU^2\frac{1}{Dm^*} \tag{B.10}$$

Rearranging leads to:

$$\frac{d^2y^*}{dt^{*2}}+2\zeta\frac{dy^*}{dt^*}+y^*=\frac{U^2}{\omega_n^2D^2}\frac{C_L}{m^*} \tag{B.11}$$

The reduced velocity of tab. B.1 is then finally used to derive the non-dimensional equations of motion for VIV:

$$\frac{d^2y^*}{dt^{*2}}+2\zeta\frac{dy^*}{dt^*}+y^*=U^{*2}\frac{C_L}{m^*} \tag{B.12}$$

C

Moving-mesh quality

The mesh quality of all the meshes were evaluated before in ch. 3, paragraph 3.1.2 throughout *ANSYS ICEM*. These evaluations were done for the stationary meshes. In order to see if the initial mesh quality was preserved during the oscillations, an additional time-dependent quality study was performed on the meshes. The mesh quality was studied by using the 1-way coupled model (in *OpenFOAM*), this allowed the specification of a certain harmonical motion trajectory.

Since the mesh quality was evaluated in *OpenFOAM*, different metrics were used. In essence, two mesh parameters were studied: skewness and non-orthogonality. The skewness ratio, computed by *OpenFOAM*, is the distance between the interpolated face centre and actual face centre locations divided by the distance of the two concerned, adjacent cell centres. The smaller this ratio, the smaller the error that is introduced by the skewness. The maximum skewness ratio for the initial mesh m2.2 was found to be $\xi_{max} = 1.0446$, which was deemed as satisfactory. Skewness is important for the convective terms being solved properly, as these terms require the computation of the face values. Besides the skewness, the non-orthogonality was also evaluated for the moving mesh. The non-orthogonality is represented by the angle between the cell-centre vector of two adjacent cells and the face-normal vector of their common face. An angle of 0° would be the best scenario. For the mesh m2.2, the maximum non-orthogonal angle was found to be $\chi_{max} \approx 26°$ and the average angle of the whole domain $\chi_{mean} \approx 9°$. These values have considered to be very well and relatively close to the ideal zero degrees. Non-orthogonality has the biggest impact on the solvability of the diffusive terms. Within *OpenFOAM*, it is possible to correct for this error by introducing an extra corrector within the PISO or PIMPLE loop, called *nNonOrthogonalCorrectors*. In the present work, this corrector was always set equal to 1.

The skewness ratio and non-orthogonality angle have been evaluated for two motion trajectories: $y^*_{max} = 0.1, f^* = 2.06$ (dynamic mesh dm1.1) and $y^*_{max} = 1, f^* = 2.06$ (dynamic mesh dm2.1). The first input motion has been used as a realistic input for the 1-way model in a couple of simulations. The second motion trajectory with the higher amplitude has been studies as a more extreme case to challenge the mesh deformation algorithm. The frequency was set higher as well in both simulations to see if the diffusion was working well for rapidly moving meshes. The peak-to-peak variations of these metrics have been tabulated in tab. C.1. The metrics did not vary significantly over time as is shown in tab. C.1.

Parameter	**dm1.1:** $A^* = 0.1, f^* = 2.06$	**dm2.1:** $A^* = 1, f^* = 2.06$
ξ_{max}	0.2%	0.19%
χ_{max}	0.8%	0.85%

Table C.1: Dynamic mesh metrics peak-to-peak variation over time

It has to be noted here, these metrics represent the global maximum found by *OpenFOAM* within the computational domain. It is possible that the metrics showed higher variations over time locally in the domain. The dynamic mesh quality was not assessed locally in the computational domain in this study.

Bibliography

[1] "OpenFOAM, Open-source Field Operation and Manipulation," 2018.

[2] G. W. Jones Jr., J. J. Cincotta, and R. W. Walker, "Aerodynamic Forces on a Stationary and Oscillating Circular Cylinder at High Reynolds Numbers," tech. rep., Washington, D.C., 1969.

[3] R. D. Blevins, *Flow-Induced Vibration.* Malabar, Fla: Krieger Publishing Company, 2nd ed., 2001.

[4] R. Gopalakrishnan, *Vortex-Induced Forces on Oscillating Bluff Cylinders.* PhD thesis, Massachusetts Institute of Technology, 1993.

[5] D. Shiels, A. Leonard, and A. Roshko, "Flow-induced vibration of a circular cylinder at limiting structural parameters," *Journal of Fluids and Structures*, vol. 15, no. 1, pp. 3–21, 2001.

[6] A. Ho and A. Mbistrova, "The European offshore wind industry - Key trends and statistics 2016," 2017.

[7] *Renewable power generation costs in 2017.* IRENA, 2018.

[8] M. Zdravkovich, *Flow Around Circular Cylinders. Fundamentals, vol. 1.* New York, N.Y.: Oxford University Press, 1997.

[9] A. Postnikov, E. Pavlovskaia, and M. Wiercigroch, "2DOF CFD calibrated wake oscillator model to investigate vortex-induced vibrations," *International Journal of Mechanical Sciences*, vol. 127, no. 7, pp. 176–190, 2017.

[10] C. Dyrbye and S. O. Hansen, *Wind Loads on Structures.* Chichester, England: John Wiley & Sons, 1997.

[11] S. Hickel and A. Vire, "Lecture notes on CFD for Aerospace Engineers," 2016.

[12] R. N. Govardhan and C. H. Williamson, "Defining the 'modified Griffin plot' in vortex-induced vibration: Revealing the effect of Reynolds number using controlled damping," *Journal of Fluid Mechanics*, vol. 561, pp. 147–180, 2006.

[13] P. W. Bearman, "Circular cylinder wakes and vortex-induced vibrations," *Journal of Fluids and Structures*, vol. 27, no. 5-6, pp. 648–658, 2011.

[14] T. Sarpkaya, "A critical review of the intrinsic nature of vortex-induced vibrations," *Journal of Fluids and Structures*, vol. 19, no. 4, pp. 389–447, 2004.

[15] C. H. Williamson and A. Roshko, "Vortex formation in the wake of an oscillating cylinder," *Journal of Fluids and Structures*, vol. 2, no. 4, pp. 355–381, 1988.

[16] J. D. Anderson, *Fundamentals of Aerodynamics.* New York, N.Y.: McGraw-Hill, 5th ed., 2011.

[17] M. Van Dyke, *An Album of Fluid Motion.* Stanford, Calif: The Parabolic Press, 4th ed., 1988.

[18] M. L. Facchinetti, E. de Langre, and F. Biolley, "Coupling of structure and wake oscillators in vortex-induced vibrations," *Journal of Fluids and Structures*, vol. 19, no. 2, pp. 123–140, 2004.

[19] G. Koopmann, *On the wind-induced vibrations of circular cylinders.* PhD thesis, Catholic University of America, 1967.

[20] J. H. Lienhard, "Synopsis of lift, drag, and vortex frequency data for rigid circular cylinders," *Washington State University College of Engineering Research Division Bulletin 300*, pp. 1–32, 1966.

[21] C. Farell, "Closure on Flow Around Fixed Circular Cylinders: Fluctuating Loads," *ASCE Journal of Engineering Mechanics*, vol. 109, no. 4, pp. 1153–1156, 1983.

[22] C. Farell and J. Blessmann, "On critical flow around smooth circular cylinders," *Journal of Fluid Mechanics*, vol. 136, pp. 375–391, 1983.

[23] E. Achenbach and E. Heinecke, "On Vortex Shedding from Smooth and Rough Cylinders in the Range of Reynolds Numbers 6x10ˆ3 to 5x10ˆ6," *Journal of Fluid Mechanics*, vol. 109, no. 1, pp. 239–251, 1981.

[24] P. W. Bearman, "On vortex shedding from a circular cylinder in the critical Reynolds number regime," *Journal of Fluid Mechanics*, vol. 37, no. 3, pp. 577–585, 1969.

[25] A. Roshko, "Experiments on the flow past a circular cylinder at very high Reynolds number," *Journal of Fluid Mechanics*, vol. 10, no. 3, pp. 345–356, 1961.

[26] R. L. Panton, *Incompressible Flow*. New York, N.Y.: Wiley-Interscience, 1984.

[27] K. M. Barnett and J. Cermak, "Turbulence induced changes in vortex shedding from a circular cylinder," Tech. Rep. 26, Colorado State University, Fort Collins, Colorado, 1974.

[28] T. Sarpkaya, "Hydrodynamic damping, flow-induced oscillations, and biharmonic response," *Journal of Offshore Mechanics and Arctic Engineering*, vol. 117, no. 4, pp. 232–238, 1995.

[29] C. Williamson and R. Govardhan, "Vortex-Induced Vibrations," *Annual Review of Fluid Mechanics*, vol. 36, no. 1, pp. 413–455, 2004.

[30] C. C. Feng, *The measurement of vortex induced effects in flow past stationary and oscillating circular and D-section cylinders*. PhD thesis, University of British Columbia, 1968.

[31] O. M. Griffin, R. A. Skop, and S. E. Ramberg, "The resonant vortex-excited vibrations of structures and cable systems," *7th Offshore Technol. Conf.*, 1975.

[32] O. M. Griffin, "Vortex-excited cross-flow vibrations of a single cylindrical tube," *Journal of Pressure Vessel Technology, ASME*, vol. 102, no. 2, pp. 158–166, 1980.

[33] R. A. Skop and S. Balasubramanian, "A new twist on an old model for vortex-excited vibrations," *Journal of Fluids and Structures*, vol. 11, no. 4, pp. 395–412, 1997.

[34] H. M. Blackburn and G. E. Karniadakis, "Two- and Three-Dimensional Simulations of Vortex-Induced Vibration of a Circular Cylinder," in *Third (1993) International Offshore and Polar Engineering Conference*, no. 3, (Singapore, Singapore), pp. 715–720, 1993.

[35] L. Wooton and C. Scruton, "Seminar on Modern Design of Wind-Sensitive Structures," in *Construction Industry Research and Information Association*, (London), pp. 65–81, 1970.

[36] J. K. Vandiver and J.-Y. Jong, "The relationship between in-line and cross-flow vortex-induced vibration of cylinders," *Journal of Fluids and Structures*, vol. 1, no. 4, pp. 381–399, 1987.

[37] R. A. Skop, O. M. Griffin, and S. E. Ramberg, "Strumming predictions for the Seacon II experimental mooring.," *Offshore Technology Conference*, vol. 3, pp. 61–66, 1977.

[38] M. Zdravkovich, "Modification of vortex shedding in the synchronization range," *Journal of Fluids Engineering, ASME*, vol. 104, no. 4, pp. 513–517, 1982.

[39] A. Ongoren and D. Rockwell, "Flow structures from an oscillating cylinder Part 1. Mechanics of phase shift and recovery in the near wake," *Journal of Fluid Mechanics*, vol. 191, pp. 197–223, 1988.

[40] A. Ongoren and D. Rockwell, "Flow structure from an oscillating cylinder Part 2. Mode competition in the near wake," *Journal of Fluid Mechanics*, vol. 191, pp. 225 – 245, 1988.

[41] J. D. Anderson, G. Degrez, J. Degroote, E. Dick, R. Grundmann, and J. Vierendeels, *Computational Fluid Dynamics: An Introduction*. A Von Karman Institute Book, Berlin: Springer, 3 ed., 2003.

[42] J. H. Ferziger and M. Peric, *Computational Methods for Fluid Dynamics*. New York, N.Y.: Springer-Verlag Berlin Heidelberg, 3 ed., 2002.

[43] G. Vaz, R. van der Wal, C. Mabilat, and P. Gallagher, "Viscous Flow Computations on Smooth Cylinders: A Detailed Numerical Study With Validation," in *26th International Conference on Offshore Mechanics and Arctic Engineering*, no. 3, pp. 849–860, 2007.

[44] U. Piomelli, "Large-eddy and direct simulation of turbulent flows," 2004.

[45] D. C. Wilcox, "Reassessment of the Scale-Determining Equation for Advanced Turbulence Models," *AIAA Journal*, vol. 26, no. 11, pp. 1299–1310, 1988.

[46] W. P. Jones and B. E. Launder, "The prediction of laminarization with a two-equation model of turbulence," *International Journal of Heat and Mass Transfer*, vol. 15, no. 2, pp. 301–314, 1972.

[47] F. R. Menter, "Two-equation eddy-viscosity turbulence models for engineering applications," *AIAA Journal*, vol. 32, no. 8, pp. 1598–1605, 1994.

[48] P. Catalano, M. Wang, G. Iaccarino, and P. Moin, "Numerical simulation of the flow around a circular cylinder at high Reynolds numbers," *International Journal of Heat and Fluid Flow*, vol. 24, no. 4, pp. 463–469, 2003.

[49] M. C. Ong, T. Utnes, L. E. Holmedal, D. Myrhaug, and B. Pettersen, "Numerical simulation of flow around a smooth circular cylinder at very high Reynolds numbers," *Marine Structures*, vol. 22, no. 2, pp. 142–153, 2009.

[50] S. P. Singh and S. Mittal, "Flow past a cylinder: shear layer instability and drag crisis," *International Journal for Numerical Methods in Fluids*, vol. 47, no. 1, pp. 75–98, 2005.

[51] G. F. Rosetti, G. Vaz, and A. L. C. Fujarra, "URANS Calculations for Smooth Circular Cylinder Flow in a Wide Range of Reynolds Numbers: Solution Verification and Validation," *Journal of Fluids Engineering, Transactions of the ASME*, vol. 134, no. 12, pp. 1–18, 2012.

[52] E. Achenbach, "Distribution of local pressure and skin friction around a circular cylinder in cross-flow up to Re = 5x10^6," *Journal of Fluid Mechanics*, vol. 34, no. 4, pp. 625–639, 1968.

[53] Z. Zheng and J. Lei, "Application of the γ-Re θ Transition Model to Simulations of the Flow Past a Circular Cylinder," *Flow, Turbulence and Combustion*, vol. 97, no. 2, pp. 401–426, 2016.

[54] A. Travin, M. Shur, M. Strelets, and P. Spalart, "Detached-Eddy Simulations Past a Circular Cylinder," *Flow ,Turbulence and Combustion*, vol. 63, no. 1-4, pp. 293–313, 2000.

[55] F. F. Grinstein and G. E. Karniadakis, "Alternative LES and hybrid RANS/LES for turbulent flows," *Journal of Fluids Engineering, ASME*, vol. 124, no. 4, pp. 821–822, 2002.

[56] M. Breuer, "A challenging test case for large eddy simulation: high Reynolds number circular cylinder flow," *International Journal of Heat and Fluid Flow*, vol. 21, no. 5, pp. 648–654, 2000.

[57] T. Staubli, "Calculation of the vibration of an elastically mounted cylinder using experimental data from forced oscillation," *Journal of Fluids Engineering, ASME*, vol. 105, no. 2, pp. 225–229, 1983.

[58] F. S. Hover, A. H. Techet, and M. S. Triantafyllou, "Forces on oscillating uniform and tapered cylinders in crossflow," *Journal of Fluid Mechanics*, vol. 363, pp. 97–114, 1998.

[59] D. Newman and G. E. Karniadakis, "Simulations of flow over a flexible cable: A comparison of forced and flow-induced vibration," *Journal of Fluids and Structures*, vol. 10, no. 5, pp. 439–453, 1996.

[60] M. Nakano and D. Rockwell, "Flow Structure in the Frequency-Modulated Wake of a Cylinder," *Journal of Fluid Mechanics*, vol. 266, pp. 93–119, 1994.

[61] M. Nakano and D. Rockwell, "The wake from a cylinder subjected to amplitude-modulated excitation," *Journal of Fluid Mechanics*, vol. 247, pp. 79–110, 1993.

[62] D. Trimarchi, *Analysis of downwind sail structures using non-linear shell finite elements*. PhD thesis, University of Southampton, 2012.

[63] C. Förster, W. A. Wall, and E. Ramm, "Artificial added mass instabilities in sequential staggered coupling of nonlinear structures and incompressible viscous flows," *Computer Methods in Applied Mechanics and Engineering*, vol. 196, no. 7, pp. 1278–1293, 2007.

[64] A. Placzek, J.-F. Sigrist, and A. Hamdouni, "Numerical simulation of an oscillating cylinder in a cross-flow at low Reynolds number: Forced and free oscillations," *Computers and Fluids*, vol. 38, no. 1, pp. 80–100, 2009.

[65] B. S. Carmo, S. J. Sherwin, P. W. Bearman, and R. H. J. Willden, "Flow-induced vibration of a circular cylinder subjected to wake interference at low Reynolds number," *Journal of Fluids and Structures*, vol. 27, no. 4, pp. 503–522, 2011.

[66] K. Schulz and Y. Kallinderis, "Unsteady Flow Structure Interaction for Incompressible Flows Using Deformable Hybrid Grids," *Journal of Computational Physics*, vol. 143, no. 2, pp. 569–597, 1998.

[67] J. Yang, S. Preidikman, and E. Balaras, "A strongly coupled, embedded-boundary method for fluid-structure interactions of elastically mounted rigid bodies," *Journal of Fluids and Structures*, vol. 24, no. 2, pp. 167–182, 2008.

[68] J. S. Leontini, M. C. Thompson, and K. Hourigan, "The beginning of branching behaviour of vortex-induced vibration during two-dimensional flow," *Journal of Fluids and Structures*, vol. 22, no. 6-7, pp. 857–864, 2006.

[69] F. Menter, M. Kuntz, and R. Langtry, "Ten Years of Industrial Experience with the SST Turbulence Model," *The Fourth International Symposium on Turbulence, Heat and Mass Tranfer*, vol. 4, pp. 625–632, 2003.

[70] F. Menter and T. Esch, "Elements of industrial heat transfer prediction," in *Proceedings of the 16th Brazilian Congress of Mechanical Engineering (COBEM)*, pp. 117–127, 2001.

[71] NASA Langley, "Turbulence Model Benchmarking Working Group Turbulence Modeling Resource Title."

[72] O. Posdziech and R. Grundmann, "A systematic approach to the numerical calculation of fundamental quantities of the two-dimensional flow over a circular cylinder," *Journal of Fluids and Structures*, vol. 23, no. 3, pp. 479–499, 2007.

[73] P. Ferrand, J. Boudet, J. Caro, S. Aubert, and C. Rambeau, "Analyses of URANS and LES capabilities to predict vortex shedding for rods and turbines," in *Unsteady Aerodynamics, Aeroacoustics and Aeroelasticity of Turbomachines*, pp. 381–392, Springer, 2006.

[74] F. R. Menter, "Improved two-equation k-omega turbulence models for aerodynamic flows," *NASA Technical Memorandum*, no. 103978, pp. 1 – 31, 1992.

[75] H. Schlichting, *Boundary-Layer theory*. McGraw-Hill series in mechanical engineering, McGraw-Hill, 7th ed., 1979.

[76] J. Slater, "Examining Spatial (Grid) Convergence," 2008.

[77] S. Gomez, B. Graves, and S. Poroseva, "On the Accuracy of RANS Simulations of 2D Boundary Layers with OpenFOAM," *44th AIAA Fluid Dynamics Conference*, no. June, 2014.

[78] D. Lindblad, "Implementation and run-time mesh refinement for the k - omega SST DES turbulence model when applied to airfoils," tech. rep., Chalmers University of Technology, 2013.

[79] C. Kassiotis, "Which strategy to move the mesh in the Computational Fluid Dynamic code OpenFOAM," *Elements*, pp. 1–14, 2008.

[80] H. Jasak, "Dynamic Mesh Handling in OpenFOAM," *47th AIAA Aerospace Sciences Meeting including The New Horizons Forum and Aerospace Exposition*, no. January 2009, 2009.

[81] B. Devolder, P. Schmitt, P. Rauwoens, B. Elsaesser, and P. Troch, "A review of the implicit motion solver algorithm in OpenFOAM to simulate a heaving Buoy," *NUTTS conference 2015 : 18th Numerical Towing Tank Symposium*, no. 2015, pp. 1–6, 2015.

[82] D. Rixen, *Numerical methods in Engineering Dynamics*. Delft, The Netherlands: TU Delft, wb1416 - l ed., 2014.

[83] A. Dullweber, B. Leimkuhler, and R. Mclachlan, "Symplectic splitting methods for rigid body molecular dynamics," *The Journal of Chemical Physics*, vol. 107, no. 15, pp. 5840–5851, 1997.

[84] J. H. Chow and E. Y. Ng, "Strongly coupled partitioned six degree-of-freedom rigid body motion solver with Aitken's dynamic under-relaxation," *International Journal of Naval Architecture and Ocean Engineering*, vol. 8, no. 4, pp. 320–329, 2016.

[85] C. Scruton, "On the wind-excited oscillations of stacks, towers and masts," in *International Conference on the Wind Effects on Buildings and Structures*, pp. 798–832, National Physical Laboratory, 1963.

[86] R. Bourguet, G. E. Karniadakis, and M. S. Triantafyllou, "Lock-in of the vortex-induced vibrations of a long tensioned beam in shear flow," *Journal of Fluids and Structures*, vol. 27, no. 5-6, pp. 838–847, 2011.

[87] C. H. Williamson and R. Govardhan, "A brief review of recent results in vortex-induced vibrations," *Journal of Wind Engineering and Industrial Aerodynamics*, vol. 96, no. 6-7, pp. 713–735, 2008.

[88] C. Norberg, "Fluctuating lift on a circular cylinder: Review and new measurements," *Journal of Fluids and Structures*, vol. 17, no. 1, pp. 57–96, 2003.

[89] Y. Tanida, A. Okajima, and Y. Watanabe, "Stability of a circular cylinder oscillating in uniform or in a wake," *Journal of Fluid Mechanics*, vol. 61, no. 4, pp. 769–784, 1973.

[90] R. Franke, W. Rodi, and B. Schönung, "Numerical calculation of laminar vortex-shedding flow past cylinders," *Journal of Wind Engineering and Industrial Aerodynamics*, vol. 35, no. C, pp. 237–257, 1990.

[91] J. Park, K. Kwon, and H. Choi, "Numerical solutions of flow past a circular cylinder at reynolds numbers up to 160," *KSME International Journal*, vol. 12, no. 6, pp. 1200–1205, 1998.

[92] C. H. K. Williamson, "Oblique and parallel modes of vortex shedding in the wake of a circular cylinder at low Reynolds numbers," *Journal of Fluid Mechanics*, vol. 206, pp. 579–627, 1989.

[93] G. H. Koopmann, "The vortex wakes of vibrating cylinders at low Reynolds numbers," *Journal of Fluid Mechanics*, vol. 28, no. 3, pp. 501–512, 1967.

[94] P. Anagnostopoulos, "Numerical sutdy of the flow past a cylinder excited transversely to the incident stream. Part 1: Lock-in zone, hydrodynamic forces and wake geometry," *Journal of Fluids and Structures*, vol. 14, no. 6, pp. 819–851, 2000.

[95] S. S. Rao, *Mechanical Vibrations*. Singapore, Singapore: Pearson Education Limited, 5th editio ed., 2011.

[96] S. Mittal and V. Kumar, "Flow-induced vibrations of a light circular cylinder at reynolds numbers 103to 104," *Journal of Sound and Vibration*, vol. 245, no. 5, pp. 923–946, 2001.

[97] A. Placzek, J.-F. Sigrist, and A. Hamdouni, "Numerical simulation of an oscillating cylinder in a cross-flow at low Reynolds number: Forced and free oscillations," *Computers and Fluids*, vol. 38, no. 1, pp. 80–100, 2009.

[98] H. Blackburn and R. Henderson, "Lock-in behavior in simulated vortex-induced vibration," *Experimental Thermal and Fluid Science*, vol. 12, no. 2, pp. 184–189, 1996.

[99] G. Schewe, "On the force fluctuations acting on a circular cylinder in crossflow from subcritical up to transcritical Reynolds numbers," *Journal of Fluid Mechanics*, vol. 133, pp. 265–285, 1983.

[100] K. D. Squires, V. Krishnan, and J. R. Forsythe, "Prediction of the flow over a circular cylinder at high Reynolds number using detached-eddy simulation," *Journal of Wind Engineering and Industrial Aerodynamics*, vol. 96, no. 10-11, pp. 1528–1536, 2008.

[101] H. K. Versteeg and W. Malalasekera, *An Introduction to Computational Fluid Dynamics: The Finite Volume Method*. Pearson Education Limited, 2nd ed., 2007.

[102] P. R. Spalart and C. L. Rumsey, "Effective Inflow Conditions for Turbulence Models in Aerodynamic Calculations," *AIAA Journal*, vol. 45, no. 10, pp. 2544–2553, 2007.

[103] R. Vos and S. Farokhi, *Introduction to Transonic Aerodynamics*. Fluid Mechanics and Its Applications, Dordrecht, The Netherlands: Springer, 2015.

[104] J. van Nunen, "Pressure and forces on a circular cylinder in a cross flow at high Reynolds numbers," *Flow Induced Structural Vibrations*, pp. 748–754, 1974.

[105] F. Lupi, H. J. Niemann, and R. Höffer, "Aerodynamic damping model in vortex-induced vibrations for wind engineering applications," *Journal of Wind Engineering and Industrial Aerodynamics*, vol. 174, no. February 2017, pp. 281–295, 2018.

[106] E. Guilmineau and P. Queutey, "Numerical simulation of vortex-induced vibration of a circular cylinder with low mass-damping in a turbulent flow," *Journal of Fluids and Structures*, vol. 19, no. 4, pp. 449–466, 2004.

[107] G. Assi, *Mechanisms for flow-induced vibration of interfering bluff bodies*. PhD thesis, Imperial College London, 2009.

[108] R. Govardhan and C. H. K. Williamson, "Modes of vortex formation and frequency response of a freely vibrating cylinder," *Journal of Fluid Mechanics*, vol. 420, no. 1, pp. 85–130, 2000.

[109] P. Causin, J. F. Gerbeau, and F. Nobile, "Added-mass effect in the design of partitioned algorithms for fluid-structure problems," *Computer Methods in Applied Mechanics and Engineering*, vol. 194, no. 42-44, pp. 4506–4527, 2005.

[110] S. J. Hulshoff, *Aeroelasticity*. Delft, The Netherlands: TU Delft, version 11 ed., 2011.

[111] W. Gu, C. Chyu, and D. Rockwell, "Timing of vortex formation from an oscillating cylinder," *Physics of Fluids*, vol. 6, no. 11, pp. 3677–3682, 1994.